A CONTINUUM COUPLED MOISTURE-MECHANICAL DAMAGE CONSTITUTIVE MODEL FOR ASPHALT CONCRETE

A Dissertation

by

MARYAM SHAKIBA

Submitted to the Office of Graduate and Professional Studies of
Texas A&M University
in partial fulfillment of the requirements for the degree of

DOCTOR OF PHILOSOPHY

Chair of Committee,	Dallas N. Little
Co-Chair of Committee,	Eyad A. Masad
Committee Members,	Junuthula N. Reddy
	Mary B. Hueste
	Anastasia H. Muliana
Head of Department,	Robin Autenrieth

December 2013

Major Subject: Civil Engineering

ABSTRACT

The presence and flow of moisture degrade engineering properties of asphalt concrete as part of thermodynamic, chemical, physical, and mechanical processes. This detrimental effect is referred to as *moisture damage*. The aim of this dissertation is the development of physically based constitutive relationships along with a computational tool for the fundamental analysis of combined mechanical and moisture induced damage of asphalt concrete. Such a tool can greatly contribute to an improved material selection procedure and give insight into the various damage inducing mechanisms in asphalt concrete.

In this dissertation, thermo-hygro-mechanical constitutive relationships are developed based on the principle of virtual power and laws of thermodynamics in order to simulate moisture-induced damage of asphalt concrete. An evolution function is proposed to consider the detrimental effect of moisture diffusion and presence inside the material. The effect of pore water pressure is incorporated using Biot's coefficient. The Continuum Damage Mechanics (CDM) theory is extended to Continuum Moisture-Mechanical Damage Mechanics (CMMDM) to incorporate the moisture degradation effect and couple it to the mechanical response of asphalt concrete. The proposed moisture damage constitutive relationships are implemented in the Pavement Analysis using Nonlinear Damage Approach (PANDA) finite element (FE) package to model the moisture damage effect on the complex environmental-mechanical response of asphalt

concrete. The developed constitutive relationship and framework are validated over different loading scenarios and a range of experimental measurements.

The developed constitutive relationship and framework are applied to simulate pavement performance. The focus is on investigating the effects of various moisture conditioning periods on permanent deformation (rutting) and fatigue damage of asphalt pavements.

The constitutive and computational models are used to develop a framework for the simulation of the effect of moisture on the microstructural response of asphalt concrete. This framework explicitly incorporates the material microstructural distribution and properties. The developed framework is used to perform two-dimensional (2D) and three-dimensional (3D) micromechanical simulations in order to study and investigate the capability of the proposed constitutive relationships to predict the microstructural response of asphalt concrete under combined effect of moisture diffusion and mechanical loading.

DEDICATION

TO MY BELOVED PARENTS

Thank you for your endless patience, unconditional support, and continuous encouragement.

ACKNOWLEDGEMENTS

I am incredibly grateful to many people who helped me. There are far too many, to mention all of them; but I would like to thank several here. First, I gratefully thank my advisory committee chair and co-chair, Dr. D. N. Little and Dr. E. A. Masad, whose guidance and support were beyond invaluable both in technical expertise and nurturing of me as a researcher. I also wish to thank my other advisory committee member, Dr. J. N. Reddy, for his support. I thank Dr. Abu Al. Rub for the fruitful discussions we had during the early stages of this work. I would also like to thank Drs. A. H. Muliana and M. B. Hueste, my other advisory committee members, for their patience in reading this dissertation and their many pertinent comments. I especially would like to thank Dr. M. K. Darabi who was not less than an advisor for me. He provided me with his deep understanding on the subject and also encouragement during difficult research days.

I wish to thank all my fellow researchers who helped me in this research. Dr. Sun-Myung Kim, Dr. Taesun You, Eisa Rahmani, and Mahsa Arastoo were supportive and very insightful. I would like to offer special thanks to Drs. Richard Kim, and Emad Kassem for providing us data from wide range experimental tests on asphalt concrete that strongly aided my understanding of the mechanical response of asphalt mixes.

I gratefully acknowledge the Asphalt Research Consortium for funding my research.

NOMENCLATURE

$\theta^s_{\max}$	Maximum moisture concentration uptake of the solid part of material
α	$= s, l, \mathrm{g}$ and mc refer to solid, liquid, and moisture concentration gas phase
θ^s	Current moisture concentration in the solid part of material
$\boldsymbol{\varepsilon}$	Linearized strain tensor
$\mathbf{d}$	Eulerian rate of deformation tensor
$\boldsymbol{\varepsilon}^{ve,vp}$	Viscoelastic/viscoplastic strain tensor
$\mathbf{E}$	Lagrangian strain tensor
η^{mc}	Solid degree of saturation
E	Lagrangian specific internal energy
θ^v	Moisture content of the material expressed in volume of fluid per unit volume in connected cracks and voids
e^α	Eulerian specific internal energy
Θ^v	Lagrangian representation of moisture content inside cracks and voids
e	Eulerian specific internal energy of the media

$\xi^{(m)}$	Internal state variable associated with the viscoelastic processes
$\mathbf{F}$	Deformation gradient
χ_m	Thermodynamic forces associated with viscoelasticity
J	Jacobian of the deformation
$\boldsymbol{\pi}$	Piola-Kirchhoff stress tensor
$\mathbf{N}$	Unit normal vector to the surface at initial configuration
ρ^{α}	Density of solid, liquid and gas phase
$\mathbf{n}$	Unit normal vector to the surface at current configuration
$\boldsymbol{\sigma}$	Cauchy stress tensor of the media
n^{v}	Eulerian porosity
$\boldsymbol{\sigma}^{\alpha}$	Cauchy stress tensor of the different phase
$\mathrm{P}_{\mathrm{int}}$	Internal power
$\overline{\boldsymbol{\sigma}}$	Effective stress tensor
P_{ext}	External power
ϕ^{v}	Lagrangian porosity
P_{mech}	Mechanical power
ϕ^{e}	Erosion damage density

p^{α}	Liquid, gas, and moisture content pressure
ϕ_{eff}	Effective damage density
$\mathbf{Q}^{th}$	Lagrangian specific heat flux
K	Kinetic energy
$\mathbf{Q}^{\alpha}$	Lagrangian relative vector of fluid mass and gas
U	Internal energy
$\mathbf{q}^{th}$	Eulerian specific heat flux
H	External heat supplied to the body
$\mathbf{q}^{\alpha}$	Eulerian relative vector of fluid mass, gas and moisture concentration
ϕ^{Mech}	Mechanical damage density
R	Lagrangian specific heat production
ψ	Lagrangian specific Helmholtz free energy
r	Eulerian specific heat production
ψ^{α}	Helmholtz free energy of different phase
Ξ^{α}	Specific Lagrangian entropy
∇_{x}	Lagrangian gradient operator
s^{l}, s^{g}	Liquid and gas degree of saturation

$\nabla_{\mathbf{x}}(.)$ Eulerian gradient operator

ζ^{α} Specific Eulerian entropy

ω Moisture damage density

T Temperature

$\mathbf{u}^{\alpha}$ Displacement vector

$\mathbf{x}$ Position vector at current configuration

$\dot{\mathbf{u}}^{\alpha}$ Eulerian velocity vector

$\mathbf{X}$ Position vector at initial configuration

Hereafter, $\|.\|$ is the Euclidean norm of a second-rank tensor, $(.)$ stands for the tensor contractions, the superimposed dot $(.)$ indicates the material differentiation with respect to time ($\frac{D}{Dt}$), the prime (a') indicates the spatial differentiation with respect to time t ($\frac{\partial}{\partial t}$), bold letters designates vectors and tensors. The material and spatial gradient of a vector $\mathbf{a}$ are defined by $\nabla_{\mathbf{X}}$ and $\nabla_{\mathbf{x}} = \nabla$, respectively. The material and spatial divergence of a tensor field $\mathbf{A}$ are also defined by $Div(\mathbf{A})$ and $div(\mathbf{A})$, respectively.

TABLE OF CONTENTS

Page

LIST OF FIGURES

Page

LIST OF TABLES

Page

1. INTRODUCTION

1.1.Problem Statement

Asphalt concrete is a composite material that comprises aggregates (i.e., crushed rocks with different sizes and proportions), asphalt binder, and air voids. Asphalt concrete is widely used in constructing roadways, pavements, and airfield pavements, which are subjected to mechanical loadings (e.g., traffic loading) and environmental conditions (e.g., moisture, temperature, and oxidation) during their service lives. The combined effects of repeated traffic loading with fluctuating environmental conditions gradually degrade the properties of asphalt concrete pavements. Moisture and relative humidity have been long recognized to contribute substantially to the premature deterioration of asphalt pavements. The process of degradation begins as moisture moves through the pavement structure, Figure 1.1, either in the form of liquid or vapor. The presence and flow of moisture degrade engineering properties of asphalt concrete as part of thermodynamic, chemical, physical, and mechanical processes. This detrimental effect is referred to as *moisture damage*.

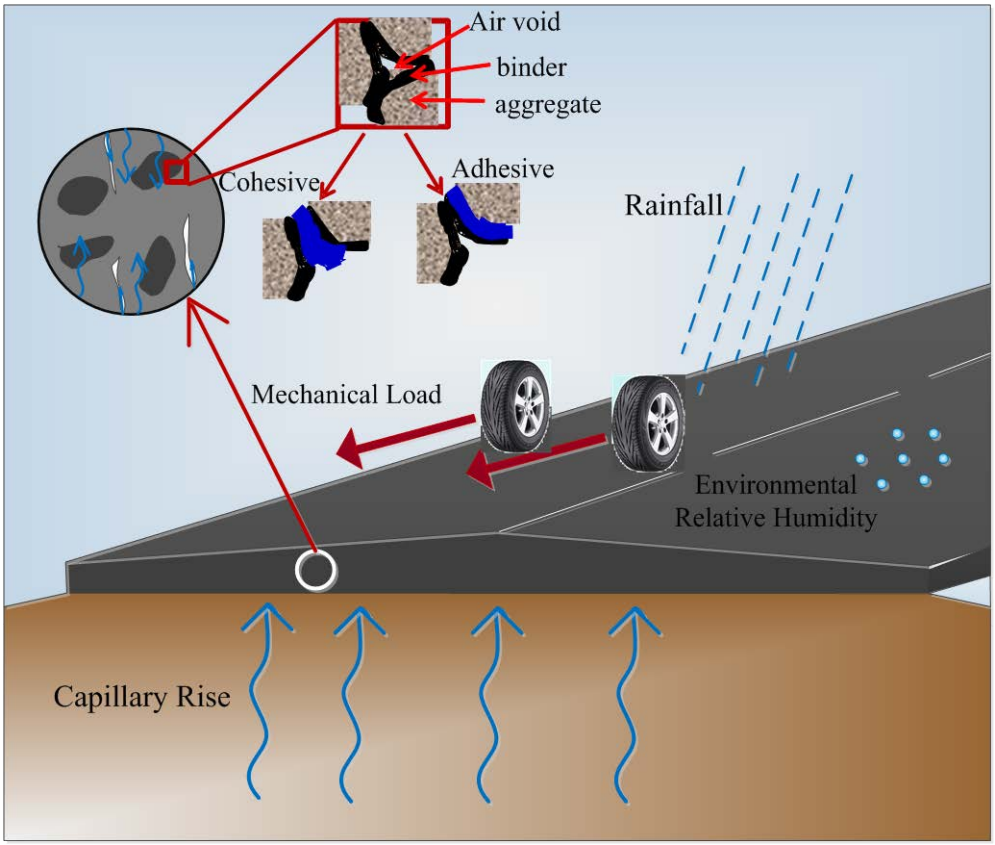

Figure 1.1. Mechanical loading and various types of moisture conditioning on a typical asphalt concrete pavement.

Expensive rehabilitation and replacement of pavements are necessary in many cases due to various types of distresses caused by moisture effects. Therefore, transforming the degradation solution from a repair to a prevention state is greatly desired. It is essential to develop a robust and comprehensive physically based constitutive relationship and computational scheme that can effectively simulate the macroscopic performance of asphalt pavements during their service life. This consists of a constitutive relationship to simulate moisture degradation effects and also a framework

to couple it to the thermo- viscoelastic, viscoplastic, and viscodamage response of asphalt concrete.

Moisture transport phenomenon and resistance of asphalt concrete to moisture-induced damage depend on aggregate mineral composition, proportions of the constituents (mix design), physical-chemical properties of the constituents, and other microstructural features (e.g., air void content and size distributions). Although the macromechanical behavior of asphalt concrete as a composite material under coupled moisture effects and mechanical loading is procurable by experimental testing, it is difficult to control microstructural features (e.g., aggregates, shape, size, and dimension) and characterize the corresponding macromechanical response. Therefore, it is desirable to develop micromechanical models that utilize proper constitutive relationships and realistic microstructural representations of asphalt concrete to account for the effects of material variations in predicting the macroscopic response of asphalt concrete subjected to combinations of mechanical loading and moisture effects.

The micromechanical analysis provides (1) the relation between the macroscopic mechanical behavior of material and its constituent's composition and geometric arrangement; and (2) the stresses, strains, and damage distributions within the material components for a single average continuum loading state.

In this work, a unified thermo-hygro-mechanical constitutive relationship is developed to simulate moisture-induced damage of asphalt concrete based on the principle of virtual power and laws of thermodynamics. The Continuum Damage

Mechanics (CDM) theory is extended to Continuum Moisture-Mechanical Damage Mechanics (CMMDM) to incorporate the moisture degradation effect and couple it to the mechanical response of asphalt concrete. The proposed moisture damage constitutive relationship is implemented in the Pavement Analysis using Nonlinear Damage Approach (PANDA) FE package to model the moisture damage effect on the complex environmental-mechanical response of asphalt concrete. The developed constitutive relationship and framework are validated over different loading scenarios and a range of experimental measurements. Finally, micromechanical simulations are conducted to study the microstructural response of asphalt concrete under combined effect of moisture diffusion and mechanical loading.

1.2.Background and State of the Art

Moisture-induced damage is a complex phenomenon that involves thermodynamic, chemical, physical, and mechanical processes. Once moisture diffuses through the solid phase, the substitution of moisture at the aggregate-binder interface is a thermodynamically favorable phenomenon, Figure 1.2(a). Moisture substitution at the aggregate-binder interface yields separation of the aggregate from the binder and is one of the most common distresses associated with moisture, known as adhesive moisture damage. The adhesion bond, which depends on the surface free energy of asphalt binder, aggregate and moisture, is an important factor that determines the moisture susceptibility of asphalt concrete. The repeated action of traffic loading and continuous diffusion of

moisture cause progressive dislodgement of aggregates, which is known as stripping or raveling.

The chemical reactions between moisture and asphalt leads to the degradation of asphalt binder and its overall cohesion, Figure 1.2(b). This type of degradation is known as cohesive moisture damage.

The presence of moisture inside the interconnected cracks and voids of the asphalt concrete may lead to fast water flow due to traffic loading on the pavements, Figure 1.2(c). The continuous action of water flowing past the mastic may have an erosion effect on the mastic and cause its particles to be removed. This is a physical moisture-induced damage process, which depends on the desorption characteristics of the mastic. The loss of mastic particles as a consequence of water flow may be referred to as 'washing away', 'scouring' or 'erosion' of the binder (Kringos et al., 2008a).

Finally, the traffic loading on a pavement with some completely saturated micro-cracks and voids locally causes intense water pressure fields in the pores, Figure 1.3(d). These excess pore pressures may even be generated away from the actual wheel path, since the water has no time to redistribute itself within the pavement. The pore pressure contributes extra stress within the asphalt concrete, which may cause additional mechanical damage within the asphalt components (Martyushev and Seleznev, 2006; Taylor and Khosla, 1983; Yang et al., 2005). Pore water pressure effect is categorized in this research as a mechanical moisture-induced damage process, since it is directly related to the application of loading to the asphalt concrete (Kringos et al., 2008a).

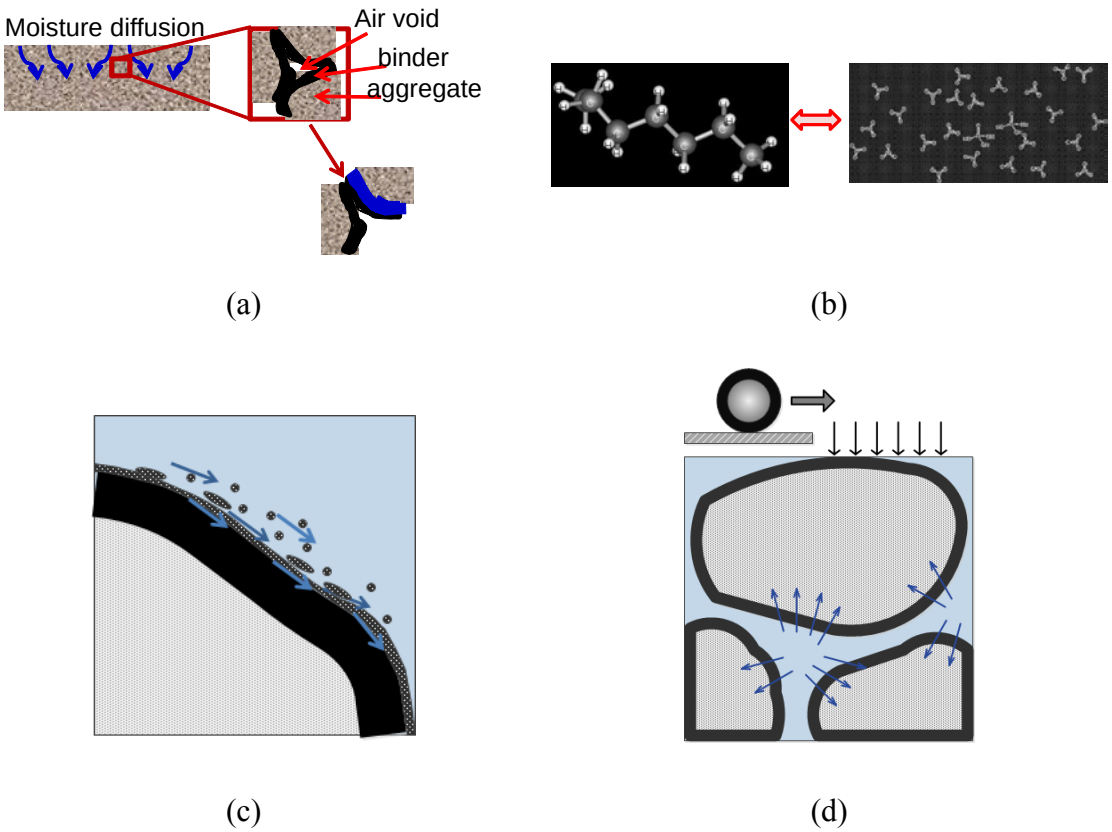

Figure 1.2. Different moisture-induced damage mechanisms; (a) Thermodynamic, (b) Chemical, (c) Physical, (d) Mechanical processes.

Extensive experimental research has been conducted on the effect of moisture on the asphalt concrete response since 1932. Initial studies were done to determine the ratio of a mechanical property of the asphalt concrete such as stiffness and tensile strength at dry and at moisture-conditioned states. Several different methods have been used to accelerate moisture damage in asphalt concrete specimen through the use of vacuum saturation and applying freeze-thaw cycles. Boiling water and immersion tests are some

qualitative tests that have been used to determine the moisture sensitivity of asphalt mixes (Al-Swailmi and Terrel, 1992; Lottman, 1982; Plancher et al.). The deficiencies of these empirical tests are presented in a number of studies (Aschenbrener et al., 1995; Tarrar and Wagh, 1992).

During the last decade, researchers conducted experimental works and developed analytical models to study mechanical, physical, chemical, and thermodynamic processes that are involved in moisture damage. Efforts were conducted to simulate moisture degradation effects and predict asphalt concrete's behavior. Thermodynamic theories on surface free energies of the materials and their bonding were used to determine the work of adhesion. Modeling efforts have sought to consider the effects of changes in the surface energy at aggregate-mastic interfaces due to moisture diffusion on the damage process (Cheng et al., 2002; Kim et al., 2004; Majidzadeh and Brovold, 1966-9). The emulsion of water droplets in binders was investigated to understand moisture susceptibility of binder due to chemical reactions (Ziegler, 1981).

Physical degradation of asphalt mixtures happens due to the fast-flowing of water through the mix upon mechanical loading on the surface. This flow may cause erosion of the binder and mastic (Kringos and Scarpas, 2008; Kringos et al., 2008b; Kringos et al., 2007). Several researchers tried to conduct experimental tests and develop analytical methods to consider pore water pressure effect inside the asphalt pavement (Kandhal, 1992; Kringos et al., 2008b).

Moisture damage mechanisms cannot be distinguished as completely separated phenomena acting individually. The moisture damage process comprises of different mechanisms acting simultaneously (e.g. adhesion bond between aggregate and mastic comprises thermodynamic, mechanical, and chemical bonding). Researchers have discussed the contribution of surface roughness and surface texture to improve adhesion in terms of mechanical interlocking between the mastic and aggregate (Masad et al., 2005a; Pocius, 1997; Tarrar and Wagh, 1991).

Prior to understanding and modeling the moisture damage mechanism, different moisture transport processes and moisture diffusion coefficient should be determined. For this popuse, several researchers determined the different types of moisture transport mechanism (Kutay et al., 2007a, b; Masad et al., 2007a; Masad et al., 2007b) and moisture diffusion coefficients (Arambula et al., 2009; Kassem et al., 2006; Kringos et al., 2008c) of asphalt concrete material.

Primarily two approaches have been used to simulate moisture damage mechanisms: micromechanical modeling and macromechanical modeling. The micromechanical modeling approach considers degradation of mastic and the aggregate-mastic interface using cohesive elements (Caro et al., 2010a). Caro et al. (2010a) embedded cohesive elements at mastic-aggregate interfaces to simulate the effect of moisture on damage evolution at the interfaces. They represented the stiffness of the embedded elements as a function of moisture content. One of the main limitations of their method was that they predefined the direction of crack propagation.

Micromechanical approaches provide insight into effect of moisture on the response of asphalt concrete materials. However, it is difficult to use this approach for predicting pavement response under repeated loading due to its high computational cost.

The macromechanical modeling approach considers the mixture as a continuum without explicitly representing the constituents. This approach provides the advantage of predicting pavement response under repeated loading and realistic boundary conditions. Kringos, Scarpas, and their co-workers (Kringos and Scarpas, 2008; Kringos et al., 2008b; Kringos et al., 2008d) proposed a moisture damage variable as a function of moisture content to explain degradation of adhesive bond strength due to moisture. Graham (2009) used the continuum damage mechanics, CDM , approach and proposed a time-dependent evolution function for the moisture damage variable. These models and relationships are time-independent and do not account for gradual degradation due to presence of constant moisture; they do not consider the effect of moisture damage level (moisture state and history); and they consider the moisture damage as a reversible phenomenon (full recovery occurs upon drying). In addition, many of the existing relationships do not distinguish between adhesive and cohesive modes of moisture damage.

Kringos et. al. (2008a) coupled the pore water pressure effect to the mechanical response of asphalt concrete by introducing an equivalent plastic deformation parameter. They used a finite element code developed to simulate a continuum porous media (Liu, 2003) to simulate a saturated pore. For the coupling between two finite element codes,

they utilized an algorithm, which is based on the differences in time scales (i.e. the passing of a wheel load over a pavement happens in such a short time, that it is justified to pose that during this time, no moisture diffusion shall take place). Therefore, two different codes communicate to each other to transfer pore water pressure and deformations at each time step. This method actually was combined the pore water pressure effect with asphalt concrete response and it is not a complete coupling. The method used a code for simulation of porous medium in a continuum level and simulated a saturated pore as a media with 100% porosity. They did not incorporate the effective stress concept of the deformable media. Birgisson et. al. (2005) proposed an experimental procedure to control the moisture damage to be only due to the effect of pore water pressure. They analyzed and simulated the experiment using a finite element code developed to simulate geo-materials. Therefore, they did not consider the thermo-viscoelastic, viscoplastic, and viscodamage aspects of the mechanical behavior of asphalt concrete.

Most of the discussed models were developed based on simplified assumptions regarding the material factors that affect moisture damage. In addition, these models have not coupled moisture effect with the thermo- viscoelastic, viscoplastic, and viscodamage behavior of asphalt concrete. Therefore, it is imperative to develop a robust and comprehensive physically based framework to model moisture damage and couple it with thermo-mechanical response of asphalt concrete.

Very few attempts have been made to simulate the impact of the microstructure of asphalt concrete subjected to mechanical loading and moisture effects since such simulations require extensive computational time and are consequently very costly. Abu Al-Rub et al. (2011a) used X-ray computed tomography (CT) imaging to create a two-dimensional (2D) finite element (FE) microstructural representation of a typical dense-graded asphalt concrete composite. They utilized a thermo-mechanical constitutive relationship (Darabi et al., 2011a) to simulate the mechanical response of asphalt concrete subjected to mechanical loading. Kringos et al. (2008b) and Graham (2009) simulated an idealized 2D FE microstructural representation of asphalt concrete to investigate the response of moisture-conditioned specimens subjected to mechanical loading. Caro et al. (2010a) constructed a simple 2D FE microstructural representation of asphalt concrete and subjected it to cycles of moisture diffusion and mechanical loading. They embedded cohesive zone elements to simulate the effect of moisture on damage evolution at aggregate-mastic interfaces.

Because of the high complexity and very expensive computational cost there have been very few attempts to model the three-dimensional (3D) microstructure of asphalt concrete at dry condition and to the authors' best knowledge there is no with moisture conditioning. Recently, Abu Al-Rub et al. (2011a) and You et al. (2012) have employed the asphalt concrete material's coupled constitutive model of Darabi et al. (2011d) for simulating the thermo-mechanical response in 3D asphalt concrete's microstructure representation. The micromechanical representations are obtained based on 2D X-ray CT images at dry condition. The moisture aggravating effect has not been

studied on the more realistic microstructure (i.e. 3D representation) of asphalt concrete material. Thus, the 3D simulation of coupled moisture-mechanical response of asphalt concrete is imperative.

1.3.Research Objectives and Approaches

The conducted research includes three major objectives for the development, verification, and application of a moisture damage constitutive model to simulate and predict asphalt concrete behavior under combined effect of mechanical loading and moisture degradation.

1.3.1 Development of a Moisture Damage Constitutive Relationship and Couple it to the Mechanical Response of Asphalt Concrete

The objective is to develop a thermodynamic-based moisture damage constitutive relationship to simulate moisture degradation effects and couple it to the thermo-nonlinear-viscoelasticity, viscoplasticity, mechanical viscodamage of asphalt concrete.

The fundamental theory of continuum damage mechanics (CDM) based on the effective stress concept (Kachanov, 1958; Rabotnov, 1969) is extended to consider the moisture damaged state by introducing the undamaged-wet configuration. This new configuration modifies traditional CDM theories toward the development of a *continuum moisture-mechanical damage mechanic* (CMMDM) framework. Therefore, the complex thermo-viscoelastic, viscoplastic, and viscodamage response of asphalt concrete is

coupled to the moisture damage constitutive relationship to predict the material's response subjected to the mechanical loading and environmental conditions.

The mixture theory was used to modify the principle of virtual power and thermodynamics laws for partially saturated porous viscous media. The asphalt concrete material comprises solid phase (i.e. aggregates and mastic) and partially saturated air voids with evolving natural configurations. Moisture can flow through connected cracks and voids and diffuse through the solid phase, Figure 1.3. The principle of virtual power yields general partial differential equations that govern the viscoelastic solid, liquid, and viscodamage (moisture and mechanical) responses. The effective stress concept of CMMDM is used to define physically based moisture damage variable and couple it to the mechanical damage. The natural configuration's evolution is determined by a thermodynamic criterion, which is the maximization of the energy dissipation rate. Hence, a general thermodynamic framework is developed in this work to systematically derive constitutive relationships for partially saturated porous viscous media. The formulations are based on the use of independent state variables and emphasized on the decomposition of thermodynamic conjugate forces into energetic and dissipative components as Ziegler (1988) initially extended. A systematic procedure is used to determine the energetic and dissipative components from the Helmholtz free energy function and the rate of energy dissipation, respectively.

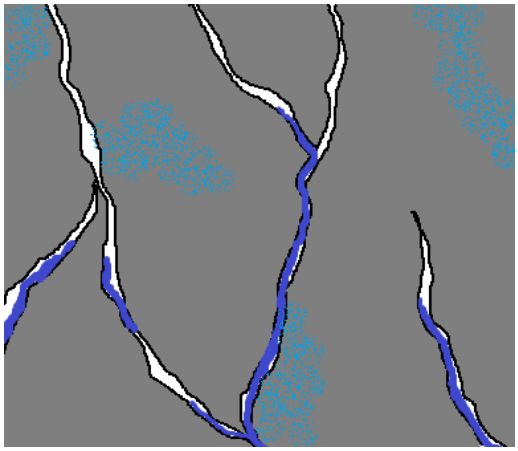

Figure 1.3. Presence and flow of moisture inside the solid phase and through the connected pores and cracks.

The explicated constitutive relationship is time-dependent, accounts for the irreversibility of moisture damage, and describes the damage process as a function of damage history and not only on the current moisture state. It is capable of considering the transition between adhesive and cohesive moisture damage. The developed constitutive relationship is also capable of considering the effect of pore water pressure on the asphalt pavement. The proposed constitutive relationship is implemented in the Pavement Analysis using Nonlinear Damage Approach (PANDA) FE package to model the moisture damage effect on the complex environmental-mechanical response of asphalt concrete.

1.3.2 Calibration and Validation of the Constitutive Relationships

The application of the proposed model to the analysis of asphalt mixes needs identification of several model parameters such as the material constants associated with

thermo- viscoelastic, viscoplastic, viscodamage, and moisture damage constitutive relationships. Researchers (Abu Al-Rub et al., 2010; Darabi et al., 2011e; Huang et al., 2011) developed consistent methods to determine the model parameters from designated experiments on the asphalt concrete mixtures. The second objective of this research is to design proper tests for determination of the developed moisture damage constitutive model parameters and validate the model with the obtained model parameters. First, different sets of aggregate-mastic pull-off tests are used to calibrate the adhesive moisture damage constitutive relationship. Then, tests are designed in such a way to propose a calibration procedure that decouples the effects of moisture conditioning period and moisture content. Modified Lottman (AASHTO, 2007) procedure is used to moisture condition the specimens. Experimental tests on dry and moisture-conditioned asphalt concrete are conducted at different stress levels, strain rates, and temperatures. Predictions of the constitutive relationship are compared with experimental measurements.

1.3.3 Application of the Developed Constitutive Relationships

The microstructural analysis of asphalt concrete is imperative to get insight into its internal behavior. This approach can also provide a design tool for road industry. Therefore, 2D and 3D micromechanical simulations are conducted to study the moisture effect on the mechanical response of asphalt concrete's microstructure. Macromechanical simulations are alos used to simulate and predict pavement performance under mechanical loading and moisture diffusion. The proposed model and

framework in this work are applicable to both micromechanical and macromechanical analyses.

Frist, Prediction of Pavement Performance Using the Proposed Constitutive Relationship. The aim of this research was to apply the developed constitutive relationship and framework to predict various distresses in pavements during their service life due to moisture-induced damage. The focus is on investigating the effects of moisture damage on the permanent deformation (rutting) and fatigue damage performance under various moisture conditioning period. However, the complex nature of the applied loading conditions, very large number of loading cycles, and complex constitutive behavior of asphalt concrete material make the accurate prediction of distresses in pavements a very difficult and challenging task. Even with the current power in computational analysis, conducting 3D finite element (FE) simulations for a pavement subjecting to millions of loading cycles and considering realistic wheel tracking and environmental loading conditions is almost impossible. 2D and 3D representation of asphalt pavement under equivalent loading and moving load is used to study the effect of moisture conditioning on the response of asphalt pavement.

*Second, Micromechanical Simulations.*To investigate the predictive capability of the proposed constitutive relationships, several 2D and 3D micromechanical numerical simulations are conducted. An X-ray Computed Tomography (CT) technique is used to capture planar images from a typical dense graded asphalt concrete specimen. The planar images are used to construct the 2D and 3D representations of the specimen. 2D

microstructural FE representation consists of aggregate, mastic and aggregate-mastic interface, which is capable to simulate independent evolution of adhesive and cohesive moisture damage density. The interface is not considered in 3D microstructural representation since it significantly increases the computational costs.

Microstructural representations are subjected to various mechanical and environmental loading conditions. These 2D and 3D micromechanical simulations illustrated the evolution of moisture-induced damage and how moisture damage affects the viscoelastic, viscoplastic, and damage response of asphalt concrete. It is shown that the modeling technique presented herein can predict crack propagation both in the mastic and at the aggregate-mastic interface without prescribing a predefined crack path.

2. CONTINUUM COUPLED MOISTURE-MECHANICAL DAMAGE MECHANICS FRAMEWORK

2.1 Classical Continuum Damage Mechanics (CDM)

Kachanov (1958) has pioneered the concept of CDM by introducing a scalar measure called continuity, ζ. He defined two configurations for a damaged material; (a) a nominal or damaged configuration, which is an apparent area of the material, and (b) an effective, intact or undamaged area, which is obtained by removing micro-damage from the damaged area and is responsible to carry the load, Figure 2.1. Then, Rabotnov (1969) physically defined the continuity variable based on these configurations as:

$$\zeta = \frac{\bar{A}}{A} \tag{2.1}$$

where A is the damaged (apparent) area and $\bar{A}$ is the real area (intact or undamaged area). The continuity parameter has, thus, values ranging from $\zeta = 1$ for intact (undamaged) material to $\zeta = 0$ indicating total rupture.

Odqvist and Hult (1961) introduced another variable, ϕ, defining the reduction of area because of the micro-damages:

$$\phi = 1 - \zeta = \frac{A - \bar{A}}{A} = \frac{A^d}{A} \tag{2.2}$$

where A^d is the area of micro-damages such that $A^d = A - \bar{A}$, Figure 2.1. ϕ is the so-called mechanical damage variable or density, which can be interpreted as the density of micro- damages (micro-cracks and micro-voids) induced due to mechanical loading with values ranging from 0 (undamaged) to 1 (complete damage). In fact, fracture or complete rupture mostly occurs when $\phi = \phi^c$, where ϕ^c is the critical damage density, which is a material property (Abu Al-Rub and Voyiadjis, 2003). In this study, isotropic damage is assumed such that the stress tensor components are degraded equally in different directions.

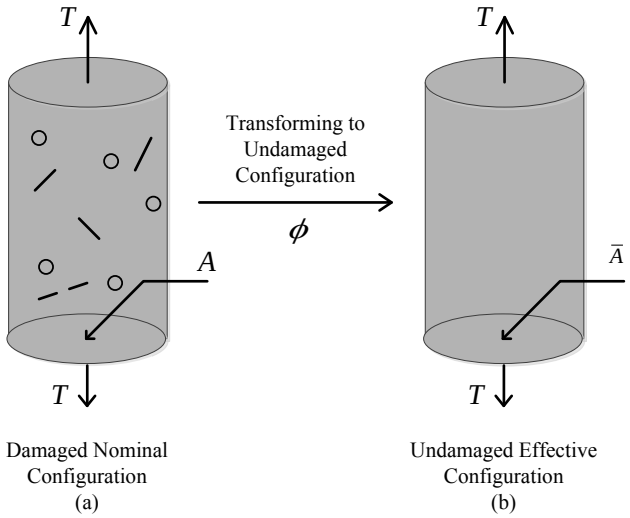

Figure 2.1. Schematic representation of the effective and nominal configurations.

Once the material degrades under mechanical loading, the intact portion of the material, which is not damaged (i.e. Undamaged configuration), will sustain further loading. Assuming that the applied forces in the nominal and effective configurations are equal, the relationship between stresses in the undamaged (effective) material and the damaged material is obtained as [see Chaboche (2003) for a concise review of effective stress in CDM]:

$$\bar{\boldsymbol{\sigma}} = \frac{\boldsymbol{\sigma}}{1-\phi} \tag{2.3}$$

where $\bar{\boldsymbol{\sigma}}$ is the effective stress tensor in the effective (undamaged) configuration and $\boldsymbol{\sigma}$ is the nominal Cauchy stress tensor in the nominal (damaged) configuration. The schematic representation of the nominal (damaged) and effective (undamaged) configurations is shown in Figure 2.1.

However, asphalt concrete is exposed to environmental conditions as well as mechanical loading. Environmental conditions especially moisture presence and flow degrade the material and reduce its sustainability. CDM theories are generalized in the next section to accommodate continuum moisture-mechanical theories by extending the effective configuration to the physically based wet-undamaged configuration. A moisture damage variable is defined within the proposed framework in order to consider the moisture aggravation effect and to couple moisture damage with mechanical damage.

2.2 Continuum Coupled Moisture-Mechanical Damage Mechanics (CMMDM)

This study modifies the well-known CDM framework to capture the moisture degradation effect on the material. The CDM configurations are extended to *wet-damaged*, *wet-undamaged*, and *dry-undamaged* natural configurations, Figure 2.2.

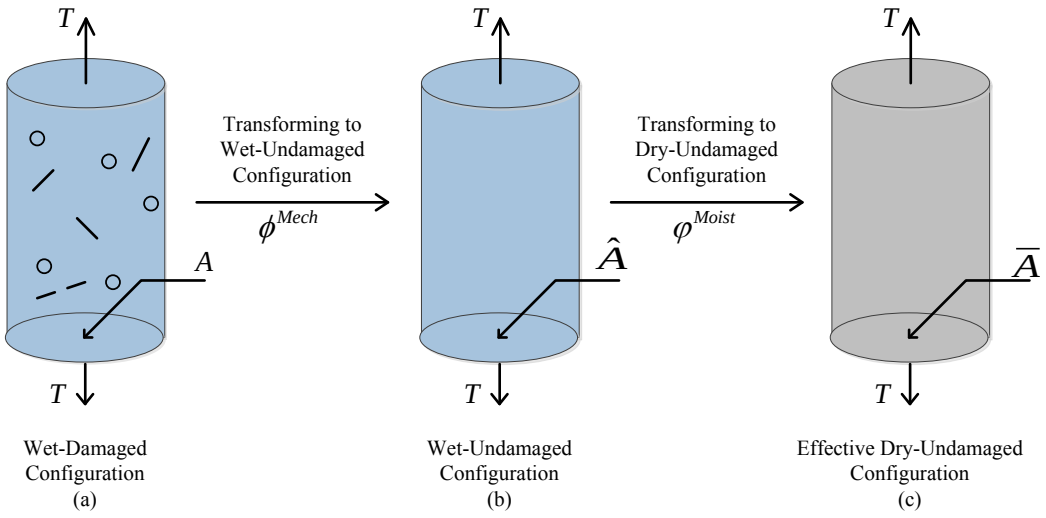

Figure 2.2. Schematic representation of (a) *wet-damaged*, (b) *wet-undamaged*, and (c) *dry-undamaged* natural configurations to develop Continuum Moisture-Mechanical Damage Mechanics framework.

Figure 2.2(a) shows a moisture conditioned cylindrical specimen subjected to uniaxial tensile load T at the current time t. Upon applying mechanical loading, micro-cracks and micro-voids nucleate and propagate through the specimen. Concurrently, as conditioning time increases, moisture causes degradation in material's stiffness and strength. Therefore, three different configurations are defined under the coupled

moisture-mechanical processes: (a) wet-damaged, (b) wet-undamaged; and (c) dry-undamaged. In the wet-damaged configuration, (a), micro-cracks and micro-voids have propagated due to mechanical loading while the material has also been degraded due to the presence of moisture. This configuration is the real configuration of the material, which has the cross-sectional area A. In the wet-undamaged configuration, (b), mechanically induced micro-cracks and micro-voids are removed from the cross-sectional area of the specimen. The cross-sectional area of this configuration is represented by $\hat{A}$. It should be noted that this configuration includes the degraded area due to the presence of the moisture. In the dry-undamaged configuration, (c), the load-bearing part of a material is represented by removing the degraded regions due to both mechanical and moisture loading conditions. This configuration has the cross-sectional area of $\overline{A}$ and includes only the virgin state of the materials (i.e. intact material). The area corresponding to undamaged-wet configuration has neither been damaged nor degraded and can be considered as the counterpart of the effective configuration of the classical CDM theories. Configuration "b" results when cracks and voids are removed from the wet-damaged configuration but the material is still degraded due to the presence of moisture, Figure 2.2(b). The effective (undamaged-dry) configuration is shown in Figure 2.2(c). This configuration includes the material that has never been mechanically damaged (intact material) because of moisture during the loading history. According to these definitions, one can write based on Figure 2.2:

$$A = A^{d} + \hat{A}; \qquad \hat{A} = A^{wd} + \overline{A} \tag{2.4}$$

where A, $\hat{A}$, and $\overline{A}$ are the cross-sectional area in the wet-damaged (nominal), wet-undamaged, and dry-undamaged (effective) configurations, respectively.

Similar to the CDM framework, it can be argued that once the material degrades under mechanical loading and moisture conditioning, further loading will be sustained only by the intact portion of the material which is damaged neither mechanically nor due to moisture (i.e. dry-undamaged configuration). It can be assumed that the applied forces in the nominal, wet, and effective configurations are equal, such that:

$$T = \sigma A = \hat{\sigma}\hat{A} = \overline{\sigma}\overline{A} \tag{2.5}$$

where σ is the nominal (apparent/effective) stress, $\hat{\sigma}$ is the stress in the wet-undamaged configuration, and $\overline{\sigma}$ is the effective stress in the dry-undamaged configuration (true or net stress). The superscripts ‘‘$-$’’ and ‘‘$\wedge$’’ designate the effective and wet-undamaged configurations, respectively. The following definitions are introduced for the mechanical and moisture damage internal state variables, respectively.

$$\omega = \frac{A^{wd}}{\hat{A}}; \qquad \phi = \frac{A^{d}}{A} \tag{2.6}$$

The term ϕ is the classical mechanical damage density variable ranging from zero to one, $0 \le \phi \le 1$, which is interpreted as micro-damage density such that $\phi = 0$ indicates no damage and $\phi = 1$ indicates complete damage (or fracture). ω is the moisture damage variable representing the aggravated material density due to moisture and similarly ranges from zero to one. $\omega = 0$ corresponds to the case when moisture

damage has not contributed to the degradation of the material and $\omega = 1$ shows that the material has been fully degraded due to moisture. Any value between zero and one (i.e. $0 < \omega < 1$) corresponds to the case that the materials integrity is only partially reduced due to moisture.

Substituting Eqs. (2.4) and (2.6) into Eq. (2.5) yields:

$$\boldsymbol{\sigma} = \bar{\boldsymbol{\sigma}}\left(1 - \phi_{eff}\right) \tag{2.7}$$

where ϕ_{eff} is the effective damage density ($0 \le \phi_{eff} \le 1$) capturing the combined effects of mechanical loading and moisture-conditioning on the mechanical responses, such that:

$$\left(1 - \phi_{eff}\right) = \left(1 - \omega\right)\left(1 - \phi\right) \tag{2.8}$$

According to Eqs. (2.7) and (2.8), $\phi_{eff} = 0$ indicates that the material has not been mechanically damaged nor moisture conditioned yet; whereas, $\phi_{eff} = 1$ indicates complete damage (or fracture) or full degradation due to coupled effects of mechanical loading and moisture damage.

The proposed configurations enhance the CDM framework to consider the moisture degradation in materials and couple it to the mechanical responses. This actually results in a strong coupling between these two types of damage. The mechanical and moisture damage components can then be coupled to the rest of the constitutive models using Eqs. (2.7) and (2.8). The proposed framework for modeling the moisture

damage mechanism naturally inherits the simplicity and robustness of the continuum damage mechanics framework. More importantly, following this framework makes the implementation of coupled moisture-mechanical models easy and avoids the complexities associated with direct coupling of moisture damage and mechanical damage to the rest of the constitutive models. Therefore, the existing numerical algorithms can easily be modified to consider the moisture effect as well. The proposed framework extends the continuum damage mechanic theories to the *continuum moisture-mechanical damage* theories.

It is noteworthy that the effective stress $\bar{\boldsymbol{\sigma}}$ is the one that drives viscoelastic and viscoplastic deformations. Moreover, it is usually argued that once the material is damaged, further loading can only affect the undamaged material skeleton. Hence, the viscoelastic, viscoplastic, and viscodamage models are defined as functions of variables in the effective configuration. The superimposed "$-$" in this work designates the effective configuration.

A transformation hypothesis is required to relate the nominal stress and strain tensors ($\boldsymbol{\sigma}$ and $\boldsymbol{\varepsilon}$) to the stress and strain tensors in the effective configuration ($\bar{\boldsymbol{\sigma}}$ and $\bar{\boldsymbol{\varepsilon}}$). For this purpose, one can either adapt the strain equivalence hypothesis (i.e. the strains in nominal and effective configurations are equal) or the strain energy equivalence hypothesis (i.e. any form of strain energy in the nominal configuration is equal to the corresponding strain energy in the effective configuration) [see Voyiadjis and Kattan (1999) for more details].

The strain energy equivalence hypothesis is intuitively more physically sound; however, it greatly complicates the constitutive models and their numerical implementation (Abu Al-Rub and Voyiadjis, 2003). Therefore, for simplicity in the finite element implementation of the subsequent complex constitutive equations, the strain equivalence hypothesis is adopted. Hence, one can assume that the nominal strain tensors $\boldsymbol{\varepsilon}$, $\boldsymbol{\varepsilon}^{nve}$, and $\boldsymbol{\varepsilon}^{vp}$ are equal to their counterparts in the effective configuration, $\overline{\boldsymbol{\varepsilon}}$, $\overline{\boldsymbol{\varepsilon}}^{nve}$, and $\overline{\boldsymbol{\varepsilon}}^{vp}$, such that:

$$\boldsymbol{\varepsilon} = \overline{\boldsymbol{\varepsilon}}, \ \boldsymbol{\varepsilon}^{nve} = \overline{\boldsymbol{\varepsilon}}^{nve}, \ \boldsymbol{\varepsilon}^{vp} = \overline{\boldsymbol{\varepsilon}}^{vp} \tag{2.9}$$

where $\boldsymbol{\varepsilon}^{nve}$ and $\boldsymbol{\varepsilon}^{vp}$ are the nonlinear viscoelastic and viscoplastic strain tensors in the nominal configuration, respectively; whereas $\overline{\boldsymbol{\varepsilon}}^{nve}$ and $\overline{\boldsymbol{\varepsilon}}^{vp}$ are the nonlinear viscoelastic and viscoplastic strain tensors in the effective configuration, respectively. This transformation hypothesis makes the numerical implementation of constitutive equations very easy and avoids the complexities associated with direct couplings between the damage model and different parts of the constitutive model. In fact, for small deformations and isotropic (scalar) damage assumptions, one can assume that the strain differences in the nominal and effective configurations are negligible (Abu Al-Rub and Voyiadjis, 2003), such that postulating the strain equivalence hypothesis seems admissible. However, the strain equivalence hypothesis results in linear variation of the stiffness modulus with the damage density, which is not experimentally motivated. To remedy this issue, Cicekli et al. (2004) and Abu Al-Rub and Voyiadjis (2004) modified Eq. (2.7), such that:

$$\bar{\boldsymbol{\sigma}} = \frac{\boldsymbol{\sigma}}{\left(1-\phi_{eff}\right)^2} \tag{2.10}$$

Eq. (2.10) allows the quadratic variation of the damaged stiffness with respect to the damage density when the strain equivalence hypothesis is use.

For the sake of simplicity, this study uses the strain equivalence hypothesis (Lemaitre and Chaboche, 1990) to relate the strain tensors in different configurations. Hence, one can assume that the nominal strain tensors (i.e. total strain, viscoelastic strain, and viscoplastic strain) are equal to their counterparts in the effective configuration (i.e. $\boldsymbol{\varepsilon} = \bar{\boldsymbol{\varepsilon}}$).

For large deformation theories when damage is significant, one may use alternative approaches such as postulating the strain energy equivalence hypothesis, power equivalence hypothesis, or taking into account the changes in the density of the damaged materials by adapting finite deformation theories (Abu Al-Rub and Darabi, 2012).

3. THERMODYNAMIC BASED FRAMEWORK FOR THE CONSTITUTIVE MODELING OF MOISTURE INDUCED DAMAGE IN A PARTIALLY SATURATED VISCOELASTIC MEDIA

Explicating thermodynamically consistent constitutive models for different materials have received great attention in recent decades. Since violating thermodynamics' models cannot trustfully describe material's behavior except under some particular and well-defined conditions. It enforces the First and Second Laws of Thermodynamics so that any model will obey these laws. Hence, the important advantage of these thermodynamic based frameworks is that the model cannot produce thermodynamically unreasonable results. This framework allows to develop more general theorems or to establish the applicability range of the existing hypothesis. Thermodynamic formulation emphasizes on the use of "internal variables" as an independent state variables to consider the past history of the material. The general theorem can be particularized to more specific material's model once a better understanding of the physics of such material achieved. Therefore, the motivation is explicating a rigorous and consistent thermodynamic based framework to describe a wide range of engineering materials.

The internal structure properties change progressively during asphalt concrete lifetime due to the activities at the micro scale level and also due to the interactions with environment. Therefore, the thermodynamic based constitutive models are essential to

model this material behavior. During past decades, several researches devoted numerous works to develop thermodynamic-based formulations for modeling viscoelastic, viscoplastic, and/or damage behavior of different materials, especially polymers, soft materials, granular materials, and bio-inspired materials (Arson and Gatmiri, 2012; Karra and Rajagopal, 2011). Krishnan and Rajagopal (2004) and Darabi et al. (2013) have recently used the thermodynamic based formulation to model the asphalt concrete material behavior. They showed that this approach could successfully describe the complicated viscoelastic-viscoplastic-viscodamage asphalt concrete material's behavior.

Formulating the moisture detrimental effect on different materials has attracted attention of researchers for a long time. Complexity of the issue caused several simplification assumptions in each speculated model. Therefore, developing a general thermodynamic based framework to prepare a robust foundation for constructing more explicit models is crucial. The thermodynamic formulation approach has been used to model the response and damage of partially saturated geo-materials. Those models are applicable to elastic material and did not consider the degradation of the solid part due to moisture diffusions, which is a case in viscoelastic porous material.

Kringos et al (2008b) introduced the fundamental moisture induced damage parameters and developed an energy based computational framework for modeling moisture-induced damage in asphalt pavements. They theorized a three dimensional elasto-visco-plastic constitutive model for mastic response that includes moisture induced damage effect. However, they did not expand the first and second law of

thermodynamic for a partially saturated and moisture-diffused media in their formulation. Kringos et al. (2008b) added the moisture damage variable as an internal state variable to the Helmholtz free energy without constituting the necessary consistent thermodynamic background. The developed moisture damage model is time-independent and allows for full moisture damage recovery (or reduction) upon drying, which is a controversial assumption. Therefore, a comprehensive and consistent thermodynamic based framework is essential to model moisture detrimental effect in a partially saturated viscoelastic porous material.

A primary objective of this study is to establish a general framework to describe continuum moisture damage mechanics in an asphalt concrete material. It focuses on developing a thermodynamic based framework that is incorporating the moisture effect by expanding the principle of virtual power, first and second law of thermodynamic for a porous partially saturated viscoelastic media.

This study considers the micro- and macro- mechanical approaches to get a simple framework for modeling moisture damage in porous media. The framework uses mixture theory to modify the thermodynamics laws for partially saturated porous viscoelastic media. The asphalt concrete material is considered to consist of wet solid part (i.e. aggregates and mastic) and partially saturated air voids with evolving natural configurations in this study. The principle of virtual power yields general partial differential equations that govern the viscoelastic solid, liquid, and viscodamage (moisture and mechanical) response. The effective stress concept of CMMDM has been

used to define physically based moisture damage variable and couple it to the mechanical damage. The natural configuration's evolution is determined by a thermodynamic criterion, which is the maximization of the energy dissipation rate in this study. Hence, a general thermodynamic framework is developed in this study to systematically derive a constitutive model for partially saturated porous viscoelastic media. The framework is based on the use of independent state variables and it emphasizes on the decomposition of thermodynamic conjugate forces into energetic and dissipative components as Ziegler (Ziegler, 1977) initially extended. Correspondingly, the strain tensor is split into two independent thermodynamic strain components. A systematic procedure used to determine the energetic and dissipative components from the Helmholtz free energy function and the rate of energy dissipation, respectively.

It should be mentioned that the developed model to illustrate this phenomenon is overly simplified. The described model here first described for general large strain and then reduced to small strain cases to avoid complexity. Crucial factors such as the shape, size, surface roughness, and distribution of aggregates are not considered in formulations. It has not considered the transmission between liquid and air. It assumes that there is no air bubble mixed in the liquid and vice versa. The study assumes all air voids to be connected. Very simple store and dissipate energy function are chosen to explain the material behavior. No claim is made here that the framework is entirely general. Some exceptions are, for instance, constitutive models developed within the approach commonly termed rational thermodynamics, in which the behavior is expressed as general functional of the history of deformation, rather than (as used here)

functions of internal parameters, which somehow encapsulate this history. In principle an infinite number of internal parameters would be needed to describe some of the models, which employ functional. In practice, however, if sufficient ingenuity is employed in their selection, a fairly small number of internal parameters can be used to construct a close approximation to the more general models.

The formulation has been developed for general cases and can consider all additional information once a better understanding of the physics achieved. It is important to ingeminate that the outlined procedure can develop a plethora of models that can store and dissipate energy in a variety of ways. Therefore, it is necessary to articulate the thermodynamic framework's requirement unlike this feature. First, what is developed is a general framework that can yield results in which the appropriate physics can be incorporated. Second, the model has a proper thermodynamic framework that delineates how energy is stored and dissipated in the material. Therefore, the general framework can be used to generate a variety of models that reflect different ways of storing and dissipating energy and can fit the data for a variety of experiments.

3.1 Preliminaries

This chapter describes the deformation and kinematics of a porous medium formed from a deformable solid skeleton and a partially saturated porous space. The description of the deformation for a porous media skeleton does not differ from a standard solid continuum when it is subjected to external forces. These descriptions are going to describe shortly below.

3.1.1 Description of Motion and Deformation Gradient

The medium particles are identified by their position vector $\mathbf{X}$ at the initial configuration (at time $t=0$) and vector $\mathbf{x}$ after deformation at their current configuration, Figure 3.1, such that:

$$\mathbf{x}=\mathbf{x}\left(\mathbf{X},t\right) \tag{3.1}$$

where the $\mathbf{X}$ identifies the material coordinates, whereas $\mathbf{x}$ identifies the spatial coordinates. The variables expressed in material coordinates are known as material or Lagrangian variables whereas variables expressed in the spatial coordinates are known as the spatial or Eulerian variables.

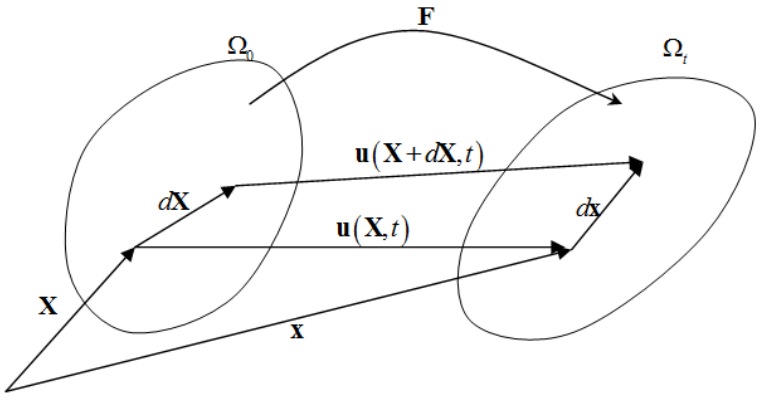

Figure 3.1. Position vectors at initial and current configurations.

The time rate of change of a quantity in a material configuration is known as a material derivative (D/Dt) whereas the time rate of change of a quantity in a spatial

configuration is known as the spatial derivative ($\partial/\partial t$). The relation between these two derivatives can be written as:

$$\frac{D(.)}{Dt} = \frac{\partial(.)}{\partial t} + \mathbf{v}\nabla_{\mathbf{x}}(.) \tag{3.2}$$

where $\mathbf{v}$ is the spatial velocity vector, $\nabla_{\mathbf{x}} = \partial(.)/\partial\mathbf{x}$ is the spatial gradient operator, and the $\partial(.)/\partial t$ shows spatial derivative with respect to time and will be indicated by prime sign in the latter and material time derivate, $\frac{D(.)}{Dt}$, will be indicated by superimposed dot.

The displacement vector, $\mathbf{u}$, of the particle from the reference position to the position at time t (current position) is given by, Figure 3.1:

$$\mathbf{u} = \mathbf{x}(\mathbf{X}, t) - \mathbf{X} \tag{3.3}$$

Considering a neighboring point for $\mathbf{X}$ at $\mathbf{X} + d\mathbf{X}$ arrives at $\mathbf{x} + d\mathbf{x}$ at current time *t*, which is related to $\mathbf{X} + d\mathbf{X}$ by:

$$\mathbf{x} + d\mathbf{x} = \mathbf{X} + d\mathbf{X} + \mathbf{u}(\mathbf{X} + d\mathbf{X}, t) \tag{3.4}$$

Subtracting Eq. (3.3) from Eq. (3.4), one obtains:

$$d\mathbf{x} = d\mathbf{X} + \mathbf{u}(\mathbf{X} + d\mathbf{X}, t) - \mathbf{u}(\mathbf{X}, t) \tag{3.5}$$

Using the definition of a vector function and the Lagrangian gradient, Eq. (3.5) becomes:

$$d\mathbf{x} = d\mathbf{X} + \nabla_{\mathbf{X}}\mathbf{u}d\mathbf{X} \tag{3.6}$$

where $\nabla_{\mathbf{X}}\mathbf{u} = \partial\mathbf{u}/\partial\mathbf{X}$ is a second-order tensor known as the Lagrangian displacement gradient. Eq. (3.6) can be written as:

$$d\mathbf{x} = \mathbf{F}d\mathbf{X} \tag{3.7}$$

where $\mathbf{F}$ is the deformation gradient and is defined by:

$$\mathbf{F} = \mathbf{I} + \nabla_{\mathbf{X}}\mathbf{u} \qquad \text{or} \qquad \mathbf{F} = \frac{\partial\mathbf{x}}{\partial\mathbf{X}} \tag{3.8}$$

3.1.2 Strain Tensor

Material deformation causes changes in both lengths of the material vectors and the angles between them. The Lagrange strain tensor $\mathbf{E}$ measures these changes in the material configuration. The variation of the scalar product of two material vectors $d\mathbf{X}$ and $d\mathbf{Y}$ transforming by deformation into $d\mathbf{x}$ and $d\mathbf{y}$, is defined such that:

$$d\mathbf{x} = \mathbf{F}d\mathbf{X}\,; \qquad d\mathbf{y} = \mathbf{F}d\mathbf{Y}\,; \qquad d\mathbf{x}.d\mathbf{y} - d\mathbf{X}.d\mathbf{Y} = 2d\mathbf{X}\mathbf{E}d\mathbf{Y} \tag{3.9}$$

Knowing that for tensors **A** and **B** and a vector **a** one can write $\mathbf{AaB}=\mathbf{aA}^{\mathbf{T}}\mathbf{B}$. Then, the Lagrangian strain tensor can be written:

$$\mathbf{E} = \frac{1}{2}\left(\mathbf{F}^{T}\mathbf{F} - \mathbf{I}\right) \tag{3.10}$$

Substituting Eq. (3.8) in Eq. (3.10) the Lagrange strain tensor can be finally expressed as a function of the displacement vector $\mathbf{u}$:

$$\mathbf{E} = \frac{1}{2}\left(\nabla_{\mathbf{X}}\mathbf{u} + \left(\nabla_{\mathbf{X}}\mathbf{u}\right)^{T} + \left(\nabla_{\mathbf{X}}\mathbf{u}\right)^{T}\nabla_{\mathbf{X}}\mathbf{u}\right) \tag{3.11}$$

In many engineering problems the displacement of every material point is very small, this infinitesimal transformation condition means:

$$\left\|\nabla\mathbf{u}\right\| \ll 1 \tag{3.12}$$

where the norm is defined by $\left\|(.)\right\| = \sqrt{(.).(.)}$. Then, for infinitesimal deformations, the Lagrange strain tensor $\mathbf{E}$ reduces to the linearized strain tensor $\boldsymbol{\varepsilon}$ as follows:

$$\mathbf{E} \simeq \boldsymbol{\varepsilon} = \frac{1}{2}\left(\nabla\mathbf{u} + \nabla\mathbf{u}^{T}\right) \tag{3.13}$$

In the context of the small deformation theory and motivated by the continuum damage mechanics, the additive decomposition of the total strain can be assumed. For the asphalt concrete subjected to an applied stress, the total deformation can be decomposed into recoverable (viscoelastic) and irrecoverable (viscoplastic) components, where the extent of each is mainly affected by time, temperature, and loading rate.

$$\boldsymbol{\varepsilon} = \boldsymbol{\varepsilon}^{ve} + \boldsymbol{\varepsilon}^{vp} \tag{3.14}$$

where $\boldsymbol{\varepsilon}$ is the total strain tensor, $\boldsymbol{\varepsilon}^{ve}$ is the viscoelastic strain tensor and $\boldsymbol{\varepsilon}^{vp}$ is the viscoplastic strain tensor. It should be mentioned that is this work it is assumed that total

strain is just due to viscoelasticity. The thermodynamic formulation will be extended based on this assumption. However, the viscoplastic strain can be added to the developed formulation in later developments.

3.1.3 Rate of Deformation

The rate of change of material vectors' length is described by the tensor $\mathbf{d}$ known as rate of deformation tensor. Considering $d\mathbf{x}$ and $d\mathbf{y}$ as two infinitesimal material vectors, $\mathbf{d}$ is defined as:

$$\frac{D}{Dt}\left(d\mathbf{x}.d\mathbf{y}\right) = 2d\mathbf{x}\mathbf{d}d\mathbf{y} \tag{3.15}$$

Knowing that:

$$\frac{D}{Dt}\left(d\mathbf{x}\right) = \nabla_{\mathbf{x}}\mathbf{v}d\mathbf{x} \tag{3.16}$$

Then the Eulerian rate of deformation tensor, $\mathbf{d}$, can be written as:

$$\mathbf{d} = \frac{1}{2}\left(\nabla_{\mathbf{x}}\mathbf{v} + \nabla_{\mathbf{x}}\mathbf{v}^{T}\right) \tag{3.17}$$

which is the symmetric part of the velocity gradient, $\mathbf{L} = \partial\mathbf{v}/\partial\mathbf{x}$.

3.1.4 Volume and Surface Transport

The current infinitesimal volume can be defined as a composed product:

$$d\Omega_t = \left(d\mathbf{x}_1, d\mathbf{x}_2, d\mathbf{x}_3\right) = d\mathbf{x}_1.\left(d\mathbf{x}_2 \times d\mathbf{x}_3\right) \tag{3.18}$$

where $\times$ designates the cross (vector) product. Since the composed product is linear and with using Eq. (3.7), Eq. (3.18) can be written as:

$$d\Omega_t = \left(\mathbf{F}d\mathbf{X}_1, \mathbf{F}d\mathbf{X}_2, \mathbf{F}d\mathbf{X}_3\right) = \det\left(\mathbf{F}\right)\left(d\mathbf{X}_1, d\mathbf{X}_2, d\mathbf{X}_3\right) \tag{3.19}$$

Therefore, any initial infinitesimal material volume, $d\Omega_0$, can transform into the infinitesimal current material volume, $d\Omega_t$, using the following relation:

$$d\Omega_t = Jd\Omega_0 \tag{3.20}$$

where $J = \det\left(\mathbf{F}\right)$ is the Jacobian of the deformation gradient.

Throughout the deformation, a material surface at the initial configuration, $d\Gamma_0$, oriented by the unit normal $\mathbf{N}$, transforms into the material surface at the current configuration, $d\Gamma_t$, that is oriented by the unit normal $\mathbf{n}$. During the deformation, these two orientations, $\mathbf{N}$ and $\mathbf{n}$, do not match. Assuming $\mathbf{a}$ be a vector attached to the current configuration and $\mathbf{A}$ the associated vector attached to the initial configuration and defined in such a way that the flow of $\mathbf{a}$ through $d\Gamma_t$ coincides with the flow of $\mathbf{A}$ through $d\Gamma_0$, then, it can be written:

$$\mathbf{a.n}d\Gamma_t = \mathbf{A.N}d\Gamma_0 \tag{3.21}$$

Integrating Eq. (3.21) over the initial and current areas Γ_0 and Γ_t followed by using of the divergence theorem gives the following relationship locally:

$$div(\mathbf{a})\, d\Omega_t = Div(\mathbf{A})\, d\Omega_0 \tag{3.22}$$

3.1.5 Eulerian and Lagrangian Porosities

Skeleton and therefore porosity of a material change during the deformation. Hence, porosity in the current configuration does not properly represent the volume change undergone by the porous space attached to the initial material volume $d\Omega_0$. This makes it necessary to define porosity for the current and initial configurations separately to write the equations in the Eulerian and Lagrangian descriptions. The porosity in the current and initial configurations is designated by n^v and ϕ^v, respectively, and defined as below (Coussy, 2004):

$$\phi^v = \frac{d\Omega_t^d}{d\Omega_0} \tag{3.23}$$

$$n^v = \frac{d\Omega_t^d}{d\Omega_t} \tag{3.24}$$

where $d\Omega_t^d$ refers to all porous volume in the material, cracks and voids volume, at the current time *t*. So, it can be concluded:

$$\phi^v d\Omega_0 = n^v d\Omega_t \tag{3.25}$$

Based on this definition, a relationship can be defined for the dilation of infinitesimal transformation cases. For infinitesimal deformation the Jacobian of deformation gradient can be written as:

$$J = \det\left(\mathbf{F}\right) \simeq 1 + div\left(\mathbf{u}\right) = 1 + \varepsilon_{ii} \tag{3.26}$$

Defining e_m as a linearized volume dilation of the material, i.e. $e_m = u_{i,i} = \varepsilon_{ii}$, Eq. (3.20) can be written;

$$d\Omega_t = \left(1 + e_m\right) d\Omega_0 \tag{3.27}$$

Using this equation and the definitions of Eulerian and Lagrangian porosities, the following relationship between the volume occupied by the solid part and overall volume can be obtained;

$$d\Omega_t^s = J^s d\Omega_0^s = \left(1 + e_s\right) d\Omega_0^s,\ d\Omega_t^s = \left(1 - n^v\right) d\Omega_t,\ d\Omega_0^s = \left(1 - \phi_0^v\right) d\Omega_0 \tag{3.28}$$

where $d\Omega_t^s$, J^s, $d\Omega_0^s$, and e_s is the volume of solid part at the current configuration, the Jacobian of the solid part, the initial volume of solid part, and the linearized volume dilation of the solid skeleton. Combining Eq.(3.28), the relation for obtaining the linearized volume dilation can be derived as:

$$e_m = \left(1 - \phi_0^v\right) e_s + \left(\phi^v - \phi_0^v\right) \tag{3.29}$$

where $\phi_0^v = n_0^v$ is the initial porosity.

Since an asphalt concrete is a three-phase composite consisting of aggregates, air voids, and mastic (binder with fine aggregates). One can argue that the aggregates are incompressible so that their change in volume is negligible. Moreover, both binder and fine aggregates can be assumed incompressible and one might neglect the changes in volume of the mastic. Also, under small deformations, rotations and rearrangement of aggregates during deformation might be negligible. Then, it might be assumed that majority of the change in volume in asphalt mixtures is due to the change in porosity (voids and cracks) and subsequent damage during loading. Thus:

$$e = \phi^v - \phi_0^v \tag{3.30}$$

3.1.6 Damage Density for Anisotropic Material

Voyiadjis and Deliktas (2000) proposed a relationship between the porosity and damage density for a damage-induced in anisotropic materials, which can be simplified for the isotropic cases. A second-order symmetric damage tensor was selected to characterize the anisotropic phenomenon of micro-cracks distribution in the material, which can be interpreted as the effective area reduction caused by distributed micro-cracks and cavities due to material damage. The deformation gradient $\mathbf{F}^{vd}$ is used to express the differential lengths $d\bar{\mathbf{x}}$ in the effective configuration in terms of the differential lengths $d\mathbf{x}$ in the current deformed damaged configuration such that:

$$d\mathbf{x} = \mathbf{F}^d d\bar{\mathbf{x}} \tag{3.31}$$

Assuming a tetrahedron with the faces lie in the principle directions, Figure 3.2, the reduction in area between the current nominal and current effective configurations may be described in terms of the eigenvalues of the second order tensor $\boldsymbol{\varphi}$, $\hat{\varphi}_1, \hat{\varphi}_2, \hat{\varphi}_3$, such that:

$$d\bar{\mathbf{a}}_1 = \left(1-\hat{\varphi}_1\right) d\mathbf{a}_1, \quad d\bar{\mathbf{a}}_2 = \left(1-\hat{\varphi}_2\right) d\mathbf{a}_2, \quad d\bar{\mathbf{a}}_3 = \left(1-\hat{\varphi}_3\right) d\mathbf{a}_3 \tag{3.32}$$

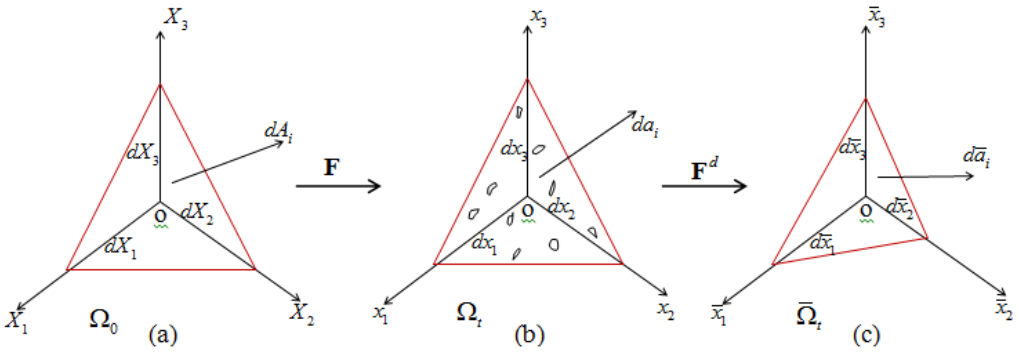

Figure 3.2. Schematic representation of the deformation gradients for micro-cracks (Voyiadjis and Deliktas, 2000).

The components of the area vector $d\mathbf{a}$ in the three-dimensional space of the current configuration, Ω_t, are given by:

$$d\mathbf{a}_1 = -\frac{1}{2} d\mathbf{x}_2 \times d\mathbf{x}_3, \quad d\mathbf{a}_2 = -\frac{1}{2} d\mathbf{x}_1 \times d\mathbf{x}_3, \quad d\mathbf{a}_3 = -\frac{1}{2} d\mathbf{x}_1 \times d\mathbf{x}_2 \tag{3.33}$$

The corresponding area vector components of $d\bar{\mathbf{a}}$ in the current effective configuration, $\bar{\Omega}_t$, are as follows:

$$d\bar{\mathbf{a}}_1 = -\frac{1}{2} d\bar{\mathbf{x}}_2 \times d\bar{\mathbf{x}}_3,\ d\bar{\mathbf{a}}_2 = -\frac{1}{2} d\bar{\mathbf{x}}_1 \times d\bar{\mathbf{x}}_3,\ d\bar{\mathbf{a}}_3 = -\frac{1}{2} d\bar{\mathbf{x}}_1 \times d\bar{\mathbf{x}}_2 \tag{3.34}$$

Substituting Eqs. (3.33) and (3.34) in Eq. (3.32) and using Eq. (3.31) one can obtain:

$$\begin{aligned} d\bar{\mathbf{x}}_2 \times d\bar{\mathbf{x}}_3 &= \left(1-\hat{\varphi}_1\right) J^d \mathbf{F}^{d^{-T}} \left(d\bar{\mathbf{x}}_2 \times d\bar{\mathbf{x}}_3\right) \\ d\bar{\mathbf{x}}_1 \times d\bar{\mathbf{x}}_3 &= \left(1-\hat{\varphi}_2\right) J^d \mathbf{F}^{d^{-T}} \left(d\bar{\mathbf{x}}_1 \times d\bar{\mathbf{x}}_3\right) \\ d\bar{\mathbf{x}}_1 \times d\bar{\mathbf{x}}_2 &= \left(1-\hat{\varphi}_3\right) J^d \mathbf{F}^{d^{-T}} \left(d\bar{\mathbf{x}}_1 \times d\bar{\mathbf{x}}_2\right) \end{aligned} \tag{3.35}$$

Knowing that in principle direction,

$$\mathbf{F} = \begin{pmatrix} \hat{F}_{11}^d & 0 & 0 \\ 0 & \hat{F}_{22}^d & 0 \\ 0 & 0 & \hat{F}_{33}^d \end{pmatrix}, J = \hat{F}_{11}^d \hat{F}_{22}^d \hat{F}_{33}^d \tag{3.36}$$

Assuming that $F_{ij} = 0$ for $i \neq j$ in order to obtain the eigenvalues of $\mathbf{F}^d$ and then solving the equations in terms of the eigenvalues of $\boldsymbol{\varphi}$:

$$\begin{aligned} \hat{F}_{11}^d &= \sqrt{\frac{\left(1-\hat{\varphi}_1\right)}{\left(1-\hat{\varphi}_2\right)\left(1-\hat{\varphi}_3\right)}}, \\ \hat{F}_{22}^d &= \sqrt{\frac{\left(1-\hat{\varphi}_2\right)}{\left(1-\hat{\varphi}_1\right)\left(1-\hat{\varphi}_3\right)}}, \\ \hat{F}_{33}^d &= \sqrt{\frac{\left(1-\hat{\varphi}_3\right)}{\left(1-\hat{\varphi}_1\right)\left(1-\hat{\varphi}_2\right)}} \end{aligned} \tag{3.37}$$

Therefore, the resulting Jacobian of the damage deformation gradient, J^d, is:

$$J^d = \hat{F}_{11}^d \hat{F}_{22}^d \hat{F}_{33}^d = 1/\sqrt{(1-\hat{\varphi}_1)(1-\hat{\varphi}_2)(1-\hat{\varphi}_3)} \tag{3.38}$$

Then, the differential volume in the effective configuration is obtained as:

$$d\Omega_t = J^d d\bar{\Omega}_t = \left(1/\sqrt{(1-\hat{\varphi}_1)(1-\hat{\varphi}_2)(1-\hat{\varphi}_3)}\right) d\bar{\Omega}_t \tag{3.39}$$

Let $d\Omega_t^d$ be the differential volume of cracks and voids such that one can write the following from Eqs. (3.24) and (3.39):

$$\left(1-n^v\right)^2 \equiv \left(\frac{d\bar{\Omega}_t}{d\Omega_t}\right)^2 = \left(\frac{d\Omega_t - d\Omega_t^d}{d\Omega_t}\right)^2 = (1-\hat{\varphi}_1)(1-\hat{\varphi}_2)(1-\hat{\varphi}_3) \tag{3.40}$$

where n^v is the Eulerian measure of volume reduction due to the presence of micro-cracks and voids caused by damage evolution. In the special case when damage is indeed isotropic, $\varphi = \hat{\varphi}_1 = \hat{\varphi}_2 = \hat{\varphi}_3$, the volume reduction becomes:

$$n^v = 1-(1-\varphi)^{3/2} \tag{3.41}$$

Eq. (3.41) shows the relationship between the Eulerian volumetric damage density and the Eulerian areal damage density. Using Eqs. (3.25) and (3.26), then the Lagrangian volumetric damage density can be expressed as follows:

$$\phi^v = Jn^v = J\left[1-(1-\varphi)^{3/2}\right] \tag{3.42}$$

In the case of the infinitesimal volume reduction, n^{v^i}, the higher order multiplications are negligible and Eq. (3.40) reduces to:

$$\left(1-n^{v^i}\right)^2 = 1-\left(\hat{\varphi}_1+\hat{\varphi}_2+\hat{\varphi}_3\right) \tag{3.43}$$

Both n^v and n^{v^i} are isotropic measures of damage. They are simplified kinematic measures of damage that are scalar valued although damage distribution may not be isotropic. Similarly in the special case when damage is indeed isotropic and the volume reduction is infinitesimal then;

$$n^{v^i} = 1-\sqrt{1-3\varphi} \text{ or } n^{v^i} \cong \frac{3}{2}\varphi \tag{3.44}$$

Moreover, in case of small deformations, $J=1$, from Eqs. (3.42) and (3.44) it can be written that;

$$\phi^v = n^{v^i} \cong \frac{3}{2}\varphi \tag{3.45}$$

3.2 Thermodynamic Framework

3.2.1 Moisture Content

The moisture movement in an asphalt concrete can be separated into two processes. One is due to a potential gradient driven flow through the interconnected porosity for which Darcy's law is used. The second is the movement of moisture through the binder and aggregates phases via a molecular diffusion process, which is driven by a moisture concentration gradient for which Fick's law of diffusion is used. The flow of moisture might cause pore water pressure effect on the mastic or wash away the mastic material during traffic loading causing erosion damage. This process has both energetic and

dissipative characteristics so it should be considered in both Helmholtz free energy and the total dissipative energy. In addition, the moisture diffusion in the material could also have both the dissipative and energetic characteristics.

The first type of moisture, which moves due to a potential gradient driven flow, is the moisture that exists inside the material's interconnected cracks and voids. In a partially saturated media, the moisture fills only some part of these spaces. A *porosity degree of saturation* of the porous media, s^l, can be defined as follows:

$$s^l = \frac{\left(d\Omega_t^l\right)^d}{d\Omega_t^d} \tag{3.46}$$

where $\left(d\Omega_t^l\right)^d$ is the volume of the liquid which occupies the interconnected cracks and voids, respectively. Then, the moisture content inside these cracks and voids is obtained from:

$$\Theta^v = s^l \phi^v, \;\; \theta^v = s^l n^v \tag{3.47}$$

where Θ^v and θ^v are the moisture content inside the interconnected cracks and voids in the initial and current configuration, respectively.

The second type of the moisture content is the moisture, which diffuses within the solid phase of material on a molecular level. *Solid degree of saturation*, η^m, in this

case is defined as the ratio of volume of moisture inside the solid phase, $\left(d\Omega^{l}\right)^{s}$, to the maximum moisture content that the solid phase can have, $\left(d\Omega^{l}_{\max}\right)^{s}$.

$$\eta^{m} = \frac{\left(d\Omega^{l}_{t}\right)^{s}}{\left(d\Omega^{l}_{t}\right)^{s}_{\max}} = \frac{\theta^{s}}{\theta^{s}_{\max}} \tag{3.48}$$

where θ^{s} is the current moisture concentration in the material, and $\theta^{s}_{\max}$ is the maximum moisture concentration uptake of the material at current configuration. In order to obtain the total moisture content in the porous material, the two moisture contents should be added:

$$\begin{aligned} \theta = \frac{d\Omega^{l}_{t}}{d\Omega_{0}} &= \frac{\left(d\Omega^{l}_{t}\right)^{d}}{d\Omega_{0}} + \frac{\left(d\Omega^{l}_{t}\right)^{s}}{d\Omega_{0}} \\ &= \frac{\left(d\Omega^{l}_{t}\right)^{d}}{d\Omega^{d}_{t}} \frac{d\Omega^{d}_{t}}{d\Omega_{0}} + \frac{\left(d\Omega^{l}_{t}\right)^{s}}{\left(d\Omega^{l}_{\max}\right)^{s}} \frac{\left(d\Omega^{l}_{\max}\right)^{s}}{d\Omega_{0}} = s^{l}\phi^{v} + \eta^{m}\theta^{s}_{\max} = \theta^{v} + \theta^{s} \end{aligned} \tag{3.49}$$

3.2.2 Mass Balance

The mass balance equation for three phases, solid, liquid and gas of the media is developed in a partially saturated porous medium (Coussy, 2004). In this study, the approximation is made that the existence of a relatively slow moisture diffusion flux through the components of the mix will not influence the fast water flow through the interconnected cracks and voids, since the time scales differ greatly. Also, it was assumed that there is not any water vapor in the gas phase. Based on these assumptions, the mass balance equation in three phases can be written as follows;

$$\frac{D}{Dt}\int_{\Omega_t}\rho^s\left(1-n^v\right)d\Omega_t=0 \tag{3.50}$$

$$\frac{D}{Dt}\int_{\Omega_t}\rho^l s^l n^v d\Omega_t=0 \tag{3.51}$$

$$\frac{D}{Dt}\int_{\Omega_t}\rho^l \eta^m \theta^s_{\max} d\Omega_t=0 \tag{3.52}$$

$$\frac{D}{Dt}\int_{\Omega_t}\rho^l s^g n^v d\Omega_t=0 \tag{3.53}$$

Applying Eq. (3.2) to the above equations, the Eulerian continuity equations is obtained:

$$\frac{\partial}{\partial t}\left[\rho^s\left(1-n^v\right)\right]+div\left(\rho^s\left(1-n^v\right)\mathbf{v}^s\right)=0 \tag{3.54}$$

$$\frac{\partial}{\partial t}\left(\rho^l s^l n^v\right)+div\left(\rho^l s^l n^v \mathbf{v}^l\right)=0 \tag{3.55}$$

$$\frac{\partial}{\partial t}\left(\rho^l \eta^m \theta^s_{\max}\right)+div\left(\rho^l \eta^m \theta^s_{\max}\mathbf{v}^{mc}\right)=0 \tag{3.56}$$

$$\frac{\partial}{\partial t}\left(\rho^l s^g n^v\right)+div\left(\rho^l s^g n^v \mathbf{v}^g\right)=0 \tag{3.57}$$

where $\mathbf{v}^s$, $\mathbf{v}^l$, $\mathbf{v}^{mc}$, and $\mathbf{v}^g$ are solid, liquid (moisture content inside interconnected cracks and voids), moisture content inside the solid phase, and gas velocities. Moreover,

$\mathbf{q}^l$, $\mathbf{q}^g$, and $\mathbf{q}^{mc}$ are the Eulerian relative vector of liquid, gas, and moisture content and defined by:

$$\begin{aligned}\mathbf{q}^l &= \rho^l s^l n^v \mathbf{v}^{ls} \\ \mathbf{q}^g &= \rho^g s^g n^v \mathbf{v}^{gs} \\ \mathbf{q}^{mc} &= \rho^l \eta^m \theta^s_{\max} \mathbf{v}^{mcs}\end{aligned} \tag{3.58}$$

Use of definition (3.58) and rearranging the Eulerian continuity equations:

$$\frac{\partial}{\partial t}\left(\rho^l s^l n^v\right) + div\left(\mathbf{q}^l + \rho^l s^l n^v \mathbf{v}^s\right) = 0 \tag{3.59}$$

$$\frac{\partial}{\partial t}\left(\rho^l \eta^m \theta^s_{\max}\right) + div\left(\mathbf{q}^{mc} + \rho^l \eta^m \theta^s_{\max} \mathbf{v}^s\right) = 0 \tag{3.60}$$

$$\frac{\partial}{\partial t}\left(\rho^l s^g n^v\right) + div\left(\mathbf{q}^g + \rho^l s^g n^v \mathbf{v}^s\right) = 0 \tag{3.61}$$

Furthermore, let $\mathbf{Q}^l$, $\mathbf{Q}^g$, and $\mathbf{Q}^{mc}$ be the Lagrangian vector attached to the initial configuration and linked to the $\mathbf{q}^l$, $\mathbf{q}^g$, and $\mathbf{q}^{mc}$ through the relations:

$$\mathbf{q}^l.\mathbf{n}d\Gamma_t = \mathbf{Q}^l.\mathbf{N}d\Gamma_0;\ \mathbf{q}^g.\mathbf{n}d\Gamma_t = \mathbf{Q}^g.\mathbf{N}d\Gamma_0;\ \mathbf{q}^{mc}.\mathbf{n}d\Gamma_t = \mathbf{Q}^{mc}.\mathbf{N}d\Gamma_0 \tag{3.62}$$

Substitution of Eq. (3.62) into Eq. (3.59) to (3.61) and making use of eq. (3.22) pre-multiplied by $d\Omega_t$ will provide the Lagrangian continuity equations in the forms of:

$$\frac{D}{Dt}\left(\rho^l \Theta^v\right) + Div\left(\mathbf{Q}^l\right) = 0 \tag{3.63}$$

$$\frac{D}{Dt}\left(\rho^{l}\Theta^{s}\right)+Div\left(\mathbf{Q}^{mc}\right)=0 \tag{3.64}$$

$$\frac{D}{Dt}\left(\rho^{l}s^{g}\phi^{v}\right)+Div\left(\mathbf{Q}^{g}\right)=0 \tag{3.65}$$

3.2.3 Principle of Virtual Power

To formulate a proper material constitutive model, the principle of virtual power and thermodynamics balance laws should be satisfied. The thermodynamic framework of Gurtin (2003) along with the consideration of viscoelasticity and damage is used to express the internal and external expenditures of powers. Although the definition of the internal and external powers is thought to be fixed, Fremond and Nedjar (1996) showed that it needs some modification to consider the effects of damage. Similar approach will be used in this work in order to derive a constitutive equation that couples viscoelastic and viscodamage behavior of time- and rate-dependent moisture-conditioned materials.

The internal expenditure of power associated with a velocity field $\mathbf{v}$ is the sum of the power develops in this field, both in the skeleton and in the fluids. Assuming the same velocities for the whole porous media, the internal power in this case becomes:

$$\mathrm{P}_{\mathrm{int}}=\int_{\Omega_t}\left[\boldsymbol{\sigma}.\mathbf{d}+\sum_{m=1}^{M_{\mathrm{int}}^{ve}}\chi^{m}\dot{\xi}^{m}+Yn^{v\prime}+W\omega^{\prime}+Z\phi^{e\prime}\right]d\Omega_t \tag{3.66}$$

where $\boldsymbol{\sigma}=\left(1-n^{v}\right)\boldsymbol{\sigma}^{s}+s^{l}n^{v}\boldsymbol{\sigma}^{l}+s^{g}n^{v}\boldsymbol{\sigma}^{g}+\eta^{m}\theta_{\max}^{s}\boldsymbol{\sigma}^{m}$ is the Cauchy stress tensor, Y is the mechanical damage force conjugate to the mechanical damage density, n^{v}, W is the moisture damage force conjugate to the moisture damage density, ω, Z is the erosion

damage force conjugate to the erosion damage density, ϕ^e, and M_{int}^{ve} thermodynamic forces, χ^m, conjugated to the M_{int}^{ve} of phenomenological internal state variables associated with viscoelastic process, ξ^m (i.e, $m = 1,...,M_{\text{int}}^{ve}; M_{\text{int}}^{ve} \geq 1$). Note that $\boldsymbol{\sigma}.\mathbf{d} = \boldsymbol{\sigma}.\nabla\dot{\mathbf{u}}$ where $\mathbf{d}$ is given by Eq. (3.17).

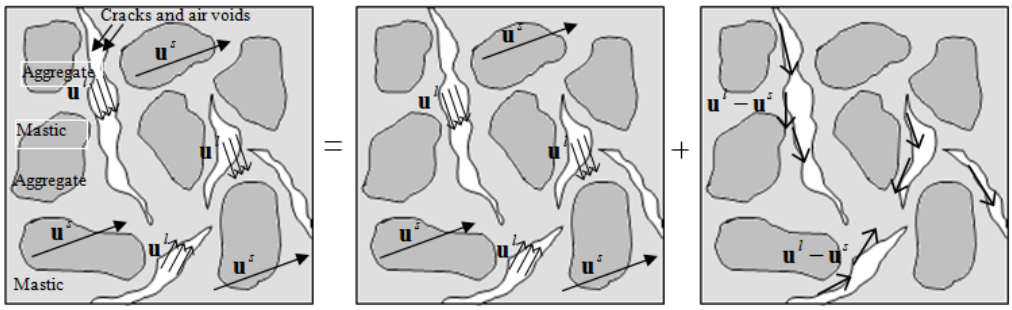

Figure 3.3. The interactions between three phases in a partially saturated media.

Since the skeleton particles and the fluids particles have different velocity fields, the internal expenditure of power as defined in Eq. (3.66) for a unique velocity field cannot account for the internal power in the actual motion of the porous medium. The total internal power should accounts not only for the power of the skeleton and the fluids continua separately, but also for the power associated with the internal interactions. This means considering the effects of the relative velocities that act as relative strains and the coupling between the three phases, Figure 3.3. Therefore, the internal expenditure of power is characterized by the Cauchy stress tensors in the solid phase, $\boldsymbol{\sigma}^s$, liquid phase,

$\boldsymbol{\sigma}^l$, moisture content, $\boldsymbol{\sigma}^{mc}$, and gas phase, $\boldsymbol{\sigma}^g$, over the current configuration, Ω_t such that the expenditure of the internal power in Eq. (3.66) can be rewritten as:

$$\mathrm{P}_{\mathrm{int}} = \int_{\Omega_t} \left[\begin{array}{l} \left(1-n^v\right)\boldsymbol{\sigma}^s.\nabla\mathbf{v}^s + s^l n^v \boldsymbol{\sigma}^l.\nabla\mathbf{v}^l + s^g n^v \boldsymbol{\sigma}^g.\nabla\mathbf{v}^g + \eta^m \theta^s_{\max} \boldsymbol{\sigma}^{mc}.\nabla\mathbf{v}^{mc} \\ + \sum_{m=1}^{M_{\mathrm{int}}^{ve}} \chi_m \xi^{(m)\prime} + \mathbf{f}^{\to l}.\mathbf{v}^{ls} + \mathbf{f}^{\to g}.\mathbf{v}^{gs} + \mathbf{f}^{\to mc}.\mathbf{v}^{mcs} + Yn^{v\prime} + W\omega' + Z\phi^{e\prime} \end{array} \right] d\Omega_t \quad (3.67)$$

where n^v, $\mathbf{v}^s$, $\mathbf{v}^l$, $\mathbf{v}^g$, $\mathbf{v}^{ls}$, $\mathbf{v}^{gs}$, $\mathbf{f}^{\to f}$ and $\mathbf{f}^{\to g}$, are Eulerian porosity, solid velocity, liquid velocity, gas velocity, Eulerian relative specific velocity of fluid (i.e. $\mathbf{v}^{ls} = \mathbf{v}^l - \mathbf{v}^s$) and gas (i.e. $\mathbf{v}^{gs} = \mathbf{v}^g - \mathbf{v}^s$) phases (i.e. specific velocity of the fluid and gas phase with respect to the solid phase), interaction force exerted by fluid on the solid phase, and the interaction force between gas and solid phases. On the other hand, the external expenditure of power is defined in terms of the macroscopic body force, $\mathbf{f}$, a macroscopic surface traction on solid, $\mathbf{t}^s$, liquid, $\mathbf{t}^l$, and gas phase, $\mathbf{t}^g$, as follows:

$$\begin{aligned} \mathrm{P}_{ext} = \mathrm{P}_{def} &= \int_{\Omega_t} \left[\rho^s \left(1-n^v\right)\mathbf{f}.\mathbf{v}^s + \rho^l s^l n^v \mathbf{f}.\mathbf{v}^l + \rho^g s^g n^v \mathbf{f}.\mathbf{v}^g + \rho^l \eta^m \theta^s_{\max} \mathbf{f}.\mathbf{v}^{mc} \right] d\Omega_t \\ &+ \int_{\Gamma_t} \left(\mathbf{t}^s.\mathbf{v}^s + \mathbf{t}^l.\mathbf{v}^l + \mathbf{t}^g.\mathbf{v}^g + \mathbf{t}^{mc}.\mathbf{v}^{mc} \right) d\Gamma_t \\ &- \int_{\Omega_t} \left[\rho^s \left(1-n^v\right)\boldsymbol{\gamma}^s.\mathbf{v}^s + \rho^l S^l n^v \boldsymbol{\gamma}^l.\mathbf{v}^l + \rho^g S^g n^v \boldsymbol{\gamma}^g.\mathbf{v}^g + \rho^l \zeta^m \theta^s_{\max} \boldsymbol{\gamma}^{mc}.\mathbf{v}^{mc} \right] d\Omega_t \end{aligned} \quad (3.68)$$

Then virtual expenditure of internal and external power can be defined when virtual ones replace the prescribed fields as follows:

$$\mathrm{P}_{\mathrm{int}}^{*}=\int_{\Omega_t}\left[\begin{array}{l}\left(1-n^{v}\right)\boldsymbol{\sigma}^{s}.\delta\nabla\mathbf{v}^{s}+s^{l}n^{v}\boldsymbol{\sigma}^{l}.\delta\nabla\mathbf{v}^{l}\\+s^{g}n^{v}\boldsymbol{\sigma}^{g}.\delta\nabla\mathbf{v}^{g}+\eta^{m}\theta_{\max}^{s}\boldsymbol{\sigma}^{mc}.\delta\nabla\mathbf{v}^{mc}\\+\sum_{m=1}^{M_{\mathrm{int}}^{ve}}\chi_{m}\delta\xi^{(m)\prime}+\mathbf{f}^{\rightarrow l}.\delta\mathbf{v}^{ls}+\mathbf{f}^{\rightarrow g}.\delta\mathbf{v}^{gs}+\mathbf{f}^{\rightarrow mc}.\delta\mathbf{v}^{mcs}\\+Y\delta n^{v\prime}+W\delta\omega^{\prime}+Z\delta\phi^{e\prime}\end{array}\right]d\Omega_{t} \tag{3.69}$$

$$\begin{aligned}\mathrm{P}_{ext}^{*}=&\int_{\Omega_t}\left[\begin{array}{l}\rho^{s}\left(1-n^{v}\right)\mathbf{f}.\delta\mathbf{v}^{s}+\rho^{l}s^{l}n^{v}\mathbf{f}.\delta\mathbf{v}^{l}\\+\rho^{g}s^{g}n^{v}\mathbf{f}.\delta\mathbf{v}^{g}+\rho^{l}\eta^{m}\theta_{\max}^{s}\mathbf{f}.\delta\mathbf{v}^{mc}\\-\rho^{s}\left(1-n^{v}\right)\boldsymbol{\gamma}^{s}.\delta\mathbf{v}^{s}-\rho^{l}s^{l}n^{v}\boldsymbol{\gamma}^{l}.\delta\mathbf{v}^{l}\\-\rho^{g}s^{g}n^{v}\boldsymbol{\gamma}^{g}.\delta\mathbf{v}^{g}-\rho^{l}\zeta^{m}\theta_{\max}^{s}\boldsymbol{\gamma}^{mc}.\delta\mathbf{v}^{mc}\end{array}\right]d\Omega_{t}\\&+\int_{\Gamma_t}\left(\mathbf{t}^{s}.\delta\mathbf{v}^{s}+\mathbf{t}^{l}.\delta\mathbf{v}^{l}+\mathbf{t}^{g}.\delta\mathbf{v}^{g}+\mathbf{t}^{mc}.\delta\mathbf{v}^{mc}\right)d\Gamma_{t}\end{aligned} \tag{3.70}$$

where $\mathrm{P}_{\mathrm{int}}^{*}$ and P_{ext}^{*} are virtual internal and external expenditures of power and note that the kinematical fields $\delta\mathbf{v}^{s,l,g}$, $\delta\mathbf{v}^{ls}$, $\delta\mathbf{v}^{gs}$, $\delta\xi^{(m)\prime}$, $\delta n^{v\prime}$, $\delta\omega^{\prime}$, and $\delta\phi^{e\prime}$ are virtual prescribed fields, where δ is the variation operator.

According to the principle of virtual power, the external expenditure of virtual power should be balanced by the internal expenditure of virtual power:

$$\mathrm{P}_{int}^{*}=\mathrm{P}_{ext}^{*} \tag{3.71}$$

That is;

$$
\begin{aligned}
&\int_{\Omega_t}\left[\begin{array}{l}
\rho^s\left(1-n^v\right)\mathbf{f}.\delta\mathbf{v}^s+\rho^l s^l n^v\mathbf{f}.\delta\mathbf{v}^l\\
+\rho^g s^g n^v\mathbf{f}.\delta\mathbf{v}^g+\rho^l\eta^m\theta^s_{\max}\mathbf{f}.\delta\mathbf{v}^{mc}\\
-\rho^s\left(1-n^v\right)\boldsymbol{\gamma}^s.\delta\mathbf{v}^s-\rho^l s^l n^v\boldsymbol{\gamma}^l.\delta\mathbf{v}^l\\
-\rho^g s^g n^v\boldsymbol{\gamma}^g.\delta\mathbf{v}^g-\rho^l\eta^m\theta^s_{\max}\boldsymbol{\gamma}^{mc}.\delta\mathbf{v}^{mc}
\end{array}\right]d\Omega_t\\
&+\int_{\Gamma_t}\left(\mathbf{t}^s.\delta\mathbf{v}^s+\mathbf{t}^l.\delta\mathbf{v}^l+\mathbf{t}^g.\delta\mathbf{v}^g+\mathbf{t}^{mc}.\delta\mathbf{v}^{mc}\right)d\Gamma_t=\\
&\int_{\Omega_t}\left[\begin{array}{l}
\left(1-n^v\right)\boldsymbol{\sigma}^s.\delta\nabla\mathbf{v}^s+s^l n^v\boldsymbol{\sigma}^l.\delta\nabla\mathbf{v}^l\\
+s^g n^v\boldsymbol{\sigma}^g.\delta\nabla\mathbf{v}^g+\eta^m\theta^s_{\max}\boldsymbol{\sigma}^{mc}.\delta\nabla\mathbf{v}^{mc}\\
+\sum_{m=1}^{M^{ve}_{\text{int}}}\chi_m\delta\xi^{(m)\prime}+\mathbf{f}^{\to l}.\delta\mathbf{v}^{ls}+\mathbf{f}^{\to g}.\delta\mathbf{v}^{gs}+\mathbf{f}^{\to mc}.\delta\mathbf{v}^{mcs}\\
+Y\delta n^{v\prime}+W\delta\omega'+Z\delta\phi^{e\prime}
\end{array}\right]d\Omega_t
\end{aligned}
\tag{3.72}
$$

Using divergence theorem Eq. (3.72) becomes:

$$
\begin{aligned}
&\int_{\Omega_t}\left[\begin{array}{l}
\rho^s\left(1-n^v\right)\left(\mathbf{f}-\boldsymbol{\gamma}^s\right).\delta\mathbf{v}^s+div\left[\left(1-n^v\right)\boldsymbol{\sigma}^s\right].\delta\mathbf{v}^s\\
+\rho^l s^l n^v\left(\mathbf{f}-\boldsymbol{\gamma}^l\right).\delta\mathbf{v}^l+div\left(s^l n^v\boldsymbol{\sigma}^l\right).\delta\mathbf{v}^l\\
+\rho^g s^g n^v\left(\mathbf{f}-\boldsymbol{\gamma}^g\right).\delta\mathbf{v}^g+div\left(s^g n^v\boldsymbol{\sigma}^g\right).\delta\mathbf{v}^g\\
+\rho^l\eta^m\theta^s_{\max}\left(\mathbf{f}-\boldsymbol{\gamma}^{mc}\right).\delta\mathbf{v}^{mc}+div\left(\eta^m\theta^s_{\max}\boldsymbol{\sigma}^{mc}\right).\delta\mathbf{v}^{mc}
\end{array}\right]d\Omega_t\\
&+\int_{\Gamma_t}\left(\mathbf{t}^s.\delta\mathbf{v}^s+\mathbf{t}^l.\delta\mathbf{v}^l+\mathbf{t}^g.\delta\mathbf{v}^g+\mathbf{t}^{mc}.\delta\mathbf{v}^{mc}\right)d\Gamma_t\\
&-\int_{\Gamma}\left[\begin{array}{l}
\left(1-n^v\right)\boldsymbol{\sigma}^s\delta\nabla\mathbf{v}^s.\mathbf{n}+s^l n^v\boldsymbol{\sigma}^l\delta\nabla\mathbf{v}^l.\mathbf{n}\\
+s^g n^v\boldsymbol{\sigma}^g\delta\nabla\mathbf{v}^g.\mathbf{n}+\eta^m\theta^s_{\max}\boldsymbol{\sigma}^{mc}\delta\nabla\mathbf{v}^{mc}.\mathbf{n}
\end{array}\right]d\Gamma_t=\\
&\int_{\Omega_t}\left[\begin{array}{l}
\sum_{m=1}^{M^{ve}_{\text{int}}}\chi_m\delta\xi^{(m)\prime}+\mathbf{f}^{\to l}.\delta\mathbf{v}^{ls}+\mathbf{f}^{\to g}.\delta\mathbf{v}^{gs}+\mathbf{f}^{\to mc}.\delta\mathbf{v}^{mcs}\\
+Y\delta n^{v\prime}+W\delta\omega'+Z\delta\phi^{e\prime}
\end{array}\right]d\Omega_t
\end{aligned}
\tag{3.73}
$$

The fields $\delta\mathbf{u}$, $\delta\xi^{(m)\prime}$, $\delta n^{v\prime}$, $\delta\omega'$, and $\delta\phi^{e\prime}$ may be arbitrary specified if and only if:

$$div\left[\left(1-n^{v}\right)\boldsymbol{\sigma}^{s}\right]+\rho^{s}\left(1-n^{v}\right)\left(\mathbf{f}-\boldsymbol{\gamma}^{s}\right)+\mathbf{f}^{\rightarrow l}+\mathbf{f}^{\rightarrow g}=0 \text{ in } \Omega \tag{3.74}$$

$$div\left(s^{l}n^{v}\boldsymbol{\sigma}^{l}\right)+\rho^{l}s^{l}n^{v}\left(\mathbf{f}-\boldsymbol{\gamma}^{l}\right)-\mathbf{f}^{\rightarrow l}=0 \text{ in } \Omega \tag{3.75}$$

$$div\left(s^{g}n^{v}\boldsymbol{\sigma}^{g}\right)+\rho^{g}s^{g}n^{v}\left(\mathbf{f}-\boldsymbol{\gamma}^{g}\right)-\mathbf{f}^{\rightarrow g}=0 \text{ in } \Omega \tag{3.76}$$

$$div\left(\eta^{m}\theta_{\max}^{s}\boldsymbol{\sigma}^{mc}\right)+\rho^{l}\eta^{m}\theta_{\max}^{s}\left(\mathbf{f}-\boldsymbol{\gamma}^{mc}\right)-\mathbf{f}^{\rightarrow mc}=0 \text{ in } \Omega \tag{3.77}$$

$$\mathbf{t}^{s}=\left(1-n^{v}\right)\boldsymbol{\sigma}^{sT}\mathbf{n} \text{ on } \Gamma \tag{3.78}$$

$$\mathbf{t}^{l}=s^{l}n^{v}\boldsymbol{\sigma}^{l^{T}}\mathbf{n} \text{ on } \Gamma \tag{3.79}$$

$$\mathbf{t}^{g}=s^{g}n^{v}\boldsymbol{\sigma}^{g^{T}}\mathbf{n} \text{ on } \Gamma \tag{3.80}$$

$$\mathbf{t}^{mc}=\eta^{m}\theta_{\max}^{s}\boldsymbol{\sigma}^{mc^{T}}\mathbf{n} \text{ on } \Gamma \tag{3.81}$$

$$\chi_{m}=0 \text{ in } \Omega,\ m=1,...,M_{\text{int}}^{ve};M_{\text{int}}^{ve}\geq 1 \tag{3.82}$$

$$Y=0 \text{ in } \Omega \tag{3.83}$$

$$W=0 \text{ in } \Omega \tag{3.84}$$

$$Z=0 \text{ in } \Omega \tag{3.85}$$

Eq. (3.74) to (3.77) express the local stress equilibrium equation or the macroforce balance for solid, liquid, moisture content, and gas phase; Eq. (3.78) to (3.81) define the macroscopic boundary traction for solid, liquid, moisture content, and

gas phase as the density of the surface forces introduced; and Eq. (3.83) to (3.85) defines different damage microforce balances that will be used in deriving the visco-mechanical, moisture, and scouring damage nucleation and growth conditions. Eq. (3.82) defines the viscoelastic microforce balance, which is new and non-classical for vis-coelastic materials (Abu Al-Rub and Darabi, 2012). It is noteworthy to mention that the effect of moisture content inside the solid part has been neglected here. Then, combining Eqs. (3.74) to (3.76) and Eqs. (3.78) to (3.80) yields:

$$\begin{cases} div\left[\left(1-n^{v}\right)\boldsymbol{\sigma}^{s}+s^{l}n^{v}\boldsymbol{\sigma}^{l}+s^{g}n^{v}\boldsymbol{\sigma}^{g}\right] \\ +\left[\rho^{s}\left(1-n^{v}\right)+\rho^{l}s^{l}n^{v}+\rho^{g}s^{g}n^{v}\right]\left(\mathbf{f}-\boldsymbol{\gamma}^{s}\right)=0 \quad \text{in } \Omega \\ div\left(\boldsymbol{\sigma}\right)+\rho\left(\mathbf{f}-\boldsymbol{\gamma}^{s}\right)=0 \end{cases} \tag{3.86}$$

$$\begin{aligned} \mathbf{t}=\mathbf{t}^{s}+\mathbf{t}^{l}+\mathbf{t}^{g} &=\left(1-n^{v}\right)\boldsymbol{\sigma}^{s}\mathbf{n}+s^{l}n^{v}\boldsymbol{\sigma}^{l}\mathbf{n}+s^{g}n^{v}\boldsymbol{\sigma}^{g}\mathbf{n} \text{ on } \Gamma \\ &=\boldsymbol{\sigma}\mathbf{n} \end{aligned} \tag{3.87}$$

3.2.4 The First Law of Thermodynamics; Energy Conservation

The balance of energy in the representative piece of material currently occupying Ω_t equates the rate of change of the energy content to the sum of the integrated rate of supply of energy to volume elements of Ω_t and on surface elements of Γ_t. The rate of change of the kinetic energy, $\mathrm{K}\left(\Omega_t\right)$, and the mechanical power, $\mathrm{P}_{mech}\left(\Omega_t\right)$, appear on opposite sides of this equation, but they do not account in full for balance of energy, first because a deformable body does not possess energy solely by virtue of its motion, and secondly because the inter-convertibility of mechanical work and heat which is a

fundamental physical principle of energy transfer would be excluded. It is therefore postulated that in each of the configurations of a moving material body there are associated with an arbitrary material region Ω_t scalars $\mathrm{U}(\Omega_t)$ and $\mathrm{H}(\Omega_t)$, referred to respectively as the internal energy content and the heating of the material occupying Ω_t, such that:

$$\frac{D}{Dt}\left\{\mathrm{K}(\Omega_t)+\mathrm{U}(\Omega_t)\right\}=\mathrm{P}_{mech}(\Omega_t)+\mathrm{H}(\Omega_t) \tag{3.88}$$

This is the *equation of energy balance* or the first law of thermodynamics and the set function $\mathrm{U}(\Omega_t)$ and $\mathrm{H}(\Omega_t)$ represent in turn the energy which the material possesses in addition to its kinetic energy and the rate at which energy is supplied to the material as a result of non-mechanical interaction with its surrounding. These components for a partially saturated porous media is expressing as:

$$\begin{aligned}\mathrm{K}(\Omega_t)=&\int_{\Omega_t^s}\frac{1}{2}\rho^s\mathbf{v}^s.\mathbf{v}^s d\Omega_t^s+\int_{\Omega_t^l}\frac{1}{2}\rho^l\mathbf{v}^l.\mathbf{v}^l d\Omega_t^l\\&+\int_{\Omega_t^g}\frac{1}{2}\rho^g\mathbf{v}^g.\mathbf{v}^g d\Omega_t^g+\int_{\Omega_t^{mc}}\frac{1}{2}\rho^l\mathbf{v}^{mc}.\mathbf{v}^{mc} d\Omega_t^{mc}\end{aligned} \tag{3.89}$$

$$\mathrm{U}(\Omega_t)=\int_{\Omega_t^s}\rho^s e^s d\Omega_t^s+\int_{\Omega_t^l}\rho^l e^l d\Omega_t^l+\int_{\Omega_t^g}\rho^g e^g d\Omega_t^g+\int_{\Omega_t^{mc}}\rho^l e^{mc} d\Omega_t^{mc} \tag{3.90}$$

$$\begin{aligned}\mathrm{P}_{mech}(\Omega_t)=&\int_{\Omega_t^s}\rho^s\mathbf{f}.\mathbf{v}^s d\Omega_t^s+\int_{\Omega_t^l}\rho^l\mathbf{f}.\mathbf{v}^l d\Omega_t^l+\int_{\Omega_t^g}\rho^g\mathbf{f}.\mathbf{v}^g d\Omega_t^g+\int_{\Omega_t^{mc}}\rho^l\mathbf{f}.\mathbf{v}^{mc} d\Omega_t^{mc}\\&+\int_{\Gamma_t}\left(\mathbf{t}^s.\mathbf{v}^s+\mathbf{t}^l.\mathbf{v}^l+\mathbf{t}^g.\mathbf{v}^g+\mathbf{t}^{mc}.\mathbf{v}^{mc}\right)d\Gamma_t\end{aligned} \tag{3.91}$$

$$\mathrm{H}\left(\Omega_t\right)=\int_{\Omega_t}\rho r d\Omega_t-\int_{\Gamma_t}\mathbf{q}^{th}\mathbf{n}d\Gamma_t \tag{3.92}$$

where e^s, e^l, e^g, ρ^s, ρ^l, ρ^g, ρ, P_{ext}, $\mathbf{q}^{th}$ and r are Eulerian specific internal energy of solid part (aggregates plus binder), Eulerian specific internal energy of liquid phase, Eulerian specific internal energy of gas phase, density of solid part, density of liquid, density of gas, density of the mixture (solid, fluid and gas), specific external power, Eulerian heat flux, and Eulerian specific heat production, respectively.

The relations between the phases' volume and the total volume can be written as:

$$\begin{aligned} d\Omega_t^s &= \left(1-n^v\right)d\Omega_t \\ d\Omega_t^l &= \theta^v d\Omega_t = s^l n^v d\Omega_t \\ d\Omega_t^g &= s^g n^v d\Omega_t \\ d\Omega_t^{mc} &= \theta^s d\Omega_t = \eta^m \theta^s_{\max} d\Omega_t \end{aligned} \tag{3.93}$$

where n^v, s^l, s^g, θ^s and θ^v are Eulerian porosity, liquid degree of saturation, gas degree of saturation, i.e. $s^g=1-s^l$, moisture content inside the solid phase, and moisture content within the interconnected cracks and voids. Substituting Eq. (3.93) into Eq. (3.89) to (3.91) the energies in total volume becomes;

$$\mathrm{K}\left(\Omega_t\right)=\int_{\Omega_t}\left[\begin{array}{l}\frac{1}{2}\rho^s\left(1-n^v\right)\mathbf{v}^s.\mathbf{v}^s+\frac{1}{2}\rho^l s^l n^v\mathbf{v}^l.\mathbf{v}^l \\ +\frac{1}{2}\rho^g s^g n^v\mathbf{v}^g.\mathbf{v}^g+\frac{1}{2}\rho^l\eta^m\theta^s_{\max}\mathbf{v}^{mc}.\mathbf{v}^{mc}\end{array}\right]d\Omega_t \tag{3.94}$$

$$\mathrm{U}\left(\Omega_t\right)=\int_{\Omega_t}\left[\rho^s\left(1-n^v\right)e^s+\rho^l s^l n^v e^l+\rho^g s^g n^v e^g+\rho^l\eta^m\theta^s_{\max}e^{mc}\right]d\Omega_t \tag{3.95}$$

$$\begin{aligned} \mathrm{P}_{mech}\left(\Omega_t\right) = & \int_{\Omega_t} \begin{bmatrix} \rho^s \left(1-n^v\right)\mathbf{f}.\mathbf{v}^s + \rho^l s^l n^v \mathbf{f}.\mathbf{v}^l \\ +\rho^g s^g n^v \mathbf{f}.\mathbf{v}^g + \rho^l \eta^m \theta^s_{\max} \mathbf{f}.\mathbf{v}^{mc} \end{bmatrix} d\Omega_t \\ & + \int_{\Gamma_t} \left(\mathbf{t}^s.\mathbf{v}^s + \mathbf{t}^l.\mathbf{v}^l + \mathbf{t}^g.\mathbf{v}^g + \mathbf{t}^{mc}.\mathbf{v}^{mc}\right) d\Gamma_t \end{aligned} \tag{3.96}$$

Getting the time derivative of the kinetic energy;

$$\frac{D}{Dt}\left\{\mathrm{K}\left(\Omega_t\right)\right\} = \frac{D}{Dt}\left\{ \int_{\Omega_t} \begin{bmatrix} \frac{1}{2}\rho^s \left(1-n^v\right)\mathbf{v}^s.\mathbf{v}^s + \frac{1}{2}\rho^l s^l n^v \mathbf{v}^l.\mathbf{v}^l \\ +\frac{1}{2}\rho^g s^g n^v \mathbf{v}^g.\mathbf{v}^g + \frac{1}{2}\rho^l \eta^m \theta^s_{\max} \mathbf{v}^{mc}.\mathbf{v}^{mc} \end{bmatrix} d\Omega_t \right\} \tag{3.97}$$

And using mass balance equation, the time derivative of the kinetic energy becomes equal to;

$$\frac{D}{Dt}\left\{\mathrm{K}\left(\Omega_t\right)\right\} = \int_{\Omega_t} \begin{bmatrix} \rho^s \left(1-n^v\right)\boldsymbol{\gamma}^s.\mathbf{v}^s + \rho^l s^l n^v \boldsymbol{\gamma}^l.\mathbf{v}^l \\ +\rho^g s^g n^v \boldsymbol{\gamma}^g.\mathbf{v}^g + \rho^l \eta^m \theta^s_{\max} \boldsymbol{\gamma}^{mc}.\mathbf{v}^{mc} \end{bmatrix} d\Omega_t \tag{3.98}$$

It is known that Eq. (3.96) minus Eq. (3.98) is equal to the external power supplied to the body and therefore equal to the internal power. Therefore Energy balance equation can be written;

$$\frac{D}{Dt}\left\{\mathrm{U}\left(\Omega_t\right)\right\} = \mathrm{P}_{\mathrm{int}}\left(\Omega_t\right) + \mathrm{H}\left(\Omega_t\right) \tag{3.99}$$

Now, getting the time derivative of the internal energy equation, Eq. (3.95);

$$\frac{D}{Dt}\left\{\mathrm{U}\left(\Omega_t\right)\right\} = \frac{D}{Dt}\left\{ \int_{\Omega_t} \begin{bmatrix} \rho^s \left(1-n^v\right)e^s + \rho^l s^l n^v e^l \\ +\rho^g s^g n^v e^g + \rho^l \eta^m \theta^s_{\max} e^{mc} \end{bmatrix} d\Omega_t \right\} \tag{3.100}$$

Knowing that $\frac{D}{Dt}\left(d\Omega_t\right) = div\left(\mathbf{v}\right)d\Omega_t$ Eq. (3.100) yields to;

$$\int_{\Omega_t}\begin{Bmatrix} \frac{D}{Dt}\left[\rho^s\left(1-n^v\right)e^s\right]+\rho^s\left(1-n^v\right)e^s div\left(\mathbf{v}^s\right) \\ \frac{D}{Dt}\left[\rho^l s^l n^v e^l\right]+\rho^l s^l n^v e^l div\left(\mathbf{v}^l\right) \\ \frac{D}{Dt}\left[\rho^g s^g n^v e^g\right]+\rho^g s^g n^v e^g div\left(\mathbf{v}^g\right) \\ \frac{D}{Dt}\left[\rho^l \theta^s e^l\right]+\rho^l \eta^m \theta^s_{\max} e^l div\left(\mathbf{v}^{mc}\right) \end{Bmatrix} d\Omega_t \tag{3.101}$$

Applying some mathematical manipulation Eq. (3.101) becomes;

$$\int_{\Omega_t}\begin{Bmatrix} \frac{\partial e}{\partial t}+div\left(\rho^s\left(1-n^v\right)e^s\mathbf{v}^s\right) \\ +div\left(\rho^l s^l n^v e^l\mathbf{v}^l\right)\pm div\left(\rho^l s^l n^v e^l\mathbf{v}^s\right) \\ +div\left(\rho^g s^g n^v e^g\mathbf{v}^g\right)\pm div\left(\rho^g s^g n^v e^g\mathbf{v}^s\right) \\ +div\left(\rho^l \eta^m \theta^s_{\max} e^l\mathbf{v}^{mc}\right)\pm div\left(\rho^l \eta^m \theta^s_{\max} e^l\mathbf{v}^s\right) \end{Bmatrix} d\Omega_t \tag{3.102}$$

where $e = \rho^s\left(1-n^v\right)e^s + \rho^l s^l n^v e^l + \rho^g s^g n^v e^g + \rho^l \theta^s e^l$

$$\int_{\Omega_t}\begin{Bmatrix} \frac{\partial e}{\partial t}+div\left[\left(\rho^s\left(1-n^v\right)e^s + \rho^l s^l n^v e^l + \rho^g s^g n^v e^g + \rho^l \eta^m \theta^s_{\max} e^l\right)\mathbf{v}^s\right] \\ +div\left[\rho^l s^l n^v e^l\left(\mathbf{v}^l-\mathbf{v}^s\right)\right] \\ +div\left[\rho^g s^g n^v e^g\left(\mathbf{v}^g-\mathbf{v}^s\right)\right] \\ +div\left[\rho^l \eta^m \theta^s_{\max} e^l\left(\mathbf{v}^{mc}-\mathbf{v}^s\right)\right] \end{Bmatrix} d\Omega_t \tag{3.103}$$

Using Eq. (3.58);

$$\int_{\Omega_t}\left\{\frac{\partial e}{\partial t}+div\left(e\mathbf{v}^s\right)+div\left(\mathbf{q}^l e^l\right)+div\left(\mathbf{q}^g e^g\right)+div\left(\mathbf{q}^{mc} e^{mc}\right)\right\}d\Omega_t \tag{3.104}$$

$$\int_{\Omega_t}\left\{\frac{De}{Dt}+ediv\left(\mathbf{v}^s\right)+div\left(\mathbf{q}^l e^l\right)+div\left(\mathbf{q}^g e^g\right)+div\left(\mathbf{q}^{mc} e^{mc}\right)\right\}d\Omega_t \tag{3.105}$$

The specific internal power, P_{int}, for deformable body is defined by Eq. (3.67), applying some mathematical manipulation, using $\boldsymbol{\sigma}=\left(1-n^v\right)\boldsymbol{\sigma}^s+s^l n^v\boldsymbol{\sigma}^l+s^g n^v\boldsymbol{\sigma}^g+\eta^m\theta^s_{\max}\boldsymbol{\sigma}^m$, and neglecting body force, fluid and gas rate of velocity, the internal power equation becomes:

$$P_{\text{int}}=\int_{\Omega_t}\begin{bmatrix}\left(1-n^v\right)\boldsymbol{\sigma}^s.\nabla\mathbf{v}^s+s^l n^v\boldsymbol{\sigma}^l.\nabla\mathbf{v}^l\\+s^g n^v\boldsymbol{\sigma}^g.\nabla\mathbf{v}^g+\eta^m\theta^s_{\max}\boldsymbol{\sigma}^{mc}.\nabla\mathbf{v}^{mc}\\+\sum_{m=1}^{M^{ve}_{\text{int}}}\chi_m\xi^{(m)\prime}+\mathbf{f}^{\to l}.\mathbf{v}^{ls}+\mathbf{f}^{\to g}.\mathbf{v}^{gs}+\mathbf{f}^{\to mc}.\mathbf{v}^{mcs}\\+Yn^{v\prime}+W\omega'+Z\phi^{e\prime}\end{bmatrix}d\Omega_t \tag{3.106}$$

Applying some mathematical manipulation;

$$P_{\text{int}}=\int_{\Omega_t}\begin{bmatrix}\left(1-n^v\right)\boldsymbol{\sigma}^s.\nabla\mathbf{v}^s+s^l n^v\boldsymbol{\sigma}^l.\nabla\mathbf{v}^l\\+s^g n^v\boldsymbol{\sigma}^g.\nabla\mathbf{v}^g+\eta^m\theta^s_{\max}\boldsymbol{\sigma}^{mc}.\nabla\mathbf{v}^{mc}\\+\sum_{m=1}^{M^{ve}_{\text{int}}}\chi_m\xi^{(m)\prime}\pm s^l n^v\boldsymbol{\sigma}^l.\nabla\mathbf{v}^s\pm s^g n^v\boldsymbol{\sigma}^g.\nabla\mathbf{v}^s\pm\eta^m\theta^s_{\max}\boldsymbol{\sigma}^{mc}.\nabla\mathbf{v}^s\\+\mathbf{f}^{\to l}.\mathbf{v}^{ls}+\mathbf{f}^{\to g}.\mathbf{v}^{gs}+\mathbf{f}^{\to mc}.\mathbf{v}^{mcs}\\+Yn^{v\prime}+W\omega'+Z\phi^{e\prime}\end{bmatrix}d\Omega_t \tag{3.107}$$

Using Eq. (3.75) and (3.76);

$$P_{\text{int}} = \int_{\Omega_t} \left\{ \begin{array}{l} \left[\left(1-n^{v}\right)\boldsymbol{\sigma}^{s} + s^{l}n^{v}\boldsymbol{\sigma}^{l} + s^{g}n^{v}\boldsymbol{\sigma}^{g} + \eta^{m}\theta^{s}_{\max}\boldsymbol{\sigma}^{mc} \right].\nabla\mathbf{v}^{s} \\ +\sum_{m=1}^{M^{ve}_{\text{int}}} \chi_{m}\xi^{(m)\prime} + s^{l}n^{v}\boldsymbol{\sigma}^{l}.\left(\nabla\mathbf{v}^{l} - \nabla\mathbf{v}^{s}\right) \\ +s^{g}n^{v}\boldsymbol{\sigma}^{g}.\left(\nabla\mathbf{v}^{g} - \nabla\mathbf{v}^{s}\right) + \eta^{m}\theta^{s}_{\max}\boldsymbol{\sigma}^{mc}.\left(\nabla\mathbf{v}^{mc} - \nabla\mathbf{v}^{s}\right) \\ +\left[div\left(s^{l}n^{v}\boldsymbol{\sigma}^{l}\right) + \rho^{l}s^{l}n^{v}\left(\mathbf{f} - \boldsymbol{\gamma}^{l}\right)\right].\mathbf{v}^{ls} \\ +\left[div\left(s^{g}n^{v}\boldsymbol{\sigma}^{g}\right) + \rho^{g}s^{g}n^{v}\left(\mathbf{f} - \boldsymbol{\gamma}^{g}\right)\right].\mathbf{v}^{gs} \\ \left[div\left(\eta^{m}\theta^{s}_{\max}\boldsymbol{\sigma}^{mc}\right) + \rho^{l}\eta^{m}\theta^{s}_{\max}\left(\mathbf{f} - \boldsymbol{\gamma}^{mc}\right)\right].\mathbf{v}^{mcs} \\ +Yn^{v\prime} + W\omega' + Z\phi^{e\prime} \end{array} \right\} d\Omega_{t} \qquad (3.108)$$

$$P_{\text{int}} = \int_{\Omega_t} \left\{ \begin{array}{l} \left[\left(1-n^{v}\right)\boldsymbol{\sigma}^{s} + s^{l}n^{v}\boldsymbol{\sigma}^{l} + s^{g}n^{v}\boldsymbol{\sigma}^{g} + \eta^{m}\theta^{s}_{\max}\boldsymbol{\sigma}^{mc} \right].\nabla\mathbf{v}^{s} \\ +\sum_{m=1}^{M^{ve}_{\text{int}}} \chi_{m}\xi^{(m)\prime} + s^{l}n^{v}\boldsymbol{\sigma}^{l}.\nabla\mathbf{v}^{ls} + div\left(s^{l}n^{v}\boldsymbol{\sigma}^{l}\right).\mathbf{v}^{ls} \\ +s^{g}n^{v}\boldsymbol{\sigma}^{g}.\nabla\mathbf{v}^{gs} + div\left(s^{g}n^{v}\boldsymbol{\sigma}^{g}\right).\mathbf{v}^{gs} \\ +\eta^{m}\theta^{s}_{\max}\boldsymbol{\sigma}^{mc}.\nabla\mathbf{v}^{mcs} + div\left(\eta^{m}\theta^{s}_{\max}\boldsymbol{\sigma}^{mc}\right).\mathbf{v}^{mcs} \\ +\rho^{l}\eta^{m}\theta^{s}_{\max}\left(\mathbf{f} - \boldsymbol{\gamma}^{mc}\right).\mathbf{v}^{mcs} \\ +\rho^{l}s^{l}n^{v}\left(\mathbf{f} - \boldsymbol{\gamma}^{l}\right).\mathbf{v}^{ls} + \rho^{g}s^{g}n^{v}\left(\mathbf{f} - \boldsymbol{\gamma}^{g}\right).\mathbf{v}^{gs} \\ +Yn^{v\prime} + W\omega' + Z\phi^{e\prime} \end{array} \right\} d\Omega_{t} \qquad (3.109)$$

And using $\boldsymbol{\sigma} = \left(1-n^{v}\right)\boldsymbol{\sigma}^{s} + s^{l}n^{v}\boldsymbol{\sigma}^{l} + s^{g}n^{v}\boldsymbol{\sigma}^{g} + \eta^{m}\theta^{s}_{\max}\boldsymbol{\sigma}^{m}$, Eq. (3.109) becomes:

$$P_{\text{int}} = \int_{\Omega_t} \left\{ \begin{array}{l} \boldsymbol{\sigma}.\nabla \mathbf{v}^s + div\left(s^l n^v \boldsymbol{\sigma}^l \mathbf{v}^{ls}\right) + div\left(s^g n^v \boldsymbol{\sigma}^g \mathbf{v}^{gs}\right) \\ + div\left(\eta^m \theta^s_{\max} \boldsymbol{\sigma}^{mc} \mathbf{v}^{mcs}\right) \\ + \rho^l s^l n^v \left(\mathbf{f} - \boldsymbol{\gamma}^l\right).\mathbf{v}^{ls} + \rho^g s^g n^v \left(\mathbf{f} - \boldsymbol{\gamma}^g\right).\mathbf{v}^{gs} \\ + \rho^l \eta^m \theta^s_{\max} \left(\mathbf{f} - \boldsymbol{\gamma}^{mc}\right).\mathbf{v}^{mcs} \\ + \sum_{m=1}^{M^{ve}_{\text{int}}} \chi_m \xi^{(m)\prime} + Yn^{v\prime} + W\omega' + Z\phi^{e\prime} \end{array} \right\} d\Omega_t \qquad (3.110)$$

Considering $\boldsymbol{\sigma}^l = -p^l \mathbf{I}$ and $\boldsymbol{\sigma}^g = -p^g \mathbf{I}$, where p^l and p^g are liquid pressure, and gas pressure, respectively.

And substituting these into Eq. (3.110) and neglecting the body force and fluid and gas acceleration:

$$P_{int} = \int_{\Omega_t} \left[\begin{array}{l} \boldsymbol{\sigma}.\mathbf{d} - div\left(\frac{p^l}{\rho^l}\mathbf{q}^l\right) - div\left(\frac{p^g}{\rho^g}\mathbf{q}^g\right) - div\left(\frac{p^m}{\rho^l}\mathbf{q}^{mc}\right) \\ + \sum_{m=1}^{M^{ve}_{\text{int}}} \chi_m \xi^{(m)\prime} + Yn^{v\prime} + W\omega' + Z\phi^{e\prime} \end{array} \right] d\Omega_t \qquad (3.111)$$

where $\mathbf{d}$ is the rate of deformation tensor. Substituting Eqs. (3.105), and (3.111) into Eq. (3.99):

$$\int_{\Omega_t}\left\{\frac{De}{Dt}+e div\left(\mathbf{v}^s\right)+div\left(\mathbf{q}^l e^l\right)+div\left(\mathbf{q}^g e^g\right)+div\left(\mathbf{q}^{mc} e^{mc}\right)\right\}d\Omega_t=$$
$$\int_{\Omega_t}\left[\begin{array}{l}\boldsymbol{\sigma}.\mathbf{d}-div\left(\frac{p^l}{\rho^l}\mathbf{q}^l\right)-div\left(\frac{p^g}{\rho^g}\mathbf{q}^g\right)-div\left(\frac{p^m}{\rho^l}\mathbf{q}^{mc}\right)\\+\sum_{m=1}^{M_{\text{int}}^{ve}}\chi_m\xi^{(m)\prime}+Yn^{v\prime}+W\omega'+Z\phi^{e\prime}\end{array}\right]d\Omega_t+ \qquad (3.112)$$
$$\int_{\Omega_t}\rho r d\Omega_t-\int_{\Omega_t}div\left(\mathbf{q}^{th}\right)d\Omega_t$$

$$\int_{\Omega_t}\left\{\begin{array}{l}\frac{De}{Dt}+e div\left(\mathbf{v}^s\right)+div\left[\mathbf{q}^l\left(e^l+\frac{p^l}{\rho^l}\right)\right]\\+div\left[\mathbf{q}^g\left(e^g+\frac{p^g}{\rho^g}\right)\right]+div\left[\mathbf{q}^{mc}\left(e^{mc}+\frac{p^m}{\rho^l}\right)\right]\end{array}\right\}d\Omega_t=$$
$$\int_{\Omega_t}\left[\boldsymbol{\sigma}.\mathbf{d}+\sum_{m=1}^{M_{\text{int}}^{ve}}\chi_m\xi^{(m)\prime}+Yn^{v\prime}+W\omega'+Z\phi^{e\prime}\right]d\Omega_t \qquad (3.113)$$
$$+\int_{\Omega_t}\rho r d\Omega_t-\int_{\Omega_t}div\left(\mathbf{q}^{th}\right)d\Omega_t$$

Also, specific enthalpy of liquid and gas phases are defined as:

$$h^l=e^l+\frac{p^l}{\rho^l}$$
$$h^g=e^g+\frac{p^g}{\rho^g} \qquad (3.114)$$

Substituting Eq. (3.114) in Eq. (3.113) finally it becomes:

$$\int_{\Omega_t}\left\{\frac{De}{Dt}+ediv\left(\mathbf{v}^s\right)+div\left(h^l\mathbf{q}^l\right)+div\left(h^g\mathbf{q}^g\right)+div\left(h^{mc}\mathbf{q}^{mc}\right)\right\}d\Omega_t=$$
$$\int_{\Omega_t}\left[\boldsymbol{\sigma}.\mathbf{d}+\sum_{m=1}^{M_{\text{int}}^{ve}}\chi_m\xi^{(m)\prime}+Yn^{v\prime}+W\omega'+Z\phi^{e\prime}\right]d\Omega_t \tag{3.115}$$
$$+\int_{\Omega_t}\rho r d\Omega_t-\int_{\Omega_t}div\left(\mathbf{q}^{th}\right)d\Omega_t$$

Transforming this equation to the initial configuration, using Eqs. (3.62) and knowing $ed\Omega_t=Ed\Omega_0$, it yields;

$$\int_{\Omega_0}\left\{\frac{DE}{Dt}+div\left(h^l\mathbf{Q}^l\right)+div\left(h^g\mathbf{Q}^g\right)+div\left(h^{mc}\mathbf{Q}^{mc}\right)\right\}d\Omega_o=$$
$$\int_{\Omega_0}\left[\boldsymbol{\pi}.\dot{\mathbf{E}}+\sum_{m=1}^{M_{\text{int}}^{ve}}\chi_m\dot{\xi}^{(m)}+Y\dot{\phi}^v+W\dot{\omega}+Z\dot{\phi}^e\right]d\Omega_0+\int_{\Omega_0}\rho R d\Omega_0-\int_{\Omega_0}div\left(\mathbf{Q}^{th}\right)d\Omega_0 D \tag{3.116}$$

where $\boldsymbol{\pi}$ is the first Piola-Kirchhoff stress tensor. Localizing the above equation yields to:

$$\dot{E}=\boldsymbol{\pi}.\dot{\mathbf{E}}+\sum_{m=1}^{M_{\text{int}}^{ve}}\chi_m\dot{\xi}^{(m)}+Y\dot{\phi}^v+W\dot{\omega}+Z\dot{\phi}^e$$
$$-Div\left(h^l\mathbf{Q}^l+h^g\mathbf{Q}^g\right)-Div\left(e^l\mathbf{Q}^{mc}\right)+\rho_0 R-Div\left(\mathbf{Q}^{th}\right) \tag{3.117}$$

It should be pointed out that in order to develop a realistic model for the porous material, it is necessary to use a Lagrangian description because it is dealt with the solid matter whose properties such as the porous structure are transported and rotated with the material. This is in contrast with the Eulerian or spatial description, which is more suitable when dealing with isotropic homogeneous fluids.

3.2.5 The Second Law of Thermodynamics; The Entropy Balance

The second law of thermodynamics for partially saturated porous media which states the entropy balance of porous media is expressed as;

$$\frac{D}{Dt}\left[\int_{\Omega_t^s}\rho^s\zeta^s d\Omega_t^s+\int_{\Omega_t^l}\rho^l\zeta^l d\Omega_t^l+\int_{\Omega_t^g}\rho^g\zeta^g d\Omega_t^g+\int_{\Omega_t^{mc}}\rho^l\zeta^{mc} d\Omega_t^{mc}\right] \geq \int_{\Omega_t}\frac{\rho r}{T}d\Omega_t-\int_{\Gamma_t}\frac{\mathbf{q}^{th}}{T}.\mathbf{n}d\Gamma_t \tag{3.118}$$

where ζ^s, ζ^l, ζ^g, and ζ^{mc} are specific Eulerian entropy of solid, liquid, gas, and moisture content inside solid part, respectively. Using Eq. (3.93) in order to consider the second law for the total volume yields:

$$\frac{D}{Dt}\int_{\Omega_t}\left[\rho^s\left(1-n^v\right)\zeta^s+\rho^l s^l n^v\zeta^l+\rho^g s^g n^v\zeta^g+\rho^l\eta^m\theta^s_{\max}\zeta^{mc}\right]d\Omega_t \geq \int_{\Omega_t}\frac{\rho r}{T}d\Omega_t-\int_{\Gamma_t}\frac{\mathbf{q}^{th}}{T}.\mathbf{n}d\Gamma_t \tag{3.119}$$

Using the divergence theorem Eq. (3.119) becomes:

$$\frac{D}{Dt}\int_{\Omega_t}\left[\rho^s\left(1-n^v\right)\zeta^s+\rho^l s^l n^v\zeta^l+\rho^g s^g n^v\zeta^g+\rho^l\eta^m\theta^s_{\max}\zeta^{mc}\right]d\Omega_t \geq \int_{\Omega_t}\frac{\rho r}{T}d\Omega_t-\int_{\Omega_t} div\left(\frac{\mathbf{q}^{th}}{T}\right)d\Omega_t \tag{3.120}$$

Applying the similar mathematical manipulation, which was used for the derivation of the first law of thermodynamics Eq. (3.120) can be expressed as:

$$\int_{\Omega_t}\left[\frac{D\zeta}{Dt}+\zeta\, div\left(\mathbf{v}^s\right)+div\left(\zeta^l\mathbf{q}^l\right)+div\left(\zeta^g\mathbf{q}^g\right)+div\left(\zeta^{mc}\mathbf{q}^{mc}\right)\right]d\Omega_t \geq \int_{\Omega_t}\frac{\rho r}{T}d\Omega_t-\int_{\Omega_t}div\left(\frac{\mathbf{q}^{th}}{T}\right)d\Omega_t \tag{3.121}$$

where $\zeta=\rho^s\left(1-n^v\right)\zeta^s+\rho^l s^l n^v\zeta^l+\rho^g s^g n^v\zeta^g+\rho^l\eta^m\theta^s_{\max}\zeta^{mc}$. In order to transport the entropy balance equation, Eq. (3.121), to the initial configuration, the relationship between the energy and flows in current and initial are defined as:

$$\zeta\, d\Omega_t=\Xi d\Omega_0,\ \zeta^i\mathbf{q}^i d\Omega_t=\zeta^i\mathbf{Q}^i d\Omega_0,\ \text{i=l, g, and mc and } \mathbf{q}^{th}d\Omega_t=\mathbf{Q}^{th}d\Omega_0 \tag{3.122}$$

Transporting the formula, Eq. (3.121), to the Lagrangian configuration by using Eq. (3.122) and localizing the equation it yields:

$$T\dot{\Xi}+TDiv\left(\zeta^l\mathbf{Q}^l+\zeta^g\mathbf{Q}^g+\zeta^{mc}\mathbf{Q}^{mc}\right)-\rho_0 R+Div\left(\mathbf{Q}^{th}\right)-\frac{\mathbf{Q}^{th}\nabla_{\mathrm{X}}T}{T}\geq 0 \tag{3.123}$$

Eq. (3.117) and (3.123) are different from the general description of 1st and 2nd law of thermodynamics since the divergence terms are added in the equations. Each divergence term physically explains energy and entropy advection caused by the fluid transport in porous media.

3.2.6 Clausius-Duhem Inequality

Let ψ denotes the overall Lagrangian specific Helmholtz free energy:

$$\psi=E-T\Xi \tag{3.124}$$

Therefore, $\frac{DE}{Dt}$ can be expressed as:

$$\frac{DE}{Dt} = \frac{D\psi}{Dt} + \frac{DT}{Dt}\Xi + T\frac{D\Xi}{Dt} \tag{3.125}$$

Substituting Eq. (3.117) into Eq. (3.123) Clausius-Duhem inequality will be obtained:

$$\begin{aligned} & T\frac{D\Xi}{Dt} + TDiv\left(\zeta^l \mathbf{Q}^l + \zeta^g \mathbf{Q}^g + \zeta^{mc} \mathbf{Q}^{mc}\right) - \frac{DE}{Dt} \\ & + \boldsymbol{\pi}.\frac{D\mathbf{E}}{Dt} + \sum_{m=1}^{M_{\text{int}}^{ve}} \chi_m \dot{\xi}^{(m)} + Y\frac{D\phi^v}{Dt} + W\frac{D\omega}{Dt} + Z\frac{D\phi^e}{Dt} \\ & - Div\left(h^l \mathbf{Q}^l + h^g \mathbf{Q}^g\right) - Div\left(e^l \mathbf{Q}^{mc}\right) - \frac{\mathbf{Q}^{th}\nabla_{\mathbf{x}} T}{T} \geq 0 \end{aligned} \tag{3.126}$$

Substituting Eq. (3.125) into Eq. (3.126)

$$\begin{aligned} & T\frac{D\Xi}{Dt} + TDiv\left(\zeta^l \mathbf{Q}^l + \zeta^g \mathbf{Q}^g + \zeta^{mc} \mathbf{Q}^{mc}\right) - \frac{D\psi}{Dt} - \frac{DT}{Dt}\Xi - T\frac{D\Xi}{Dt} \\ & + \boldsymbol{\pi}.\frac{D\mathbf{E}}{Dt} + \sum_{m=1}^{M_{\text{int}}^{ve}} \chi_m \dot{\xi}^{(m)} + Y\frac{D\phi^v}{Dt} + W\frac{D\omega}{Dt} + Z\frac{D\phi^e}{Dt} \\ & - Div\left(h^l \mathbf{Q}^l + h^g \mathbf{Q}^g\right) - Div\left(e^l \mathbf{Q}^{mc}\right) - \frac{\mathbf{Q}^{th}\nabla_{\mathbf{x}} T}{T} \geq 0 \end{aligned} \tag{3.127}$$

Rearranging Eq. (3.127):

$$
\begin{aligned}
&Div\left[\left(T\zeta^l - e^l\right)\mathbf{Q}^{mc}\right] + Div\left[\left(T\zeta^l - h^l\right)\mathbf{Q}^l\right] \\
&+Div\left[\left(T\zeta^g - h^g\right)\mathbf{Q}^g\right] \\
&-\frac{D\psi}{Dt} - \frac{DT}{Dt}\Xi + \boldsymbol{\pi}.\frac{D\mathbf{E}}{Dt} + \sum_{m=1}^{M_{\text{int}}^{ve}} \chi_m \frac{D\xi^{(m)}}{Dt} \\
&+Y\frac{D\phi^v}{Dt} + W\frac{D\omega}{Dt} + Z\frac{D\phi^e}{Dt} - \frac{\mathbf{Q}^{th}\nabla_{\mathrm{X}}T}{T} \geq 0
\end{aligned}
\tag{3.128}
$$

Substituting $T\zeta^l - h^l = \psi^l + \frac{p^l}{\rho^l}$, $T\zeta^g - h^g = \psi^g + \frac{p^g}{\rho^g}$, and $\psi^l = e^l - T\zeta^l$ in Eq.(3.128):

$$
\begin{aligned}
&\boldsymbol{\pi}.\frac{D\mathbf{E}}{Dt} + \sum_{m=1}^{M_{\text{int}}^{ve}} \chi_m \frac{D\xi^{(m)}}{Dt} + Y\frac{D\phi^v}{Dt} + W\frac{D\omega}{Dt} + Z\frac{D\phi^e}{Dt} - \frac{D\psi}{Dt} - \frac{DT}{Dt}\Xi \\
&-Div\left(\psi^l\mathbf{Q}^{mc}\right) - Div\left[\left(\psi^l + \frac{p^l}{\rho^l}\right)\mathbf{Q}^l\right] \\
&-Div\left[\left(\psi^g + \frac{p^g}{\rho^g}\right)\mathbf{Q}^g\right] - \frac{\mathbf{Q}^{th}\nabla_{\mathrm{X}}T}{T} \geq 0
\end{aligned}
\tag{3.129}
$$

Eq. (3.129) is the simplified form of the Clausius-Duhem inequality extended to the partially saturated porous media. It also can be written as:

$$
\Pi = \Pi^s + \Pi^l + \Pi^g + \Pi^{th} \geq 0 \tag{3.130}
$$

where,

$$
\begin{aligned}
\Pi^s = &\boldsymbol{\pi}.\frac{D\mathbf{E}}{Dt} + \sum_{m=1}^{M_{\text{int}}^{ve}} \chi_m \frac{D\xi^{(m)}}{Dt} - \frac{D\psi}{Dt} - \frac{DT}{Dt}\Xi - \psi^l Div\left(\mathbf{Q}^{mc}\right) \\
&-\left(\psi^l + \frac{p^l}{\rho^l}\right)Div\left(\mathbf{Q}^l\right) - \left(\psi^g + \frac{p^g}{\rho^g}\right)Div\left(\mathbf{Q}^g\right) + Y\frac{D\phi^v}{Dt} + W\frac{D\omega}{Dt} + Z\frac{D\phi^e}{Dt}
\end{aligned}
\tag{3.131}
$$

$$\Pi^l = -Div\left(\psi^l\right)\mathbf{Q}^{mc} - Div\left(\psi^l + \frac{p^l}{\rho^l}\right)\mathbf{Q}^l \tag{3.132}$$

$$\Pi^g = -Div\left(\psi^g + \frac{p^g}{\rho^g}\right)\mathbf{Q}^g \tag{3.133}$$

$$\Pi^{th} = -\frac{\mathbf{Q}^{th}\nabla_{\mathrm{X}}T}{T} \tag{3.134}$$

Using the gas and liquid mass balance, Eq. (3.64) and (3.65), and rewriting Eq. (3.131) yields:

$$\begin{aligned}\Pi^s = {} & \boldsymbol{\pi}.\frac{D\mathbf{E}}{Dt} + \sum_{m=1}^{M_{\mathrm{int}}^{ve}} \chi_m \frac{D\xi^{(m)}}{Dt} - \frac{D\psi}{Dt} - \frac{DT}{Dt}\Xi - \psi^l \frac{D\theta^s}{Dt} \\ & + \left(\psi^l + \frac{p^l}{\rho^l}\right)\frac{D\left(s^l\phi^v\right)}{Dt} + \left(\psi^g + \frac{p^g}{\rho^g}\right)\frac{D\left(s^g\phi^v\right)}{Dt} + Y\frac{D\phi^v}{Dt} + W\frac{D\omega}{Dt} + Z\frac{D\phi^e}{Dt}\end{aligned} \tag{3.135}$$

Owing to the additive character of energy and entropy, the skeleton Lagrangian densities ψ^s and ζ^s of free energy and entropy per unit of initial volume $d\Omega_0$ are given by:

$$\psi^s = \psi - \left(s^l\phi^v\right)\psi^l - \left(s^g\phi^v\right)\psi^g; \quad \zeta^s = \Xi - \left(s^l\phi^v\right)\zeta^l - \left(s^g\phi^v\right)\zeta^g \tag{3.136}$$

Substituting Eq. (3.136) in Eq. (3.135) yields to:

$$\begin{aligned}\Pi^s = {} & \boldsymbol{\pi}.\frac{D\mathbf{E}}{Dt}+\sum_{m=1}^{M_{\text{int}}^{ve}}\chi_m\frac{D\xi^{(m)}}{Dt}-\frac{D\psi^s}{Dt}-\frac{D\left(\left(s^l\phi^v\right)\right)}{Dt}\psi^l-\left(s^l\phi^v\right)\frac{D\psi^l}{Dt}\\ & -\frac{D\left(\left(s^g\phi^v\right)\right)}{Dt}\psi^g-\left(s^g\phi^v\right)\frac{D\psi^g}{Dt}\\ & -\frac{DT}{Dt}\zeta^s-\frac{DT}{Dt}\left(\left(s^l\phi^v\right)\zeta^l\right)-\frac{DT}{Dt}\left(\left(s^g\phi^v\right)\zeta^g\right)-\psi^l\frac{D\theta^s}{Dt}\\ & +\left(\psi^l+\frac{p^l}{\rho^l}\right)\frac{D\left(s^l\phi^v\right)}{Dt}+\left(\psi^g+\frac{p^g}{\rho^g}\right)\frac{D\left(s^g\phi^v\right)}{Dt}+Y\frac{D\phi^v}{Dt}+W\frac{D\omega}{Dt}+Z\frac{D\phi^e}{Dt}\end{aligned} \tag{3.137}$$

Considering $\zeta^l=-\frac{\partial\psi^l}{\partial T}$ and $\zeta^g=-\frac{\partial\psi^g}{\partial T}$ and applying some mathematical manipulation the rate of energy dissipation of the solid part becomes;

$$\begin{aligned}\Pi^s = {} & \boldsymbol{\pi}.\frac{D\mathbf{E}}{Dt}+\sum_{m=1}^{M_{\text{int}}^{ve}}\chi_m\frac{D\xi^{(m)}}{Dt}-\frac{D\psi^s}{Dt}-\frac{DT}{Dt}\zeta^s-\psi^l\frac{D\theta^s}{Dt}\\ & +p^l\frac{D\left(s^l\phi^v\right)}{Dt}+p^g\frac{D\left(s^g\phi^v\right)}{Dt}+Y\frac{D\phi^v}{Dt}+W\frac{D\omega}{Dt}+Z\frac{D\phi^e}{Dt}\end{aligned} \tag{3.138}$$

Decoupling the solid dissipation to viscoelastic and damage dissipation yields:

$$\begin{aligned}\Pi^{ve} = {} & \boldsymbol{\pi}.\frac{D\mathbf{E}}{Dt}+\sum_{m=1}^{M_{\text{int}}^{ve}}\chi_m\frac{D\xi^{(m)}}{Dt}-\frac{D\psi^s}{Dt}-\frac{DT}{Dt}\zeta^s\\ & -\psi^l\frac{D\theta^s}{Dt}+p^l\frac{D\left(s^l\phi^v\right)}{Dt}+p^g\frac{D\left(s^g\phi^v\right)}{Dt}\end{aligned} \tag{3.139}$$

$$\Pi^{vd}=Y\frac{D\phi^d}{Dt}+W\frac{D\omega}{Dt}+Z\frac{D\phi^e}{Dt} \tag{3.140}$$

The transformation is infinitesimal as soon as the condition given in Eq. (3.12) is satisfied. When this condition is fulfilled, Lagrangian strain tensor, $\mathbf{E}$, and Piola-

Kirchhoff stress tensor, $\boldsymbol{\pi}$, can be replaced by linearized strain tensor, $\boldsymbol{\varepsilon}$, and Cauchy stress tensor, $\boldsymbol{\sigma}$, respectively which is called the state of small deformation theories. Also the fluxes in both configurations become the same. Small deformation theories will be assumed for the asphalt concrete in this study. (explain aggregate 70-80% binder 8% and air void 8%), according to this assumption the first and second law of thermodynamic and the Clausius-Duhem inequality become:

$$\begin{aligned} &\dot{e} = \boldsymbol{\sigma}.\mathbf{d} + \sum_{m=1}^{M_{\text{int}}^{ve}} \chi_m \dot{\xi}^{(m)} + Y\dot{\phi}^{v} + W\dot{\omega} + Z\dot{\phi}^{e} \\ &-div\left(h^{l}\mathbf{q}^{l} + h^{g}\mathbf{q}^{g}\right) - div\left(e^{l}\mathbf{q}^{mc}\right) + \rho r - div\left(\mathbf{q}^{th}\right) \end{aligned} \tag{3.141}$$

$$T\dot{\zeta} + Tdiv\left(\zeta^{l}\mathbf{q}^{mc} + \zeta^{l}\mathbf{q}^{l} + \zeta^{g}\mathbf{q}^{g}\right) - \rho r + div\left(\mathbf{q}^{th}\right) - \frac{\mathbf{q}^{th}div\left(T\right)}{T} \geq 0 \tag{3.142}$$

$$\begin{aligned} &\boldsymbol{\sigma}.\dot{\boldsymbol{\varepsilon}} + \sum_{m=1}^{M_{\text{int}}^{ve}} \chi_m \dot{\xi}^{(m)} + Y\dot{\phi}^{d} + W\dot{\omega} + Z\dot{\phi}^{e} - \dot{\psi} - \dot{T}\zeta - div\left(\psi^{l}\mathbf{q}^{mc}\right) \\ &-div\left[\left(\psi^{l} + \frac{p^{l}}{\rho^{l}}\right)\mathbf{q}^{l}\right] - div\left[\left(\psi^{g} + \frac{p^{g}}{\rho^{g}}\right)\mathbf{q}^{g}\right] - \frac{\mathbf{q}^{th}div\left(T\right)}{T} \geq 0 \end{aligned} \tag{3.143}$$

Using the same procedure and decoupling the Clausius-Duhem inequality for the solid, liquid, gas, and thermal dissipation in small deformation theory, it becomes:

$$\Pi = \Pi^{s} + \Pi^{l} + \Pi^{g} + \Pi^{th} \geq 0 \tag{3.144}$$

where,

$$\Pi^s = \boldsymbol{\sigma}.\dot{\boldsymbol{\varepsilon}} + \sum_{m=1}^{M_{\text{int}}^{ve}} \chi_m \dot{\xi}^{(m)} + Y\dot{\phi}^d + W\dot{\omega} + Z\dot{\phi}^e - \dot{\psi} - \dot{T}\zeta - \psi^l div\left(\mathbf{q}^{mc}\right) - \left(\psi^l + \frac{p^l}{\rho^l}\right) div\left(\mathbf{q}^l\right) - \left(\psi^g + \frac{p^g}{\rho^g}\right) div\left(\mathbf{q}^g\right) \geq 0 \tag{3.145}$$

$$\Pi^l = div\left(\psi^l\right)\mathbf{q}^l - div\left(\psi^l + \frac{p^l}{\rho^l}\right)\mathbf{q}^l \geq 0 \tag{3.146}$$

$$\Pi^g = -div\left(\psi^g + \frac{p^g}{\rho^g}\right)\mathbf{q}^g \tag{3.147}$$

$$\Pi^{th} = -\frac{\mathbf{q}^{th} div(T)}{T} \geq 0 \tag{3.148}$$

Then applying the same procedure as Eqs. (3.135) to (3.138), the solid part of energy dissipation becomes:

$$\Pi^s = \boldsymbol{\sigma}.\dot{\boldsymbol{\varepsilon}} + \sum_{m=1}^{M_{\text{int}}^{ve}} \chi_m \dot{\xi}^{(m)} + Y\dot{\phi}^d + W\dot{\omega} + Z\dot{\phi}^e - \dot{\psi}^s - \dot{T}\zeta - \theta^s \dot{\psi}^l + p^l \frac{\partial\left(s^l \phi^v\right)}{\partial t} + p^g \frac{\partial\left(s^g \phi^v\right)}{\partial t} \geq 0 \tag{3.149}$$

In developing the thermodynamic-based constitutive equations, it is assumed that the state of materials is characterized by suitable internal state variables that implicitly describe important microstructural mechanisms that affect the macroscopic behavior of the material under specific loading and (initial) boundary conditions. The Helmholtz free energy is considered as the thermodynamic state potential depending on the internal state variables. This assumption is consistent with the assumed expression for the internal

power. Hence, the Helmholtz free energy density function ψ^s in this study is expressed as:

$$\psi^s = \psi^s\left(\boldsymbol{\varepsilon}^{ve}, \xi^{(m)}, \theta^s, \theta^v, \phi^d, \omega, \phi^e, T\right) \tag{3.150}$$

The internal state variables associated with the viscoelastic processes, $\xi^{(m)}$, are considered as hidden variables. These hidden variables are associated with internal phenomenon such as the chain mobility in polymers and cause the evolution of the viscoelastic strain, $\boldsymbol{\varepsilon}^{ve}$, which is an observable variable that can be measured experimentally. Moreover, it is usually argued that once the material is damaged, further loading can only affect the undamaged material skeleton. Hence, the viscoelastic and viscodamage models are defined as functions of variables in the effective configuration. This assumption makes the assumed state variables independent, as it should be in formulating a thermodynamically consistent constitutive model. Therefore, in the following all the strain and stress variables are substitute by equivalent effective strain and stress in the dry-undamaged configuration.

Using the chain rule and taking the time derivative of the Helmholtz free energy gives:

$$\begin{aligned}\dot{\psi}^s = {} & \frac{\partial \psi^s}{\partial \overline{\boldsymbol{\varepsilon}}^{ve}} \cdot \dot{\overline{\boldsymbol{\varepsilon}}}^{ve} + \frac{\partial \psi^s}{\partial \xi^{(m)}} \dot{\xi}^{(m)} + \frac{\partial \psi^s}{\partial \theta^v} \dot{\theta}_v + \frac{\partial \psi^s}{\partial \theta^s} \dot{\theta}^s \\ & + \frac{\partial \psi^s}{\partial T} \dot{T} + \frac{\partial \psi^s}{\partial \phi^d} \dot{\phi}^d + \frac{\partial \psi^s}{\partial \omega} \dot{\omega} + \frac{\partial \psi^s}{\partial \phi^e} \dot{\phi}^e\end{aligned} \tag{3.151}$$

Substituting Eq. (3.151) in Eq. (3.149) yields;

$$\begin{aligned}
&\overline{\boldsymbol{\sigma}}.\dot{\overline{\boldsymbol{\varepsilon}}}^{ve}+\sum_{m=1}^{M_{\text{int}}^{ve}}\chi_m\dot{\xi}^{(m)}-\frac{\partial\psi^{ve}}{\partial\overline{\boldsymbol{\varepsilon}}^{ve}}.\dot{\overline{\boldsymbol{\varepsilon}}}^{ve}-\frac{\partial\psi^{ve}}{\partial\xi^{(m)}}\dot{\xi}^{(m)}-\frac{\partial\psi^{ve}}{\partial\theta^{v}}\dot{\theta}^{v}-\frac{\partial\psi^{ve}}{\partial\theta^{s}}\dot{\theta}^{s}-\frac{\partial\psi^{ve}}{\partial T}\dot{T}\\
&-\frac{\partial\psi^{ve}}{\partial\phi^{d}}\dot{\phi}^{d}-\frac{\partial T}{\partial t}\zeta^{s}-\psi^{l}\frac{\partial\theta^{s}}{\partial t}+p^{l}\frac{\partial\left(S^{l}\phi^{v}\right)}{\partial t}-p^{g}\frac{\partial\left(S^{l}\phi^{v}\right)}{\partial t}+p^{g}\dot{\phi}^{d}\\
&+Y\dot{\phi}^{d}+W\dot{\omega}+Z\dot{\phi}^{e}-\frac{\partial\psi^{vd}}{\partial\phi^{d}}\dot{\phi}^{d}-\frac{\partial\psi^{vd}}{\partial\omega}\dot{\omega}-\frac{\partial\psi^{vd}}{\partial\phi^{e}}\dot{\phi}^{e}
\end{aligned}\tag{3.152}$$

Using Eq. (3.14) and $s^{g}=1-s^{l}$;

$$\begin{aligned}
&\left(\overline{\boldsymbol{\sigma}}-\frac{\partial\psi^{ve}}{\partial\overline{\boldsymbol{\varepsilon}}^{ve}}\right).\dot{\overline{\boldsymbol{\varepsilon}}}^{ve}+\sum_{m=1}^{M_{\text{int}}^{ve}}\left(\chi_m-\frac{\partial\psi^{ve}}{\partial\xi^{(m)}}\right)\dot{\xi}^{(m)}-\left(\frac{\partial\psi^{ve}}{\partial T}+\zeta^{s}\right)\dot{T}\\
&-\left(\psi^{l}+\frac{\partial\psi^{ve}}{\partial\theta^{s}}\right)\dot{\theta}^{s}+\left(p^{l}-p^{g}-\frac{\partial\psi^{ve}}{\partial\theta^{v}}\right)\dot{\theta}^{v}\\
&+\left(p^{g}+Y-\frac{\partial\psi^{ve}}{\partial\phi^{d}}\right)\dot{\phi}^{d}+\left(W-\frac{\partial\psi^{ve}}{\partial\omega}\right)\dot{\omega}+\left(Z-\frac{\partial\psi^{ve}}{\partial\phi^{e}}\right)\dot{\phi}^{e}
\end{aligned}\tag{3.153}$$

All processes and physical reactions should satisfy the Clausius-Duhem inequality as an accepted thermodynamic requirement. Thereafter, the internal energy should be conjectured properly to comply the energy dissipation inequality and obtain the conjugate forces. Ziegler (1977), in his celebrated book on Continuum Thermodynamics, stated that the correct estimation of energy dissipation needs the conjugate forces' decomposition to energetic (or quasi-conservative according to his notion) and dissipative components. Zeigler showed that the energetic parts of the thermodynamic conjugate forces are related to Helmholtz free energy function, and the dissipative parts are related to the rate of energy dissipation. Therefore, according to Ziegler the Helmholtz free energy and the rate of energy dissipation should be chosen appropriately to describe how energy is stored and and to determine the rate of energy

dissipation in the materia. Several researchers have applied Ziegler's approach to constitute models for predicting different materials' behavior. However, Gurtin et. al. (2003) expressed the dissipative conjugate forces based on constitutive assumptions instead of obtaining them from the rate of energy dissipation. They also considered the thermodynamic conjugate forces' decomposition for certain associate independent variables and not all of them. Krishnan and Rajagopal (2004) and Abu Al-Rub et. al. (2012) incorporated Ziegler's approach to formulate the mechanical response, mechanical damage and healing of asphalt concrete material, respectively. A stored energy function that represents the elastic response and a rate of dissipation function that describes the viscosity effect are identifying the asphalt concrete material's viscoelastic response in their work. They corroborated the capabilities and robustness of this approach to model and predict asphalt concrete behavior through several examples. Krishnan and Rajagopal (2004) obtained a model, upper convected Burgurs model, usually using to model asphalt concrete by assuming specific forms for Helmholtz free energy and the rate of dissipation functions. Abu Al-Rub et. al. (2012) derived Schapery-type thermo-viscoelasticity, Perzyna-type thermo-viscoplasticity, the thermo-viscodamage constitutive relationships (Darabi et al., 2011a), and the micro-damage healing model (Abu Al-Rub and Darabi, 2012). Although several researchers have extended Ziegler's work, his robust and capable thermodynamic approach specifically, in using the energetic and dissipative conjugate forces, has not been used to construct constitutive model for partially saturated viscous media.

In order to obtain non-zero dissipation resulting from the viscoelasticity dissipative processes, the following energetic thermodynamics conjugate forces that depend on the Helmholtz free energy are defined from Eq.(3.153), such that:

$$\overline{\boldsymbol{\sigma}}^{ene} = \frac{\partial \psi^{ve}}{\partial \overline{\boldsymbol{\varepsilon}}^{ve}}; \tag{3.154}$$

$$\chi^{m^{ene}} = \frac{\partial \psi^{ve}}{\partial \xi^{(m)}} \; m \in \left[1,...,M_{\text{int}}^{ve}\right] \tag{3.155}$$

$$\left(p^{l} - p^{g}\right)^{ene} = S_{suction}^{ene} = \frac{\partial \psi^{ve}}{\partial \theta^{v}} \tag{3.156}$$

$$\psi^{l^{ene}} = -\frac{\partial \psi^{ve}}{\partial \theta^{s}} \tag{3.157}$$

$$\left(p^{g} + Y\right)^{ene} = \frac{\partial \psi^{ve}}{\partial \phi^{d}} \tag{3.158}$$

$$W^{ene} = \frac{\partial \psi^{ve}}{\partial \omega} \tag{3.159}$$

$$Z^{ene} = \frac{\partial \psi^{ve}}{\partial \phi^{e}} \tag{3.160}$$

where $\overline{\boldsymbol{\sigma}}^{ene}$, $\chi^{m^{ene}}$, $S_{suction}^{ene}$, $(p^{g} + Y)^{ene}$, W^{ene}, and Z^{ene} are the conjugate forces corresponding to the internal state variables $\overline{\boldsymbol{\varepsilon}}^{ve}$, $\xi^{(m)}$, θ^{v}, ϕ^{v}, ω, and ϕ^{e} respectively.

By substituting Eq.(3.154) to (3.156) into Eq. (3.153) and decoupling the viscoelastic and viscodamage solid energy dissipation, Π, become:

$$\Pi^{ve} = \left(\bar{\boldsymbol{\sigma}} - \bar{\boldsymbol{\sigma}}^{ene}\right).\dot{\bar{\boldsymbol{\varepsilon}}}^{ve} + \sum_{m=1}^{M_{\text{int}}^{ve}} \left(\chi^{m} - \chi^{m^{ene}}\right)\dot{\xi}^{(m)} + \left(S_{suction} - S_{suction}^{ene}\right)\dot{\theta}^{v} - \left(\frac{\partial \psi^{s}}{\partial T} + \zeta^{s}\right)\dot{T} + \left(-\psi^{l} + \psi^{l^{ene}}\right)\dot{\theta}^{s} \geq 0 \tag{3.161}$$

$$\Pi^{vd} = \left(Y - Y^{ene}\right)\dot{\phi}^{v} + \left(W - W^{ene}\right)\dot{\omega} + \left(Z - Z^{ene}\right)\dot{\phi}^{e} \geq 0 \tag{3.162}$$

Eq. (3.161) shows that in order to make the total energy dissipation resulting from different mechanisms (i.e. viscoelasticity and viscodamage) to be positive the thermodynamic conjugate forces should have dissipative components. Hence, rewriting Eq. (3.161) implies:

$$\Pi^{ve} = \bar{\boldsymbol{\sigma}}^{dis}.\dot{\bar{\boldsymbol{\varepsilon}}}^{ve} + \sum_{m=1}^{M_{\text{int}}^{ve}} \chi^{m^{dis}}\dot{\xi}^{(m)} + S_{suction}^{dis}\dot{\theta}^{v} - \frac{\partial \psi^{s}}{\partial T}\dot{T} - \dot{T}\zeta^{s} - \left(\psi^{l} + \frac{\partial \psi^{ve}}{\partial \theta^{s}}\right)\dot{\theta}^{s} \geq 0 \tag{3.163}$$

$$\Pi^{vd} = Y^{dis}\dot{\phi}^{v} + W^{dis}\dot{\omega} + Z^{dis}\dot{\phi}^{e} \geq 0 \tag{3.164}$$

where $\boldsymbol{\sigma}^{dis}$, $\chi^{m^{dis}}$, and $S_{suction}^{dis}$ are dissipative components of thermodynamic forces conjugate to the rate of viscoelastic strain tensor, $\dot{\boldsymbol{\varepsilon}}^{ve}$, the rate of viscoelasticity state variables, $\dot{\xi}^{(m)}$, and the rate of change of the moisture content inside cracks and voids, $\dot{\theta}^{v}$, respectively and defined as follows:

$$\bar{\boldsymbol{\sigma}}^{dis} = \bar{\boldsymbol{\sigma}} - \bar{\boldsymbol{\sigma}}^{ene} \tag{3.165}$$

$$\chi^{m^{dis}} = \chi^{m} - \chi^{m^{ene}} \tag{3.166}$$

$$S_{suction}^{dis} = S_{suction} - S_{suction}^{ene} \tag{3.167}$$

, and Y^{dis}, W^{dis}, and Z^{dis} are dissipative components of thermodynamic forces conjugate to the rate of mechanical damage variable, $\dot{\phi}^{d}$, the rate of moisture damage, $\dot{\omega}$, and the rate of erosional damage variable, $\dot{\phi}^{e}$, respectively and defined as follows:

$$Y^{dis} = Y - Y^{ene} \tag{3.168}$$

$$W^{dis} = W - W^{ene} \tag{3.169}$$

$$Z^{dis} = Z - Z^{ene} \tag{3.170}$$

Now the constraint function D for the solid energy dissipation can be written as:

$$D^{ve} = \Pi^{ve} - \left[\boldsymbol{\sigma}^{dis} . \dot{\boldsymbol{\varepsilon}}^{ve} + \sum_{m=1}^{M_{\text{int}}^{ve}} \chi^{m^{dis}} \dot{\xi}^{(m)} + S_{suction}^{dis} \dot{\theta}^{v} - \frac{\partial \psi^{s}}{\partial T} \dot{T} - \frac{\partial T}{\partial t} \zeta^{s} - \psi^{l^{dis}} \dot{\theta}^{s} \right] = 0 \tag{3.171}$$

$$D^{vd} = \Pi^{vd} - \left[Y^{dis} \dot{\phi}^{v} + W^{dis} \dot{\omega} + Z^{dis} \dot{\phi}^{e} \right] = 0 \tag{3.172}$$

3.2.7 Maximum Energy Dissipation Principle

One approach to finalize the constitutive relationships derivation is using the maximum rate of energy dissipation principle. This maximization principle means that over all probable different materials' response, the naturally happening response is the one that

maximize the energy dissipation's rate. Ziegler (1977) affirmed that applying the maximum rate of energy dissipation is valid for arbitrary process following the laws of linear non-equilibrium thermodynamics. Several other researchers have elaborated on the validity and the range of applicability of the maximum rate of energy dissipation in describing the natural behavior of materials (for more details refer to (Grandy, 2008; Martyushev and Seleznev, 2006; Yang et al., 2005; Ziegler, 1981). Although this is not a fundamental principle and there are other methodologies depending upon the process not requiring the maximization, this is a practical approach to derive consistent constitutive models. These models have been used extensively in the literature to explicate various types of material behavior. In this study, the rate of energy dissipation maximization principle is applied to explicate the associated constitutive relationships. The capabilities and robustness of the presented thermodynamic framework is shown through several examples, which derive Schapery-type thermo-viscoelasticity, Perzyna-type thermo-viscoplasticity, the thermo-viscodamage constitutive relationships proposed by Darabi et al. (2012b), and the micro-damage healing model proposed by Abu Al-Rub et al. (2012).

The rate of internal state variables associated with damage is obtained by utilizing the calculus of several variables with the Lagrange multiplier λ. The dissipation function, Π, is subjected to constraint $D = 0$, and in order to maximize the energy dissipation an objective function Ω define as:

$$\Omega = \Pi - \lambda D \tag{3.173}$$

Then applying the maximum energy dissipation function for maximizing an objective function yields:

$$\frac{\partial \Omega^{ve}}{\partial \dot{\boldsymbol{\varepsilon}}^{ve}} = 0; \frac{\partial \Omega^{ve}}{\partial \dot{\xi}^{(m)}} = 0; \frac{\partial \Omega^{ve}}{\partial \dot{\theta}^{v}} = 0; \frac{\partial \Omega^{ve}}{\partial \dot{\theta}^{s}} = 0 \tag{3.174}$$

$$\frac{\partial \Omega^{vd}}{\partial \dot{\phi}^{v}} = 0; \frac{\partial \Omega^{vd}}{\partial \dot{\omega}} = 0; \frac{\partial \Omega^{vd}}{\partial \dot{\phi}^{e}} = 0 \tag{3.175}$$

By substituting Eq. (3.173) into the above relations;

$$\boldsymbol{\sigma}^{dis} = \Lambda^{ve} \frac{\partial \Pi^{ve}}{\partial \dot{\boldsymbol{\varepsilon}}^{ve}} \tag{3.176}$$

$$\chi^{m^{dis}} = \Lambda^{ve} \frac{\partial \Pi^{ve}}{\partial \dot{\xi}^{(m)}} \tag{3.177}$$

$$S_{suction}^{dis} = \Lambda^{ve} \frac{\partial \Pi^{ve}}{\partial \dot{\theta}^{v}} \tag{3.178}$$

$$Y^{dis} = \Lambda^{vd} \frac{\partial \Pi^{vd}}{\partial \dot{\phi}^{v}} \tag{3.179}$$

$$W^{dis} = \Lambda^{vd} \frac{\partial \Pi^{vd}}{\partial \dot{\omega}} \tag{3.180}$$

$$Z^{dis} = \Lambda^{vd} \frac{\partial \Pi^{vd}}{\partial \dot{\phi}^{e}} \tag{3.181}$$

where $\Lambda^{ve} = 1 - \frac{1}{\lambda^{ve}}$ and λ^{ve} is the Lagrange multiplier for viscoelastic component of dissipation function; and $\Lambda^{vd} = 1 - \frac{1}{\lambda^{vd}}$ and λ^{vd} is the Lagrange multiplier for viscodamage components of dissipation function. By substituting Eqs. (3.176) to (3.178) in (3.163) the viscoelastic and viscodamage Lagrange multipliers can be determined as:

$$\Lambda^{ve} = \frac{\Pi^{ve} + \frac{\partial \psi^{ve}}{\partial T}\dot{T} + \frac{\partial T}{\partial t}\zeta^{s} + \left(\psi^{l} + \frac{\partial \psi^{ve}}{\partial \theta^{s}}\right)\dot{\theta}^{s} \geq 0}{\frac{\partial \Pi^{ve}}{\partial \dot{\boldsymbol{\varepsilon}}^{ve}}\dot{\boldsymbol{\varepsilon}}^{ve} + \frac{\partial \Pi^{ve}}{\partial \dot{\xi}^{(m)}}\dot{\xi}^{(m)} + \frac{\partial \Pi^{ve}}{\partial \dot{\theta}^{v}}\dot{\theta}^{v}} \tag{3.182}$$

$$\Lambda^{vd} = \frac{\Pi^{vd}}{\frac{\partial \Pi^{vd}}{\partial \dot{\phi}^{v}}\dot{\phi}^{v} + \frac{\partial \Pi^{vd}}{\partial \dot{\omega}}\dot{\omega} + \frac{\partial \Pi^{vd}}{\partial \dot{\phi}^{e}}\dot{\phi}^{e}} \tag{3.183}$$

This section concludes the general thermodynamic framework for determining the energetic and dissipative components of the thermodynamic conjugate forces. In the following sections, focus is on showing the capabilities of the presented thermodynamic framework through examples that derives a temperature-dependent viscoelastic, visco-moisture and mechanical damage constitutive relationships.

Formulating a general thermodynamic framework that properly estimates the stored and dissipative energies during different processes is one of the most challenging tasks. This issue has been addressed in this work by decomposing the thermodynamic conjugate forces into energetic and dissipative components and enforcing the positive-definite rate of dissipation for these processes. However, careful experimental studies

should be performed to develop the proper forms of the Helmholtz free energy and rate of energy dissipation functions based on the material type.

In the following subsections, the presented thermodynamic framework is used to derive thermo-viscoelastic and thermo-visco- moisture and mechanical damage constitutive equations. The objective is to derive thermodynamic consistent Schapery-type viscoelasticity, damage model proposed by Darabi et al. (2012b), moisture damage constitutive relationship and pore water pressure effect on the solid phase. The viscoplastic strain of asphalt concrete material has been neglected in this part of work as it is mentioned earlier. However, it can be easily coupled and incorporated in the formulation.

Assuming a decoupled or a separable material, the Helmholtz free energy is decomposed into thermo-viscoelastic and thermo-viscodamage components, such that:

$$\psi^s = \psi^{tve}\left(\bar{\boldsymbol{\varepsilon}}^{ve}, \xi^{(m)}, \theta^s, \theta^v, T\right) + \psi^{tvd}\left(\phi^v, \omega, \theta^s, \theta^v, T\right) \tag{3.184}$$

where ψ^{tve} and ψ^{tvd} are thermo-viscoelastic and thermo-viscodamage components of the Helmholtz free energy.

Thermo-Viscoelastic Constitutive Equations, Both the viscoelastic strain tensor, $\bar{\boldsymbol{\varepsilon}}^{ve}$, and the viscoelastic internal state variables, $\xi^{(m)}$, are considered to contribute to the viscoelastic component of the Helmholtz free energy at a dry state (Darabi et al., 2012b). Moisture content inside the solid part and cracks and voids also contribute to the

Helmholtz free energy. Hence, the thermo-viscoelastic component of the Helmholtz free energy can be assumed as follows;

$$\psi^{tve} = \psi^{tve}\left(\overline{\boldsymbol{\varepsilon}}^{ve}, \xi^{(m)}, \theta^{s}, \theta^{v}, T\right) \tag{3.185}$$

$$\psi^{tve} = \begin{pmatrix} \frac{1}{2} a_{0\left(\bar{\varepsilon}^{ve}\right)} \overline{\boldsymbol{\varepsilon}}^{ve} \mathbf{L}^{(1)} \overline{\boldsymbol{\varepsilon}}^{ve} + \frac{1}{2} \mathbf{L}^{(2)} \xi^{(m)} \xi^{(n)} + a_{1\left(\bar{\varepsilon}^{ve}\right)} \overline{\boldsymbol{\varepsilon}}^{ve} \mathbf{L}^{(3)} \xi^{(m)} \\ + \frac{1}{2} M \left(\beta e - \theta^{v}\right)^{2} \end{pmatrix} \vartheta^{ve} \tag{3.186}$$

where $a_{0\left(\bar{\varepsilon}^{ve}\right)}$ and $a_{1\left(\bar{\varepsilon}^{ve}\right)}$ are nonlinear dependency scalars, which are introduced in the Helmholtz free energy to make the viscoelastic model nonlinear (Schapery, 1969). These parameters are functions of the viscoelastic strain tensor. $\mathbf{L}^{(1)}$, $\mathbf{L}^{(2)}$, and $\mathbf{L}^{(3)}$ are positive definite matrices. M and β are Biot's coeffiecient (Biot, 1954). This term is considering the energy contribution of moisture content inside the interconnected cracks and voids to the Helmholtz free energy. It should mention that the contribution of moisture content inside the solid part is neglected in this assumption. ϑ^{ve} is an Arrhenius-type temperature term for coupling temperature to the viscoelastic constitutive law and is defined as follows;

$$\vartheta^{ve} = \frac{1}{a_T} \tag{3.187}$$

where a_T is a time-temperature shift factor. Other parameters in Eq. (3.186) are defined as follows:

$$\mathbf{L}^{(1)} = \left. \frac{\partial \psi^{tve}}{\partial \overline{\boldsymbol{\varepsilon}}^{ve} \partial \overline{\boldsymbol{\varepsilon}}^{ve}} \right|_{T=T_0} \tag{3.188}$$

$$\mathbf{L}^{(3)} = \left. \frac{\partial \psi^{tve}}{\partial \overline{\boldsymbol{\varepsilon}}^{ve} \partial \xi^{(m)}} \right|_{T=T_0}, m \in \left[1,...,M_{\text{int}}^{ve}\right] \tag{3.189}$$

$$\mathbf{L}^{(2)} = \left. \frac{\partial \psi^{tve}}{\partial \xi^{(m)} \partial \xi^{(n)}} \right|_{T=T_0}, m,n \in \left[1,...,M_{\text{int}}^{ve}\right] \tag{3.190}$$

The energetic component of the effective stress can be easily derived using Eqs. (3.154) and (3.186), such that:

$$\boldsymbol{\sigma}^{ene} = \left[\mathbf{A}^{(0)} \mathbf{L}^{(1)} \overline{\boldsymbol{\varepsilon}}^{ve} + \mathbf{A}^{(1)} \mathbf{L}^{(3)} \xi^{(n)} + \beta M \left(\beta e - \theta^{v} \right) \mathbf{I} \right] \vartheta^{ve} \tag{3.191}$$

where $\mathbf{A}^{(0)}$ and $\mathbf{A}^{(1)}$ are nonlinear parameters related to the instantaneous and transient viscoelastic responses, respectively. Eq. (3.191) shows that the instantaneous nonlinear parameters are no longer a scalar for 3D models and defined as:

$$\mathbf{A}^{(0)} = a_0 \mathbf{I} \times \mathbf{I} + \frac{1}{2} \frac{\partial a_0}{\partial \overline{\boldsymbol{\varepsilon}}^{ve}} \overline{\boldsymbol{\varepsilon}}^{ve} \tag{3.192}$$

$$\mathbf{A}^{(1)} = a_1 \mathbf{I} \times \mathbf{I} + \frac{1}{2} \frac{\partial a_1}{\partial \overline{\boldsymbol{\varepsilon}}^{ve}} \overline{\boldsymbol{\varepsilon}}^{ve} \tag{3.193}$$

The energetic part of the viscoelastic conjugate forces and suction also is obtained as:

$$\chi^{m^{ene}} = \left[\mathbf{L}^{(2)} \xi^{(m)} + a_{1\left(\overline{\varepsilon}^{ve}\right)} \overline{\boldsymbol{\varepsilon}}^{ve} \mathbf{L}^{(3)} \right] \vartheta^{ve} \tag{3.194}$$

$$S_{suction}^{ene} = \left[-M\left(\beta e - \theta^{v}\right)\right]\vartheta^{ve} \tag{3.195}$$

The dissipation mechanism results from the viscoelastic strain rate, the rate of the viscoelastic internal state variables, which are related to the chain mobility and friction between the polymer chains, and dissipation due to molecular diffusion of liquid inside the solid phase. In this work, the following simple quadratic form is postulated for the viscoelastic component of the rate of energy dissipation:

$$\Pi^{tve} = \left(\dot{\bar{\boldsymbol{\varepsilon}}}^{ve}\boldsymbol{\mu}\dot{\bar{\boldsymbol{\varepsilon}}}^{ve} + \mathbf{P}\dot{\xi}^{(m)}\dot{\xi}^{(n)} + M\dot{\theta}^{v}\dot{\theta}^{v}\right)\vartheta^{ve} \tag{3.196}$$

The dissipation part of stress, the viscoelastic conjugate force and suction are determined using Eq. (3.176), (3.177) and (3.178), such that:

$$\boldsymbol{\sigma}^{dis} = \left(1 - \frac{1}{\lambda^{ve}}\right)\frac{\partial \Pi^{ve}}{\partial \dot{\bar{\boldsymbol{\varepsilon}}}^{ve}} = \left(\boldsymbol{\mu}\dot{\bar{\boldsymbol{\varepsilon}}}^{ve}\right)\vartheta^{ve} \tag{3.197}$$

$$\chi^{m^{dis}} = \left(1 - \frac{1}{\lambda^{ve}}\right)\frac{\partial \Pi^{ve}}{\partial \dot{\xi}^{(m)}} = \left(\mathbf{P}\dot{\xi}^{(m)}\right)\vartheta^{ve} \tag{3.198}$$

$$S_{suction}^{dis} = \left(1 - \frac{1}{\lambda^{ve}}\right)\frac{\partial \Pi^{ve}}{\partial \dot{\theta}^{v}} = \left(M\dot{\theta}^{v}\right)\vartheta^{ve} \tag{3.199}$$

Substituting Eqs. (3.191), (3.194), (3.195), (3.197), (3.198), and (3.199) into Eqs. (3.165), (3.166), and (3.167) yields:

$$\boldsymbol{\sigma} = \left[\mathbf{A}^{(0)}\mathbf{L}^{(1)}\bar{\boldsymbol{\varepsilon}}^{ve} + \mathbf{A}^{(1)}\mathbf{L}^{(3)}\xi^{(n)} + \beta M\left(\beta e - \theta^{v}\right)\mathbf{I}\right]\vartheta^{ve} + \boldsymbol{\mu}\dot{\bar{\boldsymbol{\varepsilon}}}^{ve} \tag{3.200}$$

$$\chi^m = \left[\mathbf{L}^{(2)} \xi^{(m)} + a_{1\left(\bar{\varepsilon}^{ve}\right)} \bar{\boldsymbol{\varepsilon}}^{ve} \mathbf{L}^{(3)} + \mathbf{P} \dot{\xi}^{(m)} \right] \vartheta^{ve} = 0 \tag{3.201}$$

$$S_{suction} = \left[-M \left(\beta e - \theta^v \right) + M \dot{\theta}^v \right] \vartheta^{ve} \tag{3.202}$$

Using the Laplace transform to solve the micro force balance equation, Eq. (3.82) , associated with internal state variables $\xi^{(m)}$, yields (Abu Al-Rub and Darabi, 2012);

$$\xi^{(m)} = -\frac{\mathbf{L}^{(3)}}{\mathbf{L}^{(2)}} \int_0^t \left(1 - \exp\left[-\psi^t \left(t - \tau \right) \right] \right) \frac{d}{d\tau} \left(a_{1\left(\bar{\varepsilon}^{ve}\right)} \bar{\boldsymbol{\varepsilon}}^{ve} \right) d\tau \tag{3.203}$$

where $\psi^t = \frac{\mathbf{L}^{(2)}}{\mathbf{P}}$. Substituting Eq. (3.203) in Eq. (3.200), the stress is obtained as;

$$\boldsymbol{\sigma} = \left\{ \begin{array}{l} \mathbf{A}^{(0)} \mathbf{L}^{(1)} \bar{\boldsymbol{\varepsilon}}^{ve} \\ + \mathbf{A}^{(1)} \mathbf{L}^{(3)} \left[-\frac{\mathbf{L}^{(3)}}{\mathbf{L}^{(2)}} \int_0^t \left(1 - \exp\left[-\psi^t \left(t - \tau \right) \right] \right) \frac{d}{d\tau} \left(a_{1\left(\bar{\varepsilon}^{ve}\right)} \bar{\boldsymbol{\varepsilon}}^{ve} \right) d\tau \right] \\ + \beta M \left(\beta e - \theta^v \right) \mathbf{I} \end{array} \right\} \vartheta^{ve} + \boldsymbol{\mu} \dot{\bar{\boldsymbol{\varepsilon}}}^{ve} \tag{3.204}$$

Assuming that the porous media is completely saturated, the pore water pressure inside the media by using Eq. (3.202) becomes;

$$p^l = \left[-M \left(\beta e - \theta^v \right) \right] \vartheta^{ve} \tag{3.205}$$

Substituting Eq. (3.205) to Eq. (3.204) the stress in a completely saturated media can be obtained as;

$$\boldsymbol{\sigma} = \left\{ \begin{array}{l} \mathbf{A}^{(0)}\mathbf{L}^{(1)}\overline{\boldsymbol{\varepsilon}}^{ve} \\ +\mathbf{A}^{(1)}\mathbf{L}^{(3)}\left[-\dfrac{\mathbf{L}^{(3)}}{\mathbf{L}^{(2)}}\int_0^t \left(1-\exp\left[-\psi^t\left(t-\tau\right)\right]\right)\dfrac{d}{d\tau}\left(a_{1\left(\overline{\varepsilon}^{ve}\right)}\overline{\boldsymbol{\varepsilon}}^{ve}\right)d\tau \right] \end{array} \right\} \vartheta^{ve} - \beta p^l \mathbf{I} + \boldsymbol{\mu}\dot{\overline{\boldsymbol{\varepsilon}}}^{ve} \quad (3.206)$$

Thermo-Viscodamage Constitutive Equations, It has been shown that the rate-dependent damage (viscodamage) condition can be derived directly from the principle of virtual power and laws of thermodynamics (Abu Al-Rub and Darabi, 2012). Abu AL-Rub et. al. (2012) proved that the microforce balance is in fact the damage growth condition. Similar procedure to the mechanical damage development is used here to develop the moisture damage constitutive relationship. Damage microforce balances are:

$$Y = 0 \Rightarrow Y^{dis} + Y^{ene} = 0 \quad (3.207)$$

$$W = 0 \Rightarrow W^{dis} + W^{ene} = 0 \quad (3.208)$$

$$Z = 0 \Rightarrow Z^{dis} + Z^{ene} = 0 \quad (3.209)$$

The following form is postulated for the thermo-visco moisture mechanical damage component of the Helmholtz free energy to consider the confinement effects, the different effects of damage in tensile and compressive loading conditions, the effect of temperature on damage evolution and growth, and the effect of moisture presence on degradation of solid phase, such that:

$$\rho\psi^{vd} = \left\{ \frac{1}{b_1}\left(1-\phi^d\right)^{b_1}\left[\frac{\overline{\tau}-\alpha I_1}{b_2}\right]\exp\left(b_3\overline{\varepsilon}_{eff}\right) + \frac{1}{k_3}\theta^{s^{k_2}}\left(1-\omega\right)^{k_3}\right\}\vartheta^{vd} \tag{3.210}$$

where b_1, b_2, b_3, k_2, and k_3 are material parameters. Note that when $\phi^d = 0$ and $\omega = 0$ (i.e. no damage) the damage component of the Helmholtz free energy has its initial value. However, when the damage variable increases and material becomes more damaged the free energy function due to the damage decreases and eventually reaches zero at complete failure. Also, the damage component of the Helmholtz free energy is assumed to be a function of the total effective strain in the effective configuration (i.e. $\overline{\boldsymbol{\varepsilon}}_{eff} = \sqrt{\overline{\boldsymbol{\varepsilon}}.\overline{\boldsymbol{\varepsilon}}}$) to enhance more couplings between viscoelasticity and viscodamage. The contribution of erosion of mastic is not considered in this study. Therefore, the energetic part of conjugate force to mechanical damage and conjugate force to moisture damage is obtained as;

$$\left(Y + p^g\right)^{ene} = \left\{-\left(1-\phi^d\right)^{b_1-1}\left[\frac{\overline{\tau}-\alpha I_1}{b_2}\right]\exp\left(b_3\overline{\varepsilon}_{eff}\right)\right\}\vartheta^{vd} \tag{3.211}$$

$$W^{ene} = \left[-\theta_s^{k_2}\left(1-\omega\right)^{k_3-1}\right]\vartheta^{vd} \tag{3.212}$$

The following equation is postulated to define the dissipative energy due to viscodamage processes;

$$\Pi^{vd} = b_0\Gamma^{vd}\left(\frac{\dot{\phi}^d}{\Gamma^{vd}\vartheta^{vd}}\right)^{1+\frac{1}{q^d}} + \frac{\dot{\omega}}{k_1}\left(1+\frac{1}{q}\right) \tag{3.213}$$

where b_0, q^d, k_1 and q are material constants, and Γ^{vd} is the viscodamage fluidity parameter which controls the rate of damage evolution. Moreover, b_0 can be assumed to be dependent on $-Y^{ene}$ (Abu Al-Rub and Darabi, 2012). Then, the dissipative component of the damage thermodynamic force, Y^{dis}, can be obtained by substituting Eq. (3.213) into Eqs. (3.179) and (3.180), which yields:

$$Y^{dis} = b_0 \Gamma^{vd} \left(\frac{\dot{\phi}^d}{\Gamma^{vd} \vartheta^{vd}} \right)^{1+\frac{1}{q}} \tag{3.214}$$

$$W^{dis} = \frac{\dot{\omega}}{k_1} \tag{3.215}$$

Now we can obtain the rate-dependent damage surface by substituting Eqs. (3.211) and (3.214) into Eq. (3.207) and rate dependent moisture damage surface by substituting Eqs. (3.212) and (3.215) into Eq. (3.208) that results in the following equation:

$$\left(1-\phi^d\right)^{b_1-1} \left[\frac{\overline{\tau} - \alpha I_1}{b_2} \right] \exp\left(b_3 \overline{\varepsilon}_{eff}\right) \vartheta^{vd} + b_0 \Gamma^{vd} \left(\frac{\dot{\phi}^d}{\Gamma^{vd} \vartheta^{vd}} \right)^{1+\frac{1}{q}} = 0 \tag{3.216}$$

$$\theta_s^{k_2} \left(1-\omega\right)^{k_3-1} \vartheta^{vd} + \frac{\dot{\omega}}{k_1} = 0 \tag{3.217}$$

Eq. (3.216) represents the dynamic viscodamage loading condition and Eq. (3.217) represents the dynamic visco-moisture damage loading condition for temperature

and rate dependent damage. These equations can be solved for the rate of damage parameter, such that:

$$\dot{\phi}^d = \Gamma^{vd}\left[\frac{\left(1-\phi^d\right)^{b_1-1}\left(\bar{\tau}-\alpha I_1\right)}{b_0 b_2}\right]^q \exp\left(b_3 q\bar{\varepsilon}_{eff}\right)\vartheta^{vd^{1+\frac{1}{q}}} \tag{3.218}$$

$$\dot{\omega} = k_1\theta_s^{k_2}\left(1-\phi^T\right)^{k_3} \tag{3.219}$$

It is assumed that the moisture content inside the interconnected cracks and voids has a dominant energetic effect while the moisture content inside the solid phase has a dominant dissipative feature. This moisture damage constitutive relationship will be calibrated and validated against some experimental data and also will be used to conduct some parametric study at micro and macro level.

4. COUPLED MOISTURE-MECHANICAL CONSTITUTIVE RELATIONSHIPS FOR ASPHALT CONCRETE

4.1 Moisture-Induced Damage Constitutive Relationship

The transformed moisture inside the asphalt pavement can degrade the material through different mechanism and different time scales. Therefore, the moisture content inside the asphalt pavement was categorized to two parts; molecular diffusion of moisture through the solid phase and flow of moisture through interconnected cracks and voids. The moisture diffusion through the solid phase follows Fick's diffusion equation and causes degradation of physical properties of the solid phase. Moisture flow through interconnected cracks and voids follows Darcy's law and can cause pore water pressure and mastic washing away of the asphalt concrete. The constitutive relationships were proposed to consider the detrimental effect of moisture presence and effect of pore water pressure inside cracks and voids in the following sub-sections.

4.1.1. Moisture-Induced Damage due to Moisture Presence

Despite the detrimental effect of moisture during the damage process, few macroscale models are available to model moisture-induced damage in asphalt concrete materials and pavements. The effect of moisture in degrading mechanical properties is observed in two physical mechanisms: adhesive moisture damage, defined as degradation of bond strength at the aggregate-mastic interface; and cohesive moisture damage, defined as

degradation of cohesive strength of the asphalt mastic (Caro et al., 2008; Kringos et al., 2007). In this study, both phenomena are modeled independently such that the fundamental physics associated with each mechanism can be modeled separately by assuming proper evolution functions. The combined effect of adhesive and cohesive damage as well as the transition between them can be modeled by defining the total moisture damage such that:

$$\left(1-\omega\right)=\left(1-\omega^{a}\right)\left(1-\omega^{c}\right) \tag{4.1}$$

where ω^{a} is the internal variable representing the adhesive moisture-induced damage and ω^{c} is the variable capturing the effect of cohesive moisture-induced damage on the degradation of material's properties. The decay in the aggregate-mastic and mastic cohesive damage variable due to the presence of moisture are modeled using similar evolution function as:

$$\dot{\omega}^{i}(t)=\dot{\omega}^{i}(\theta(t)), i=a,c \tag{4.2}$$

where the superimposed "•" designates the time derivative. The term $\omega^{i}\left(t\right)$ is the aggregate–mastic adhesive damage variable for $i = a$ (adhesive), and the mastic cohesive damage variable for $i = c$ (cohesive) at time t and $\dot{\omega}^{i}\left(\theta(t)\right)$ is the rate of decay of the adhesive or cohesive strength for a normalized moisture content θ at time t.

A first approximation of the evolution of moisture damage, $\dot{\omega}^{i}(\theta)$, is to assume it a linear function of moisture content, $\theta_{(t)}$, (Graham, 2009). However, experimental

results show that rate of moisture-damage variable, $\dot{\omega}^i(\theta)$, decreases as the level of damage increases. Hence, in order to consider the effect of damage history on the bond strength of the material and also to consider the coupling between the mechanical and moisture damage mechanisms, the following evolution function is proposed:

$$\dot{\omega}^i\left(\theta(t)\right) = k^i\theta(t)\left\langle 1-\frac{\phi_{eff}}{\phi_{cr}}\right\rangle^q, i = a, c \tag{4.3}$$

where k^a and k^c are model parameters that describe the degradation rate of adhesive and cohesive damage variables, respectively; ϕ_{eff} is the effective damage variable as defined in Eq. (2.10); q is the damage history exponent parameter; ϕ_{cr} is the critical damage; and $\langle\ \rangle$ is the Macaulay brackets defined by $\langle\xi\rangle = \left(\xi + |\xi|\right)/2$. Eq. (4.3) shows that the rate of moisture damage decreases as damage propagates through the material. Moisture diffuses slowly through the material at initial stages so the aggravation rate is low. Induced effective damage due to moisture and mechanical loading causes cracks and voids to propagate through the material. The cracks' propagation leads to increased diffusivity and so moisture penetrates more easily through the material causing more moisture damage. However, by gradually increasing the cracks and voids, moisture can easily flow out of the material. After this stage, the rate of moisture damage evolution decreases as damage level increases. The incorporation of the effective damage variable enables the constitutive relationship, Eq. (4.3), to consider the damage history effect.

The evolution equation proposed in this study differs from the previously proposed moisture damage models in the literature (Graham, 2009; Kringos et al., 2008b). First, the constitutive relationship proposed in Eq. (4.3) is time-dependent, such that the material can be degraded gradually with time even at a fixed moisture content level. Second, it accounts for the irreversibility of moisture damage, such that the degraded stiffness and strength due to the presence of moisture cannot be recovered upon drying. Third, it describes the damage process as a function of the damage history and not only on the current moisture state. Finally, unlike the models based on the cohesive zone elements, it can predict crack propagation both in the matrix and at the interface without prescribing a predefined crack path. Using the proposed framework and the moisture damage model, the aggregate-mastic bond strength and mastic cohesive strength at the current time t due to the presence of moisture can be related to the initial dry bond strength of the material, such that:

$$X_{(t)}^{i} = X_{0}^{i}\left(1-\omega^{i}\right);\ \ i=a,c \tag{4.4}$$

where $X_{(t)}^{a}$ and $X_{(t)}^{c}$ are the average aggregate–mastic adhesive strength and mastic-mastic cohesive strength, respectively. The terms X_{0}^{a} and X_{0}^{c} correspond respectively to adhesive and cohesive initial bond strengths. Eq. (4.4) shows that for the dry state of the material (i.e. $\omega^{i}=0$) the adhesive and/or cohesive strength are equal to the initial dry strength (i.e. $X_{(t)}^{i}=X_{0}^{i}$). Also, when the material is completely degraded (i.e. $\omega^{i}=1$), all adhesive or cohesive strength is lost (i.e. $X_{(t)}^{i}=0$).

Fick's second law is used to simulate the moisture diffusion through the pavement structure and asphalt concrete microstructure, such that:

$$\frac{\partial \theta}{\partial t} = D\nabla^2\theta \tag{4.5}$$

where θ is the normalized moisture content, D is the moisture diffusion coefficient, and ∇^2 is the Laplace operator. Abaqus (2008) built in tools is used to obtain the evolution of normalized moisture content within the model for a given moisture content boundary condition.

4.1.2. Moisture-Induced Damage due to Pore Water Pressure

Pore water pressure effect is categorized as a mechanical moisture-induced damage phenomenon, since it is directly related to the application of loading to the asphalt concrete (Kringos et al., 2008a). These pore pressures contribute extra stresses within the asphalt concrete, which may cause added mechanical damage (Kandhal, 1992; Kiggundu and Roberts, 1988). To incorporate the effect of pore water pressure in this work, it is assumed that water is incompressible and the flow of water through the connected cracks and voids follows Darcy's equation;

$$\mathbf{Q} = -\mathbf{k}\nabla p \tag{4.6}$$

Pore water pressure degrades the material property through inducing higher stress level on the solid phase and causing more mechanical damage. It causes an extra

stress on the solid phase due to fast traffic loading on the pavement. To corporate this stress on the solid phase, an appropriate function, $f\left(p^l\right)$, should be assumed;

$$\boldsymbol{\sigma} = \boldsymbol{\sigma}^T - f\left(p^l\right)\mathbf{I} \tag{4.7}$$

The effect of pore water pressure has been well explored in soil mechanics as an extra-induced stress on an elastic solid phase. The Biot's equation that considers the effect of pore water pressure on a compressible material was used in this work, as obtained in chapter III) to incorporate the effect of pore water pressure on the asphalt concrete,

$$f\left(p^l\right) = \beta p^l \tag{4.8}$$

Numerical algorithms for the proposed moisture damage constitutive relationship and pore water pressure effect are implemented in the Pavement Analysis using Nonlinear Damage Approach program (PANDA) to model the effect of moisture damage on the complex mechanical response of asphalt concrete at macro-scales and will be explained in next section. PANDA was developed and continues to be refined by the authors and their collaborators and includes Schapery's nonlinear viscoelasticity (1969), Perzyna-type (1971a) viscoplasticity, and the viscodamage model proposed by Darabi et al. (2011a). A summary of PANDA are presented in the following section.

4.2 Thermo-Viscoelastic Constitutive Relationship

The total deformation of asphalt concrete subjected to an applied stress can be decomposed into recoverable and irrecoverable components, where the extent of each is mainly affected by time, temperature, and loading rate. In this study, small deformations are assumed such that the total strain is additively decomposed into a viscoelastic (recoverable) component and a viscoplastic (irrecoverable) component:

$$\overline{\boldsymbol{\varepsilon}} = \overline{\boldsymbol{\varepsilon}}^{nve} + \overline{\boldsymbol{\varepsilon}}^{vp} \tag{4.9}$$

where $\overline{\boldsymbol{\varepsilon}}$, $\overline{\boldsymbol{\varepsilon}}^{ve}$, and $\overline{\boldsymbol{\varepsilon}}^{vp}$ are the total, viscoelastic, and viscoplastic strain tensors, respectively.

The Schapery's nonlinear viscoelasticity theory (Schapery, 1969) is used to model the viscoelastic response of asphalt concrete. The Schapery's viscoelastic one-dimensional single integral model is expressed here in terms of the effective stress, $\overline{\boldsymbol{\sigma}}$, Eq. (2.7), as follows:

$$\overline{\boldsymbol{\varepsilon}}^{nve,t} = g_{0\left(\overline{\boldsymbol{\sigma}}^{t}\right)} D_0 \overline{\boldsymbol{\sigma}}^{t} + g_{1\left(\overline{\boldsymbol{\sigma}}^{t}\right)} \int_0^{\psi^t} \Delta D^{\left(\psi^t - \psi^\tau\right)} \frac{d\left(g_{2\left(\overline{\boldsymbol{\sigma}}^{t}\right)} \overline{\boldsymbol{\sigma}}^{\tau} \right)}{d\tau} d\tau \tag{4.10}$$

where D_0 is the instantaneous compliance; ΔD is the transient compliance; g_0, g_1, and g_2 are the nonlinear parameters which are functions of the confinement level and effective deviatoric stress measures in the effective configuration (Rahmani et al., in press); and ψ^t is the reduced-time. The parameter g_0 is the nonlinear instantaneous compliance parameter that measures the reduction or the increase in the instantaneous

compliance. The transient nonlinear parameter g_1 measures nonlinearity effects in the transient compliance. The nonlinear parameter g_2 accounts for the loading rate effect on the creep response. Note that D_0, ΔD, g_0, g_1 and g_2 should be determined for undamaged material. In Eq. (4.10), ψ^t is the reduced-time given by:

$$\psi^t = \int_0^t \frac{d\xi}{a_T a_s a_e} \tag{4.11}$$

where a_T, a_s, and a_e are the temperature, strain or stress, and environment (e.g. moisture, aging) shift factors, respectively. It is noteworthy to mention assuming g_0, g_1 and g_2 to be constant and equal to one simplified the Schapery's nonlinear viscoelastic model [Eq. (4.10)] to the Boltzmann superposition integral for linear viscoelastic materials. For numerical convenience, the Prony series is used to represent the transient compliance ΔD, such that:

$$\Delta D^{\psi^t} = \sum_{n=1}^{N} D_n \left[1 - \exp\left(-\lambda_n \psi^t\right)\right] \tag{4.12}$$

where N is the number of terms, D_n is the n^{th} coefficient of Prony series associated with the n^{th} retardation time λ_n. In the above and subsequent equations, the superimposed t and τ designate the response at a specific time. It is noteworthy that the model in Eq. (4.10) is referred to as the nonlinear viscoelastic model since the stress-strain relationship depends also on the nonlinear parameters g_0, g_1, and g_2 that are

functions of the stress and the strain magnitudes. Moreover, asphalt mixtures show a nonlinear viscoelastic response even at small deformations where the properties of the asphalt mix change with deformation; therefore, a linear viscoelastic model (i.e. setting $g_0 = g_1 = g_2 = 1$) is insufficient to predict the response of asphaltic mixtures (Huang et al., 2007). This phenomenon has been also demonstrated for other materials such as polymers by several other researchers (e.g. Haj-Ali and Muliana, 2004a; Lai and Bakker, 1996a).

Lai and Bakker (1996a) generalized Schapery's one-dimensional nonlinear viscoelastic model, Eq. (4.10), to three-dimensional problems by decomposing the nonlinear viscoelastic strain into its deviatoric and volumetric components, such that:

$$\bar{\boldsymbol{\varepsilon}}^{nve} = \bar{\mathbf{e}}^{nve} + \frac{1}{3} tr\left(\bar{\boldsymbol{\varepsilon}}^{nve}\right)\mathbf{I} = \frac{1}{2\bar{G}}\bar{\mathbf{S}} + \frac{tr\left(\bar{\boldsymbol{\sigma}}\right)}{9K}\mathbf{I} = \frac{\bar{J}}{2}\bar{\mathbf{S}} + \frac{\bar{B}}{9} tr\left(\bar{\boldsymbol{\sigma}}\right)\mathbf{I} \tag{4.13}$$

where $\boldsymbol{e}^{ve}$ and $tr\left(\bar{\boldsymbol{\varepsilon}}^{nve}\right)$ are the deviatoric strain tensor and the volumetric strain, respectively. $\bar{\mathbf{S}}$ is the deviatoric stress tensor ($\bar{\mathbf{S}} = \bar{\boldsymbol{\sigma}} - tr\left(\bar{\boldsymbol{\sigma}}\right)\mathbf{I}/3$) where $\mathbf{I}$ is the Identity tensor); $tr\left(\bar{\boldsymbol{\sigma}}\right)$ is the volumetric stress; and $\bar{G}$ and $\bar{K}$ are the effective shear and bulk moduli for the undamaged material, respectively, and are expressed as:

$$\bar{G} = \frac{\bar{E}}{2\left(1+\bar{\nu}\right)}, \qquad \bar{K} = \frac{\bar{E}}{3\left(1-2\bar{\nu}\right)} \tag{4.14}$$

where $\bar{E}$, $\bar{\nu}$, $\bar{J}$, and $\bar{B}$ are the Young's modulus, Poisson's ratio, shear compliance, and bulk compliance in the effective configuration, respectively. Applying the

Schapery's model in Eq. (4.10), the deviatoric and volumetric components of nonlinear viscoelastic strain at time t can be expressed as:

$$\overline{\mathbf{e}}^{nve,t} = \frac{1}{2} g_0^t \overline{J}_0 \overline{\mathbf{S}}^t + \frac{1}{2} g_1^t \int_0^{\psi^t} \Delta \overline{J}^{\left(\psi^t - \psi^\tau\right)} \frac{d\left(g_2^\tau \overline{\mathbf{S}}^\tau\right)}{d\tau} d\tau \tag{4.15}$$

$$tr\left(\overline{\boldsymbol{\varepsilon}}^{nve,t}\right) = \frac{1}{3} g_0^t \overline{B}_0 tr\left(\overline{\boldsymbol{\sigma}}^t\right) + \frac{1}{3} g_1^t \int_0^{\psi^t} \Delta \overline{B}^{\left(\psi^t - \psi^\tau\right)} \frac{d\left(g_2^\tau tr\left(\overline{\boldsymbol{\sigma}}^\tau\right)\right)}{d\tau} d\tau \tag{4.16}$$

where $\overline{J}_0$ and $\overline{B}_0$ are the instantaneous effective elastic shear and bulk compliances, respectively. Assuming that the Poisson's ratio in the effective configuration $\overline{\nu}$ is time-independent and using Prony series in Eq. (4.12), the deviatoric and volumetric components of the total strain tensor can be presented in terms of the hereditary integral formulation as follows (Haj-Ali and Muliana, 2004b):

$$\begin{aligned} \mathbf{e}^{ve,t} = & \frac{1}{2}\left[g_0^t \overline{J}_0 + g_1^t g_2^t \sum_{n=1}^{N} \overline{J}_n - g_1^t g_2^t \sum_{n=1}^{N} \overline{J}_n \frac{1-\exp\left(-\lambda_n \Delta\psi^t\right)}{\lambda_n \Delta\psi^t} \right] \overline{\mathbf{S}}^t \\ & - \frac{1}{2} g_1^t \sum_{n=1}^{N} \overline{J}_n \left[\exp\left(-\lambda_n \Delta\psi^t\right) \mathbf{q}_n^{t-\Delta t} - g_2^{t-\Delta t} \frac{1-\exp\left(-\lambda_n \Delta\psi^t\right)}{\lambda_n \Delta\psi^t} \overline{\mathbf{S}}^{t-\Delta t} \right] \end{aligned} \tag{4.17}$$

$$\begin{aligned} tr\left(\overline{\boldsymbol{\varepsilon}}^{ve,t}\right) = & \frac{1}{3}\left[g_0^t \overline{B}_0 + g_1^t g_2^t \sum_{n=1}^{N} \overline{B}_n - g_1^t g_2^t \sum_{n=1}^{N} \overline{B}_n \frac{1-\exp\left(-\lambda_n \Delta\psi^t\right)}{\lambda_n \Delta\psi^t} \right] tr\left(\overline{\boldsymbol{\sigma}}^t\right) \\ & - \frac{1}{3} g_1^t \sum_{n=1}^{N} \overline{B}_n \left[\exp\left(-\lambda_n \Delta\psi^t\right) tr\left(\mathbf{q}_n^{t-\Delta t}\right) - g_2^{t-\Delta t} \frac{1-\exp\left(-\lambda_n \Delta\psi^t\right)}{\lambda_n \Delta\psi^t} tr\left(\overline{\boldsymbol{\sigma}}^{t-\Delta t}\right) \right] \end{aligned} \tag{4.18}$$

where Δt is the time increment, $\mathbf{q}_n$ and $tr(\mathbf{q}_n)$ are the deviatoric and volumetric hereditary integrals associated with each Prony series term n, respectively.

4.3 Thermo-Viscoplastic Constitutive Relationship

In order to calculate the viscoplastic (unrecoverable) deformations of asphalt concrete, Perzyan-type viscoplasticity constitutive equations which has been modified to be expressed in terms of the effective stress tensor is used (Darabi et al., 2011a). The constitutive equations are defined in the effective configurations since it is argued that once the material is damaged, further loading can only affect the undamaged region such that the viscoplasticity can only affect the undamaged material skeleton. Rewriting Eq. (4.9) the total strain rate, $\dot{\bar{\boldsymbol{\varepsilon}}}$, is expressed as:

$$\dot{\bar{\boldsymbol{\varepsilon}}} = \dot{\bar{\boldsymbol{\varepsilon}}}^{nve} + \dot{\bar{\boldsymbol{\varepsilon}}}^{vp} \tag{4.19}$$

where $\dot{\bar{\boldsymbol{\varepsilon}}}^{nve}$ is the viscoelastic strain rate and $\dot{\bar{\boldsymbol{\varepsilon}}}^{vp}$ is the viscoplastic strain rate tensors in the effective configuration. Perzyna (1971b) proposed the following viscoplastic flow rule as follows:

$$\dot{\bar{\boldsymbol{\varepsilon}}}^{vp} = \Gamma^{vp} \left\langle \Phi(f) \right\rangle^{N} \frac{\partial g}{\partial \bar{\boldsymbol{\sigma}}} \tag{4.20}$$

where g is the viscoplastic potential function, N is the viscoplastic rate sensitivity exponent, $\langle\ \rangle$ is the Macaulay bracket defined by $\langle x \rangle = (\|x\| + x)/2$, and Γ^{vp} is the

viscoplastic viscosity parameter, which is assumed to be a function of a time-temperature shift factor a_T, such that:

$$\Gamma^{vp} = \frac{\Gamma_0^{vp}}{a_T} \tag{4.21}$$

where Γ_0^{vp} is the viscoplastic viscosity at the reference temperature where $1/\Gamma_0^{vp}$ characterizes the viscoplastic relaxation time. The function Φ in Eq. (4.20) is the overstress function expressed in terms of the yield function f, such that:

$$\Phi(f) = \frac{f}{\sigma_y^0} \tag{4.22}$$

where σ_y^0 is a yield stress quantity. In this work, the modified Drucker-Prager yield function, f, that distinguishes between the distinct behavior of asphalt concrete in tension and compression, and also takes into account the pressure sensitivity is adopted (Masad et al., 2007c). This modified Drucker-Prager yield function is expressed here in the effective configuration as:

$$f = \overline{\tau} - \alpha \overline{I}_1 - \kappa\left(\varepsilon_e^{vp}\right) \le 0 \tag{4.23}$$

where α is a material parameter related to the material's internal friction, $\overline{I}_1$ is the first invariant of $\overline{\boldsymbol{\sigma}}$, ε_e^{vp} is the effective viscoplastic strain, expressed as (Dessouky, 2006):

$$\dot{\varepsilon}_e^{vp} = A^{-1}\sqrt{\dot{\boldsymbol{\varepsilon}}^{vp}.\dot{\boldsymbol{\varepsilon}}^{vp}} \tag{4.24}$$

where $A = \sqrt{1 + 2\left(\frac{0.5 + \beta/3}{1 - \beta/3}\right)^2}$, and $\kappa\left(\varepsilon_e^{vp}\right)$ is an isotropic hardening function associated with the cohesive characteristics of the material and expressed as (Lemaitre and Chaboche, 1990):

$$\kappa = \kappa_0 + \kappa_1 \left\{1 - \exp\left[-\kappa_2 \left(\varepsilon_e^{vp}\right)\right]\right\} \tag{4.25}$$

where κ_0, κ_1, and κ_2 are material parameters, which define the initial yield stress, the saturated yield stress, and the strain hardening rate, respectively. In addition, $\bar{\tau}$ is the deviatoric effective shear stress modified to distinguish between the asphaltic material behavior under compression and extension loading conditions and can be expressed as follows (Tashman et al., 2005):

$$\bar{\tau} = \frac{\sqrt{\bar{J}_2}}{2}\left[1 + \frac{1}{d} + \left(1 - \frac{1}{d}\right)\frac{\bar{J}_3}{\sqrt{\bar{J}_2^3}}\right] \tag{4.26}$$

where $\bar{J}_2 = 3\bar{\mathbf{S}}.\bar{\mathbf{S}}/2$ and $\bar{J}_3 = (9/2)\bar{\mathbf{S}}\bar{\mathbf{S}}\bar{\mathbf{S}}$ are the second and third effective deviatoric stress invariants, respectively, and d is a material parameter representing the ratio of the yield stress in uniaxial tension to the one in uniaxial compression. Therefore, d gives the distinction of asphalt concrete behavior in tension and compression loading and considers the confinement effects. The d value should have a range of $0.778 \le d \le 1$ to ensure that the yield surface convexity condition is maintained (Masad et al., 2007c).

However, because the use of an associative flow rule (i.e. $g = f$) overestimates the dilation compared with experimental measurements (Masad et al., 2007c; Masad et al., 2005b), α in Eq. (4.23) is replaced with β to define the viscoplastic potential function in Eq. (4.27); β represents the dilation or contraction behavior of the material. Therefore, one can define the following viscoplastic potential to estimate the non-associative viscoplastic flow rule in Eq. (4.20):

$$g = \overline{\tau} - \beta \overline{I}_1 \tag{4.27}$$

4.4 Thermo-Viscodamage Constitutive Relationship

Time-, rate-, and temperature-independent evolution equations for the mechanical damage variable, ϕ, are not appropriate for predicting the damage nucleation and growth in asphalt concrete. The damage evolution, $\dot{\phi}$, should be a function of the following variables:

$$\dot{\phi} = F\left[\overline{\boldsymbol{\sigma}}(t), \mathrm{tr}\left[\overline{\boldsymbol{\sigma}}(t)\right], \boldsymbol{\varepsilon}(t), \dot{\boldsymbol{\varepsilon}}(t), T(t), \phi(t)\right] \tag{4.28}$$

In this study, an exponential type of the damage evolution law, proposed by Darabi et al. (2011b), is used.

$$\dot{\phi} = \Gamma^{vd} \exp\left(k^{vd} \varepsilon_{eff}^{Tot}\right)\left(1-\phi\right)^2 \tag{4.29}$$

where Γ^{vd} is a damage viscosity parameter, k^{vd} is a material parameter, and $\varepsilon_{eff}^{Tot} = \sqrt{\boldsymbol{\varepsilon}.\boldsymbol{\varepsilon}}$ is the total effective strain. In addition, the damage viscosity parameter Γ^{vd} is assumed to be stress- and temperature- dependent as follows:

$$\Gamma^{vd} = \Gamma_0^{vd} \left(\frac{\overline{Y}}{Y_0} \right)^{q^{vd}} G(T) \tag{4.30}$$

where Γ_0^{vd} and Y_0 are the reference damage viscosity parameter and the reference damage force, respectively; q^{vd} is the stress-dependency parameter; and $\overline{Y}$ is the damage driving force in the effective undamaged configuration, which can be assumed to have the following form that is capable of describing the difference in damage due to compression and extension loading conditions:

$$\overline{Y} = \overline{\tau} - \alpha \overline{I}_1 \tag{4.31}$$

where $\overline{\tau}$ is given in Eq. (4.26). The temperature-dependent function $G(T)$ is assumed as follows (Darabi et al., 2011a):

$$G(T) = \exp\left[-\xi \left(1 - \frac{T}{T_{ref}} \right) \right] \tag{4.32}$$

where T_{ref} is a reference temperature and ξ is a material constant.

Substituting Eqs. (4.30), (4.31), and (4.32) into Eq. (4.29) gives the following thermo-viscodamage evolution law:

$$\dot{\phi} = \Gamma_0^{vd} \left[\frac{\overline{\tau} - \alpha \overline{I}_1}{Y_0} \right]^q (1-\phi)^2 \exp\left(k\varepsilon_{eff}^{Tot}\right) \exp\left[-\xi \left(1 - \frac{T}{T_{ref}} \right) \right] \tag{4.33}$$

For more details on the numerical integration for the nonlinear viscoelastic, viscoplastic, and viscodamage model, see Darabi et al. (2011c). The numerical algorithms for the mechanical responses of asphalt concrete and the coupling to moisture degradation effect are implemented in the Pavement Analysis using Nonlinear Damage Approach program (PANDA). PANDA is a software which uses the well-known commercial finite element software Abaqus via the user material subroutine (UMAT) and is used in this study to simulate macro- and micro- representation of asphalt concrete.

5. NUMERICAL IMPLEMENTATION OF THE COUPLED MOISTURE-MECHANICAL CONSTITUTIVE RELATIONSHIPS

This chapter includes the numerical integration of the thermo- viscoelastic, viscoplastic, and visco moisture-mechanical-damage constitutive relationships presented in the previous chapter. As mentioned in chapter 2, the constitutive models are presented in the effective configuration. This approach substantially simplifies the numerical implementation since it avoids the complexities associated with the direct couplings of the moisture and mechanical damage to the viscoelastic and viscoplastic models. In other words, we can first update the stress tensor in the effective configuration, $\bar{\boldsymbol{\sigma}}$, using the viscoelastic and viscoplastic models, then calculate the damage variables which are functions of the stress in the effective configuration, and finally update the strain and stress tensors in the damaged (nominal) configuration. However, at the beginning of the analysis the strain increment in the damaged (nominal) configuration is known $\Delta\boldsymbol{\varepsilon}^t$ which is not the same as the strain increment in the effective configuration $\Delta\bar{\boldsymbol{\varepsilon}}^t$. Hence, an iterative method is needed to obtain the strain increment in the effective configuration at current time t. The increment of the total strain in the damaged configuration at current time t, the values of the internal variables (e.g. ϕ and φ), and the stress tensor at the previous increment $t-\Delta t$ are known. The objective here is to update the current stress tensor and determine the current viscoelastic and viscoplastic strain increments.

Hence, we start with a trial strain increment in the effective configuration, such that:

$$\Delta\bar{\boldsymbol{\varepsilon}}^{tr,t} = \left(1-\phi_{eff}^{t-\Delta t}\right)\Delta\bar{\boldsymbol{\varepsilon}}^{t} \tag{5.1}$$

The trial strain increment in the effective configuration will then be fed to the viscoelastic and viscoplastic constitutive models to update viscoelastic and viscoplastic state variables in the effective configuration. The next step is to calculate the moisture and mechanical damage variables based on the obtained variables in the effective configuration. At the end of the analysis, the new and old values of the strain increments in the effective configuration will be compared in order to check convergence. However, in the following developments the superimposed "tr" is removed from the strain increment in the effective configuration for simplicity purposes.

5.1 Moisture Damage Constitutive Relationship

Different procedures were developed in the previous chapter to corporate the moisture-induced damage due to moisture presence and pore water pressure through interconnected cracks and voids. The algorithms to implement these two procedures to simulate moisture-induced damage are presented in the following sub-sections.

5.1.1. Moisture-Induced Damage Due to Moisture Presence

Using the effective stress concept in the effective configuration of CDM greatly simplifies the numerical implementation of the proposed constitutive relationship for moisture damage due to moisture presence. One can first update the effective stress, $\bar{\boldsymbol{\sigma}}$,

based on the nonlinear viscoelasticity and viscoplasticity equations, which are expressed in the effective (dry-undamaged) configuration. Simultaneously, the moisture content throughout the model is determined using Fick's second law. The next step is to determine the damage density based on Eq. (2.8), and the updated nominal stress, $\boldsymbol{\sigma}$, using Eq. (2.10). Knowing the strain increment, $\Delta\boldsymbol{\varepsilon} = \boldsymbol{\varepsilon}^{t} - \boldsymbol{\varepsilon}^{t-\Delta t}$, and values of the stress and internal variables from the previous step (i.e. at time $t - \Delta t$), one can obtain the updated values at the end of the time increment (i.e. at time t).

$$\begin{aligned} \boldsymbol{\varepsilon}^{t} &= \boldsymbol{\varepsilon}^{ve,t} + \boldsymbol{\varepsilon}^{vp,t} = \boldsymbol{\varepsilon}^{t-\Delta t} + \Delta\boldsymbol{\varepsilon}^{t} \\ &= \boldsymbol{\varepsilon}^{ve,t-\Delta t} + \Delta\boldsymbol{\varepsilon}^{ve,t} + \boldsymbol{\varepsilon}^{vp,t-\Delta t} + \Delta\boldsymbol{\varepsilon}^{vp,t} \end{aligned} \tag{5.2}$$

$$\bar{\boldsymbol{\sigma}}^{t} = \bar{\boldsymbol{\sigma}}^{t-\Delta t} + \Delta\bar{\boldsymbol{\sigma}}^{t} \tag{5.3}$$

Then, Eq. (2.7) can be used to obtain the final nominal stress. The effective configuration concept is attractive numerically since it allows one to calculate effective stresses decoupled from damage, which eliminates the complexities due to the coupling of damage with viscoelasticity and viscoplasticity.

Moisture diffusion within the microstructure of the asphalt mixture is assumed to follow Fick's second law, Eq. (4.5). Therefore, to simulate the dispersion of moisture, the diffusion equation is solved using Abaqus's built-in facilities for solving mass diffusion, where moisture content is used in place of mass. Moisture content at each node is computed using implicit standard method and writing the weak formulation of the Fick's second law. The solution provides moisture content at each node at each time step according to the imposed moisture content boundary condition. The obtained weak

form of the equation is a first order differential equation and can be solved via classical time integration algorithms, Abaqus (2008) is using the backward difference scheme where the time derivative is computed as:

$$\dot{\theta}_{n+1} = \frac{1}{\Delta t}\left(\theta_{n+1} - \theta_n\right) \tag{5.4}$$

where n is the number of load step. Having the moisture content at each time step obtained from Fick's second law Eq. (4.5) can be solved discretely, so at time t following a time step of Δt,

$$\omega^{i,t} = \omega^{i,t-\Delta t} + k^i \theta^i < 1 - \frac{\phi^{T(t-\Delta t)}}{\phi_{cr}} >^q \Delta t, i = a, c, \tag{5.5}$$

The above formulated numerical algorithms are implemented in PANDA linked to the well-known commercial finite element code Abaqus (2008). Figure 5.1 shows the flowchart for implementation of the coupled moisture-mechanical constitutive model.

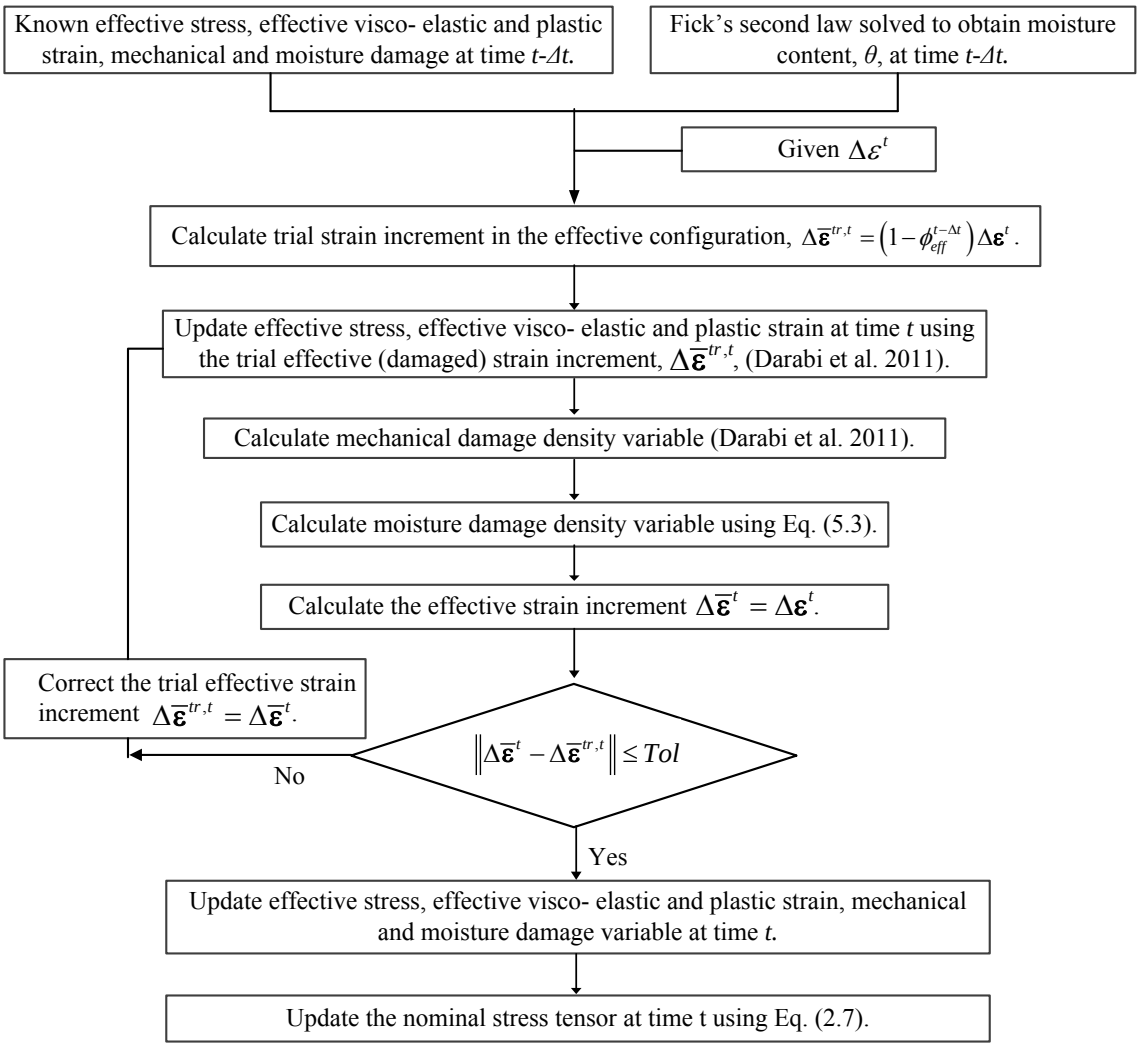

Figure 5.1. Flowchart for implementation of the coupled moisture-mechanical 3constitutive model.

5.1.2. Moisture-Induced Damage Due to Pore Water Pressure

Pore water pressures contribute extra stresses on the solid phase within the asphalt concrete causing added mechanical damage within the asphalt components. The effective stress concept in the saturated deformable media was used for its simulation. One can first update the effective stress, $\bar{\boldsymbol{\sigma}}$, based on the nonlinear viscoelasticity and

viscoplasticity equations, which are expressed in the effective (dry-undamaged) configuration. Simultaneously, the pore pressure throughout the model is determined using Abaqus built-in facilities.

$$\Delta\varepsilon^{pore\ pressure,t} = -\beta'\Delta p \tag{5.6}$$

$$\begin{aligned}\boldsymbol{\varepsilon}^{t} &= \boldsymbol{\varepsilon}^{ve,t} + \boldsymbol{\varepsilon}^{vp,t} = \boldsymbol{\varepsilon}^{t-\Delta t} + \Delta\boldsymbol{\varepsilon}^{t} \\ &= \boldsymbol{\varepsilon}^{ve,t-\Delta t} + \Delta\boldsymbol{\varepsilon}^{ve,t} + \boldsymbol{\varepsilon}^{vp,t-\Delta t} + \Delta\boldsymbol{\varepsilon}^{vp,t} + \boldsymbol{\varepsilon}^{pp,t-\Delta t} + \Delta\boldsymbol{\varepsilon}^{pp,t}\end{aligned} \tag{5.7}$$

$$\begin{aligned}\overline{\boldsymbol{\sigma}}^{ve,vp,t} &= \overline{\boldsymbol{\sigma}}^{ve,vp,t-\Delta t} + \Delta\overline{\boldsymbol{\sigma}}^{ve,vp,t} \\ \Delta\overline{\boldsymbol{\sigma}}^{t} &= \Delta\overline{\boldsymbol{\sigma}}^{ve,vp,t} + \Delta\overline{\boldsymbol{\sigma}}^{pp,t}\end{aligned} \tag{5.8}$$

Moisture flow within the microstructure of the asphalt mixture is assumed to follow Darcy's law, Eq. (4.6). Therefore, Abaqus's built-in facilities were used to simulate the pore pressure within the microstructure.

5.2 Thermo-Viscoelastic Constitutive Relationship

The volumetric and deviatoric components of the viscoelastic strain tensor can be written such that:

$$\overline{\boldsymbol{\varepsilon}}^{nve} = \overline{\mathbf{e}}^{nve} + \frac{1}{3}tr\left(\overline{\boldsymbol{\varepsilon}}^{nve}\right)\mathbf{I} = \frac{1}{2\overline{G}}\overline{\mathbf{S}} + \frac{tr\left(\overline{\boldsymbol{\sigma}}\right)}{9\overline{K}}\mathbf{I} = \frac{\overline{J}}{2}\overline{\mathbf{S}} + \frac{\overline{B}}{3}tr\left(\overline{\boldsymbol{\sigma}}\right)\mathbf{I} \tag{5.9}$$

where $\overline{\mathbf{e}}^{nve}$ and $tr\left(\overline{\boldsymbol{\varepsilon}}^{nve}\right)$ are the deviatoric and the volumetric strain tensors, respectively, of the viscoelastic strain tensor. $\overline{\mathbf{S}}$ is the deviatoric stress tensor which can be written as follows:

$$\overline{\mathbf{S}} = \overline{\boldsymbol{\sigma}} - \frac{1}{3}\overline{\boldsymbol{\sigma}}\mathbf{I} \tag{5.10}$$

Deviatoric and volumetric components of the viscoelastic strain tensor can be rewritten as follows by using Eqs. (4.12) and (4.13) (Haj-Ali and Muliana, 2004b; Lai and Bakker, 1996b):

$$\begin{aligned}\overline{\mathbf{e}}^{ve,t} = &\frac{1}{2}\left[g_0^t \overline{J}_0 + g_1^t g_2^t \sum_{n=1}^{N} \overline{J}_n - g_1^t g_2^t \sum_{n=1}^{N} \overline{J}_n \frac{1-\exp(-\lambda_n \Delta t^t)}{\lambda_n \Delta t^t} \right] \overline{\mathbf{S}}^t \\ &- \frac{1}{2} g_1^t \sum_{n=1}^{N} \overline{J}_n \left[\exp\left(-\lambda_n \Delta t^t\right) \mathbf{q}_n^{t-\Delta t} - g_2^{t-\Delta t} \frac{1-\exp(-\lambda_n \Delta t^t)}{\lambda_n \Delta t^t} \overline{\mathbf{S}}^{t-\Delta t} \right] \equiv \hat{J}^t \overline{\mathbf{S}}^t - \hat{\mathbf{d}}\end{aligned} \tag{5.11}$$

$$\begin{aligned}tr\left(\overline{\boldsymbol{\varepsilon}}^{ve,t}\right) = &\frac{1}{3}\left[g_0^t \overline{B}_0 + g_1^t g_2^t \sum_{n=1}^{N} \overline{B}_n - g_1^t g_2^t \sum_{n=1}^{N} \overline{B}_n \frac{1-\exp(-\lambda_n \Delta t^t)}{\lambda_n \Delta t^t} \right] tr\left(\overline{\boldsymbol{\sigma}}^t\right) \\ &- \frac{1}{2} g_1^t \sum_{n=1}^{N} \overline{B}_n \left[\exp\left(-\lambda_n \Delta t^t\right) tr\left(\mathbf{q}_n^{t-\Delta t}\right) - g_2^{t-\Delta t} \frac{1-\exp(-\lambda_n \Delta t^t)}{\lambda_n \Delta t^t} tr\left(\overline{\boldsymbol{\sigma}}^{t-\Delta t}\right) \right] \\ &\equiv \hat{B}^t tr\left(\overline{\boldsymbol{\sigma}}^t\right) - tr\left(\hat{\mathbf{V}}\right)\end{aligned} \tag{5.12}$$

where the variables $\mathbf{q}_n^{t-\Delta t}$ and $tr\left(\mathbf{q}_n^{t-\Delta t}\right)$ are the deviatoric and volumetric components of the hereditary integrals for each term n of the Prony series at the previous time step $t - \Delta t$. The hereditary integrals are updated at the end of each converged time increment, which will be used for the next time increment, and are expressed as follows (Haj-Ali and Muliana, 2004b):

$$\mathbf{q}_n^t = \exp(-\lambda_n \Delta t^t) \mathbf{q}_n^{t-\Delta t} + (g_2^t \overline{\mathbf{S}}^t - g_2^{t-\Delta t} \overline{\mathbf{S}}^{t-\Delta t}) \frac{1-\exp(-\lambda_n \Delta t^t)}{\lambda_n \Delta t^t} \tag{5.13}$$

$$tr\left(\mathbf{q}_n^t\right)=\exp(-\lambda_n\Delta t^t)tr\left(\mathbf{q}_n^{t-\Delta t}\right)+\left[g_2^t tr\left(\overline{\boldsymbol{\sigma}}^t\right)-g_2^{t-\Delta t}tr\left(\overline{\boldsymbol{\sigma}}^{t-\Delta t}\right)\right]\frac{1-\exp(-\lambda_n\Delta t^t)}{\lambda_n\Delta t^t} \quad (5.14)$$

where Δt^t and $\Delta t^{t-\Delta t}$ are time increments at times t and $t-\Delta t$, respectively.

The deviatoric and volumetric increments of the strain increment can be expressed using Eqs. (5.2), (5.11) and (5.12) as follows:

$$\begin{aligned}\Delta\overline{\mathbf{e}}^{ve,t} &= \overline{\mathbf{e}}^{ve,t}-\overline{\mathbf{e}}^{ve,t-\Delta t}\\ &= \overline{J}^t\overline{\mathbf{S}}^t-\overline{J}^{t-\Delta t}\overline{\mathbf{S}}^{t-\Delta t}-\frac{1}{2}\sum_{n=1}^{N}\overline{J}_n\left[g_1^t\exp(-\lambda_n\Delta t^t)-g_1^{t-\Delta t}\right]\mathbf{q}_n^{t-\Delta t}-\\ &\quad \frac{1}{2}g_2^{t-\Delta t}\sum_{n=1}^{N}\overline{J}_n\left\{g_1^{t-\Delta t}\left[\frac{1-\exp(-\lambda_n\Delta t^{t-\Delta t})}{\lambda_n\Delta t^{t-\Delta t}}\right]-g_1^t\left[\frac{1-\exp(-\lambda_n\Delta t^t)}{\lambda_n\Delta t^t}\right]\right\}\overline{\mathbf{S}}^{t-\Delta t}\end{aligned} \quad (5.15)$$

$$\begin{aligned}tr\left(\Delta\overline{\boldsymbol{\varepsilon}}^{ve,t}\right) &= tr\left(\overline{\boldsymbol{\varepsilon}}^{ve,t}\right)-tr\left(\overline{\boldsymbol{\varepsilon}}^{ve,t-\Delta t}\right)\\ &= \overline{B}^t tr\left(\overline{\boldsymbol{\sigma}}^t\right)-\overline{B}^{t-\Delta t}tr\left(\overline{\boldsymbol{\sigma}}^{t-\Delta t}\right)-\frac{1}{3}\sum_{n=1}^{N}\overline{B}_n\left[g_1^t\exp(-\lambda_n\Delta t^t)-g_1^{t-\Delta t}\right]tr\left(\mathbf{q}_n^{t-\Delta t}\right)-\\ &\quad \frac{1}{3}g_2^{t-\Delta t}\sum_{n=1}^{N}\overline{B}_n\left\{g_1^{t-\Delta t}\left[\frac{1-\exp(-\lambda_n\Delta t^{t-\Delta t})}{\lambda_n\Delta t^{t-\Delta t}}\right]-g_1^t\left[\frac{1-\exp(-\lambda_n\Delta t^t)}{\lambda_n\Delta t^t}\right]\right\}tr\left(\overline{\boldsymbol{\sigma}}^{t-\Delta t}\right)\end{aligned} \quad (5.16)$$

The problem in solving Eqs. (5.15) and (5.16) is that the nonlinear functions are not known at the current increment t. Therefore, an iterative method can be used to find the correct stress state. Hence, Eqs. (5.15) and (5.16) are further linearized by assuming that $g_\alpha^t=g_\alpha^{t-\Delta t}$, such that the trial stress increment can be written as follows:

$$\Delta\overline{\mathbf{S}}^{t,tr}=\frac{1}{\hat{J}^{t,tr}}\left\{\Delta\overline{\mathbf{e}}^t+\frac{1}{2}g_1^{t,tr}\sum_{n=1}^{N}J_n\left[\exp(-\lambda_n\Delta t)-1\right]\mathbf{q}_n^{t-\Delta t}\right\} \quad (5.17)$$

$$tr\left(\Delta\bar{\boldsymbol{\sigma}}^{t,tr}\right)=\frac{1}{\hat{B}^{t,tr}}\left\{tr\left(\Delta\bar{\boldsymbol{\varepsilon}}^{t}\right)+\frac{1}{3}g_1^{t,tr}\sum_{n=1}^{N}B_n\left[\exp(-\lambda_n\Delta t)-1\right]tr\left(\mathbf{q}_n^{t-\Delta t}\right)\right\} \tag{5.18}$$

where $\hat{J}^{t,tr}$ and $\hat{B}^{t,tr}$ can be obtained using Eqs. (4.14) and (4.15) when the nonlinear parameters are functions of the trial stress. This study employs the iterative scheme to obtain the correct stress for a given strain increment. Before the onset of viscoplasticity, the residual strain will be defined as follows:

$$\bar{\mathbf{R}}^{ve,t}=\Delta\bar{\mathbf{e}}^{ve,t}+\frac{1}{3}tr\left(\Delta\bar{\boldsymbol{\varepsilon}}^{ve,t}\right)-\Delta\bar{\boldsymbol{\varepsilon}}^{t} \tag{5.19}$$

The Newton-Raphson method will be used to minimize the strain residual in Eq. (5.19). Moreover, when the strain is totally viscoelastic, the program uses the consistent Jacobian matrix which is the consistent tangent compliance and is determined as:

$$\begin{aligned}\bar{\mathbf{S}}^{ve}=\frac{\partial\bar{\mathbf{R}}^{ve,t}}{\partial\bar{\boldsymbol{\sigma}}^{t}}&=\hat{J}^{t}\mathbf{I}\times\mathbf{I}+\frac{1}{3}\left(\hat{B}^{t}-\hat{J}^{t}\right)\mathbf{I}\times\mathbf{I}\\&+\frac{\partial\bar{\sigma}_{eff}^{t}}{\partial\boldsymbol{\sigma}^{t}}\left\{\frac{\partial\hat{J}^{t}}{\partial\bar{\sigma}_{eff}^{t}}\bar{\boldsymbol{\sigma}}^{t}+\frac{1}{3}\left(\frac{\partial\hat{B}^{t}}{\partial\bar{\sigma}_{eff}^{t}}-\frac{\partial\hat{J}^{t}}{\partial\bar{\sigma}_{eff}^{t}}\right)\bar{\boldsymbol{\sigma}}^{t}\mathbf{I}\right.\\&-\frac{1}{2}\frac{\partial g_1^{t}}{\partial\bar{\sigma}_{eff}^{t}}\sum_{n=1}^{N}\hat{J}_n\left[\exp(-\lambda_n\Delta t^{t})\mathbf{q}_n^{t-\Delta t}-g_2^{t-\Delta t}\left(\frac{1-\exp(-\lambda_n\Delta t^{t})}{\lambda_n\Delta t^{t}}\right)\bar{\mathbf{S}}^{t-\Delta t}\right]\\&-\frac{1}{9}\frac{\partial g_1^{t}}{\partial\bar{\sigma}_{eff}^{t}}\sum_{n=1}^{N}\hat{B}_n\left[\begin{array}{l}\exp(-\lambda_n\Delta t^{t})tr\left(\mathbf{q}_n^{t-\Delta t}\right)\\-g_2^{t-\Delta t}\left(\frac{1-\exp(-\lambda_n\Delta t^{t})}{\lambda_n\Delta t^{t}}\right)tr\left(\bar{\boldsymbol{\sigma}}^{t-\Delta t}\right)\end{array}\right]\mathbf{I}\end{aligned} \tag{5.20}$$

It should be noted that Eqs. (5.19) and (5.20) are not valid in the presence of viscoplastic deformations. These equations will be updated in the next subsection.

Figure 5.2 shows the flowchart for the implementation of the viscoelastic model. Note that, this flowchart is valid in the absence of viscoplasticity.

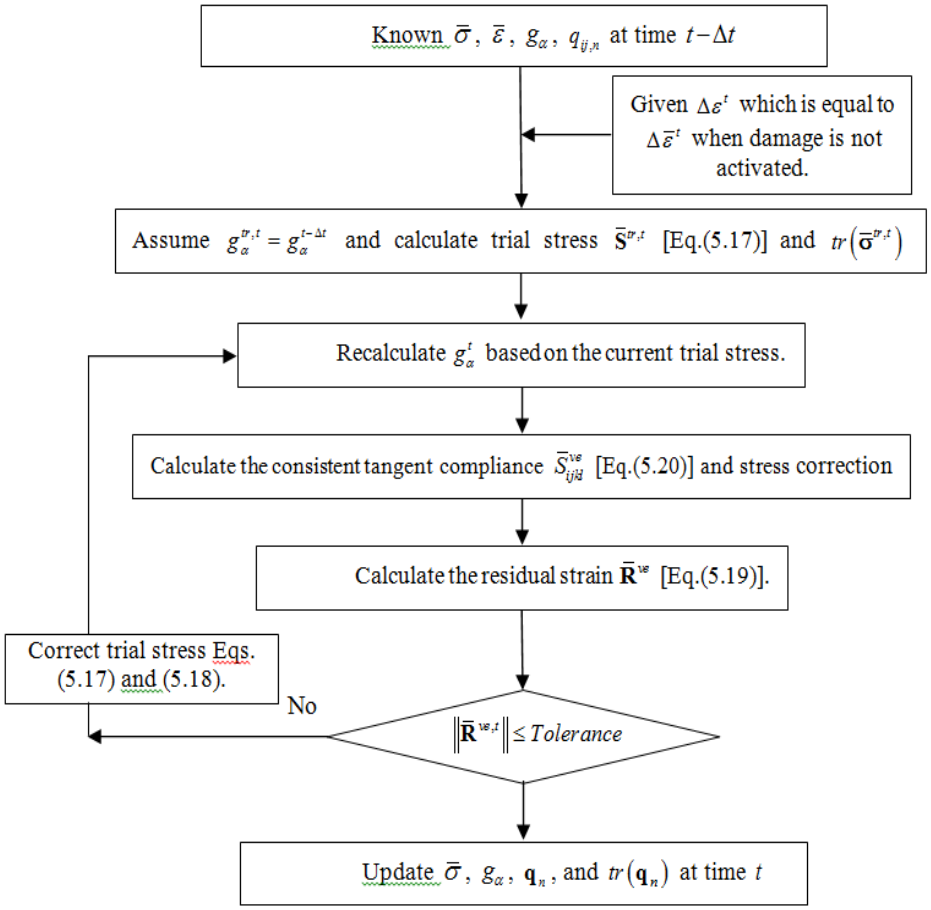

Figure 5.2. The flow chart of the recursive-iterative algorithm for implementation of the viscoelastic model. Note that since damage is not present the strains and strain increments in the damaged (nominal) and effective configurations are the same (Darabi et al., 2012a).

5.3 Thermo-Viscoplastic Constitutive Relationship

The viscoplastic strain increment in Eqs. (4.17) can be rewritten as follows:

$$\Delta\bar{\boldsymbol{\varepsilon}}^{vp,t} = \Gamma^{vp}\left\langle\Phi\left(f\right)\right\rangle^{N}\frac{\partial g}{\partial\bar{\boldsymbol{\sigma}}}\Delta t = \Delta\bar{\gamma}^{vp,t}\frac{\partial g}{\partial\bar{\boldsymbol{\sigma}}} \tag{5.21}$$

where $\Delta\bar{\gamma}^{vp,t}$ can be written from Eqs. (4.18) and (4.19) as follows:

$$\Delta\bar{\gamma}^{vp,t} = \Delta t\Gamma^{vp}\left\langle\Phi\left(f\right)\right\rangle^{N} = \Delta t\Gamma^{vp}\left[\frac{f\left(\bar{\boldsymbol{\sigma}}^{t},\bar{\varepsilon}_{e}^{vp,t}\right)}{\sigma_{y}^{0}}\right]^{N} \tag{5.22}$$

Substituting Eqs. (4.21), and (5.21) into Eq. (5.2), the effective viscoplastic strain increment can be written as:

$$\bar{\varepsilon}_{e}^{vp,t} = \bar{\varepsilon}_{e}^{vp,t-\Delta t} + \Delta\bar{\varepsilon}_{e}^{vp,t} = \bar{\varepsilon}_{e}^{vp,t-\Delta t} + \frac{\Delta\bar{\gamma}^{vp,t}}{\sqrt{1+2\left(\dfrac{0.5+\beta/3}{1-\beta/3}\right)^{2}}}\sqrt{\frac{\partial g}{\partial\bar{\boldsymbol{\sigma}}}\frac{\partial g}{\partial\bar{\boldsymbol{\sigma}}}} \tag{5.23}$$

Deviatoric and volumetric increments of the trial stress for starting the coupled nonlinear viscoelastic and viscoplastic algorithm can be expressed as follows [see Huang et al. (2011)]:

$$\Delta\bar{\mathbf{S}}^{t,tr} = \frac{1}{\bar{J}^{t,tr}}\left\{\Delta\bar{\mathbf{e}}^{t} + \frac{1}{2}g_{1}^{t,tr}\sum_{n=1}^{N}J_{n}\left[\exp(-\lambda_{n}\Delta\psi^{t})-1\right]\mathbf{q}_{n}^{t-\Delta t}\right\} \tag{5.24}$$

$$tr\left(\Delta\bar{\boldsymbol{\sigma}}^{t,tr}\right) = \frac{1}{\bar{B}^{t,tr}}\left\{tr\left(\Delta\bar{\boldsymbol{\varepsilon}}^{t}\right) + \frac{1}{3}g_{1}^{t,tr}\sum_{n=1}^{N}B_{n}\left[\exp(-\lambda_{n}\Delta\psi^{t})-1\right]tr\left(\mathbf{q}_{n}^{t-\Delta t}\right)\right\} \tag{5.25}$$

According to Wang et al. (2012), one can define a consistency condition for rate-dependent plasticity (viscoplasticity) similar to the classical rate-independent plasticity theory such that a dynamic (rate-dependent) yield surface, χ, can be expressed from Eqs. (4.17), (4.18), (4.19), and (4.20) as follows:

$$\chi = \overline{\tau} - \alpha \overline{I}_1 - \kappa\left(\overline{\varepsilon}_e^{vp}\right) - \sigma_y^0 \left(\frac{\dot{\overline{\gamma}}^{vp}}{\Gamma^{vp}} \right)^{1/N} \leq 0 \tag{5.26}$$

The Kuhn-Tucker loading-unloading condition (consistency) is valid also for the dynamic yield surface χ, such that:

$$\chi \leq 0; \quad \dot{\overline{\gamma}}^{vp} \geq 0; \quad \dot{\overline{\gamma}}^{vp} \chi = 0; \quad \dot{\chi} = 0 \tag{5.27}$$

A trial dynamic yield surface function χ^{tr} can be defined from Eq. (5.26) as:

$$\chi = \overline{\tau}^{tr} - \alpha \overline{I}_1^{tr} - \kappa\left(\overline{\varepsilon}_e^{vp,t-\Delta t}\right) - \sigma_y^0 \left(\frac{\Delta \overline{\gamma}^{vp,t-\Delta t}}{\Delta t \Gamma^{vp}} \right)^{1/N} \tag{5.28}$$

In order to calculate $\overline{\varepsilon}_e^{vp,t}$, one can iteratively calculate $\Delta \overline{\gamma}^{vp,t}$ through using the Newton-Raphson scheme. Once $\Delta \overline{\gamma}^{vp,t}$ is obtained, the viscoplastic strain increment $\Delta \overline{\boldsymbol{\varepsilon}}^{vp}$ can be calculated from Eq. (5.21). In the Newton-Raphson scheme, the differential of χ with respect to $\Delta \overline{\gamma}^{vp}$ is needed, which can be expressed as follows:

$$\frac{\partial \chi}{\partial \Delta \gamma^{vp}} = -\frac{\partial \kappa}{\partial \Delta \overline{\varepsilon}_e^{vp}} \frac{\partial \Delta \overline{\varepsilon}_e^{vp}}{\partial \Delta \overline{\gamma}^{vp}} - \frac{\sigma_y^0}{\Delta \overline{\gamma}^{vp} N} \left(\frac{\Delta \overline{\gamma}^{vp}}{\Delta t \Gamma^{vp}} \right)^{\frac{1}{N}} \tag{5.29}$$

At the k+1 iteration, the viscoplastic multiplier can be calculated as follows:

$$\left(\Delta\bar{\gamma}^{vp,t}\right)^{k+1} = \left(\Delta\bar{\gamma}^{vp,t}\right)^{k} - \left[\left(\frac{\partial\chi}{\partial\Delta\bar{\gamma}^{vp,t}}\right)^{k}\right]^{-1}\chi^{k} \tag{5.30}$$

The above recursive-iterative algorithm with the Newton-Raphson method is used to obtain the current effective stress and the updated values of viscoelastic and viscoplastic strain increments by minimizing the residual strain defined as:

$$\mathbf{R}^{t} = \Delta\bar{\boldsymbol{\varepsilon}}^{nve,t} + \Delta\bar{\boldsymbol{\varepsilon}}^{vp,t} - \Delta\bar{\boldsymbol{\varepsilon}}^{t} \tag{5.31}$$

The stress increment at the k+1 iteration is calculated by:

$$\left(\Delta\bar{\boldsymbol{\sigma}}^{t}\right)^{k+1} = \left(\Delta\bar{\boldsymbol{\sigma}}^{t}\right)^{k} - \left[\left(\frac{\partial\mathbf{R}^{t}}{\partial\bar{\boldsymbol{\sigma}}^{t}}\right)^{k}\right]^{-1}\left(\mathbf{R}^{t}\right)^{k} \tag{5.32}$$

where the differential of $\mathbf{R}^{t}$ gives the consistent tangent compliance, which is necessary for speeding convergence and can be derived as follows:

$$\frac{\partial\mathbf{R}^{t}}{\partial\bar{\boldsymbol{\sigma}}} = \frac{\partial\Delta\bar{\boldsymbol{\varepsilon}}^{nve,t}}{\partial\bar{\boldsymbol{\sigma}}} + \frac{\partial\Delta\bar{\boldsymbol{\varepsilon}}^{vp,t}}{\partial\bar{\boldsymbol{\sigma}}} \tag{5.33}$$

where $\partial\Delta\bar{\boldsymbol{\varepsilon}}^{nve,t}/\partial\bar{\boldsymbol{\sigma}}$ is the nonlinear viscoelastic tangent compliance which is derived in Huang et al. (2011); whereas, the viscoplastic tangent compliance is derived from Eqs. (4.20), (5.21), and (5.22), such that:

$$\begin{aligned}\frac{\partial \Delta\bar{\boldsymbol{\varepsilon}}^{vp,t}}{\partial\bar{\boldsymbol{\sigma}}} &= \frac{\partial g}{\partial\bar{\boldsymbol{\sigma}}}\frac{\partial \Delta\bar{\gamma}^{vp,t}}{\partial\bar{\boldsymbol{\sigma}}} + \Delta\bar{\gamma}^{vp,t}\frac{\partial^2 g}{\partial\bar{\boldsymbol{\sigma}}\partial\bar{\boldsymbol{\sigma}}} \\ &= \frac{\Delta t\Gamma N}{\sigma_y^0}\left(\frac{f}{\sigma_y^0}\right)^{N-1}\frac{\partial g}{\partial\bar{\boldsymbol{\sigma}}}\frac{\partial f}{\partial\bar{\boldsymbol{\sigma}}} + \Delta t\Gamma\left(\frac{f}{\sigma_y^0}\right)^{N}\frac{\partial^2 g}{\partial\bar{\boldsymbol{\sigma}}\partial\bar{\boldsymbol{\sigma}}}\end{aligned} \tag{5.34}$$

where $\partial^2 g/\partial\bar{\boldsymbol{\sigma}}\partial\bar{\boldsymbol{\sigma}}$ is given by:

$$\begin{aligned}\frac{\partial^2 g}{\partial\bar{\sigma}_{ij}\partial\bar{\sigma}_{kl}} &= 1.5\left(\delta_{ik}\delta_{jl} - \frac{1}{3}\delta_{ij}\delta_{kl}\right)\left[\frac{1+1/d}{2\sqrt{J_2}} - \frac{J_3\left(1-1/d\right)}{J_2^2}\right] \\ &+1.5\bar{S}_{kl}\left[\frac{-\dfrac{\partial\bar{J}_2}{\partial\bar{\sigma}_{ij}}\left(1+1/d\right)J_2^{-1.5}}{4} + \left(1-1/d\right)\left(2\bar{J}_3\bar{J}_2^{-3}\frac{\partial\bar{J}_2}{\partial\bar{\sigma}_{ij}} - \bar{J}_2^{-2}\frac{\partial\bar{J}_3}{\partial\bar{\sigma}_{ij}}\right)\right] \\ &+\frac{\left(1-1/d\right)}{2\bar{J}_2^2}\left[\frac{27\left(\delta_{ik}\bar{S}_{lj}+\delta_{jl}\bar{S}_{ik}\right)}{2} - 9\left(\delta_{kl}\bar{S}_{ij}+\delta_{ij}\bar{S}_{kl}\right)\right] \\ &-\left(\frac{27}{4}\bar{S}_{km}\bar{S}_{ml} - 1.5J_2\bar{S}_{kl}\right)\left[\frac{\left(1-1/d\right)\dfrac{\partial\bar{J}_2}{\partial\bar{\sigma}_{ij}}}{\bar{J}_2^2}\right]\end{aligned} \tag{5.35}$$

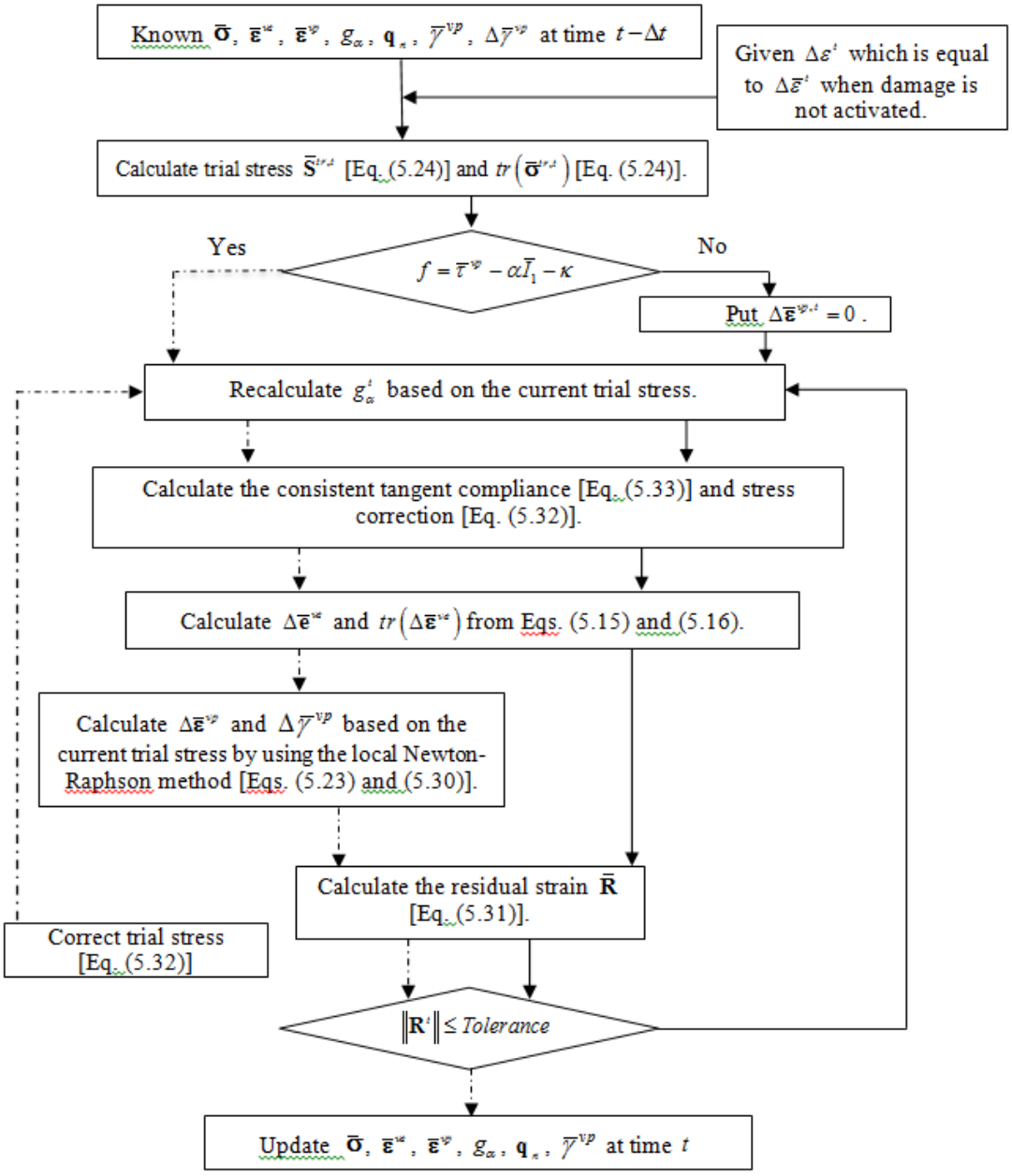

Figure 5.3. The flow chart of the recursive-iterative Newoton-Raphson algorithm for implementation of the coupled viscoelastic-viscoplastic model. Note that since damage is not present the strains and strain increments in the damaged (nominal) and effective configurations are the same (Darabi et al., 2012a)**.**

5.4 Thermo-Viscodamage Constitutive Relationship

Mechanical damage is formulated using the concept of effective configuration presented in the previous chapter. The use of the effective configuration concept substantially simplifies the numerical implementation of mechanical damage constitutive models. The stress in the effective configuration can first be updated using the viscoelastic and viscoplastic constitutive models. The mechanical damage force which is expressed in terms of the quantities in the effective configuration can be calculated and used to calculate the damage rate. In this section, we show the implementation procedure for obtaining the mechanical damage density at the current time t.

We can define the damage condition by rearranging Eq. (4.30), such that:

$$\chi^{vd} = \left[\frac{\bar{Y}\left(1-\phi\right)}{Y_0}\right]^q \exp\left(k\bar{\varepsilon}_{eff}\right) - \frac{\dot{\phi}}{\Gamma^{vd}} = 0 \tag{5.36}$$

where $\bar{Y}$ is the damage force and χ^{vd} is the damage loading condition. A trial value for viscodamage loading surface can be defined as:

$$\chi^{vd,tr} = \left[\frac{\bar{Y}\left(1-\phi^{t-\Delta t}\right)}{Y_0}\right]^q \exp\left(k\bar{\varepsilon}_{eff}\right) - \frac{\Delta\phi^{t-\Delta t}}{\Gamma^{vd}\Delta t} = 0 \tag{5.37}$$

Similar to viscoplasticity, the mechanical damage increment can be obtained using the Newton-Raphson scheme. However, it should be noted that the values of $\bar{Y}$ and $\bar{\varepsilon}_{eff}$ are constant during these trials, which substantially simplifies the implementation, since they are expressed in the effective configuration. However, the

differential of the χ^{vd}, Eq. (5.36), with respect to $\Delta\phi$ is needed which can be expressed as follows:

$$\frac{\partial \chi^{vd}}{\partial \Delta\phi} = -q\left(\frac{\overline{Y}}{Y_0}\right)\left[\frac{\overline{Y}(1-\phi)}{Y_0}\right]^{q-1} \exp\left(k\overline{\varepsilon}_{eff}\right) - \frac{1}{\Gamma^{vd}\Delta t} \tag{5.38}$$

Hence, the damage density increment at the $k+1$ iteration can be obtained as follows:

$$\left(\Delta\phi^t\right)^{k+1} = \left(\Delta\phi^t\right)^k - \left[\left(\frac{\partial \chi^{vd}}{\partial \Delta\phi^t}\right)^k\right]^{-1} \chi^{vd} \tag{5.39}$$

The damage density ϕ can then be obtained, such that:

$$\phi^t = \phi^{t-\Delta t} + \dot{\phi}^t \Delta t \tag{5.40}$$

This procedure for implementation of the viscodamage constitutive model and its coupling to the viscoelastic and viscoplastic response of asphalt concrete is schematically represented in Figure 5.4.

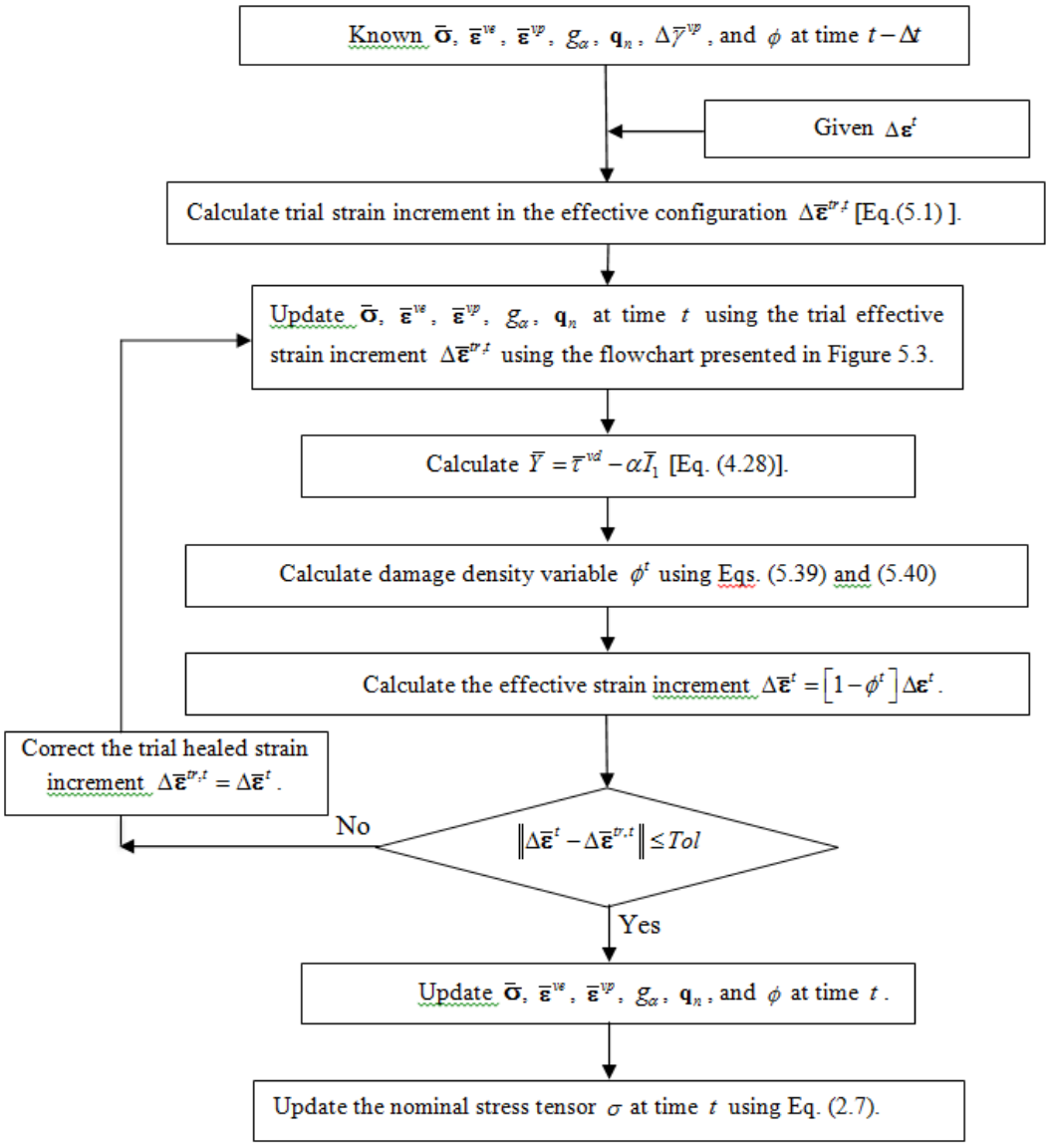

Figure 5.4. The flow chart for implementation of the coupled viscoelastic-viscoplastic-viscodamage model (Darabi et al., 2012a).

6. CALIBRATION AND VALIDATION OF THE MOISTURE DAMAGE CONSTITUTIVE RELATIONSHIP USING EXPERIMENTAL DATA

The continuum moisture damage constitutive relationship described in the previous chapter, is calibrated against pull-off tests results available in the literature (Kringos et al., 2008c; Pinto et al., 2009; Youtcheff and Aurilio, 1997). Pull-off tests results provide the possibility of calibrating the developed adhesive moisture damage constitutive relationship. Then, uniaxial constant strain rate experimental tests conducted at North Carolina State University and Texas A&M University are used to calibrate the developed constitutive moisture damage relationship at a continuum level without distinguishing between adhesive and cohesive moisture damage variables. The calibrated constitutive relationship is validated against a set of experimental tests conducted on samples with similar material and characteristics. The modified Lottman procedure (AASHTO, 2007) was used in these experiments to saturate the specimen to certain levels. The specimens were subjected to 2 different moisture-conditioning periods, 12 and 24 hours, after saturation.

6.1.Calibration of the Moisture Damage Constitutive Relationship

The developed moisture damage constitutive relationship along with CMMDM coupling framework is calibrated in this section. A few models consider the adhesive bond

strength of the aggregate-binder or aggregate-mastic (asphalt binder and aggregates smaller than 74 μm) interface (e.g. Kringos and Scarpas, 2008; 2008b; 2008c; Pinto et al., 2009; Youtcheff and Aurilio, 1997). These models are based on pull-off tests and used to investigate the effect of moisture diffusion on aggregate-mastic adhesive bond strength. These experimental works were used to calibrate the adhesive moisture damage evolution functions. Then, the moisture damage constitutive relationship was calibrated against uniaxial constant strain rate test results. The model parameters associated to the thermo- nonlinear-viscoelastic, viscoplastic, and mechanical damage constitutive relationships were obtained based on the procedure developed by Darabi et. al. (Darabi et al., 2012a) prior to moisture damage calibration and validation.

6.1.1 Identification of Adhesive Moisture Damage Constitutive Relationship Model Parameters

Youtcheff and Aurilio (Youtcheff and Aurilio, 1997) and Pinto et. al. (Pinto et al., 2009) performed the pull-off tests on different aggregate-binder combinations varying in size and material type while Kringos et. al. (Kringos et al., 2008c) conducted the pull-off tests on different aggregate-mastic combinations. These three different sets of experiments were simulated numerically to calibrate and validate the moisture damage constitutive relationship. Although this section describes the pull-off tests on aggregate-binder, the testing procedure and set up were similar in these sets of experiments. These tests aimed to measure the moisture susceptibility of the aggregate-binder bond strength for different periods of moisture conditioning. In these tests, a thin layer of binder was

adhered between an aggregate substrate and a metal pull-stub. The system was pulled apart in uniaxial tension at a constant displacement rate to determine the aggregate-binder bond strength. Prior to testing, the sample was conditioned in a water bath for varying conditioning times. Moisture was forced to diffuse through the aggregate to avoid the occurrence of mixed weakening of both the binder and the aggregate-binder interface, Figure 6.1. The ultimate tension stresses, representing the bond strengths, associated with each conditioning time were recorded for different samples.

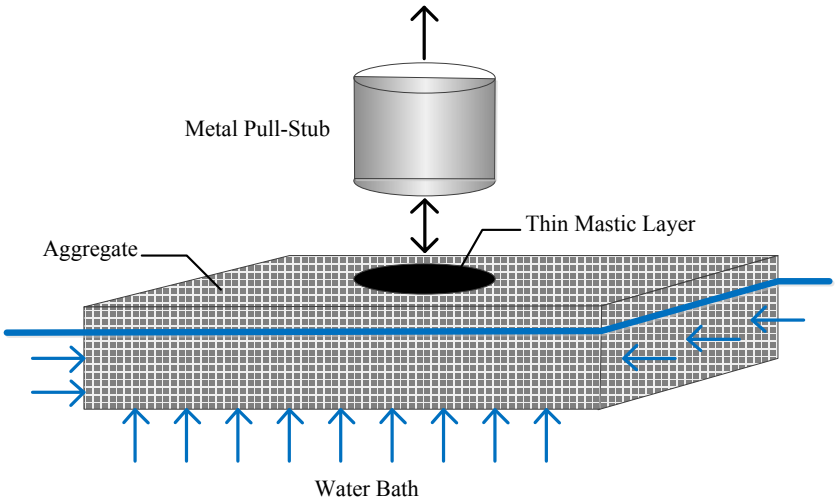

Figure 6.1. Schematic of the pull-off test experiment.

FE representations of the experimental tests were constructed in Abaqus (2008) based on the dimensions of the aggregate and binder in each experiment. Figure 6.2 shows the FE mesh constructed to simulate the pull-off tests. The FE model consists of the aggregate substrate, the adhered binder, and the interface between the aggregate and

the binder. The interface is assumed to be thin and is modeled by two rows of elements adhered to the aggregate without embedding the cohesive zone elements. The built-in algorithms in Abaqus FE package were used to solve Fick's second law in order to computationally determine the evolution of the moisture content within the adhered binder.

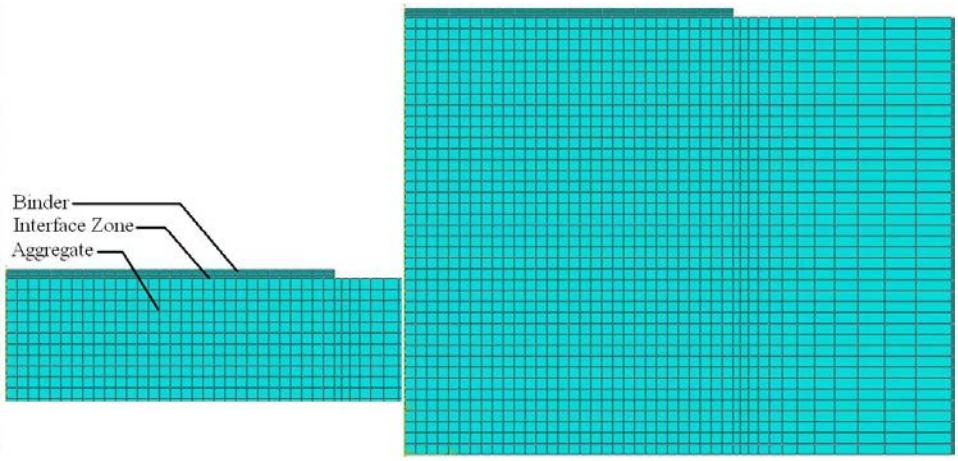

Figure 6.2. Finite element mesh.

In these simulations, aggregate particles were assumed as isotropic linear elastic solids with Young's modulus of $E_{agg} = 1GPa$ and a Poisson's ratio of $v_{agg} = 0.16$. The interfacial transition zone (ITZ) was defined at the aggregate-binder interface to distinguish between adhesive and cohesive moisture damage. The ITZ properties were assumed to be weaker than that of the binder.

To calibrate the constitutive relationship based on pull-off experiments, moisture content must be known at the interface. Figure 6.3 illustrates a typical regime of moisture diffusion through the structure after 48 hours of moisture conditioning.

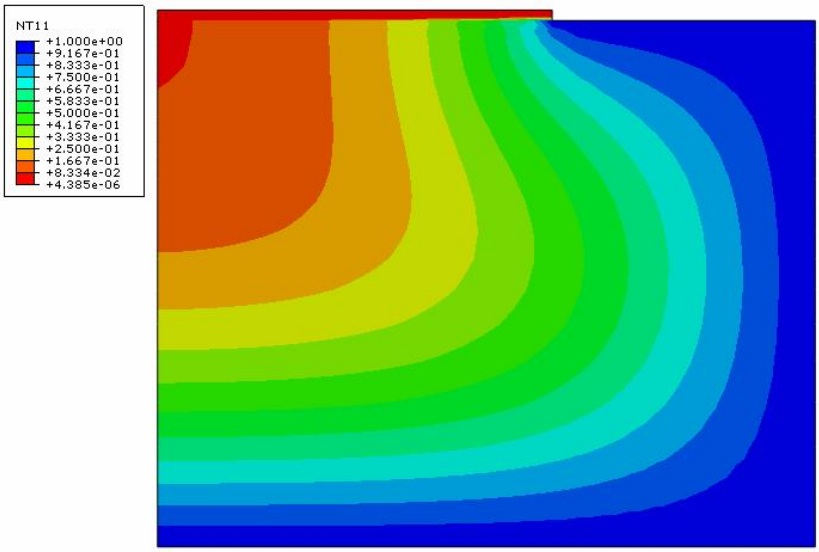

Figure 6.3. Moisture diffusion profile after 48 hours while the moisture is constrained to diffuse from all around the aggregate and not the mastic.

Using the Fick's second law, the moisture content at the aggregate-binder interface was obtained. The moisture damage varible for each conditioning time was calculated from the ultimate uniaxial tensile strength using Eq. (4.4). Since moisture was the sole reason for damage and the only contributor to the effective damage variable, it was assumed that mechanical damage does not evolve during the conditioning period. Integrating the evolution function at the end of each conditioning period implies:

$$\int_0^{\omega} \frac{d\omega^i}{\left(1-\phi_{eff}\right)^q} = \int_0^t k^i \theta(t) dt, \quad i = a, c \tag{6.1}$$

The adhesive moisture damage paramters can be obtained numerically through solving the following equation:

$$\omega_{(t)}^i = 1 - \left[k^i \theta_{(t)} \left(q-1\right) + 1 \right]^{1/1-q}, \ i = a, c \tag{6.2}$$

Figure 6.4 schematically illustrates the calibration procedure for the moisture damage evolution function. Finally, the moisture damage constitutive relationship, which is implemented in the PANDA, was used to calculate the moisture damage variable and the uniaxial tensile strength for varying conditioning times. It should be emphasized that these data were only used for calibration purposes in order to show that the model can predict the resoponse of the moisture conditioned aggregate-binder interface. The pull-off tests cannot be used for model validation because different materials were used in different sets of pull-off test experiments.

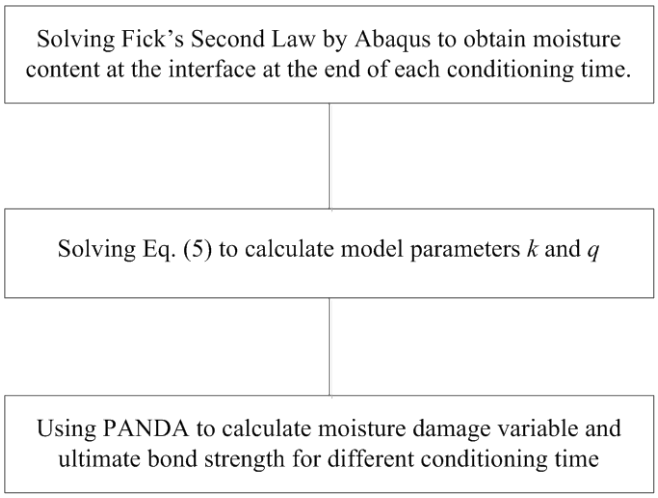

Figure 6.4. The flowchart representing moisture damage model calibration process.

The moisture damage constitutive relationship was first calibrated against the experimental tests reported by Youtcheff et. al. (1997). These tests included pull-off tests for three types of aggregates with one binder, and three types of binders with one of the aggregates. Coupled temperature-displacement analysis was used to calculate the moisture content at the aggregate-binder interface, which is an input for PANDA to obtain the value of moisture damage variable. The moisture damage parameters obtained from the calibration procedure are listed in Table 6.1. Figure 6.5 shows the model prediction of the bond strength versus moisture conditioning time for the set of experimental data reported by Youtcheff et. al (Youtcheff and Aurilio, 1997). The results confirm the capability of the constitutive relationship in simulating the bond strength as a function of the conditioning time.

Table 6.1. Model parameters obtained from model calibration of Youtcheff (1997) experimental work.

		Model parameters	
Binder	Porous material	k (1/min)	q
AAD	Ceramic	0.95	5
AAG	Ceramic	0.051	4
AAM	Ceramic	0.009	3
AAD	Brick	1.83×10^{-4}	3
AAD	Steel	0.0127	8

Figure 6.6 demonstrates a typical evolution of the adhesive moisture damage at the interfaces. It is important to mention that the experimental result in Figure 6.5 demonstarte the reduction of the rate of decay with increase in conditioning time. This effect is refered to as the history effect and the results in Figure 6.6 show that the model can capture it.

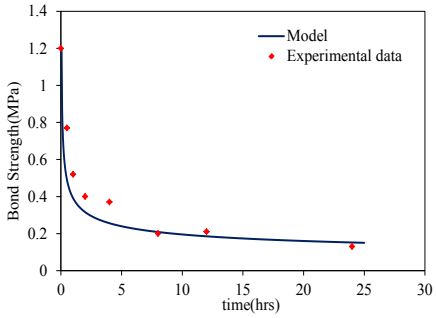

(C1)

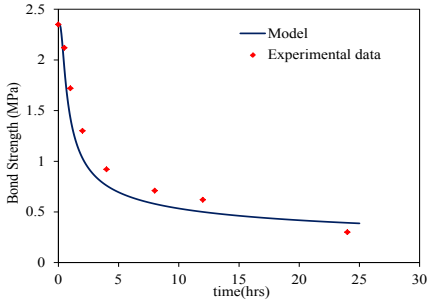

(C2)

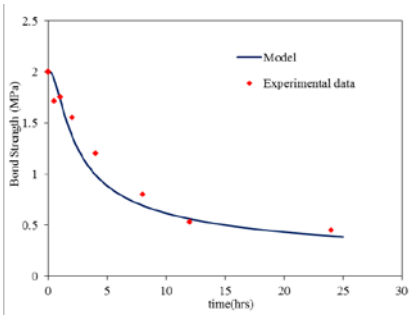

(C3)

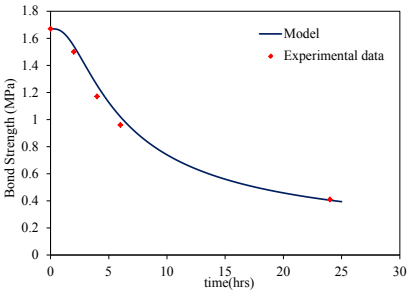

(C4)

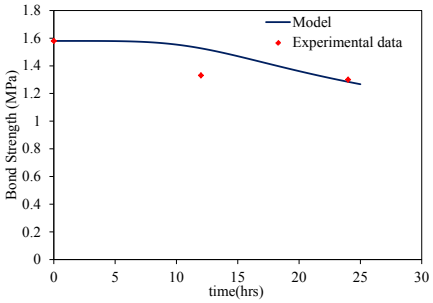

(C5)

Figure 6.5. Comparison between the uniaxial bond strength measurement (C1 to C5) (Youtcheff and Aurilio, 1997) (C1) for combination AAD/ceramic, k_a=0.95 1/min and q=5, (C2) for combination AAG/ ceramic, k_a=0.051 1/min and q=4, (C3) for combination AAM/ ceramic, k_a=0.009 1/min and q=3, (C4) for combination AAD/brick, k_a=0.011 1/min and q=3, (C5) for combination AAD/steel, k_a=0.76 1/min and q=8.

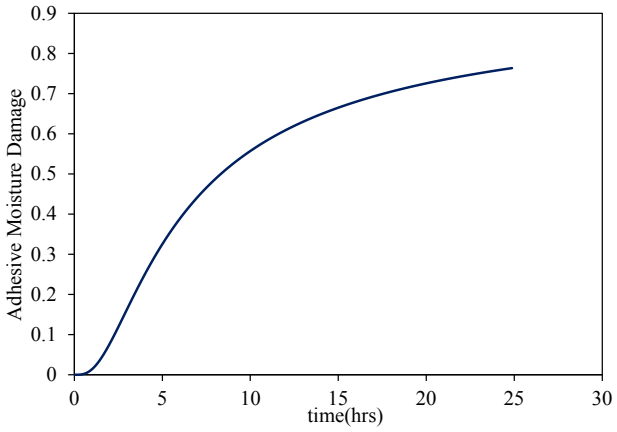

Figure 6.6. A typical evolution of adhesive moisture damage variable versus conditioning time.

Kringos et al. (2008c) performed pull-off tests on six different aggregate-mastic combinations using two types of aggregates (sandstone and granite) and four different types of mastics. . Details of these experiments are described in Table 6.2. Figure 6.7 (C1 to C6) shows the experimental results as compared to the calculated bond strength using the moisture damage evolution function. The parameters calibrated using these combinations are presented in Table 6.3. Model predictions presented in these figures show that the moisture damage evolution function is capable of predicting the degradation of the bond strength as the conditioning time increases.

Table 6.2. The summary of test conditions and results of experiment conducted by Kringos et al. (2008c).

Aggregate Type	Mastic Type			
	I	II	III	IV
Sandstone	Comb2	Comb3	Comb4	Comb6
Granite	Comb1			Comb5

	Mastic Type I	Mastic Type II	Mastic Type III	Mastic Type IV	Sandstone	Granite
Diffusion Coefficient mm2/hr	$0.47\pm0.02\times10^{-3}$	$11.08\pm0.2\times10^{-3}$	$1.31\pm0.04\times10^{-3}$	$1.15\pm0.15\times10^{-3}$	0.72	0.44

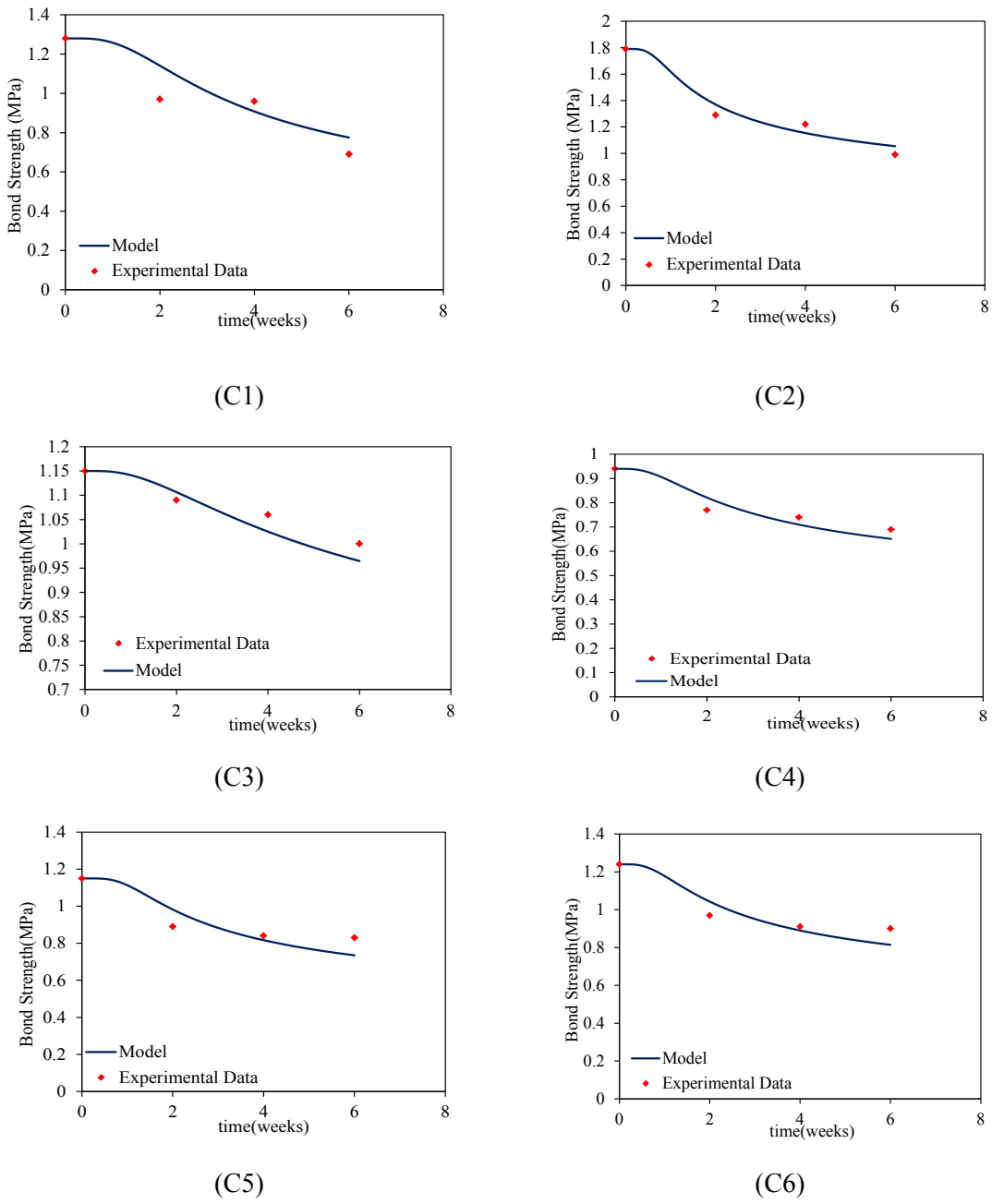

Figure 6.7. Comparison between the uniaxial bond strength measurement (C1 to C6) versus moisture conditioning time for combination 1 to 6 (Kringos et al., 2008c) with obtained model parameters for each combination as; (C1) k_a=0.69 1/week and q=8, (C2) k_a= 0.236 1/week and q=8, (C3) k_a=0.105 1/week and q=8, (C4) k_a=0.638 1/week and q=8, (C5) k_a=0.704 1/week and q=8, (C6) k_a=0.766 1/week and q=8.

Table 6.3. Model parameters obtained from model calibration of Kringos et al. (2008c) experimental work.

	Model parameters	
Combination	k (1/week)	q
1	0.69	8
2	0.236	8
3	0.105	8
4	0.638	8
5	0.704	8
6	0.766	8

The moisture damage constitutive relationship was also calibrated against the pull-off test results reported by Pinto et al. (2009). They used three different additives to investigate the effect of additive type on the maximum adhesive bond strength. Similarly, they used a thin layer of mastic adhered to an aggregate and exposed to moisture diffusion before applying the load. The specimens were conditioned in a water bath for 24 and 48 hours. The moisture diffusivity used for simulating these experiments were 1.6×10^{-4} mm^2/s for aggregate (sandstone) and 2.5×10^{-8} mm^2/s for binder (Kringos et al., 2007).

Figure 6.8 (C1 to C3) illustrates the comparison between model prediction using Eq. (4.3) and test results observed from cases of three different additives. It is clear that moisture damage evolution function successfully predicts the progressive degradation of

the bond strength with increase in the moisture conditioning time. The moisture damage parameters associated with these tests are listed in Table 6.4.

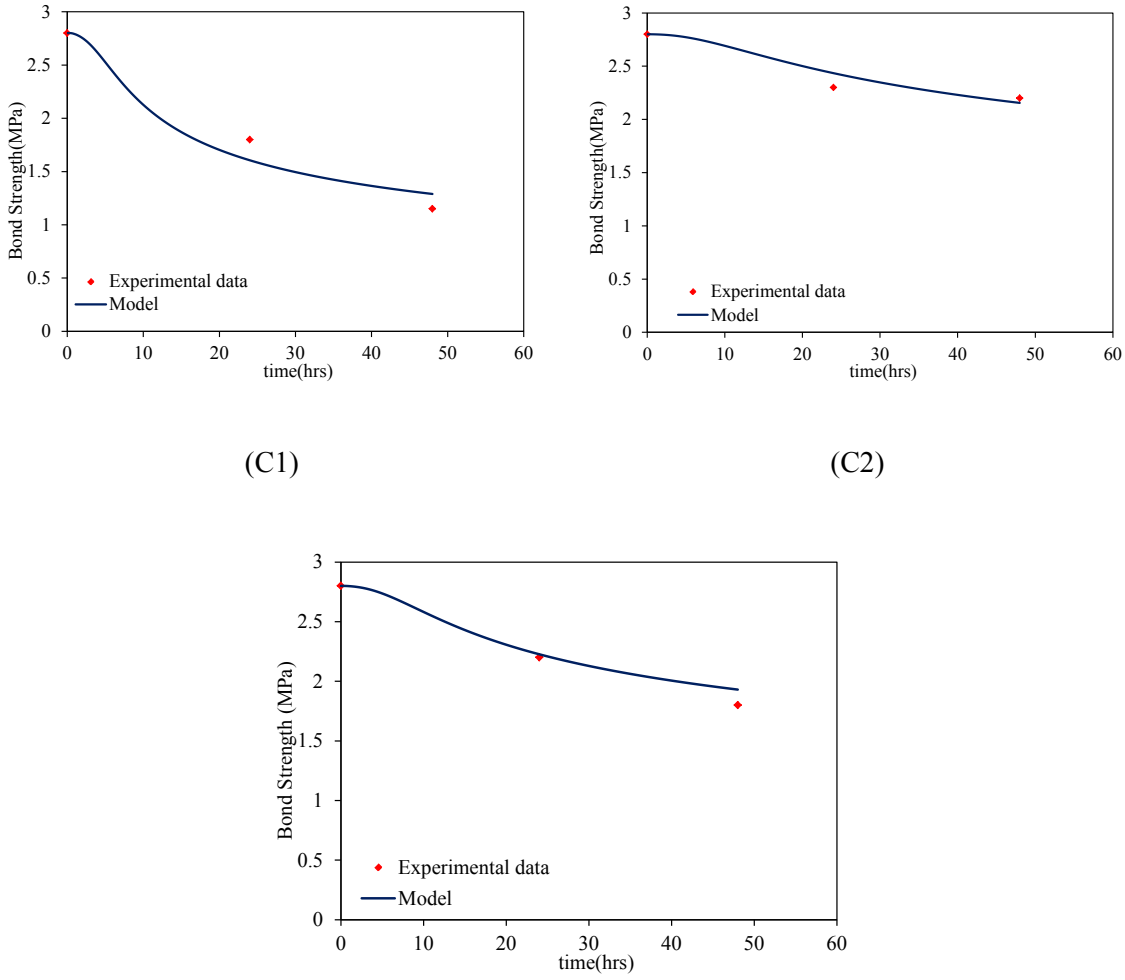

Figure 6.8. Comparison between the uniaxial bond strength measurement (C1 to C3) for the model (Pinto et al., 2009) (C1) without additive, k_a=0.643 1/hr and q=6, (C2) with hydrated lime as an additive, k_a=0.051 1/hr and q=8, (C3) with fly ash as an additive, k_a=0.129 1/hr and q=8.

Table 6.4. Model parameters obtained from model calibration of Pinto et al. (2009) experimental work.

	Model parameters	
additive	k (1/hr)	q
Without additive	0.643	6
Hydrated lime	0.051	8
Fly ash	0.129	8

The computational results confirm that the moisture damage relationship presented in chapter 4 is capable of capturing the degredation in the bond strength as a function of the conditioning time.

6.1.2 Identification of Moisture Damage Constitutive Relationship Model Parameters

The uniaxial constant strain rate tests under tension on moisture-conditioned specimen were used to obtain moisture damage model parameters at 5°C. The modified Lottman (AASHTO, 2007) procedure without freezing was used to moisture conditioned the specimen.

Cylindrical specimens were prepared in laboratory using a Superpave Gyratory Compactor (SGC). The SGC was used to compact 15.2 cm diameter by 17.8 cm height specimens. These specimens were cored and cut to 10 cm diameter by 15.2 cm height. The average air voids percentage of the specimens were 7.0 ± 0.5%. Limestone aggregate and binder PG 67–22 were used to prepare the test specimens. The aggregate

blend includes 30% Type C rock, 36% Type F rock, 24% washed screening, and 10% of manufactured sand. This mixture was used as a surface course with a nominal maximum aggregate size of 19.0 mm. Table 6.5 and Figure 6.9 summarize the sieve analysis and mixture gradation.

Table 6.5. Limestone mixture gradation.

Aggregate Type	Limestone Type C	Limestone Type F	Limestone Washed Screening	Manufactured Sand	Combined Gradation
Individual Percent	30 Percent	36 Percent	24 Percent	10 Percent	
Sieve Size: (mm)	Cumulative Percent Passing	Cumulative Percent Passing	Cumulative Percent Passing	Cumulative Percent Passing	Cumulative Percent Passing
25	100	100	100	100	100
19	98.7	100	100	100	99.6
9.5	21.5	93	100	100	74
4.75	3.4	65.3	99.4	97.4	58.1
2.36	1.4	29	74.8	85.3	37.3
0.6	1.3	8.9	40	64.5	19.7
0.3	1.3	3.8	20	15	8.1
0.075	1	3.6	3.6	2.5	2.8

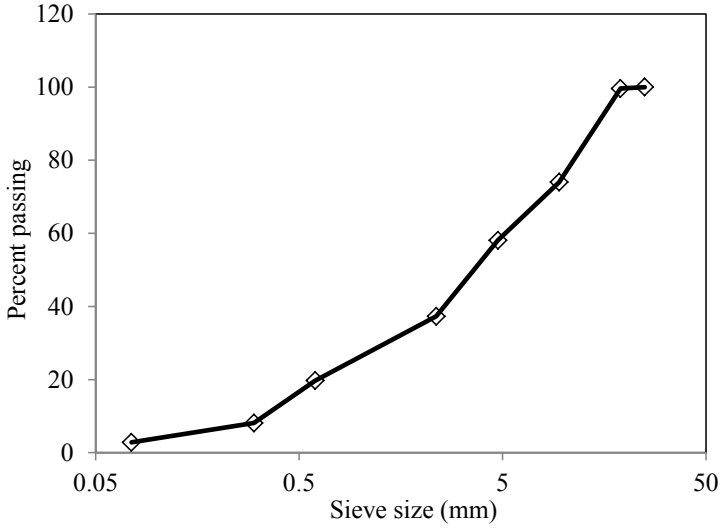

Figure 6.9. Sieve analysis for Limestone aggregate used in the mixture.

In the conditioning procedure, Modified Lottman method, the specimens were placed in a vacuum container supported a minimum of 1 in. (25*mm*) above the container bottom. The container was filled with potable water at room temperature so that the specimens have at least 1 in. (25*mm*) of water above their surface. A vacuum of 10-26 in.Hg partial pressure (13-67*kPa* absolute pressure) was applied for approximately 5 to 10 minutes. The vacuum was removed and the specimen was left submerged in water for approximately 5 to 10 minutes. The degree of saturation was determined based on the weight of the absorbed water for each specimen. The specimens were placed in the water bath for conditioning periods. After conditioning, the specimens were removed and placed in a water bath at 77 ± 1°F (25 ± 0.5°C) for 2 hours ± 10 minutes. The mechanical testing were conducted on the specimens afterwards. The tension stresses and strains associated with each conditioning time were recorded for these experiments.

A constant strain rate test, $1.15\times10^{-5}/mm$, at temperature of 5°C, which has been used to calibrate mechanical damage parameters was used to calibrate moisture damage model parameters in this section.

In order to calibrate the moisture damage constitutive relationship, the thermo-viscoelastic, viscoplastic, and viscodamage model parameters were obtained according to procedure developed by Darabi et. Al. (2012a). These model parameters are tabulated at Table 6.6. FE representations of the experimental tests were constructed in Abaqus (2008). Since the specimens were saturated to a certain level, a predefined moisture contents were defined for them using Abaqus built-in facilities.

The moisture damage varible for each conditioning period was calculated from the ultimate uniaxial tensile strength using Eq. (4.4). Since moisture content is constant through the specimen, the moisture damage evolution function can be integrated at the end of each conditioning period as;

$$\int_0^{\omega} \frac{d\omega}{(1-\omega)^q} = k\theta(t)\int_0^t (1-\phi)^q \, dt \tag{6.3}$$

Table 6.6. Obtained viscoelastic, viscoplastic, mechanical damage, and temperature dependent model parameters.

Viscoelastic model parameters

n	1	2	3	4	5	6	7	8	9
λ_n (Sec^{-1})	11097.551	1116.3292	112.29422	11.295944	1.1362861	0.1143017	0.0114979	0.0011566	0.0001163
D_n (kPa^{-1})	1.108×10^{-5}	2.373×10^{-5}	4.047×10^{-5}	1.002×10^{-4}	2.26×10^{-4}	5.122×10^{-4}	7.229×10^{-4}	3.498×10^{-3}	3.618×10^{-3}
D_0 (kPa^{-1})	5.171E-05								

Viscoplastic model parameters

α	β	Γ^{vp}	N	κ_0(kPa)	κ_1(kPa)	κ_2
0.3	0.25	0.0165	1.026	65	1800	467.18

Viscodamage model parameters

$\Gamma_0^{\varphi}(sec^{-1})$	Y_0(kPa)	q^m	k^m
5.16×10^{-22}	1000	3.24	-2.47

Viscoelastic-viscoplastic temperature-dependent parameter

Temperature (°C)	a_T	g_0
20	1	0.43
40	0.02	1
55	0.0006	5.7

Knowing the mechanical damage model paramters and calculating it at each time step, the moisture damage paramters can be obtained numerically through solving the following equation:

$$\omega_{(t)}^{i} = 1 - \left[k\theta_{(t)}(q-1) + \int_0^t (1-\phi)^q \, dt \right]^{1/1-q} \tag{6.4}$$

Eq. (6.4) was solved numerically to find model parameters associated with moisture damage evolution function. The obtained model paramters are $k = 3.1\times10^{-4}$

$/kPa$ and $q = 10$. Finally, the moisture damage constitutive relationship, which is implemented in the PANDA, was used to calculate the moisture damage variable and the tensile stress-strain response. Figure 6.10 illustrates the comparison between the obtained stress-strain using PANDA and test results. The obtained model parameters from uniaxial constant strain rate test were used to validate the proposed moisture damage constitutive relationship through predicting different creep-recovery tests.

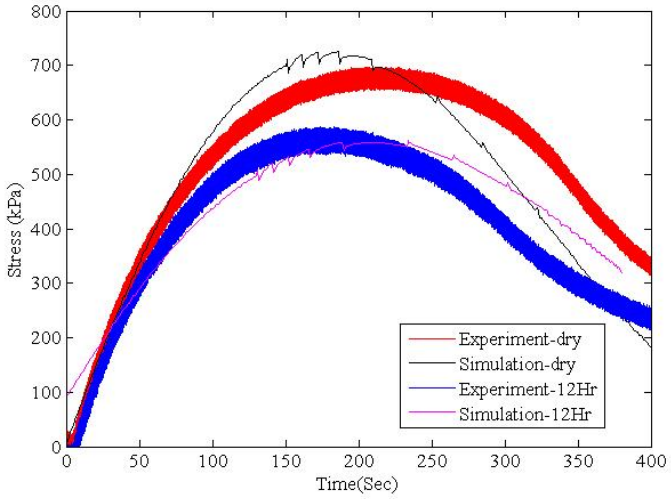

Figure 6.10. Comparison between experimental and simulation stress versus time results for dry and 12 hours conditioning time at constant strain rate test under tension.

6.2.Validation of the Moisture Damage Constitutive Relationship

The identified model parameters for moisture damage constitutive relationship obtained from uniaxial constant strain rate tests were used to predict mechanical response of

moisture-conditioned asphalt concrete specimens. The same material and procedure were used to construct and conditioned the specimens. The ultimate goal of the current work is to develop a unified continuum model for predicting the behavior of asphalt concrete during their service life. However, pavements are subjected to repeated loading during the service life where fatigue damage becomes very important. Therefore, repeated creep-recovery tests over a range of stress levels and loading-unloading times under both tension and compression for moisture-conditioned specimen were used for validation purpose. The obtained thermo- viscoelasticity, viscoplasticity, visco-moisture-mechanical damage model parameters, which are tabulated in Table 6.6, were used for validation purpose.

6.2.1 Repeated Creep-Recovery Test with Various Resting (RCRT-VRT) Time in Tension

The stress level is constant in RCRT-VRT test. This test was conducted at 19°C with 750 kPa stress level. The confinement level is equal to zero in this test. As shown in Figure 6.11, a cyclic creep and recovery loading history was applied on the specimens. The resting time starts at 0.9s and increases with the factor of 1.2 for the next resting time until it reaches 30s. For the next loading block, the similar resting times were applyed. Figure 6.11 schematically illustrates the applied stress history for the RCRT-VRT test. Each test was conducted on two replicates. The strain response reported in this study is the average of the strain responses obtained from each replicate. Four axial

LVDTs were 90° spaced and mounted on the specimen to capture axial strain responses during this test. Figure 6.12 shows the experimental testing setup.

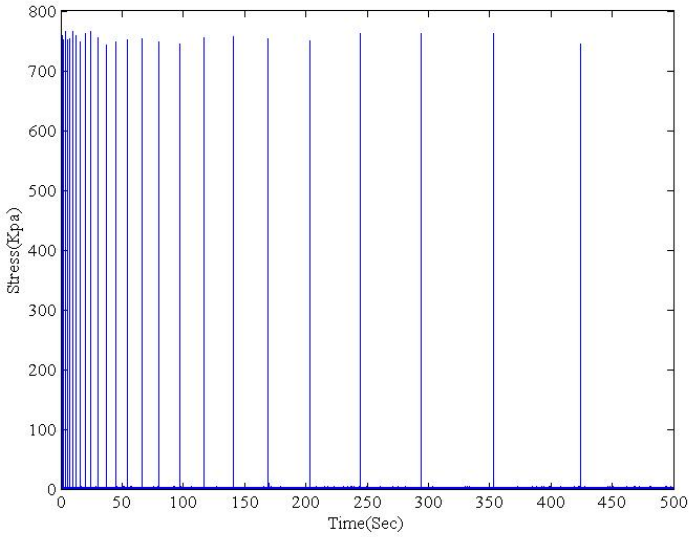

Figure 6.11. Stress input for RCRT-VRT experiment.

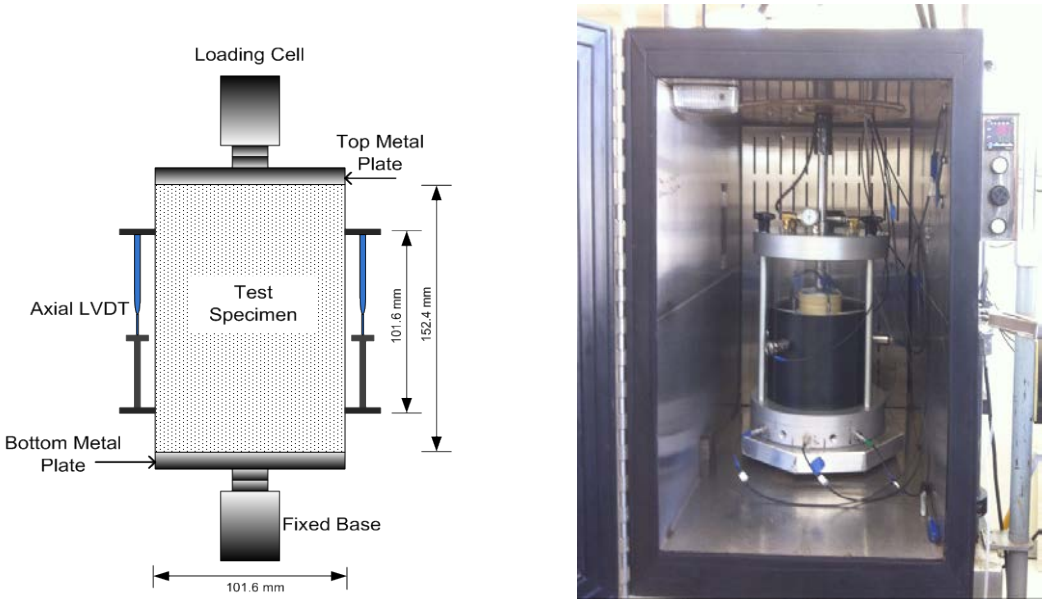

Figure 6.12. Experimental testing setup. (a) Schematic view of test specimen with mounted axial LVDTs. (b) Tri-axial cell equipped with radial LVDTs inside environmental chamber (Rahmani et al., 2013).

The tests were conducted on a dry and 12 hours conditioning time specimens. Figure 6.13 illustrates the comparison between model prediction and experimental data at dry state. Figure 6.14 illustrates the same comparison focused on time between 50s to 250s. These two figures illustrates that the mechanical constitutive relationships can accurately predict the strain response during loading and unloading.

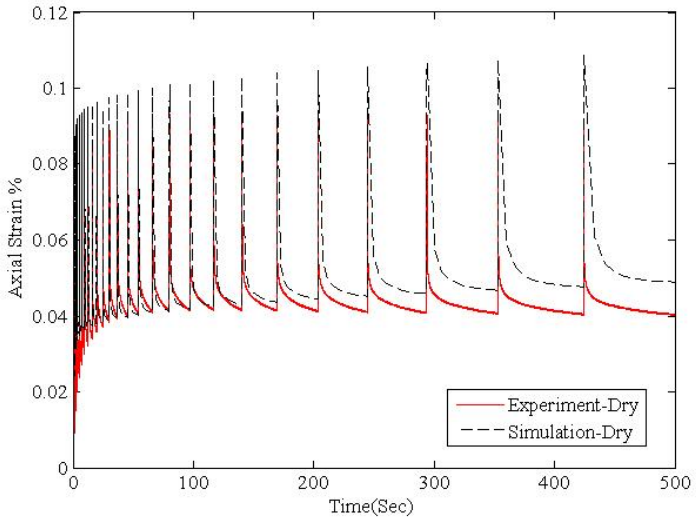

Figure 6.13. Strain versus time response of experimental test and simulation results of RCRT-VRT under tension at 19°C for dry specimen.

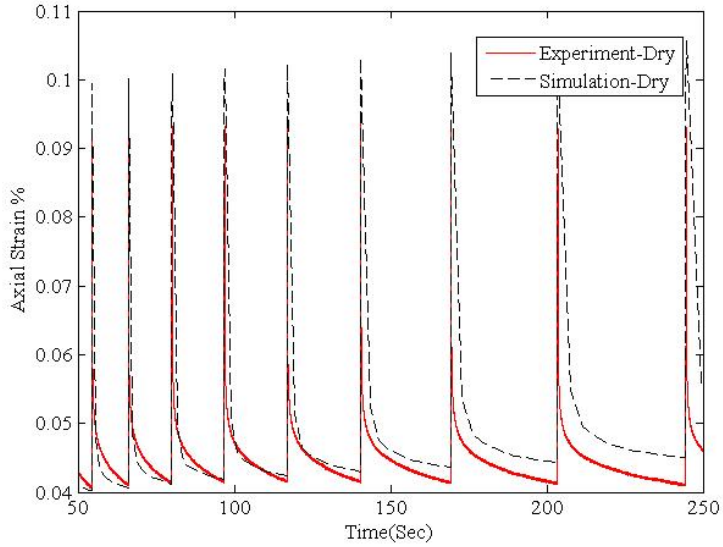

Figure 6.14. Strain versus time response of experimental test and simulation results of RCRT-VRT under tension at 19°C between 50s and 250s for dry specimen.

Figure 6.15 demonstrates the experiment and simulation strain response for moisture-conditioned specimen. Figure 6.16 illustrates the experiment and simulation results for dry and moisture conditioned specimens and Figure 6.17 demonstrates the same results at the first 100s. These figures clearly demonstrate that the model can predict the strain response of RCRT-VRT test at dry and moisture-conditioned state during loading and unloading. Figure 6.17 declares that the moisture damage constitutive relationship has the capability of predicting increased strain due to moisture degradation effect.

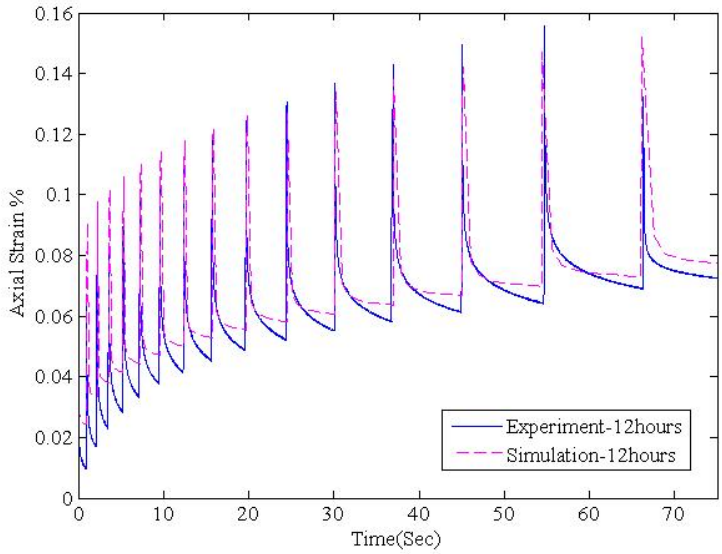

Figure 6.15. Strain versus time response of experimental test and simulation results of RCRT-VRT under tension at 19°C for moisture conditioned specimen.

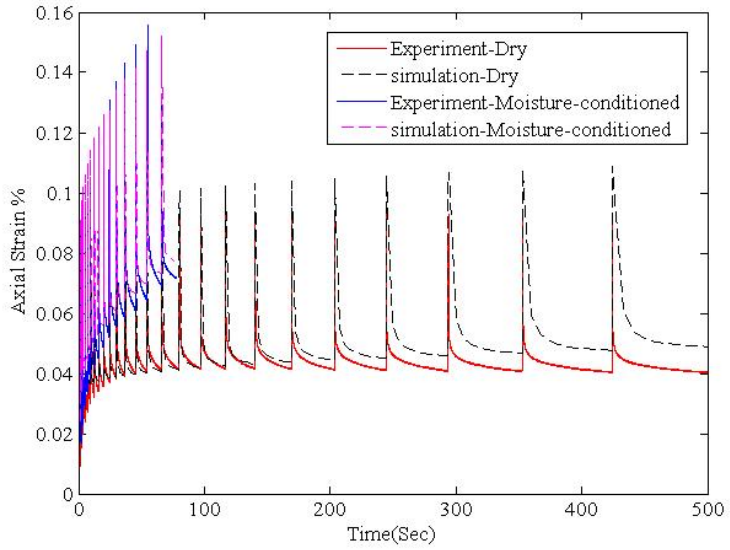

Figure 6.16. Strain versus time response of experimental test and simulation results of RCRT-VRT under tension at 19°C for dry and moisture conditioned specimen.

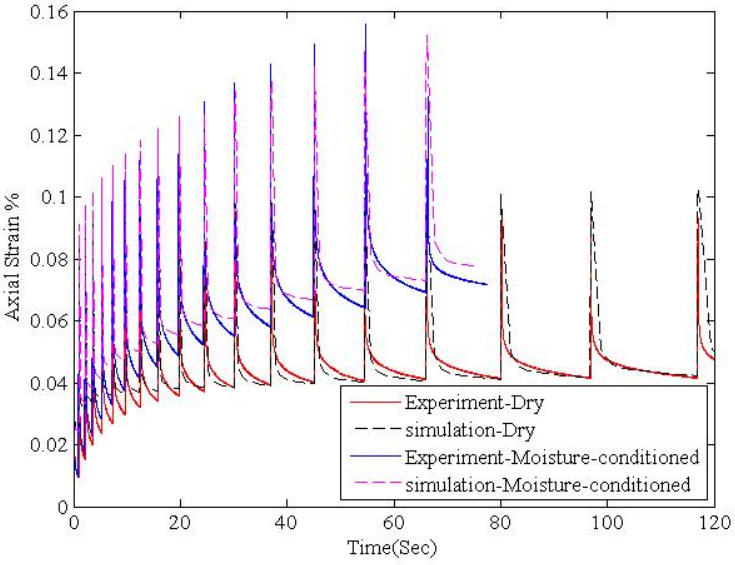

Figure 6.17. Strain versus time response of experimental test and simulation results of RCRT-VRT under tension at 19°C between 0 and 120s for dry and moisture conditioned specimen.

6.2.2 Repeated Creep-Recovery Test with Various Stress (RCRT-VS) Level in Compression

The loading and unloading times were kept constant during the RCRT-VS test. This test was conducted at 55°C with loading time of 0.4s followed by 30s unloading time. The number of loading blocks varies depending on the confinement level at which the test was conducted. Each loading block includes eight creep-recovery cycles with increasing applied axial stresses. This test was conducted in compression 140kPa confinement level, which was kept constant during the test. Specimens were pre-conditioned for 2 hours under the confinement pressure until the strain response reached a constant value. After 2 hours, according to Figure 6.18 the cyclic creep and recovery loading history was applied. The axial stress level starts from 140kPa at the beginning of the first loading block and increases with the factor of 1.2 for the next axial stress until it reaches the last creep-recovery within that block. For the next loading block, the first axial stress level is identical to the third axial stress level in the previous block. Figure 6.18 schematically illustrates the applied stress history for the RCRT-VS test. Each test was conducted on two replicates. The strain response reported in this study is the average of the strain responses obtained from each replicate. Three axial and three radial LVDTs were 120° spaced and mounted on the specimen to capture axial and radial strain responses during this test.

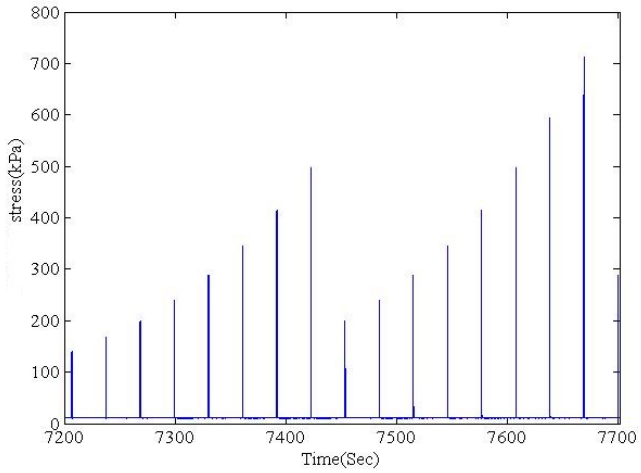

Figure 6.18. Stress input for RCRT-VS experiment.

Thermo- viscoelastic, viscoplastic and visco-moisture-mechanical damage constitutive relationships were used to predict the RCRT-VRT test response. Figure 6.19 illustrates the comparison between model prediction and experimental data for dry and 12 hours moisture-conditioned specimen. Figure 6.20 demonstrates the comparison between experiment and simulation results during time interval of 7100s to 7500s. These figures illustrates that the mechanical constitutive relationships can predict mechanical response of asphalt specimen at dry condition during loading and unloading. The moisture damage constitutive relationship can predict the increase in strain response of asphalt concrete due to detrimental effect of moisture.

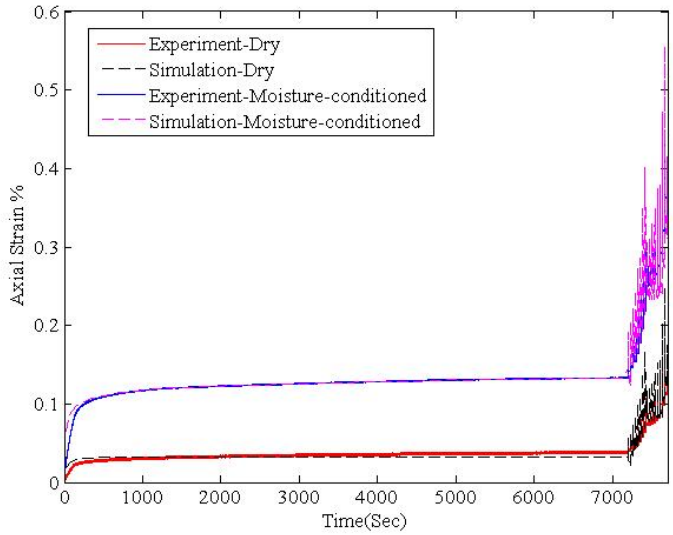

Figure 6.19. Strain versus time response of experimental test and simulation results of RCRT-VS under compression at 40°C for dry and moisture conditioned specimen.

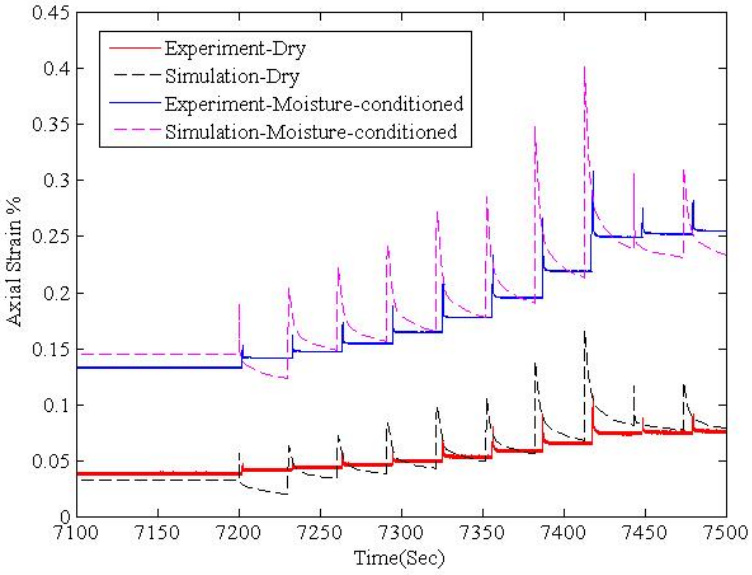

Figure 6.20. Strain versus time response of experimental test and simulation results of RCRT-VS under compression at 40°C between 7100s to 7500s for dry and moisture conditioned specimen.

7. CAPABILITIES OF MOISTURE-MECHANICAL DAMAGE CONSTITUTIVE RELATIONSHIPS

The aim of the research documented in this chapter was applying the developed constitutive relationship and framework to predict the various distresses in pavements during their service life due to moisture-induced damage. First, the capabilities of the developed moisture induced damage constitutive relationship are presented through a parametric study. Then, the implemented constitutive relationship is used to simulate the permanent deformation in moisture-conditioned pavement due to a pulse and moving load in 2D and 3D representation of asphalt pavement.

7.1 Capability of Moisture Damage Constitutive Relationship

This section first investigates the effect of moisture damage model parameters on the adhesive or cohesive bond strength. Then, it shows the proposed moisture damage constitutive model capabilities through a cyclic moisture-conditioning-drying simulation. The results confirm that the explicated model in this work is time-dependent and is capable to consider the history effect and the irreversibility of moisture damage.

7.1.1. Behavior of Moisture Damage Evolution Function

A two-dimensional plane strain coupled diffusion-displacement element with reduced integration point was used for these simulations and normalized moisture content were applied in place of mass. No mechanical loading was applied in this part of the analysis

in order to demonstrate the moisture damage constitutive model behavior more clearly. The moisture damage evolution function was assumed the same for the adhesive and cohesive moisture damage. The moisture diffusivity was assumed to be 0.001 mm/s and the initial bond strength to be 1.0 *MPa*. The viscoelastic model parameters obtained by Darabi et al. (2011a) were used in this study. A moisture content was assumed at the top of the element, and moisture was allowed to diffuse with time throughout the element.

Effect Of Moisture Content and Moisture-Damage Evolution Function's Parameters on the Evolution of Adhesive/Cohesive Bond Strength, Different moisture content levels and various range of model parameters associated with the moisture damage constitutive model were employed to scrutinize their effect on moisture damage variable evolution and bond strength. Figure 7.1 illustrates the effect of moisture content level on the evolution of the moisture damage variable and the associated bond strength. It is clear that a higher moisture content during the same period of time leads to a higher moisture damage variable and less bond strength. Figure 7.1 indicates how the moisture presence inside the material weakens its properties. It illustrates that at lower moisture content levels the rate of damage increase is almost constant because the damage level is low and consequently the damage history effect is negligible. Therefore, the bond strength reduces at a constant rate. At higher moisture content levels the rate of damage evolution increases and then gradually decreases since the damage history effect becomes noticeable. Figure 7.1 clearly demonstrates the effect of moisture content level as well as damage history in the constitutive model response.

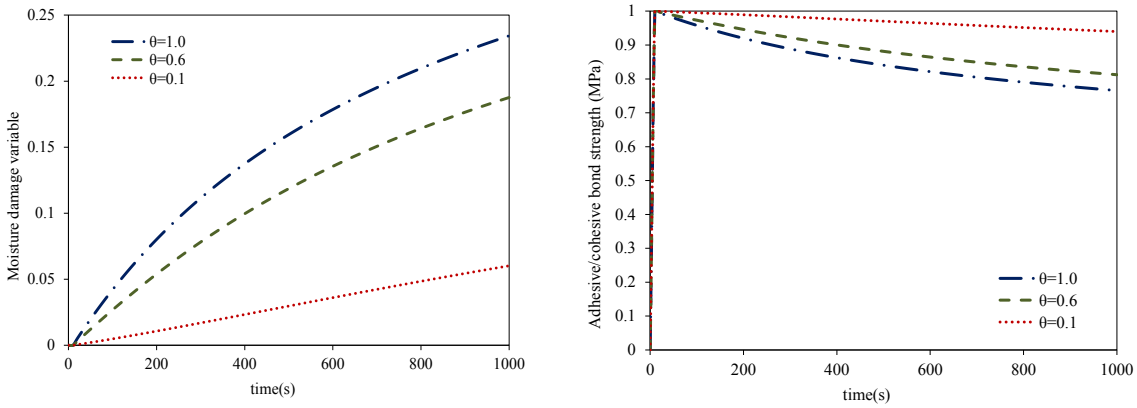

(a) (b)

Figure 7.1. Effect of the different moisture content on (a) moisture damage variable and (b) bond strength ($k = 0.001$ /sec and $q = 8.0$).

Figure 7.2 illustrates the effect of model parameters associated with the moisture damage constitutive model, Eq. (4.3), on the evolution of the moisture damage variable. Figure 7.2(a) demonstrates the effect of k on the moisture damage variable while the moisture content is equal to 1.0 on top and q is 8.0. It illustrates that moisture damage increases with increasing this coefficient, which is controlling the degradation rate due to moisture. This parameter directly controls the rate of damage evolution and consequently the rate at which the material's bond strength degrades. Similar to the previous results, the effect of damage history is clear here. As long as the damage level is low the rate of damage increases gradually. However, the rate of damage decreases as the level of damage increases and the effect of history becomes more distinct. Figure 7.2(b) shows the effect of q while $\theta = 1.0$ and $k = 0.01$. Figure 7.2(b) shows that at lower levels of moisture damage, the damage variable is almost the same for different

values of the moisture damage history parameter q. However, these responses deviate as the level of moisture damage increases illustrating the effect of moisture damage history model parameter q.

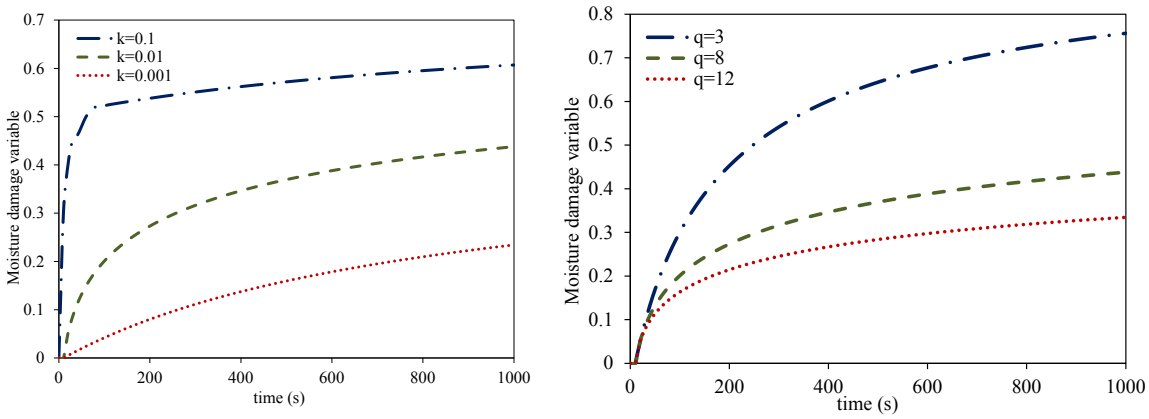

(a) (b)

Figure 7.2. Effect of the moisture damage model parameters, (a) k /sec ($\theta = 1.0$ and $q = 8.0$) and (b) q ($\theta = 1.0$ and $k = 0.01$ /sec) on the moisture damage variable.

Capabilities of Moisture Damage Evolution Function, Cycles of moisture conditioning and drying are applied to the specimen to show that the constitutive model is time-dependent and able to consider the history effect and the irreversibility of moisture damage. The specimen is conditioned for 100s by applying a normalized moisture content equal to one on top of it and then the moisture content inside the specimen kept constant for 500s. Following the moisture-conditioning step, the specimen is dried for 100s and kept dry for 500s. The whole cycle of conditioning and

drying repeats one more time, Figure 7.3(a). Figure 7.3(b) shows the moisture damage evolution, Eq. (4.3), under the explained moisture conditioning and drying processes. This figure compared the proposed constitutive model in this work's result with the typical result obtained from previous developed models (Caro, Masad, Bhasin and Little, 2010, Kringos, Scarpas, Copeland and Youtcheff, 2008). Moisture damage variable increases as an 'S' shape function at the first step by diffusion of moisture through the specimen. The moisture damage variable evolves during the time that the moisture content is constant through the specimen while other models' prediction only evolve with increase of moisture content and stay constant after that. Therefore, the constitutive model in this work can capture the presence of constant moisture content effect inside the asphalt pavement through time and is time-dependent. Figure 7.3(b) shows that upon drying the specimen the damage did not recover through the specimen unlike previous models' prediction. Lost stiffness and strength due to the presence of moisture cannot be fully recovered upon drying. In fact, the material can be partially healed upon drying. Healing effect in the asphalt pavement has been implemented in PANDA. This is a future work to couple the moisture damage evolution and healing effect, as there is no experimental data available to validate this coupling. After conditioning the specimen for the second time, moisture damage variable evolves and becomes greater than its value at the first cycle, since the material is already degraded due to moisture. It is noteworthy to mention that the rate of damage evolution decreases compare to the first cycle. This feature of the model, which mentions as a history effect has also been neglected in the previous available models.

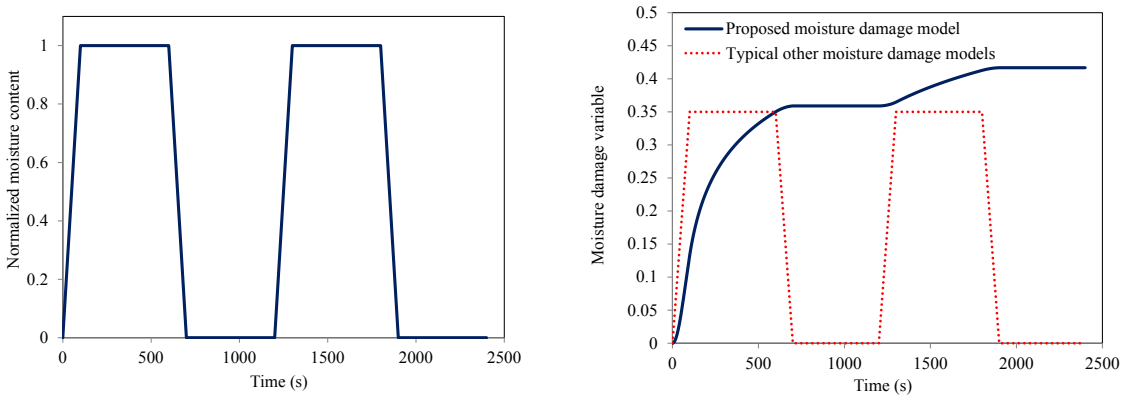

(a) (b)

Figure 7.3. Cycles of moisture conditioning and drying effect; (a) moisture content under the cycles and (b) moisture damage variable obtained from the proposed model and previous models under the cycles.

7.1.2. Effect of Moisture Presence on the Asphalt Concrete's Response

This section investigates the moisture effect on the mechanical response of the asphalt concrete. The same element type and moisture boundary condition used in the previous section is employed here. The investigation is conducted through different examples. First, it evaluates the effect of different moisture content on the mechanical response while a constant displacement rate load is applied on the specimen after specific conditioning time. This part shows that the model considers the effect of moisture content level on the mechanical response of asphalt concrete. Second, a constant displacement rate load is applied to the specimen after different conditioning time to show that the model can capture the effect of conditioning time on the mechanical response. Third is applying cycles of moisture diffusion and loading on the specimen. This type of loading tries to represent a real loading condition on asphalt concrete when

pavement is exposed to cycles of raining and traffic loading during its performance. Finally, last example tries to scrutinize the effect of different moisture content level on the level of permanent deformation of asphalt pavements.

Moisture Content Effect on Mechanical Response, This part studies the different moisture content effect on the mechanical response of asphalt concrete. The specimen was moisture conditioned for 1000s at different moisture content level while k=0.01 /sec and q=8. Then, the load was applied on top of the model at a constant displacement rate of 10^{-4} mm/s. Figure 7.4(a) illustrates the effect of moisture content on the evolution of the effective damage variable. This figure depicts the effect of moisture conditioning on the evolution of the mechanical damage and subsequently the evolution of the effective damage variable. As shown in Figure 7.4, moisture conditioning the specimen at higher levels of moisture content significantly increases the value of the total effective damage density since the material was already aggravated before the load is applied. Figure 7.4(b) shows the stress-strain diagram for this case. Moisture content degrades the material and causes more damage. This causes lower stress level for aggravated material. These figures demonstrate that the model can capture the impact of distress caused by a given moisture state at a given time on the effective damage and the total stress-strain response of material.

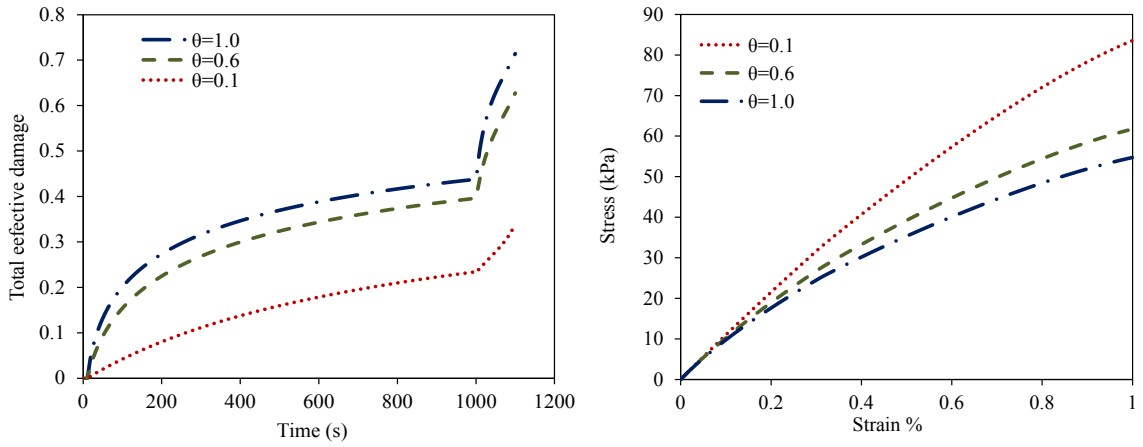

(a) (b)

Figure 7.4. (a) Effect of moisture content on the total effective damage while mechanical load is applying, (b) Effect of moisture content on the stress-strain response (k =0.01 /sec and q =8).

Moisture Conditioning Period Effect on the Mechanical Response, It has been argued that this model is capable of considering the effect of moisture conditioning time. Therefore, the simulations were repeated when the specimen was pre-conditioned at a constant moisture content of 0.5 but for three different conditioning periods, t=100, 600, and 1000s. The load was applied after the respective conditioning time for 100s. Similarly, k =0.01 /sec and q =8 were assumed for these simulations. Figure 7.5(a) shows the effective damage density for three cases. It demonstrates that the material was degrading at constant moisture content. Figure 7.5(b) shows the decrease in the stress level of the material due to moisture damage. These figures clearly illustrate that the model can take into account the moisture conditioning time effect. This means that at

constant moisture content the material is weakened over time, which most of the continuum existent model cannot consider.

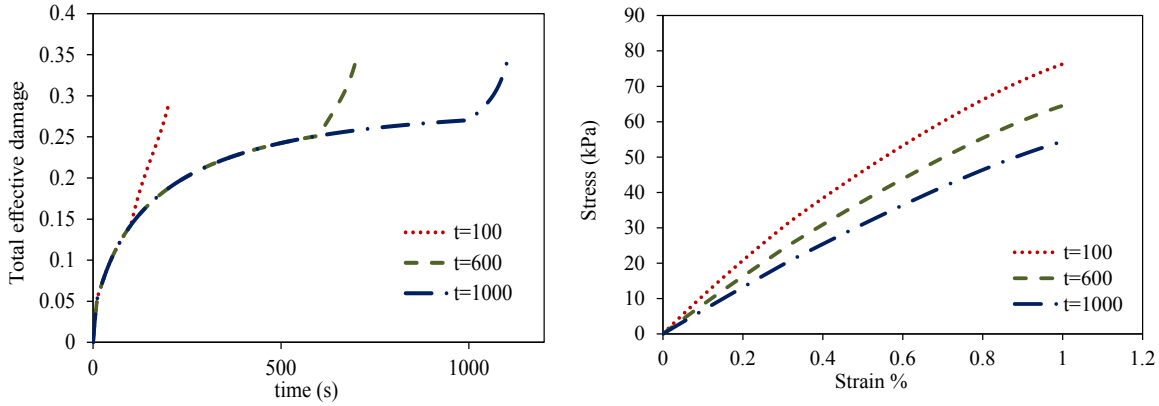

(a) (b)

Figure 7.5. (a) Effect of moisture conditioning time on the total effective damage while mechanical loading is applying total time, (b) Effect of moisture conditioning time on the stress-strain response (k =0.01 /sec and q =8).

Moisture Conditioning and Drying Cycles Effect on the Mechanical Response, Asphalt pavements are exposed to million cycles of moisture conditioning, drying, and traffic loading. To predict the behavior of asphalt pavement, it should be modeled under this realistic loading condition. A parametric study was conducted to show that the model is able to capture the effect of cycles of moisture diffusion and loading/unloading on the specimen. The similar specimen as used in the previous parts exposed to 10 cycles of 1000s moisture conditioning and 10s of loading. The load is applied to the specimen in two different ways, constant displacement rate and constant load. Moisture

was allowed to diffuse through the specimen for 1000s after which a 10s load and unload applied. These two steps repeated 10 times sequentially. Since the moisture diffusion is a slower process than the mechanical loading cycles, in the analyses the specimen was conditioning to cycles of 1000s of moisture diffusion. Moisture damage model parameters as k =0.01 /sec and q =8 were assumed for these simulations.

Figure 7.6 illustrates stress response of the material under cycles of loading and unloading for dry and cyclic conditioning cases. The load is applied on the specimen at a constant displacement rate of 0.001 *mm/s*. Blue lines represent the stress responses under cycles of moisture diffusion, 1000s, loading, 10s, and unloading, 10s, while red line shows the stress responses under cycles of loading and unloading without moisture conditioning. Figure 7.6(a) shows the stress versus time results. This figure clearly illustrates the degradation of the stress resistance of the specimen with increasing number of conditioning and loading cycles. Figure 7.6(b) demonstrates the stress response of the specimen at the third cycle. This figure obviously shows that the material strength reduces under cycles of moisture diffusion and loading. It illustrates that the model is capable of predicting the reduction in bond strength of the material under cycles of moisture diffusion and mechanical loading. Figure 7.6(c) represent the stress-strain diagram under this cyclic loading. It demonstrates that the stress-strain response is constant under cyclic loading at dry condition while damage was not considered. Although, the stress resistance of the material reduces as the moisture diffuses through the material through cycles of conditioning.

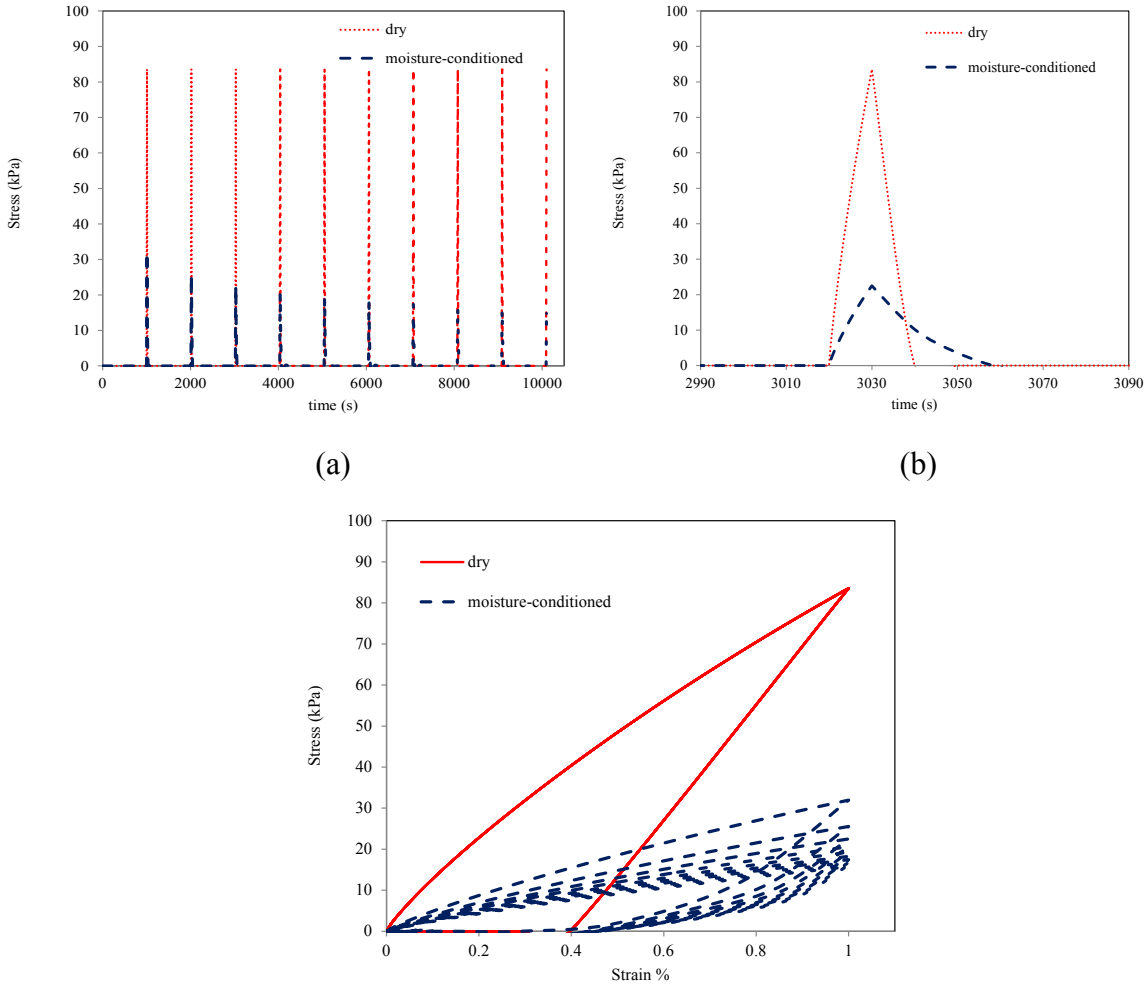

Figure 7.6. Stress response under cycles of loading and unloading (as a constant displacement rate of 0.001 *mm/s*) for dry and moisture conditioned cases (a) Stress vs. time for 10 cycles, (b) Stress vs. time at the third cycles, and (c) Stress-strain diagram.

Figure 7.7 shows strain results while the specimen was exposed to cycles of moisture diffusion, loading, and unloading as a constant pressure on it. The stress was applied on the specimen as a constant pressure 100*kPa*. Similarly blue lines represented results associated to the moisture conditioned case and red lines represented dry case.

Figure 7.7(a) shows the strain versus time for 10 cycles of loading. This figure clearly illustrates that the strain increases with increased number of cycles of diffusion and loading. Figure 7.7(b) demonstrates the strain results at the third cycle of loading. This figure demonstrates that the model is able to consider the coupled effect of moisture and mechanical loading. These results prove that the presented framework and approach can simulate the effect of moisture and mechanical loading and their coupling at the same time.

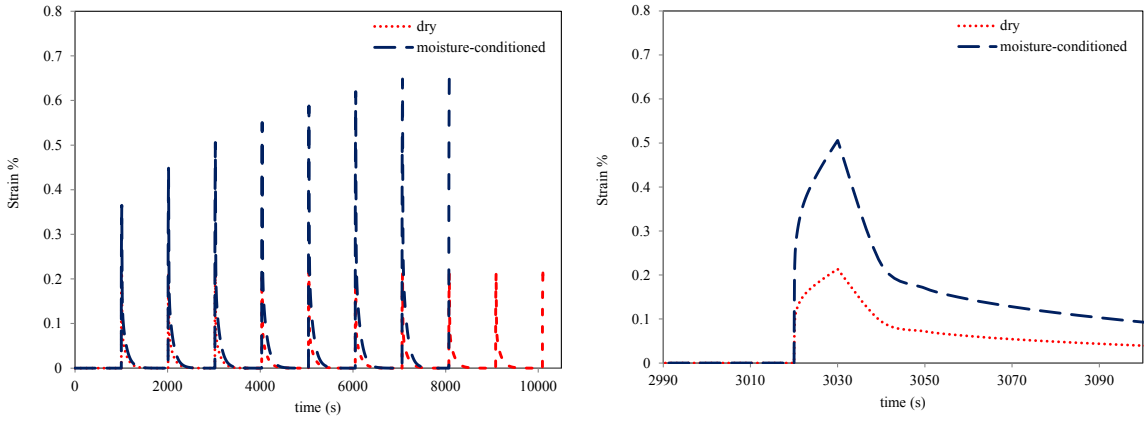

(a) (b)

Figure 7.7. Strain response under cyclic loading and unloading (as a constant pressure of 100kPa) for dry and moisture conditioned cases (a) Strain vs. time for 10 cycles and (b) Strain vs. time for the third cycle.

7.1.3. Effect of Pore Water Pressure on the Asphalt Concrete's Response

This section tries to investigate the effect of pore water pressure on the mechanical response and damage distribution of an asphalt concrete. Since pore water pressure acts

as an extra stress on the surrounding of pores, a very simple FE micromechanical representation of asphalt concrete was constructed to study the effect of pore water pressure on the mechanical response of asphalt concrete. The FE representation consists of two aggregates, coated with a mastic film and a saturated macro-pore. The aggregate-mastic interface was considered to simulate the effect of adhesive moisture damage. Figure 7.8 illustrates the constructed microstructural representation of asphalt concrete. Figure 7.9 demonstrate the FE mesh of the reconstructed microstructural representation.

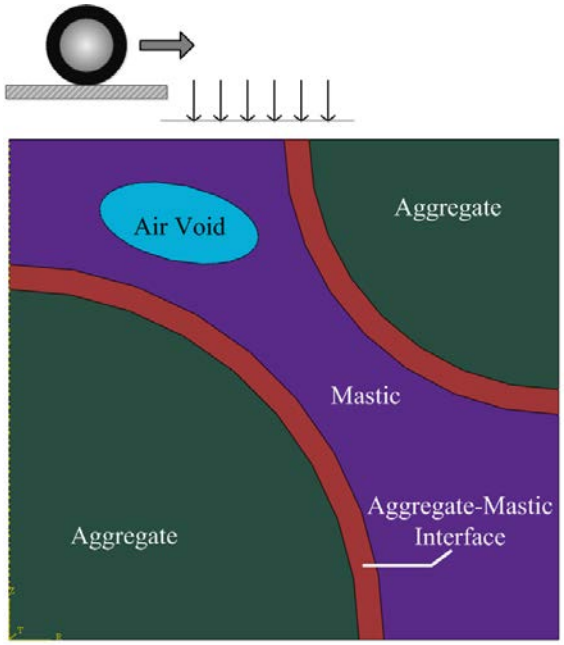

Figure 7.8. A microstructural representation of asphalt concrete consists of two aggregates, mastic, the mastic-aggregate interfaces, and an air void.

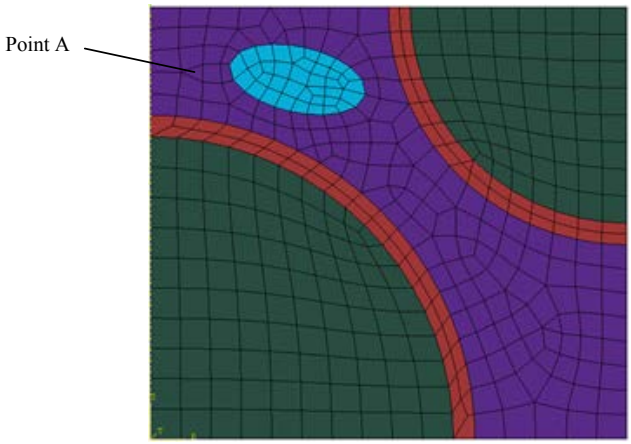

Figure 7.9. The FE mesh of the reconstructed microstructural representation of asphalt concrete.

In these simulations, aggregate particles were assumed as isotropic linear elastic solids with Young's modulus of E_{agg}=1GPa and a Poisson's ratio of v_{agg}=0.16. The viscoelastic and viscodamage model parameters obtained by Darabi et al. (2011a) were assumed to simulate mastic and the interfacial transition zone (ITZ). The ITZ moisture damage properties were assumed to be weaker than that of the mastic. The load was applied on the top edge at a constant displacement rate of 0.001 *mm/s*. Horizontal movement at the left side and vertical movement at the bottom were prevented. Different cases were simulated to study the pore water pressure effect on the mechanical response of asphalt concrete and it's coupling to moisture and mechanical damage. Moisture damage model parameters were assumed as k=5×10^{-4} $/MPa$, q=10, and β =0.001.

In the following the effect of pore water pressure and its coupling to the different response of the asphalt concrete material is investigated through two different cases of simulations.

Case I. Pore Water Pressure Plus Viscoelasticity

Figure 7.10 illustrate the stress distribution through the asphalt representation while asphalt concrete considered as a viscoelastic material. In this case the effect of moisture and mechanical damage were not considered. Figure 7.10 demonstrates the stress distribution through the FE representation when; (a) there does not exist an air void in the mastic, (b) there is a saturated air void but pore pressure effect is not considered, and (c) there is a saturated air void in the mastic and pore water pressure is considered. This figure clearly illustrates that the stress is concentrated around the air void where the pore water pressure is acting on its surrounding. This figures clearly demonstrates that pore water pressure increase the induced stress on the air void's surrounding. The increased stress causes more damage around the air void and decreases the material properties. In the following sub section the coupling between pore water pressure and damage is investigated.

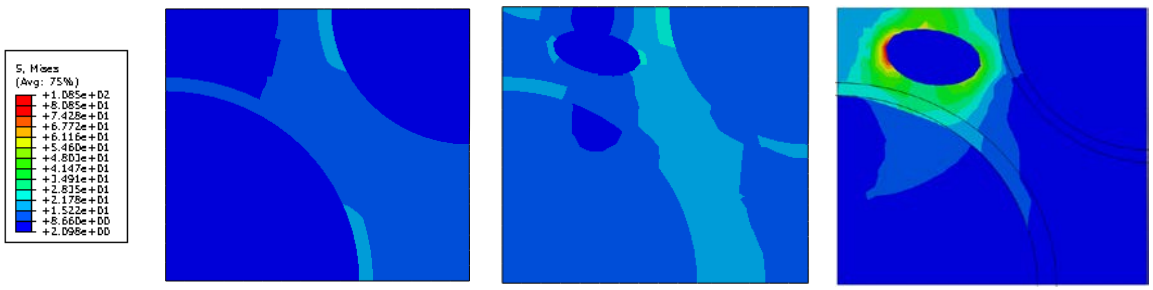

(a) (b) (c)

Figure 7.10. Stress distribution in FE representation of asphalt concrete when; (a) there does not exist an air void in the mastic, (b) there is a saturated air void but pore pressure effect is not considered, and (c) there is a saturated air void in the mastic and pore water pressure is considered.

Case II. Pore Water Pressure Plus Viscoelasticity and Viscodamage

The same example presented in the previous section is used to investigate the coupling effect of pore water pressure and moisture-mechanical damage constitutive relationships. The mastic is assumed as a viscoelastic and viscodamage material. Figure 7.11 illustrates the damage evolution through the FE representation of asphalt concrete when; (a) there is a saturated air void but pore pressure effect is not considered and (b) there is a saturated air void in the mastic and pore water pressure is considered. This figure clearly illustrates that the damage is concentrated around the air void where the pore water pressure is acting on its surrounding. The extra-induced stress by the pore water pressure on the surrounding causes more damage around the air void. The increased stress causes more damage around the air void and decreases the material properties. Figure 7.12 illustrates the mechanical damage variable evolution at point A. This diagram demonstrates how pore water pressure increases the rate of damage evolution around the

air void. Figure 7.13 demonstrates the stress-strain diagram at point A, shown in Figure 7.9. This figure demonstrates how the induced damage due to pore water pressure decreases the ultimate strength of the mastic.

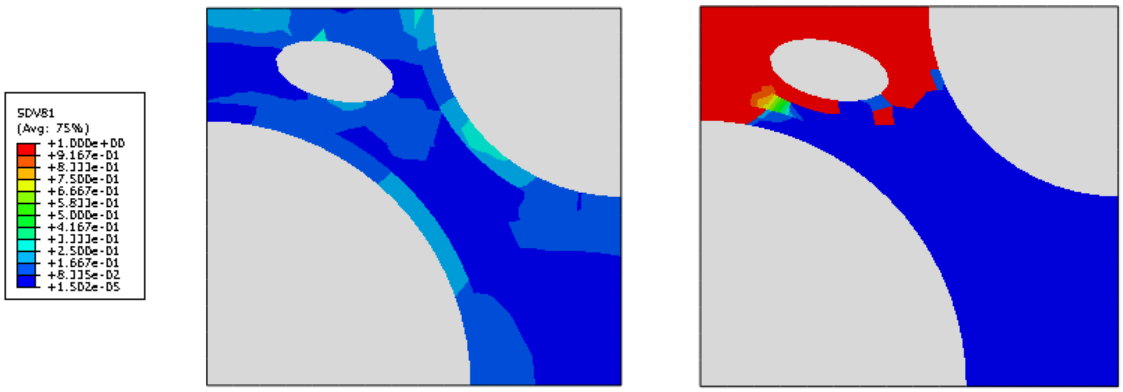

(a) (b)

Figure 7.11. Mechanical damage evolution through the FE representation when; (a) pore water pressure effect is not considered and (b) pore water pressure effect is considered.

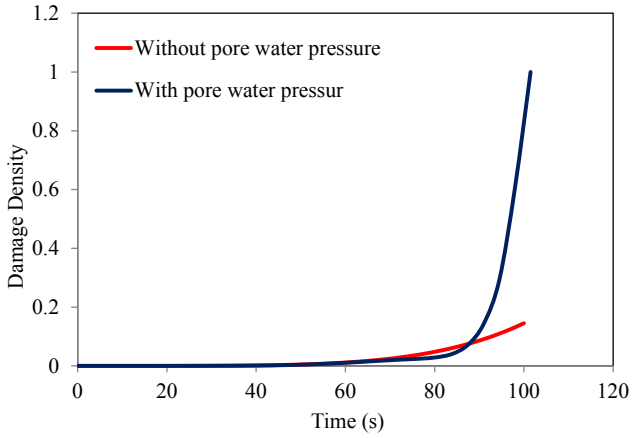

Figure 7.12. Mechanical damage density evolution for two cases of with and without considering pore water pressure effect at point A.

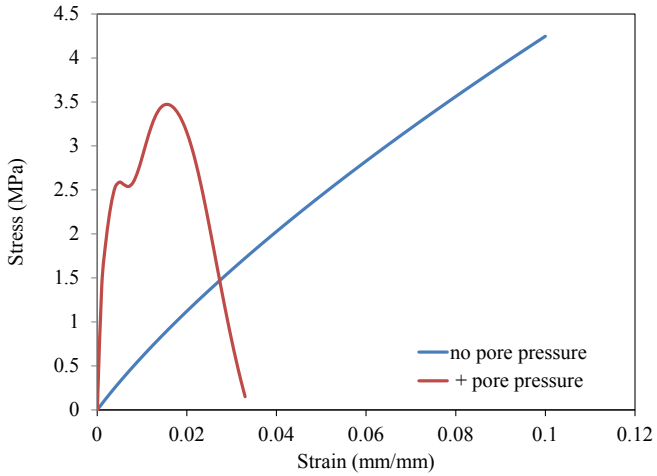

Figure 7.13. Stress-strain evolution for two cases of with and without considering pore water pressure effect at point A.

Existence of an air void close to the aggregate is known to cause severe moisture damage through an asphalt concrete. This happens due to the effect of pore water pressure on its surrounding. Pore water pressure induced extra stress and therefore more mechanical damage on its surrounding. The coupling effect of increased mechanical damage and moisture damage at the aggregate-mastic interface causes the severe degradation of interface leading to separation of aggregate from the mastic. To investigate this effect, another finite element representation of asphalt concrete similar to the previous one was constructed. An air void is located with a different angle and closer to the interface in this FE representation. Similar material properties, loading, and boundary conditions were used for these simulations. Figure 7.14 and Figure 7.15 illustrate the stress and total damage distribution through the constructed FE representation with and without considering the effect of pore water pressure. Figure 7.14(b) demonstrates the concentration of stress around the saturated air voids

when the effect of pore water pressure is considered. Figure 7.15(b) clearly illustrates the evolution of damage through the mastic-aggregate interface due to the induced extra mechanical damage and its coupling to the moisture damage.

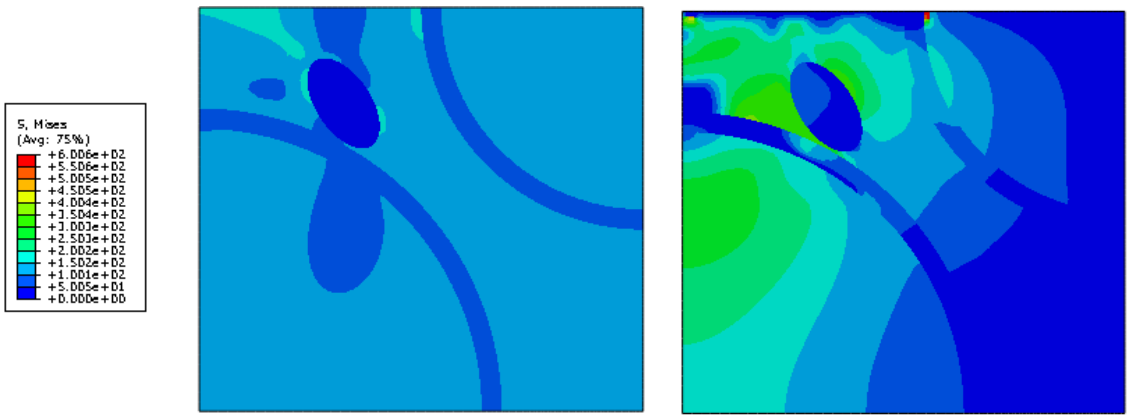

(a) (b)

Figure 7.14. Stress distribution in FE representation of asphalt concrete for two cases of (a) without and (b) with considering pore water pressure effect.

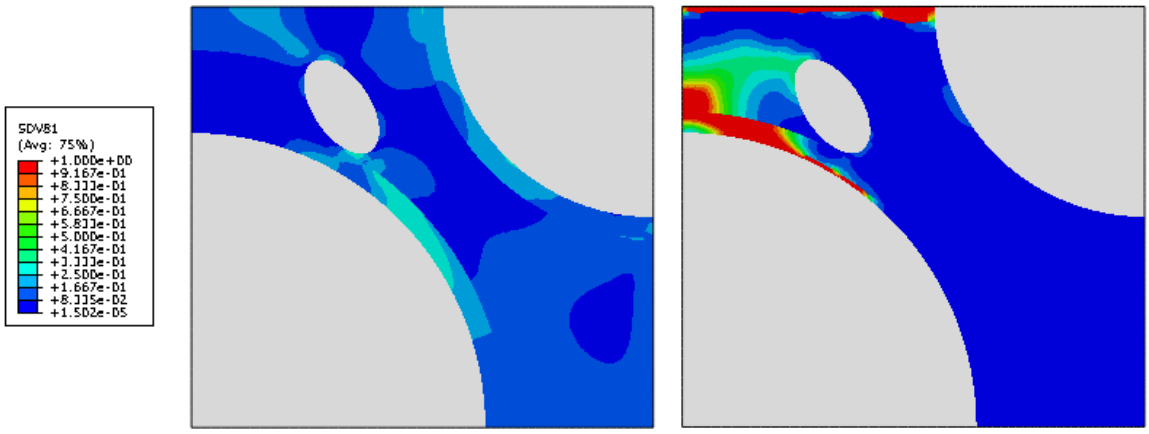

(a) (b)

Figure 7.15. Damage distribution in FE representation of asphalt concrete for two cases of (a) without and (b) with considering pore water pressure effect.

7.2 Effect of Moisture on the Pavement Performance

The aim of this research was applying the developed constitutive relationship and framework to predict the various distresses in pavements during their service life due to moisture-induced damage. Many studies have concluded that moisture conditioning appears to play a significant role in increase of permanent deformation (Coussy, 2004). Therefore, the focus was on investigating the effects of moisture damage on the permanent deformation (rutting) and fatigue damage performance of asphalt pavements under various moisture conditioning period. However, the complex nature of the applied loading conditions, very large number of loading cycles, and complex constitutive behavior of asphalt concrete material, which include thermo- viscoelastic, viscoplastic, and viscodamage behaviors make the accurate prediction of distresses in pavements a very difficult and challenging task. Even with the current power in computational analysis, conducting 3D finite element (FE) simulations for a pavement subjecting to

millions of loading cycles and considering realistic wheel tracking and environmental loading conditions is almost impossible.

This section used different simplified 2D and more realistic 3D loading techniques to simulate the asphalt rutting. Rutting is one of the most serious distresses in asphalt pavements affecting the pavement performance and service life. Therefore, the accurate simulation of rutting in asphalt pavements is essential for improving their performance and management. The main mechanism of rutting is the accumulation of permanent deformation that increases progressively with increasing number of loading cycles. Therefore, an efficient and realistic loading conditions and material constitutive models that can simulate the pavement rutting performance for a very large number of loading cycles which is developed by Abu Al-Rub et. Al. (Shakiba et al., 2013) has been used to simulate rutting for dry and moisture-conditioned pavement.

The Wheel Tracking Test was used to simulate loading on the pavement. The geometry of the Wheel Tracking Test is illustrated in Figure 7.16.

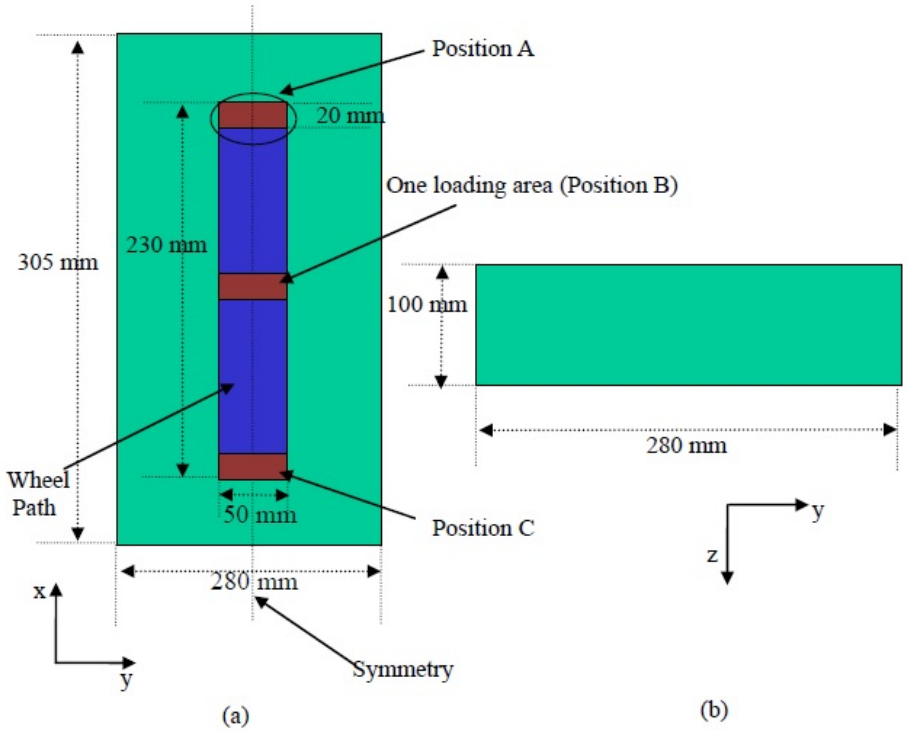

Figure 7.16. The geometry of the simulated Wheel Tracking Test. (a) X-Y plane; (b) Y-Z plane (Shakiba et al., 2013).

The wheel tracking test consists of an asphalt slab of dimensions of 305×280×100 mm^3 in length, width, and depth, respectively. A wheel load is applied at the middle of the slab along the width and moved bake and forth along the length of the slab. The wheel moves with a speed of 40 passes per minute over a wheel path of 230mm length, which is equivalent to a 0.55 km/hr speed. The wheel loading area is assumed as a rectangular shape with dimensions of 20×50 mm2 in width and length, respectively. The employed asphalt layer, dimensions of the loading area, and the wheel speed are from the Wheel Tracking Test conducted by Hunter et al. (2007). The loading

is applied as a step load within each loading cycle. This test can be simulated at both 2D and 3D states.

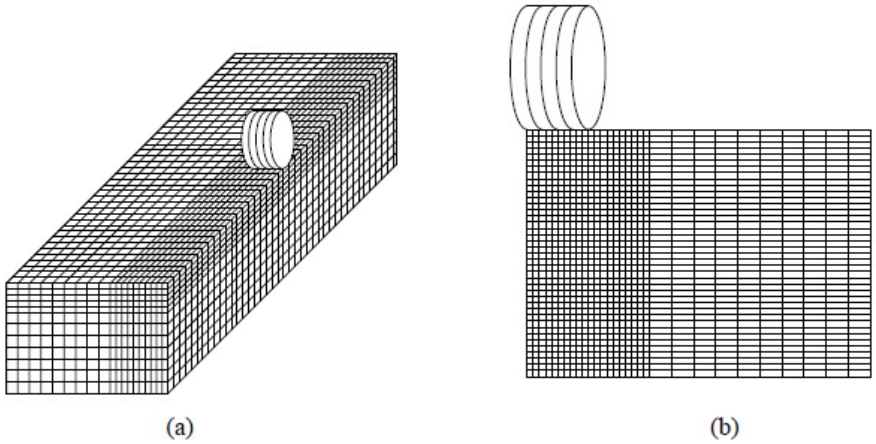

Figure 7.17. The FE mesh in (a) the 3D simulations and (b) the 2D simulations (Shakiba et al., 2013).

The boundary conditions in both 2D and 3D FE models are imposed such that the horizontal direction on the opposite side of the symmetric boundary is fixed; while the bottom of the slab is fixed in the vertical direction. The used element types in the 2D FE simulations in Abaqus are plane strain coupled diffusion-displacement four-node element with reduced integration; whereas, 3D eight-node element coupled diffusion-displacement with reduced integration are used for conducting FE simulations. Moreover, a maximum element aspect ratio of 2 is used for the 2D and 3D elements, respectively. From a convergence study that is not reported here, the constructed 2D and 3D meshes were sufficient to get converged results that are independent of the mesh

density (Abu Al-Rub et al., 2011b). The loading level is 770 kPa and is applied on the top of the asphalt layer. For simplicity, the shape of the applied load is assumed rectangular. Moreover, frictional and tangential loadings from the contact of the wheel with the asphalt top surface are neglected in this study.

The analysis was performed under both dry conditions and with moisture content applied on the top of the structure to represent a rainy day. In both the dry and moist conditions, the viscoelastic-viscoplastic-viscodamage material properties were selected from the study by Darabi et. al. (2011a). The moisture damage model parameters for these simulations were chosen according to the previous parametric study (k =0.01 /sec and q =8).

The magnitude of rutting was calculated numerically by integrating the magnitude of the viscoplastic deformation through the pavement's thickness (Abu Al-Rub et al., 2011b).

$$u_{rutting} = \sum_{i=1}^{k} \varepsilon^{vp(i)} h^{(i)} \tag{7.1}$$

where $u_{rutting}$ is the permanent displacement (rutting), $\varepsilon^{vp(i)}$ is the vertical viscoplastic strain at i^{th} layer through the depth of the asphalt layer, and $h^{(i)}$ is the i^{th} layer thickness.

It should be noted that one would expect different rutting results using plane strain simulations (loading modes 1 and 2) or using their 3D counterparts (loading

modes 7 and 8) comparing to the realistic loading conditions. However, the qualitative comparison of the changes in the results using these simplifications is of great importance in deciding on when to use these simplifications depending on the problem under study.

2D Simulation, In the 2D FE simulations, the loading is applied on an infinite stripe bar along the length of the pavement. This case is simulated using 2D plane strain FE models. Moreover, two loading durations are assumed for each of the cases. The loading duration is the equivalent loading mode. This loading assumption represents the equivalent loading time by accumulating the loading time from all loading cycles and then applying the wheel loading at once in one loading cycle for the period of accumulated time such that the unloading or resting time is neglected. The advantage of this loading model is that only one step loading is applied instead of applying large number of loading steps, and thus reducing greatly the computational cost (Abu Al-Rub et al., 2011b). an equivalent loading cycle of 108.7s was considered for these simulations.

Finite element analysis of a 2D representation of a pavement structure was used in this work to demonstrate the ability of the model to capture the effect of moisture on permanent deformation. Figure 7.18(a) shows the finite element mesh, boundary and loading condition used by Abu Al-Rub et. al. (Abu Al-Rub et al., 2011b; Voyiadjis and Kattan, 1992). This pavement model was subjected to a constant load of $770kPa$. Figure 7.18(b) illustrates the amount of rutting at different moisture content levels. It is

clear that with increasing moisture content the material degrades and the amount of permanent deformation increases. These results show that the model is capable of predicting the permanent deformation of asphalt concrete material under mechanical loading and moisture condition. Figure 7.19 illustrates the moisture diffusion contour through the model, the vertical strain, the mechanical damage contour, and the effective damage contour, respectively, when the normalized moisture content equal to one is applied on top of the model. Figure 7.19(b) demonstrates that the maximum total strain occurs at the top of the middle part of the asphalt layer which is consistent with previous studies (Abu Al-Rub et al., 2011b; Voyiadjis and Kattan, 1992). Also, mechanical damage distribution contour, Figure 7.19(c), shows that the maximum damage occurs at the top of the middle part of asphalt layer, which is exactly the region where the maximum strain occurs. Figure 7.19(d) shows how the moisture damage alters the mechanical damage paradigm causes damage to distribute more through the model instead of concentrating under the load.

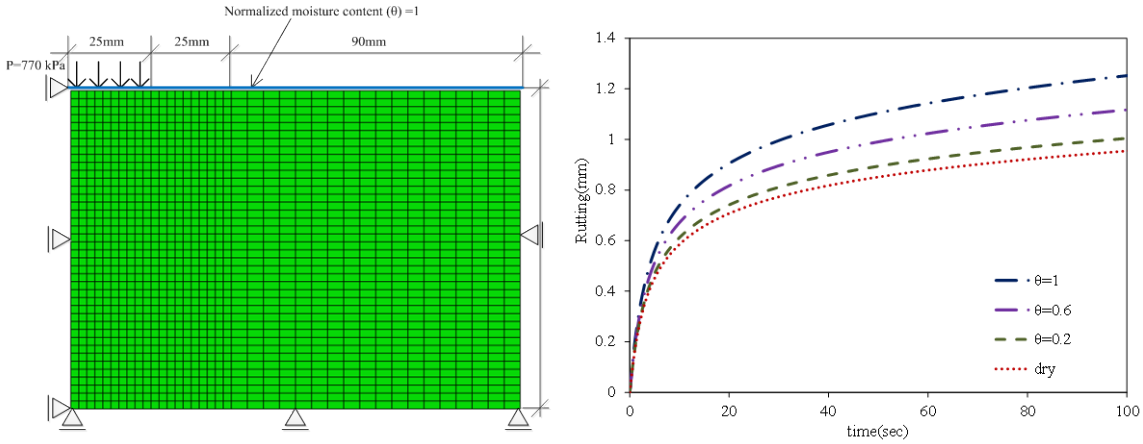

(a) (b)

Figure 7.18. (a) The finite element mesh, boundary and loading condition used for rutting simulations and (b) the amount of rutting under different moisture content (k =0.01 /sec and q =8).

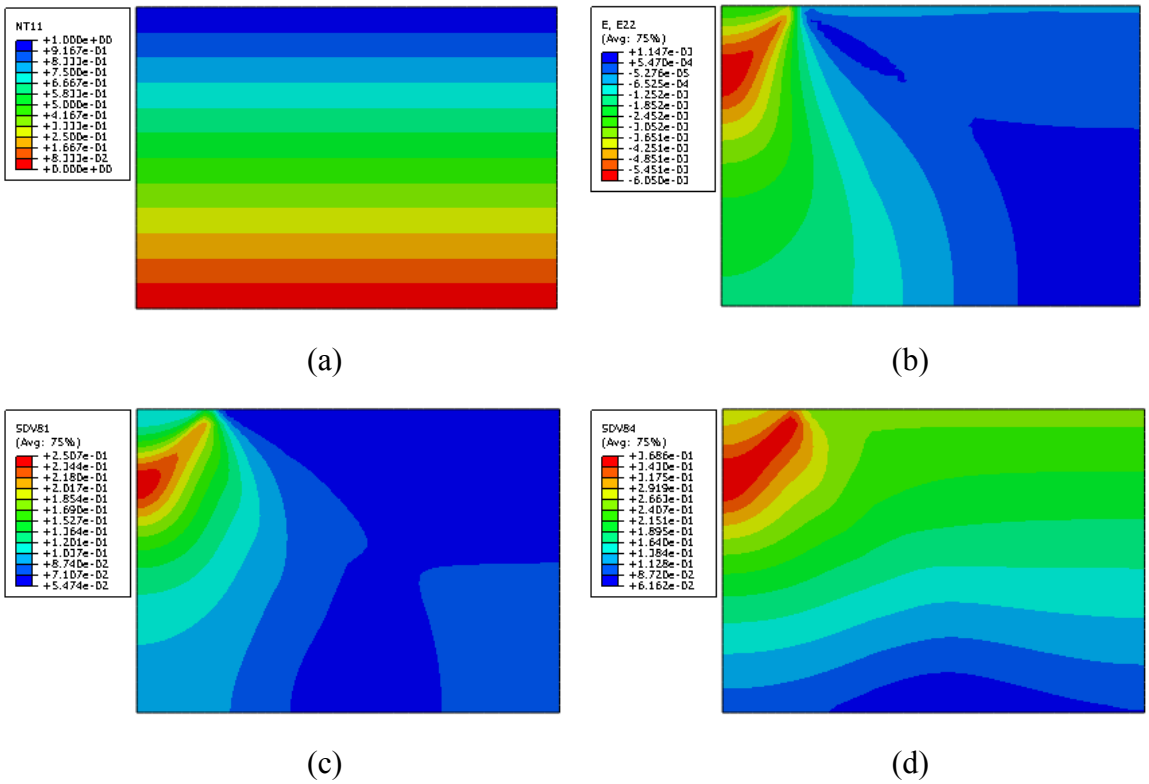

(a) (b)

(c) (d)

Figure 7.19. (a) the moisture diffusion contour through the model, (b) the vertical strain, (c) the mechanical damage, and (d) the effective damage when the normalized moisture content equal to one is applied.

3D Simulations, The moving loading where the wheel movement is simulated by applying the wheel loading on one set of elements (one loading area) was used for 3D simulations. The load at the beginning of the wheel path is located at position A in Figure 7.16. This load remains on the shaded area shown in Figure 7.20(a) for 0.109 sec $(t_2 - t_1)$ and then moving it forward to the next set of elements shown in Figure 7.20(b). The load remains on the same set of elements shown in Figure 7.20 for the same loading duration of 0.109 sec $(t_3 - t_2)$ and then moves to another set of elements shown in Figure 7.20(c) until it reaches to the end of the wheel path (position C in Figure 7.16).

This approach of simulating the moving load is followed in the current study due to its simplicity and the significant reduction in the computational cost as compared to explicitly simulating a real tire with considering dynamic effects.

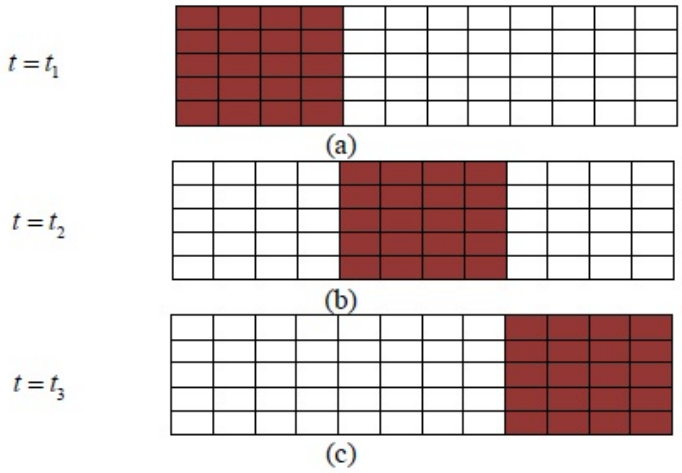

Figure 7.20. A schematic representation of the simplified wheel moving loading scenario. The shaded area is the region at which the wheel load is applied over a set of elements and then moved in the traffic direction to a new set of elements (Shakiba et al., 2013).

In the following, the rutting is only calculated at the center of the slab (position B in Figure 7.16) for the purpose of conducting the numerical comparisons. Figure 7.21 illustrates the amount of rutting for dry and 3days moisture-conditioned asphalt pavement subjected to moving load while $k = 10^{-4}$ /sec and q=10. This figure demonstrate the effect of moisture conditioning the asphalt pavement in increasing the amount of its permanent deformation. Figure 7.22 illustrates the mechanical damage

contour and the total viscoplastic strain contour, respectively, when the normalized moisture content equal to one is applied on top of the model for 3days.

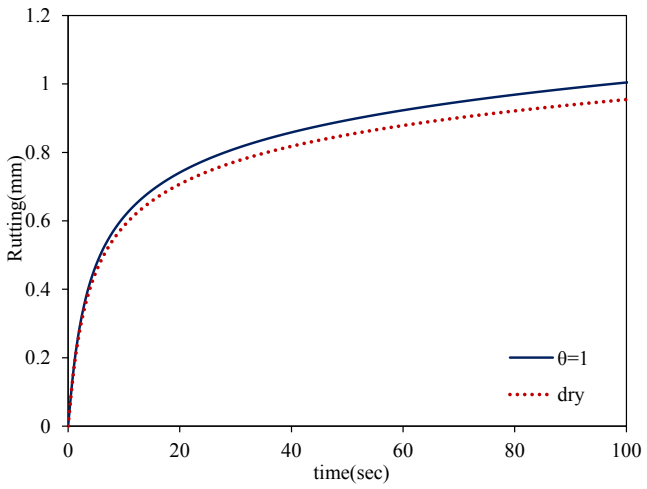

Figure 7.21. The amount of rutting for dry and 3days moisture-conditioned asphalt pavement subjected to moving load ($k = 10^{-4}$ */sec* and q =10).

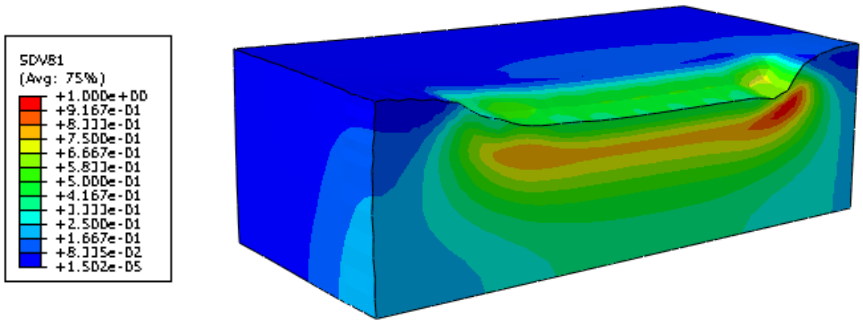

(a)

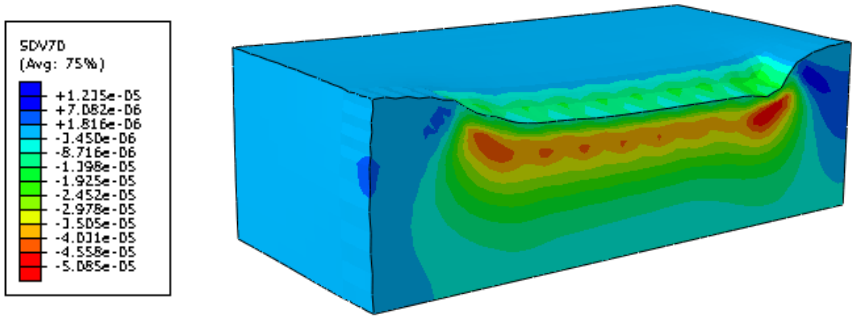

(b)

Figure 7.22. (a) The mechanical damage, and (d) the viscoplastic strain when the normalized moisture content equal to one is applied.

8. SIMULATIONS OF MICROSTRUCTURAL REPRESENTATION OF ASPHALT CONCRETE

The proposed moisture damage evolution function, which is implemented in PANDA, was used in this chapter to conduct micromechanical simulations. Micromechanical simulations provide insights on the effects of microstructural configuration as well as from the properties of the constituents on the overall response of asphalt composite. These simulations can also be used in selecting constituents of asphalt concrete for more sustainable design. The following sections present a procedure to build a FE representation of a typical dense-graded asphalt concrete microstructure. Then, the constructed FE model is used to conduct FE simulations to investigate the moisture effect on the asphalt concrete mechanical behavior.

8.1 Simulation of Two Dimensional Finite Element Microstructural Representations

First, this section will investigate the detrimental moisture effect on the mechanical response of a 2D FE representation of an asphalt concrete. The 2D FE representation as it will be explained in detail comprises of aggregate and mastic, where an interface zone were embedded between mastic and aggregate without defining a cohesive zone element to simulate the adhesive degradation.

8.1.1 Finite Element Representation of Asphalt Concrete Microstructure

An X-ray computed tomography (CT) system was used to capture a 2D image of the microstructure of a typical dense graded asphalt concrete (Abu Al-Rub et al., 2011a). The digitized image consists of 512 by 512 pixels. Each pixel has a gray intensity ranging from 0 to 255, with the lowest value representing black and the highest value representing white. The planar image includes aggregates, mastic, and air voids. A threshold filtering was used to convert this gray-scale image to two different phases: white for aggregates and black for the mastic. This study does not explicitly distinguish binder, fine aggregates, and air voids in order to lower the computational cost. However, an average moisture diffusivity was assigned to the mastic phase in order to implicitly account for fine aggregates as well as the air voids. The FE microstructure accounts for the aggregate-mastic interfaces through defining ITZ at aggregate-mastic interfaces The ITZ was assumed to consist of narrow elements surrounding the aggregates without defining the cohesive zone element. Defining ITZ enables one to investigate the moisture effect on degradation of adhesive bond strength within the asphalt concrete microstructure.

The aggregate was assumed to be isotropic-linear elastic while the mastic phase was assumed to be a viscoelastic-viscoplastic material in which the mechanical damage can evolve with the damage parameters reported by Darabi et al. (2011a), Table 8.1. Mastic and aggregate diffusivities were assumed to be 5.56×10^{-6} mm^2/sec and $2.44\times10^{-4} mm^2/sec$, respectively (Caro et al., 2010b).

Table 8.1. Visco- elastic, plastic, and mechanical damage model parameters at the reference temperature, $T = 20^{o}C$, and temperature dependent model parameters (Darabi et al., 2011a).

Viscoelastic model parameters					
n	1	2	3	4	5
λ_n (Sec^{-1})	10	1	0.1	0.01	0.001
D_n (MPa^{-1})	1.98×10^{-4}	1.48×10^{-3}	6.56×10^{-4}	1.43×10^{-3}	2.47×10^{-3}
D_0 (MPa^{-1})	3.5×10^{-3}				

Viscodamage model parameters			
$\Gamma_0^{vp}(sec^{-1})$	Y_0(MPa)	q^m	k^m
4×10^{-6}	0.7	5	30

Viscoplastic model parameters						
α	β	Γ^{vp}	N	κ_0(MPa)	κ_1(MPa)	κ_2
0.3	0.15	5×10^{-4}	3.63	35×10^{-3}	610×10^{-3}	215

Viscoelastic-viscoplastic temperature-dependent parameter		
Temperature (°C)	a_T	g_0
10	7	0.43
20	1	1
40	0.008	5.7

Figure 8.1 shows a sample mesh consisting of different shapes and dimensions of aggregates which are surrounded by a very thin ring of elements representing ITZ. The load was applied on the top edge at a constant displacement rate of 0.02 mm/s. Horizontal movement at the left side and vertical movement at the bottom were prevented.

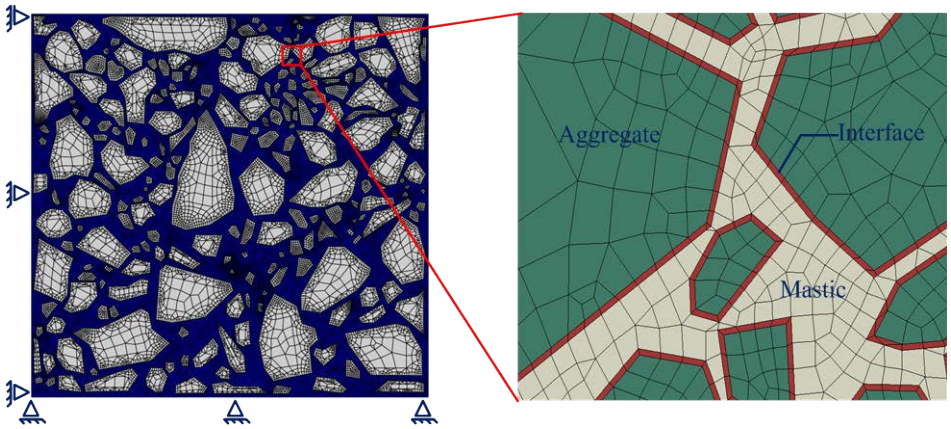

Figure 8.1. (a) Geometry, boundary condition, and mesh representation of the micromechanical representation of asphalt concrete (aggregate, mastic, and interface).

To illustrate the model's capabilities of performing micromechanical simulations, 2D simulations were performed and their results are presented herein. Although parameters associated with thermo- viscoelastic, viscoplastic, and viscodamage presented here were obtained from experiments conducted at the macro-scale, they are well-suited to be applied to the asphalt mastic; which exhibits time-dependent deformation and degrades with mechanical loading and environmental effects (e.g. exposure of the mastic to moisture).

8.1.2 Numerical Simulations of Asphalt Concrete Under Moisture And Mechanical Loading

In order to investigate the effect of moisture on the rate-dependent mechanical response of asphalt concrete, uniaxial constant strain rate tests were simulated at different strain rates and temperatures with different moisture conditioning times. Figure 8.2 (a))

illustrates the moisture diffusion within the microstructure exposed to the moisture content of one on top (fully saturated on the top surface) and half on lateral sides (partially saturated) for ten days.

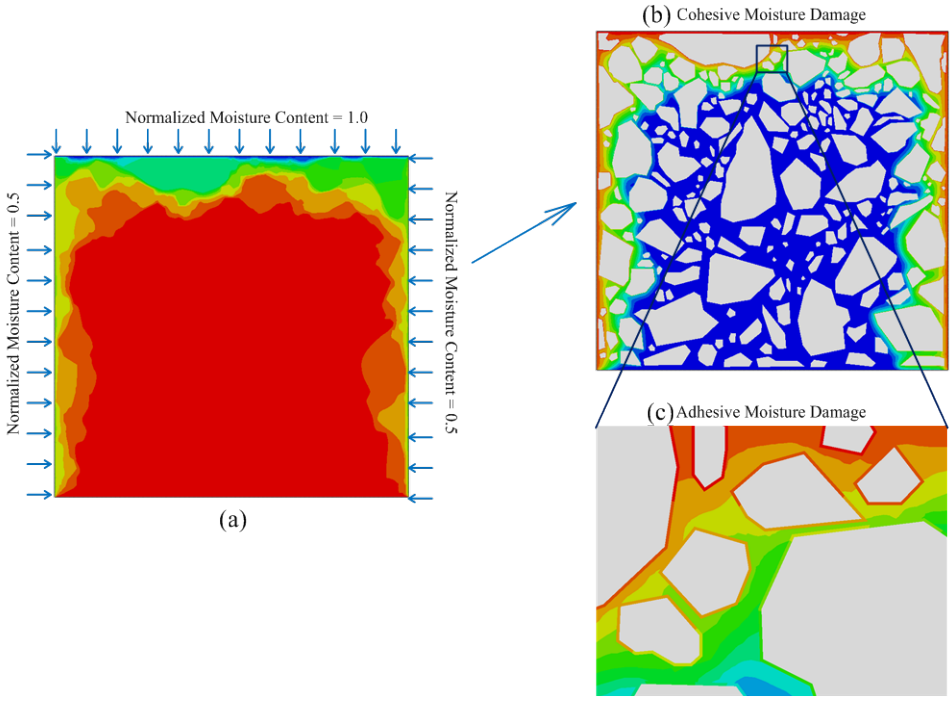

Figure 8.2. (a) Moisture diffusion (the model was exposed to the moisture content equal to one on top and 0.5 on the two lateral sides for 10 days), (b) Moisture damage evolution contours for the corresponding conditioning, and (c) Focused part of the micromechanical representation to show independent evolution of the cohesive and adhesive moisture damage.

The moisture content was not assumed fixed through the material. The commercial software Abaqus (2008) has been used to solve the Fick's second law to computationally determine the moisture content inside the mixture. The moisture content

evolves with time based on the imposed boundary condition. Figure 8.2 (b) and (c) illustrate the evolution of the cohesive and adhesive moisture damage, respectively. Figure 8.2 (b), areas close to the top and lateral surfaces are significantly damaged due to moisture presence. The reason for this moisture damage pattern is that moisture starts to diffuse from surfaces, such that areas adjacent to external surfaces are exposed to higher moisture level for longer period. Results shown in Figure 8.2 (b) demonstrate that the material is susceptible to stripping or raveling phenomena, which is the dislodgement of aggregates from the bulk material. The vulnerable interfaces are highly aggravated due to higher moisture content close to the top and lateral surfaces, Figure 8.2 (c). This degradation can lead to easy separation of aggregates from the mastic at the surfaces. This figure shows the capability of the proposed moisture damage constitutive relationship in considering adhesive and cohesive moisture evolution independently. These results also illustrate the capability of the model to predict the tendency of striping in asphalt concrete due to the susceptibility of the adhesive bond strength between the aggregate and the mastic to moisture. The tendency for stripping is represented by the case in which the adhesive moisture damage is higher than the cohesive moisture damage leading to separation of aggregate from the mastic.

The Effect of Moisture Conditioning Level, The effect of moisture conditioning level on the ultimate strength of the asphalt concrete pavements under compressive and tensile loading was investigated and results are presented in this section. Simulated pavements were exposed to different periods of moisture conditioning. Mechanical loading was then applied on the top of the pavement structure with a constant rate under

a constant temperature of 20°C. As it has been discussed, Figure 8.2 (a) shows the normalized moisture content contours when the top surface of microstructure was saturated and lateral surfaces were partially saturated. Figure 8.2 (b) and (c) illustrate cohesive and adhesive moisture damage after 10 days of moisture conditioning, respectively. These figures show the capability of the proposed moisture damage constitutive relationship to evaluate the concurrent evolution of both adhesive and cohesive moisture damage.

Figure 8.3 (a) illustrates the average stress-strain diagram for uniaxial compressive loading for various conditions. It shows that the stiffness modulus and ultimate strength of the material are reduced as the period of exposure to moisture increases. Figure 8.4 shows the corresponding induced mechanical damage density distribution for different moisture conditioning times. Similarly Figure 8.3 (b) andFigure 8.5 show the average stress-strain diagram and damage distribution under tensile loading. Damage distribution and propagation slightly differs between tensile and compressive loading especially in the dry condition. The damage distribution contours illustrate that the damage density gradually concentrates in the vicinity of the edges, where the moisture have already degraded the material, as the exposure time increases.

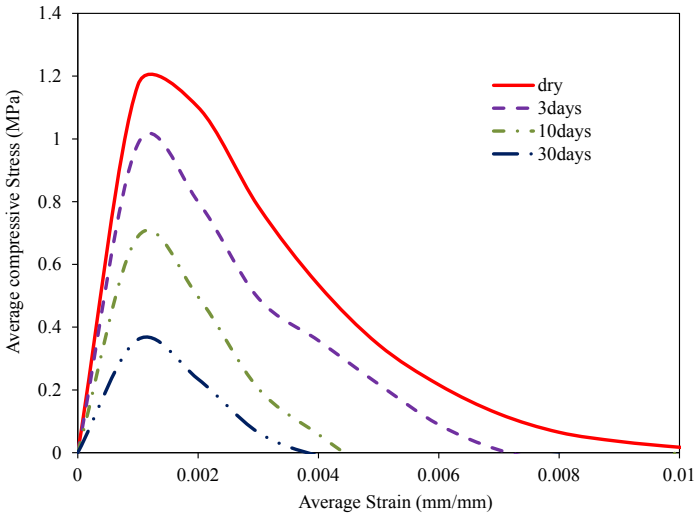

(a)

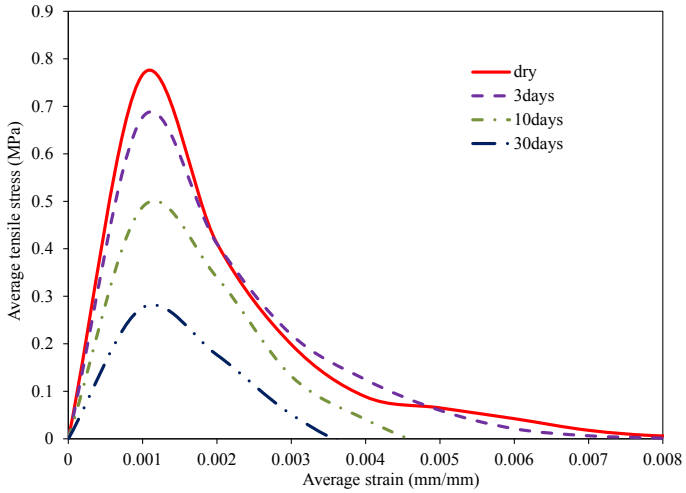

(b)

Figure 8.3. Average Stress-Strain diagram for (a) compressive loading, and (b) for tensile loading.

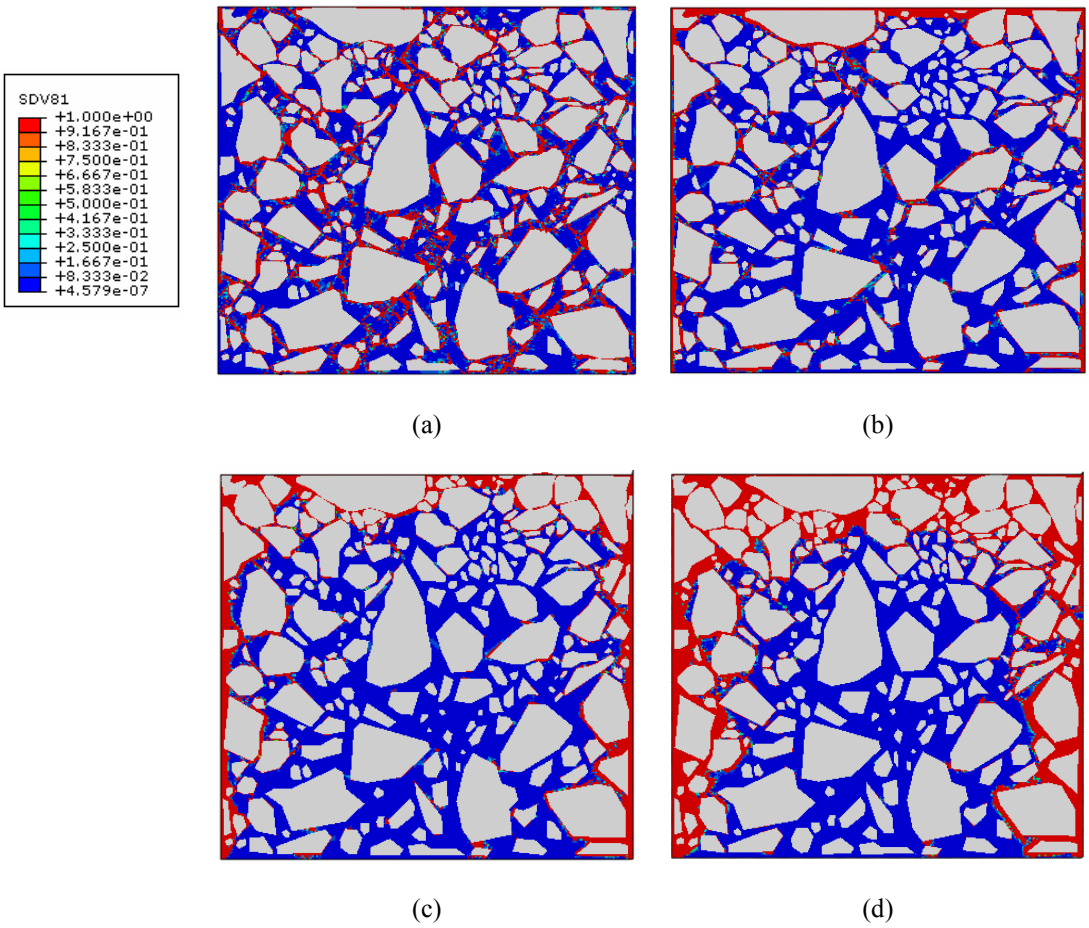

Figure 8.4. Mechanical and total damage distribution due to compressive loading at (a) dry condition, (b) 3days moisture conditioning, (c) 10days moisture conditioning, (d) 30days moisture conditioning time.

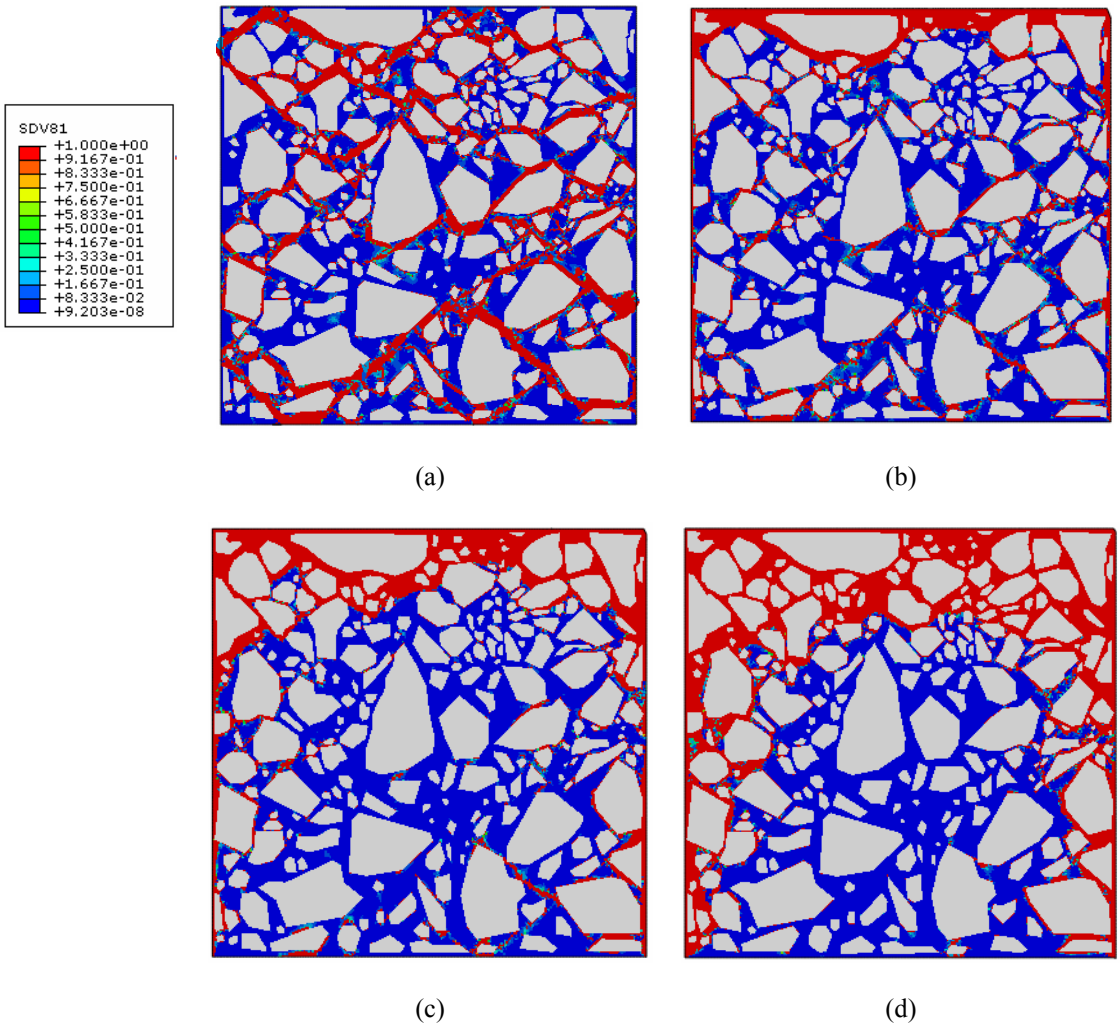

Figure 8.5. Mechanical and total damage distribution due to tensile loading at (a) dry condition, (b) 3days moisture conditioning, (c) 10days moisture conditioning, (d) 30days moisture conditioning time.

The Effect of Strain Rate, Strain rate has a considerable impact on the response of asphalt concrete because of its viscoelastic and viscoplastic constitutive behavior. Three different strain rates were considered in this analysis. Figure 8.6 shows the average stress-strain diagram for the different strain rates under compressive loading at a dry

condition and when the specimen is moisture conditioned for 5 days. The specimen is exposed to moisture at the top and lateral sides of the model for 5 days. As it is expected, the ultimate strength is higher for higher strain rates, and asphalt concrete takes more time to relax when the strain rate is lower. The constitutive model which is used in this study can predict the impact of loading rate on the initial stiffness, ultimate strength, strain to failure of the material, and the coupling effect of moisture damage and strain rate. Figure 8.7 shows that the damage density increases as the rate of loading increases for both dry and moisture conditioned specimens. Damage distribution for the moisture-conditioned cases increases with increase in strain rate. At a lower strain rate, damage concentrates at regions of higher moisture damage density before loading. However, as strain rate increases, larger portions of the material become damaged and the induced damage propagates more rapidly throughout the microstructure.

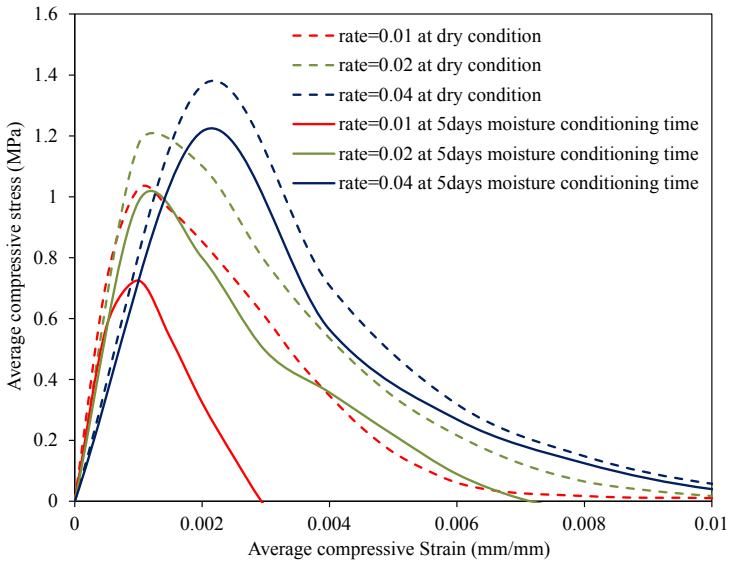

Figure 8.6. Average Stress-Strain diagram for different rate of displacement at dry condition and after 5 days moisture conditioning time.

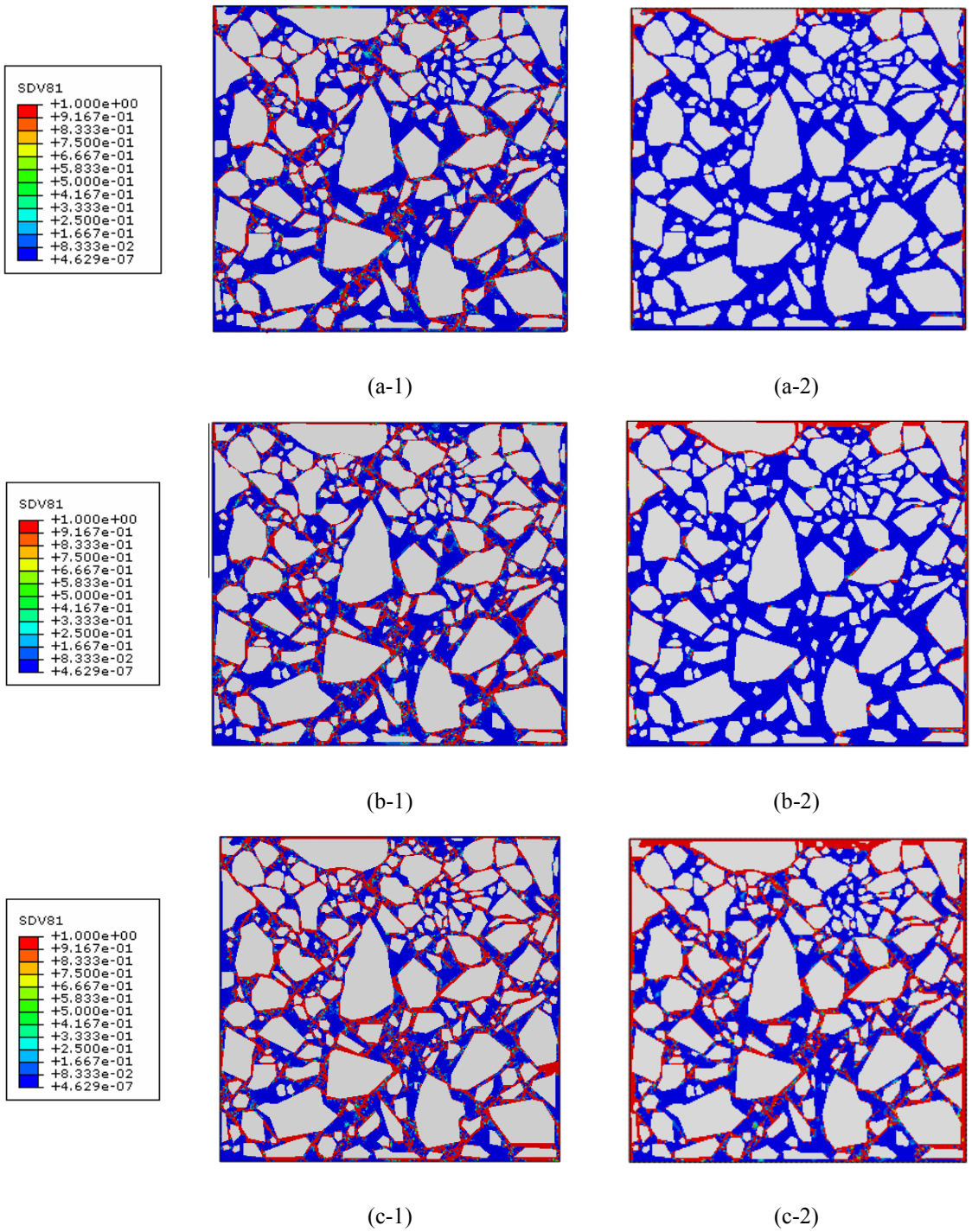

Figure 8.7. Damage distribution due to (a)-1&2 compressive loading at dry condition and 5days moisture conditioning time at displacement rate=0.01, (b)-1&2 compressive loading at dry condition and 5days moisture conditioning time at displacement rate=0.02 and (c)-1&2 compressive loading at dry condition and 5days moisture conditioning time at displacement rate=0.04.

The Effect of Temperature, To scrutinize the effect of temperature on the behavior of asphalt concrete material, the RVE was simulated at three different temperatures in a dry condition and after 5 days of conditioning and then the RVE was subjected to compressive loading. The model parameters associated with different temperatures are presented in Table 8.1. Figure 8.8 shows the stress-strain response at three different temperatures for dry and 5 days moisture conditioned specimens. The corresponding damage contours are shown in Figure 8.9. It is notable that the material response is highly dependent on temperature. The material's ultimate compressive strength and modulus of elasticity decrease as the temperature increases. The material becomes more brittle and prone to damage as temperature decreases. Therefore, at specific strain levels, damage increases as temperature decreases.

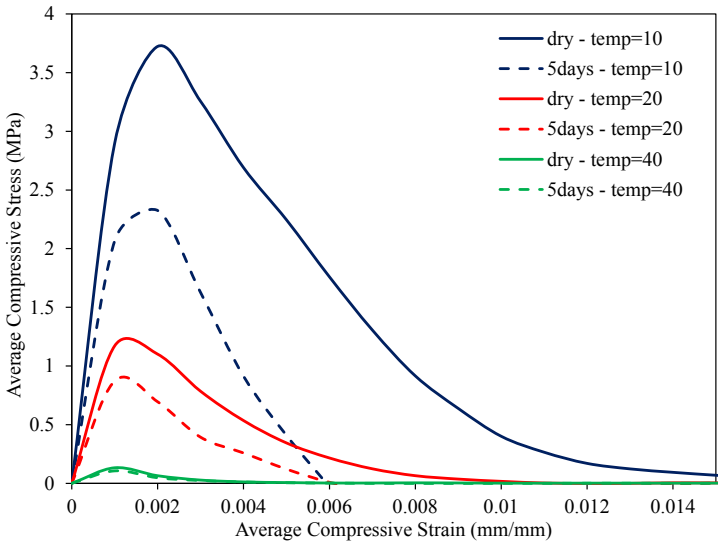

Figure 8.8. Average Stress-Strain diagram for three different temperatures at dry condition and after 5 days moisture conditioning time.

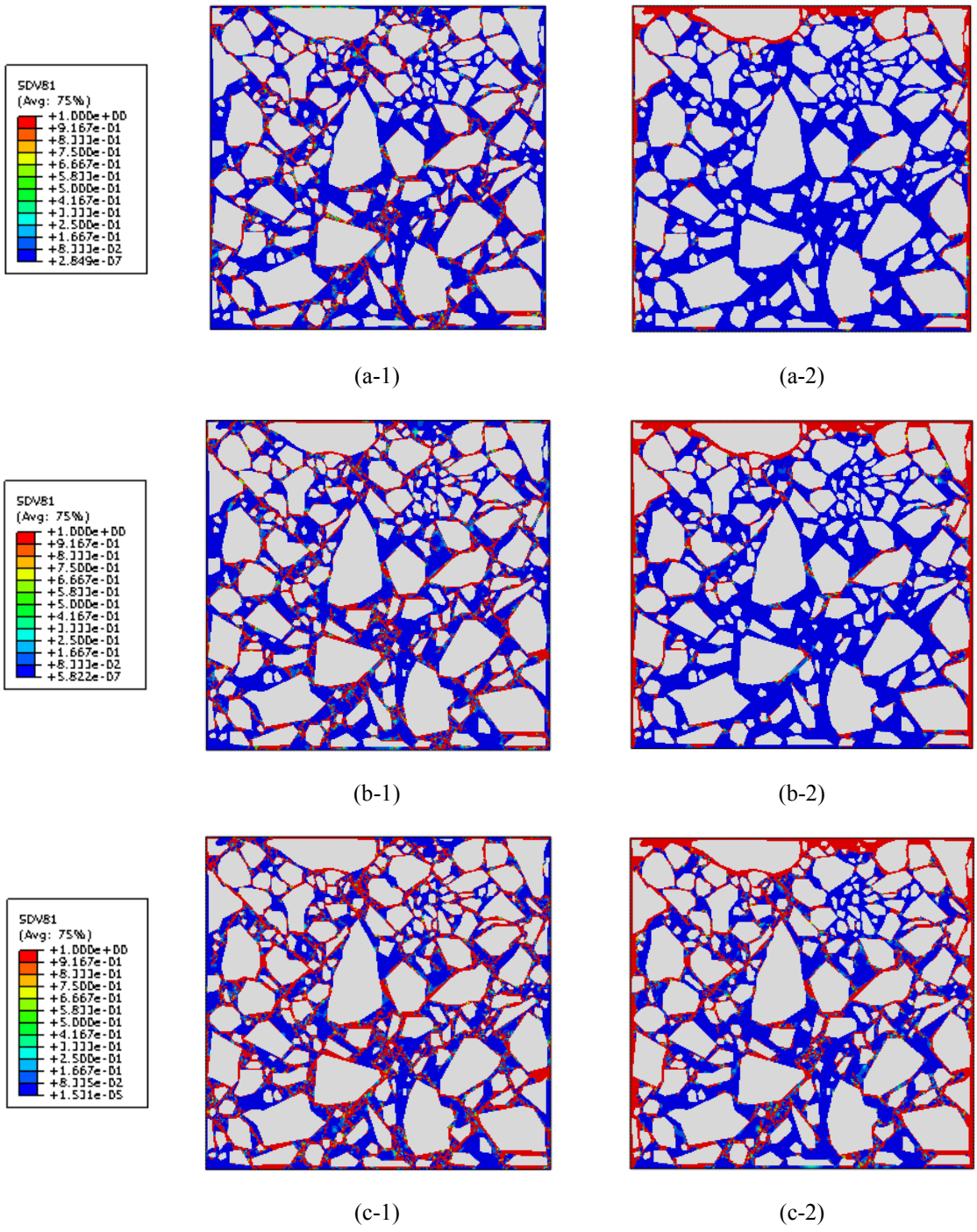

Figure 8.9. Damage distribution due to (a)-1&2 compressive loading at dry condition and 5days moisture conditioning time at 10°C, (b)-1&2 compressive loading at dry condition and 5days moisture conditioning time at 20°C and (c)-1&2 compressive loading at dry condition and 5days moisture conditioning time at 40°C.

Creep-Recovery Response, Repeated compressive and tensile creep-recovery tests at two different moisture content levels were simulated at 20 ºC. Figure 8.10 (a) shows the stress input for creep-recovery tests when the loading time is 100s. The simulation results during the repeated creep-recovery test (strain versus time response) are presented in Figure 8.10 (b) and (c) for compression and tension, respectively. The corresponding damage density distributions are shown in Figure 8.11 and Figure 8.12 for compression and Figure 8.13 and Figure 8.14 for tension at dry and two different moisture contents following 5 days of conditioning. The results demonstrate that the average strain increases as the moisture conditioning period increases.

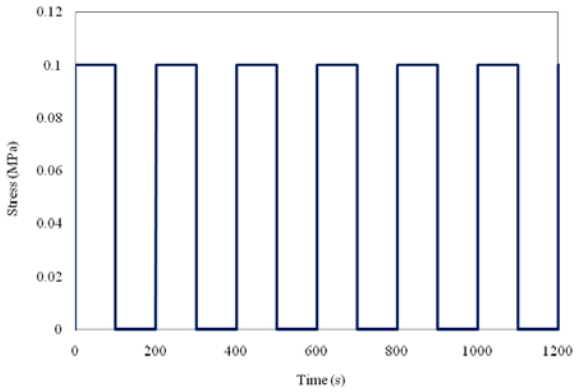

(a)

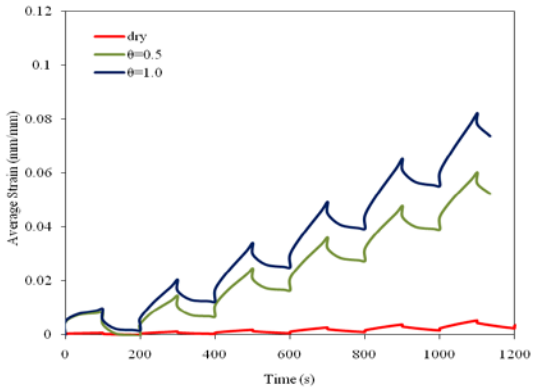

(b)

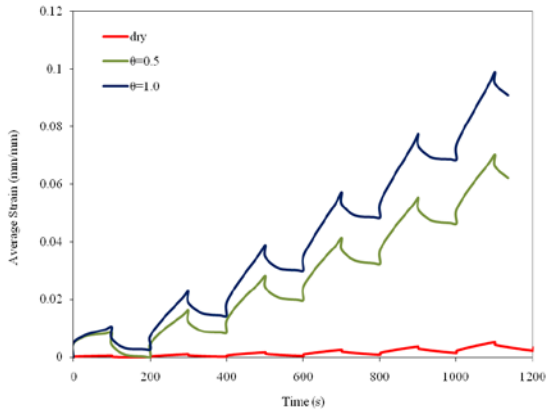

(c)

Figure 8.10. (a) Stress-time diagram for creep-recovery test, (b)Average strain versus time diagram for creep compressive test, and (c) Average strain versus time diagram for creep tensile test after 5days moisture conditioning time for different moisture content.

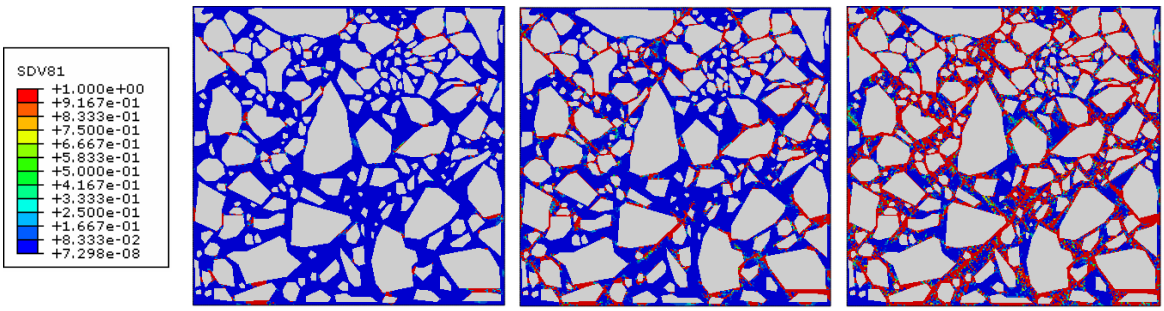

(a) (b) (c)

Figure 8.11. Mechanical damage distribution at compressive creep-recovery at dry condition and at (a) 400s, (b) 800s and (c) failure.

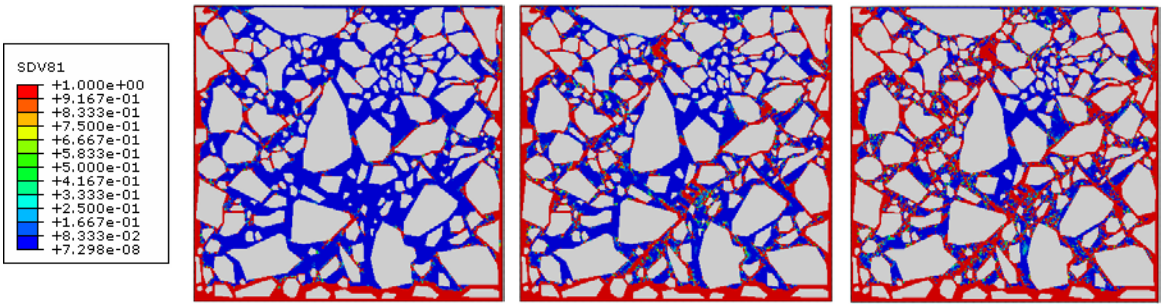

(a) (b) (c)

Figure 8.12. Mechanical damage distribution at compressive creep-recovery test for moisture content equal to 1.0 at (a) 400s, (b) 800s and (c) failure.

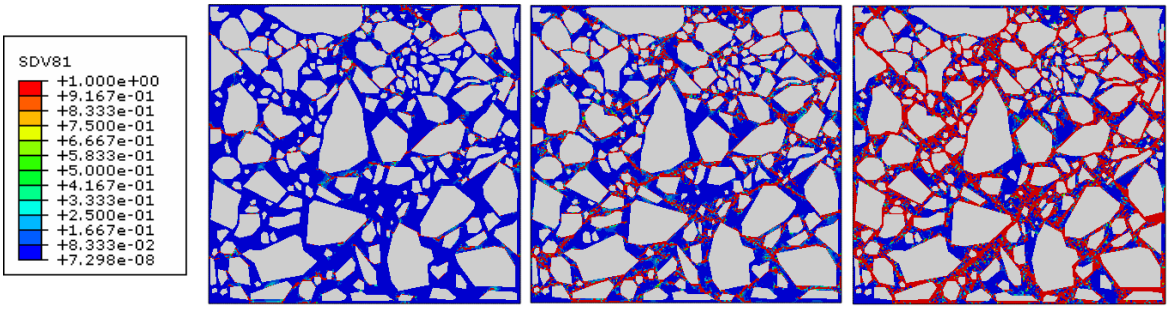

(a) (b) (c)

Figure 8.13. Mechanical damage distribution at tensile creep-recovery test at dry condition and at (a) 400s, (b) 800s and (c) failure.

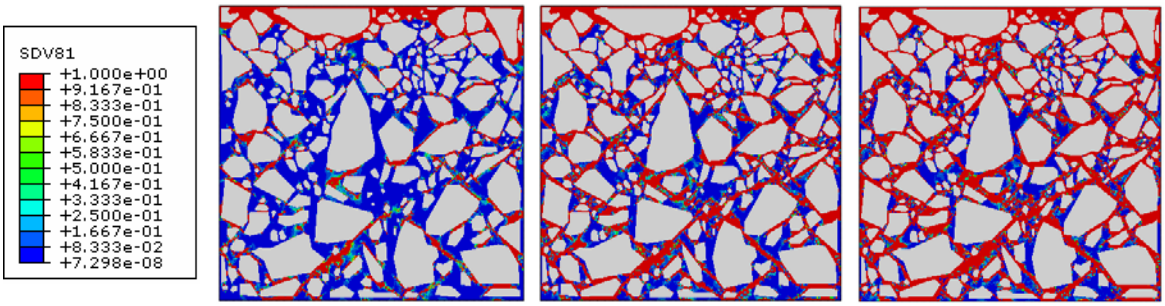

(a) (b) (c)

Figure 8.14. Mechanical and total damage distribution at tensile creep-recovery test for moisture content equal to 1.0 at (a) 400s, (b) 800s and (c) failure.

It can be concluded via these results that the presented coupled moisture-mechanical constitutive relationship is well-suited to conduct micromechanical simulations of asphalt concrete. It can predict damage propagation throughout the mixture. The micromechanical results have not been verified against experimental results. However, it should be mentioned that the trend is compatible with experimental

observations and can be used to obtain an insight toward microstructural behavior of such complicated materials.

8.2 Simulation of Three Dimensional Finite Element Microstructural Representation

The 3D microstructural representations of asphalt concrete are more realistic representation of asphalt concrete and therefore necessary to obtain a better understanding of the real samples. To observe the changes occurring at material's microstructure under different loading conditions 3D micromechanical simulations were conducted to help their continuum behavior's prediction and understanding.

8.2.1 Three Dimensional Representation of Material's Microstructure

An X-ray CT technique is a non-destructive technology using to capture the material's interior arrangement. The X-ray CT technique was used to construct the 3D representation of asphalt concrete's internal structure. You et al. (2012) utilized X-ray CT device of the Advanced Characterization of Infrastructure Materials (ACIM) lab at Texas A&M University to obtain 2D images from a cylindrical asphalt concrete specimen, Figure 8.15 (a). They used Stone Matrix Asphalt (SMA) mixture to prepare the specimen for getting the images. The planar images include aggregates, matrix, and air voids. A 3D microstructural representation of the asphalt concrete was constructed based on the planar images. You et al. (2012) did not consider the air voids as a separate phase in their model for simplicity and it is the subject of the research group's future work since it significantly increases the computational costs. The same model will be

used here to study the internal behavior of asphalt concrete material exposed to both moisture and mechanical loading.

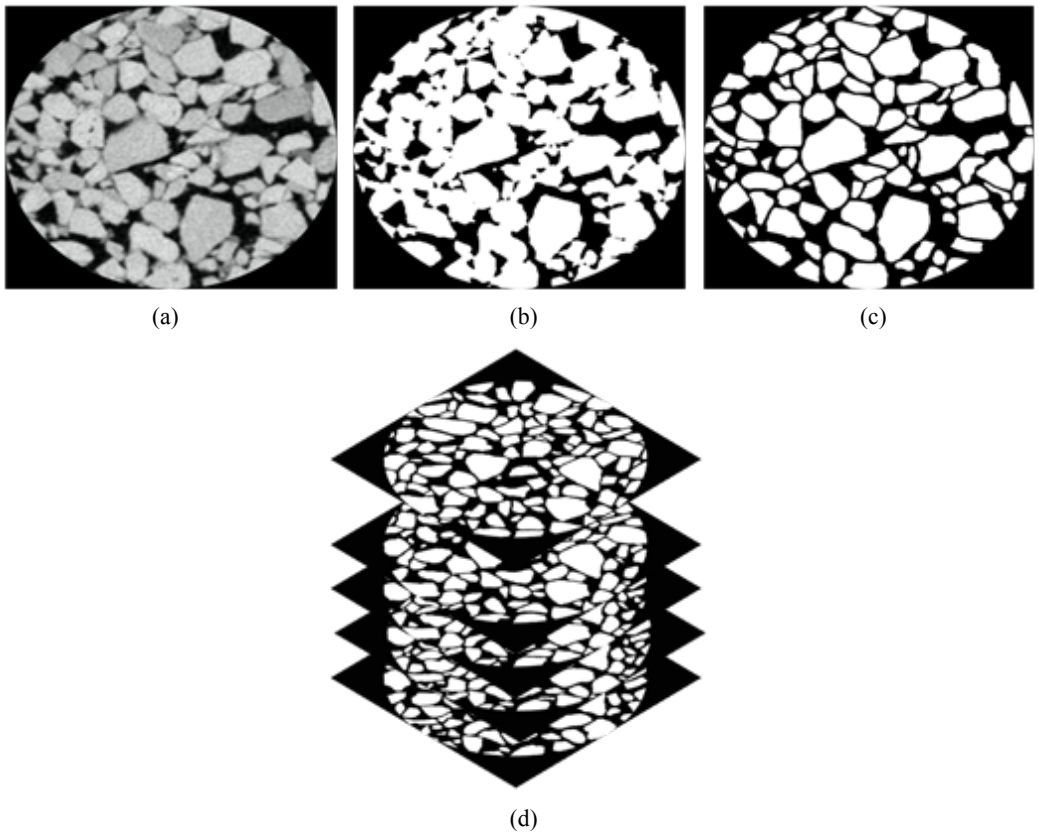

Figure 8.15. X-ray CT images: (a) gray-scale image, (b) contrasted image, (c) image with well-separated aggregates, and (d) slices of processed image (You et al., 2011).

In the obtained CT images the materials pixels have a gray-scale with 0 to 255 intensities representing aggregates, mastic, and air voids. The denser materials have a lower intensity and the lighter one, the higher intensity. To convert this gray-scale to two

different phases, white as an aggregate (i.e. intensity of 255) and black as a matrix (i.e. intensity of 0) a threshold filtering should be used, Figure 8.15 (a). Although aggregates and matrix are distinguishable they are connected to each other, Figure 8.15 (b). This causes a challenge to the finite element microstructural simulations as it treated the connected particles as a single one. You et al. (2012) applied a threshold segmentation technique in the commercial visualization software Avizo (Avizo, 2009) to overcome this challenge and divide the connected aggregates, Figure 8.15 (c). This is an important step, since the mastic and aggregate percentages should remain almost the same before and after the separation to obtain a realistic model. Using a very small thickness of binder for dividing the connected aggregates may significantly increases computational cost and time. Since the minimum thickness of the binder between the adjacent disconnected aggregates exert the minimum element size in the generated finite element model later. Therefore, an optimum thickness for separating the aggregates to balance the desired accuracy and the possible computational capacity should be determined.

The 2D processed sliced images are constructing the asphalt concrete 3D microstructure, Figure 8.15 (d). For this purpose, these slices are connected along the vertical direction with equivalent 1mm spacing. The aggregates form single aggregates while the matrix constitutes a single phase, Figure 8.16. The model finally is a cylindrical specimen with a 50*mm* diameter and 75*mm* height dimensions. The final modification step is removing fine aggregates of the sizes less than 2.34*mm* and considering them as the mastic in the microstructural representation to reduce computational costs. Considering fine aggregates as well as air voids in the model is the

future work's subject by the research group. For simplicity, the mastic phase is perfectly bonded to the aggregate phase, since the experimental identification of the interfacial properties is a very challenging task. Other interfacial conditions (bond, slip, friction) are also subjects of a future work.

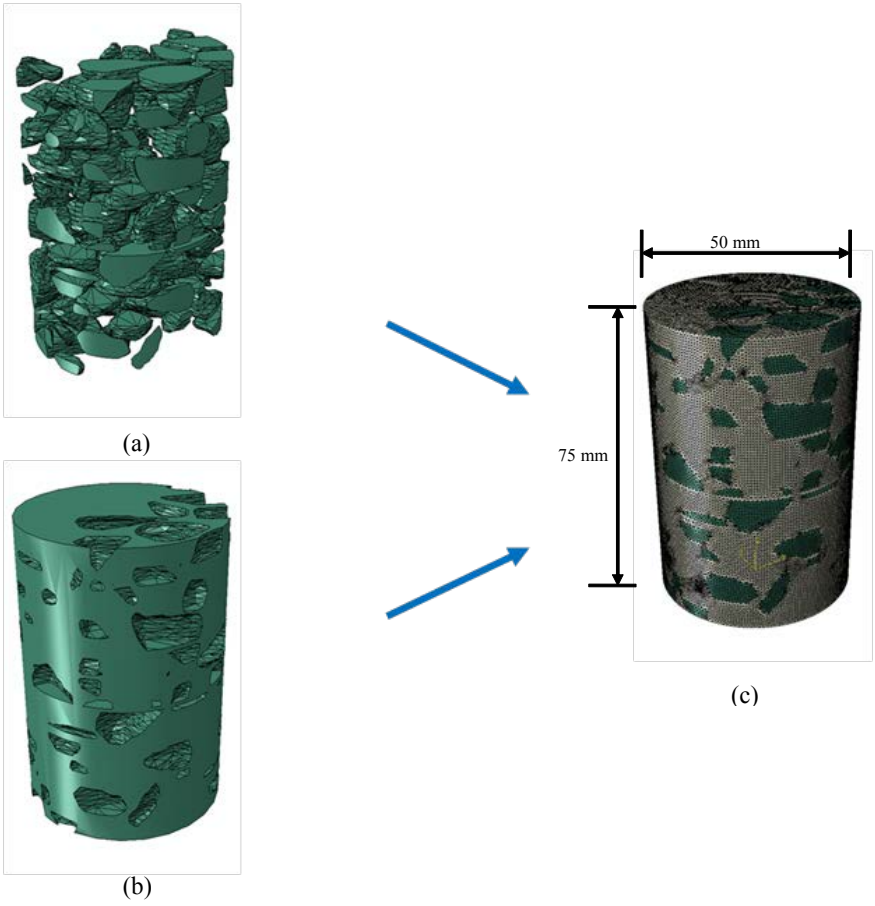

Figure 8.16. Reconstructed three-dimensional asphalt concrete microstructural model: (a) aggregates, (b) matrix, and (c) finite element meshed model (You et al., 2011).

This representative volume element (RVE) was used in this work to investigate the effect of moisture on the mechanical response of asphalt at micro-scale level. Figure 8.16 (c) shows the geometry and finite element mesh of the generated asphalt concrete specimen comprises 1.7 million element in the well-known commercial finite element software Abaqus (2008). Four-node 3D coupled temperature-displacement elements (CPE4RT) are constructing the mesh for the current 3D microstructure. The coupled temperature-displacement element was used instead of coupled diffusion-displacement element since equations for heat transfer and mass diffusion are the same. Normalized moisture content is applied in place of temperature for simulations. The specimen's bottom is constrained from moving in the vertical direction. The top of the specimen is exposed to moisture in the moisture-conditioned cases. The load is applied on the top of the specimen with a constant displacement rate. The micromechanical simulations in this study were conducted using the supercomputer HYDRA in the supercomputer facility at Texas A&M University. HYDRA is an IBM p575 massive parallel supercomputer with cumulative capacity of 640 processors and 1632 GB of memory. The average CPU time to run a simulation is around 40 hours.

8.2.2 Numerical Simulation of Asphalt Concrete Under Moisture And Mechanical Loading

Asphalt concrete is a rate- and temperature- dependent material. To scrutinize the moisture effect on the rate-dependent mechanical response of asphalt concrete, uniaxial constant displacement rate tests were conducted for different moisture conditioning

states, strain rates, moisture boundary conditions, and temperatures. Thus, the following sections focus on investigating the different moisture conditioning periods and boundary conditions effect on the overall thermo-mechanical response of 3D representation of the asphalt concrete specimen at different strain rate and temperature.

Although the material models presented by Darabi et al. (2011a) and Shakiba et al. (2004) are developed to model asphalt concretes as a continua, it is extremely well suited to the asphalt mastic. Mastic exhibits time-dependent recoverable and irrecoverable deformations and degrades with loading and moisture presence. For these simulations, finite element meshes were constructed with two types of regions: aggregates, and asphalt mastic bulk. Since the aggregates' response is usually stiff and timetable, they are considered as isotropic linear elastic material with Young's modulus E_{agg} = 25GPa and Poisson's ratio v_{agg} = 0.16. The mastics are modeled as a viscoelastic-viscoplastic material in PANDA with model parameters reported by Darabi et. al. (Darabi et al., 2011a) and presented in table (6.2). Mastic and aggregate diffusivities are $5.56 \times 10^{-6}\ mm^2/s$ and $2.44 \times 10^{-4}\ mm^2/s$, respectively (Caro et al., 2010b). The analysis in this study assumes that moisture diffuses through both matrix and aggregate phases. The diffusion rate through each phase depends on their associated diffusion coefficients. Therefore, moisture diffuses through the matrix at a slower rate comparing to its diffusion rate through the aggregate. This study also assumes that the aggregates are fully coated with the matrix. Therefore, moisture has to diffuse first through the matrix in order to move from one aggregate particle to another.

The entire bottom of the specimen is constrained from moving in the vertical direction and the load is applied on the specimen's top surface. Figure 8.17 (a) shows the moisture diffusion through the model while it is exposed to a normalized moisture content equal to one on top for ten days. The assumed moisture boundary condition in this paper aims to represent the exposure of the asphalt pavement to the moisture during a rainy day. In this case, the normalized moisture content on the asphalt pavement's surface is equal to one. Furthermore, the commercial software Abaqus (2008) is used to solve the heat transfer equation (Fick's second law equivalent equation) to obtain the moisture content inside the mixture at each time. The moisture content is being calculated based on the imposed boundary condition and time. Figure 8.17 (a) and (b) show the moisture diffusion and the corresponding cohesive moisture damage of the model with the same boundary conditions and conditioning time, respectively. This figure shows that the model is capable of considering the cohesive moisture damage through the material. The area close to the top is significantly damaged due to moisture. The moisture starts to diffuse from the top surface so volume adjacent to this surface is exposed to higher moisture level for a longer time. The simulation results in this figure clearly demonstrate the stripping or raveling phenomenon, which is the dislodgement of aggregates from the mixture. This figure can explain the severe stripping of asphalt concretes during the wet season once the mechanical load is applied. The vulnerable asphalt mastic is highly aggravated due to higher moisture content close to the top. This degradation leads to easy separation of aggregates from the mastic at the surface.

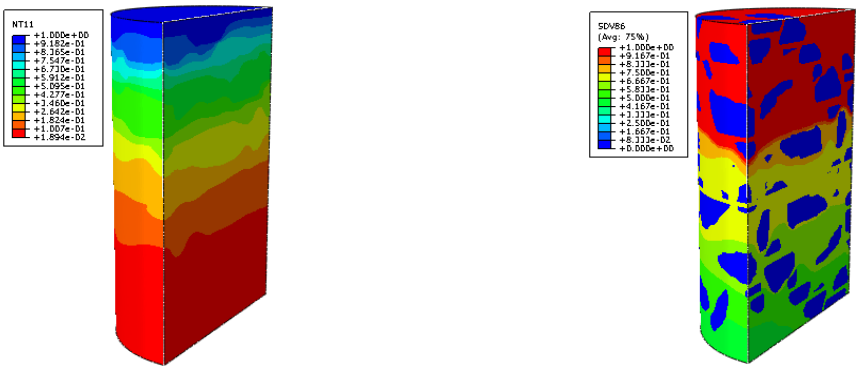

(a) (b)

Figure 8.17. (a) moisture diffusion, (b) moisture damage contour through the 3D model after 10 days moisture conditioning time.

The Effect of Moisture Conditioning Period, The effect of moisture conditioning time on the ultimate strength of the asphalt pavement at the compressive and tensile loading is investigated in this section. The specimen is exposed to a normalized moisture content equal to one on the top surface for different conditioning time, 5, 24 and 36 hours. Then, the load is applied on top of the model with a constant strain rate of 6.66×10^{-4} 1/s at temperature 20 °C**.** Figure 8.18 shows the average stress-strain diagram due to compressive loading at a dry and moisture conditioned samples with different conditioning time. It obviously shows that the composite stiffness, ultimate strength, and the strain to failure are reducing with increasing the exposure time to the moisture. Figure 8.19 shows the moisture and mechanical damage distribution in these cases at 3 different strain levels. These figures illustrate that the mechanical damage density gradually concentrates on top of the specimen, where the material already degraded by the moisture, as the exposure time increases. Similarly Figure 8.20 shows the average

stress-strain diagram for the similar sample and conditioning under tensile loading. The ultimate strength under tensile loading is less than the ultimate strength under compressive loading as the material is more easily falling apart under tensile condition. Figure 8.21 demonstrates moisture and mechanical damage distribution under tensile loading. Damage distribution and propagation slightly differs between tensile and compressive loadings especially at dry condition but their general attitudes are the same, by increasing the moisture conditioning time damage is concentrated at the top where we have more moisture damage. These figures also clearly declares that the current modeling can take into account the different behavior of asphalt concrete under compressive and tensile loading condition, where the ultimate asphalt concrete's strength in compression is greater than that in tension. Finally, it should be mentioned that the reduction of maximum strength in compressive loading is greater than its equivalence under tensile loading with increase in moisture conditioning time. These model predictions of the behavior of asphalt concrete due to moisture degradation are qualitatively in good agreement with experimental results. Experimental results in chapter 6 had shown that ultimate strength and stiffness modulus decrease due to more conditioning time as the degraded material is more brittle.

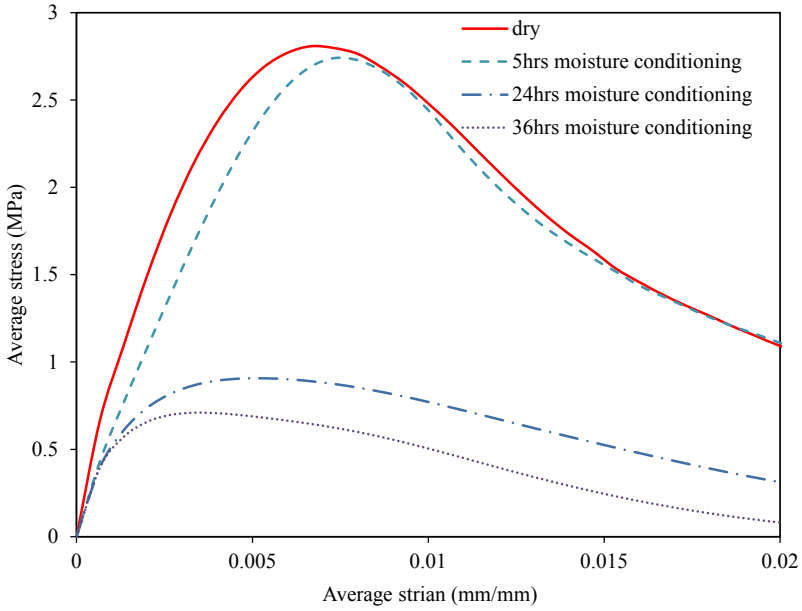

Figure 8.18. Average stress-strain diagram for different conditioning time under compressive loading (strain rate= 6.66 $\times 10^{-4}$ 1/s-temperature 20°C).

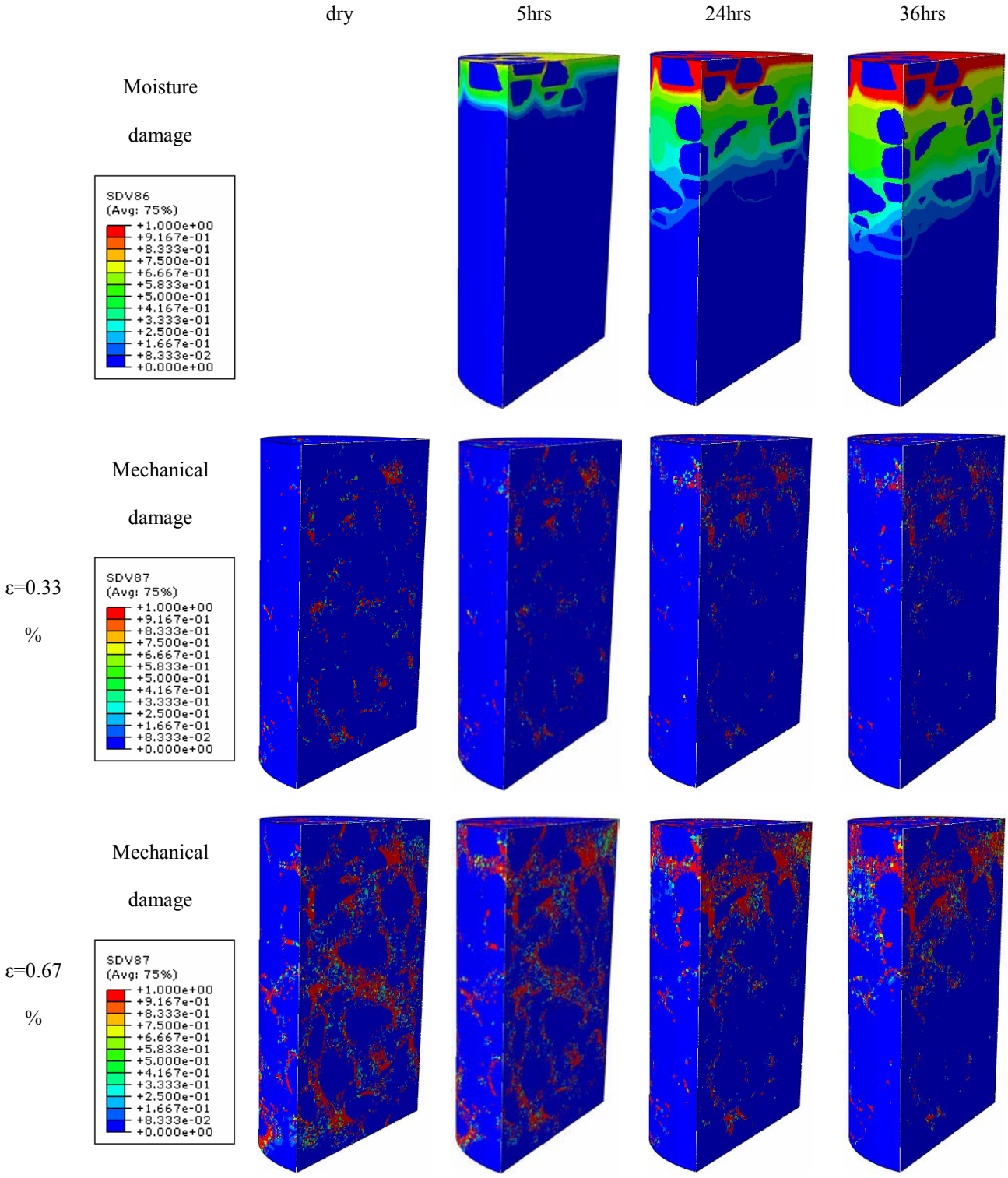

Figure 8.19. Damage distribution due to moisture conditioning and compressive loading at different strain level (strain rate= 6.66×10^{-4} 1/s-temperature 20°C).

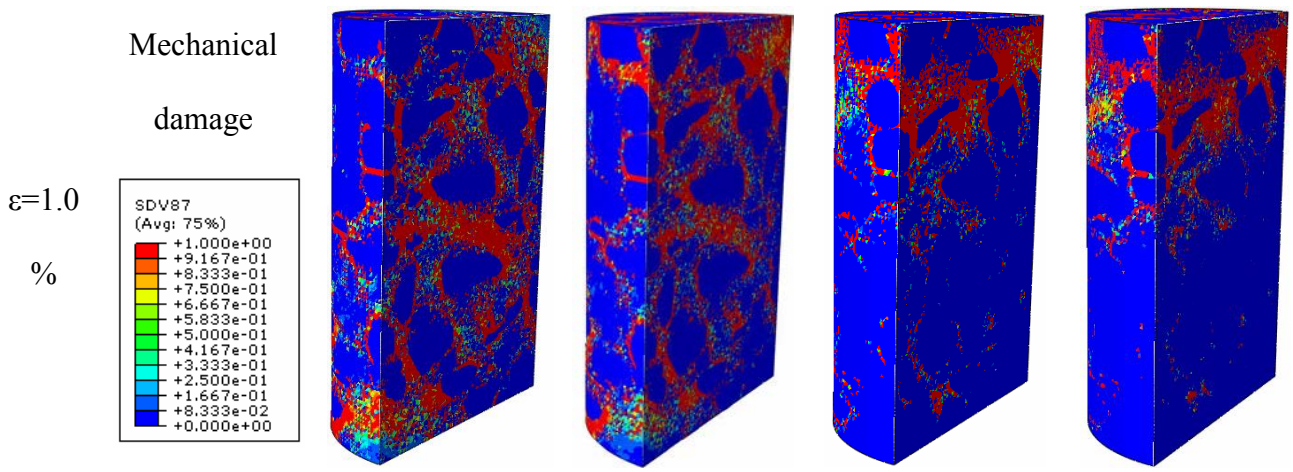

Figure 8.19. Conituned.

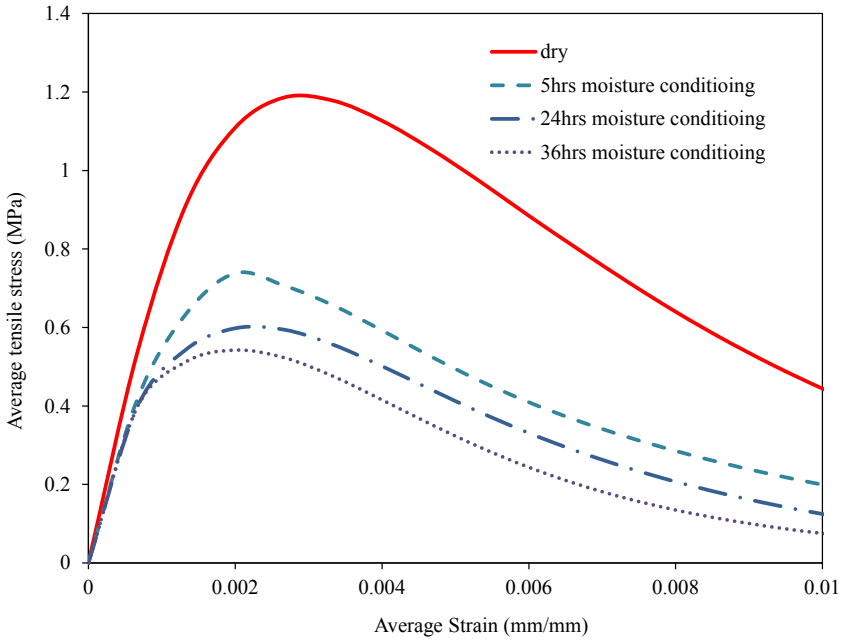

Figure 8.20. Average stress-strain diagram for different conditioning time under tensile loading (strain rate= 6.66 $\times 10^{-4}$ 1/s-temperature 20°C).

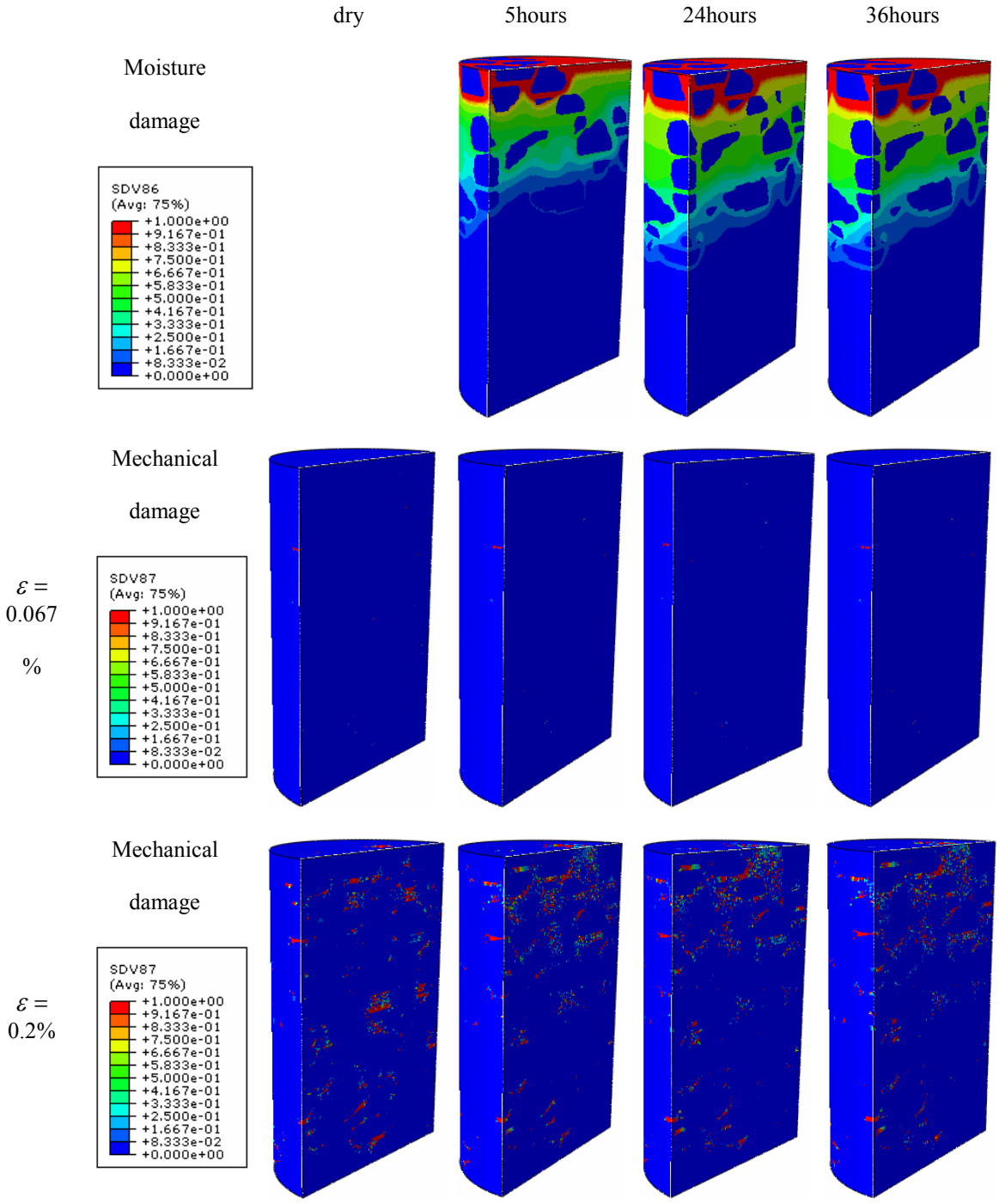

Figure 8.21. Damage distribution due to moisture conditioning and tensile loading at different strain level (strain rate= 6.66 $\times 10^{-4}$ 1/s-temperature 20°C).

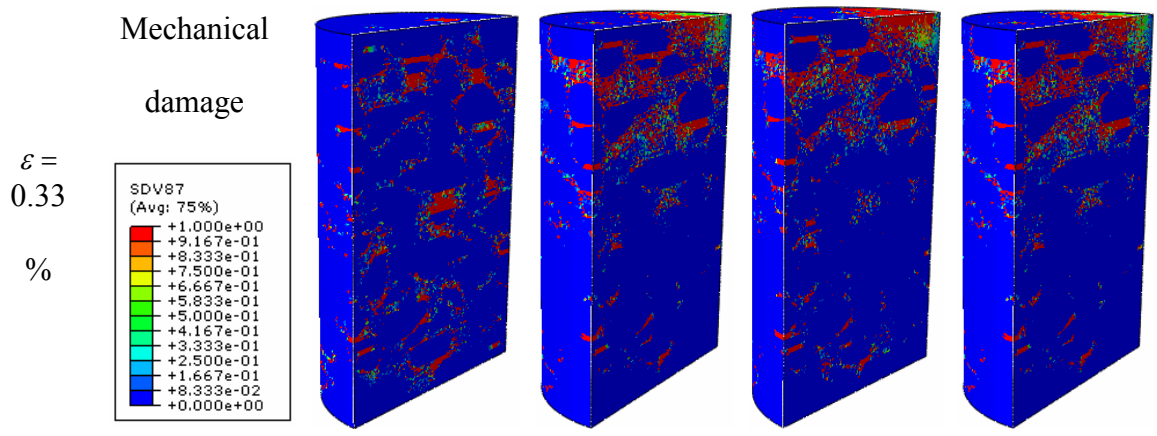

Figure 8.21. Continued.

The Effects of Different Moisture Boundary Condition, To clarify the effects of different environmental boundary conditions three different boundary conditions are defined. The specimens were exposed to moisture content equal to one from three different surfaces: top, bottom, and the lateral surfaces of the specimen for 3days. Then, the compressive and tensile uniaxial loading with a constant strain rate of 6.66×10^{-4} *1/s* at temperature 20 °C was applied on top of the specimens. Figure 8.22 shows stress-strain diagram for compressive and tensile uniaxial loading for different moisture boundary conditions. The corresponding moisture and mechanical damage density distributions in compression and tension are presented in Figure 8.23 and Figure 8.24, respectively. Figure 8.22(a) shows that at compressive loading the moisture diffusion from the top of the specimen where the load is applying can significantly reduce its total strength compare to the diffusion from the bottom of the specimen. At tensile loading the total strength does not differ by changing the diffusion from the top or bottom of the

specimen. It is explainable such that at compressive loading when the moisture is diffusing from the top of the specimen, the load is applying on the completely damaged part. However, at tensile loading it does not matter which part is completely damaged. It should be mentioned that generally total strength at compressive loading is greater than total strength at tensile loading as the material is easily falling apart under tensile loading. In addition, it is completely clear from Figure 8.22 that the side diffusion of moisture significantly increases material's softening. Since there exists more area of diffusion, more diffusion, and consequently more damaged material. Damage distribution contours in Figure 8.23 and Figure 8.24 confirm this phenomenon. These figures show that there is less mechanical damage when there is lateral side diffusion in the material as the material is largely exposed and degraded due to moisture.

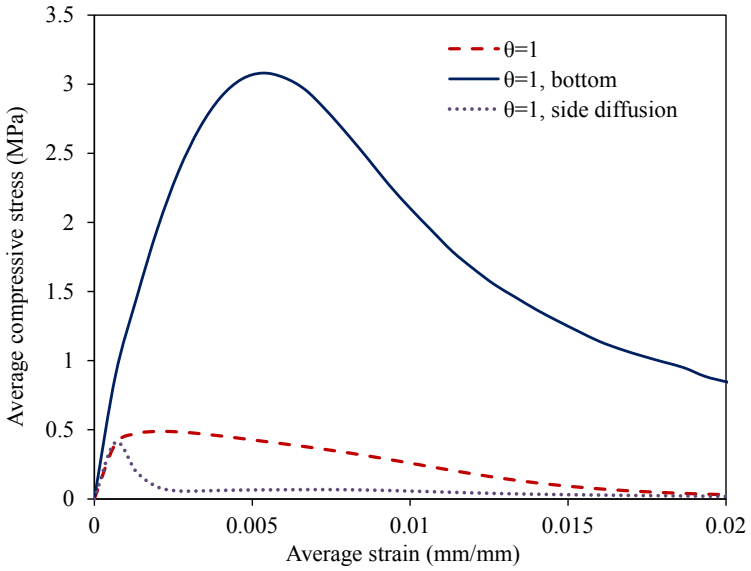

(a)

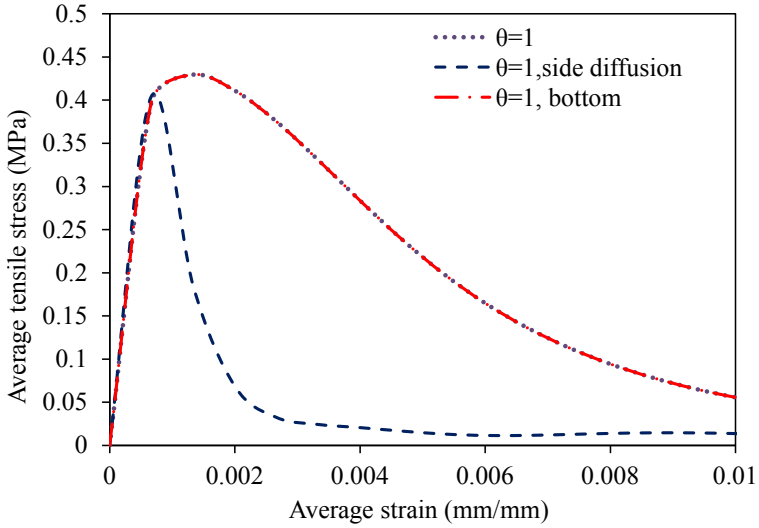

(b)

Figure 8.22. Stress-strain diagram for moisture contents on top, bottom, and lateral side surfaces for 3 days moisture conditioning time and under (a) compression (b) tensile loading (strain rate= 6.66 $\times 10^{-4}$ 1/s-temperature 20°C).

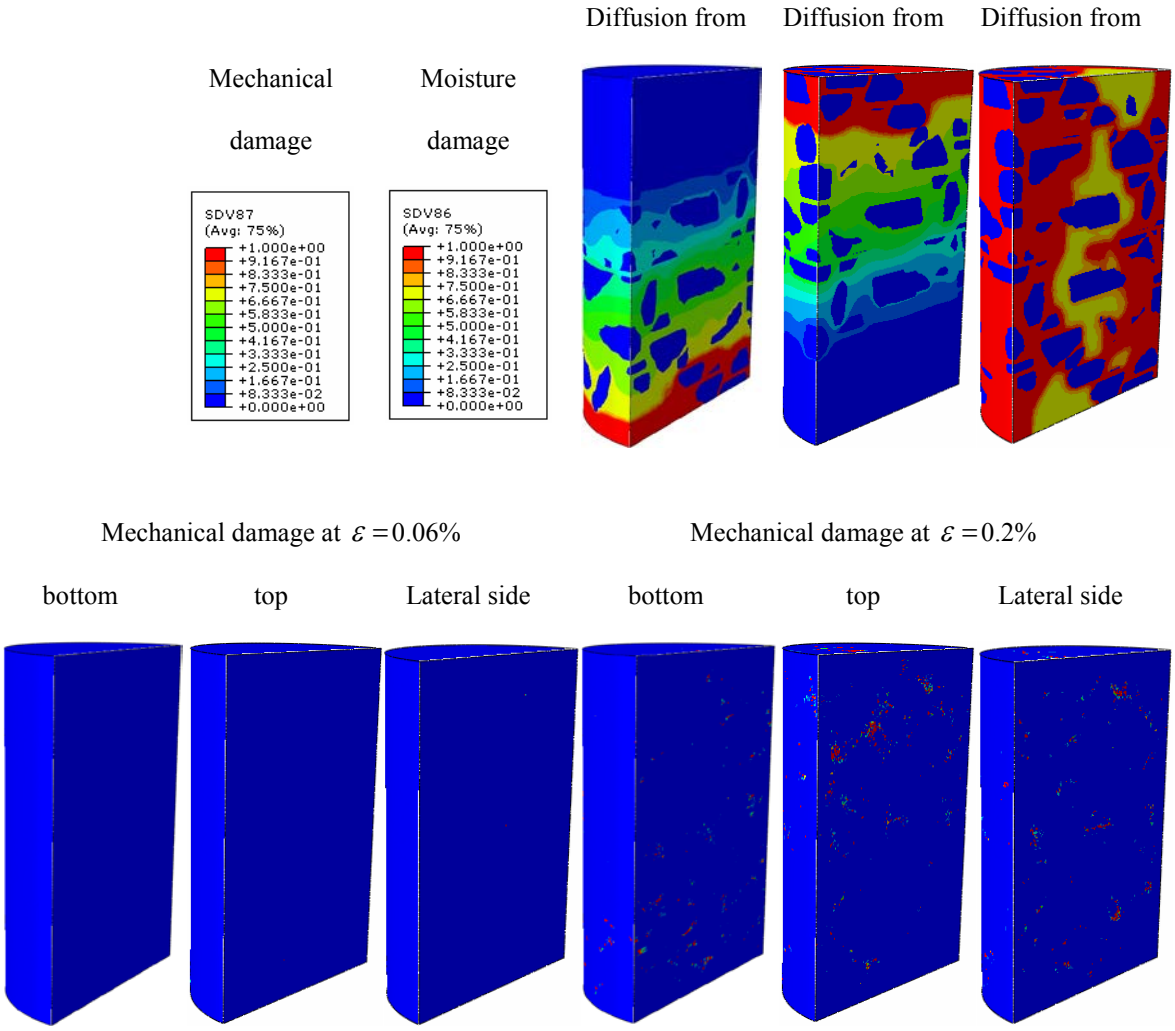

Figure 8.23. Damage distribution due to compressive loading at two different strain level and three different moisture conditioning boundary condition (strain rate= 6.66×10^{-4} 1/s-temperature 20°C).

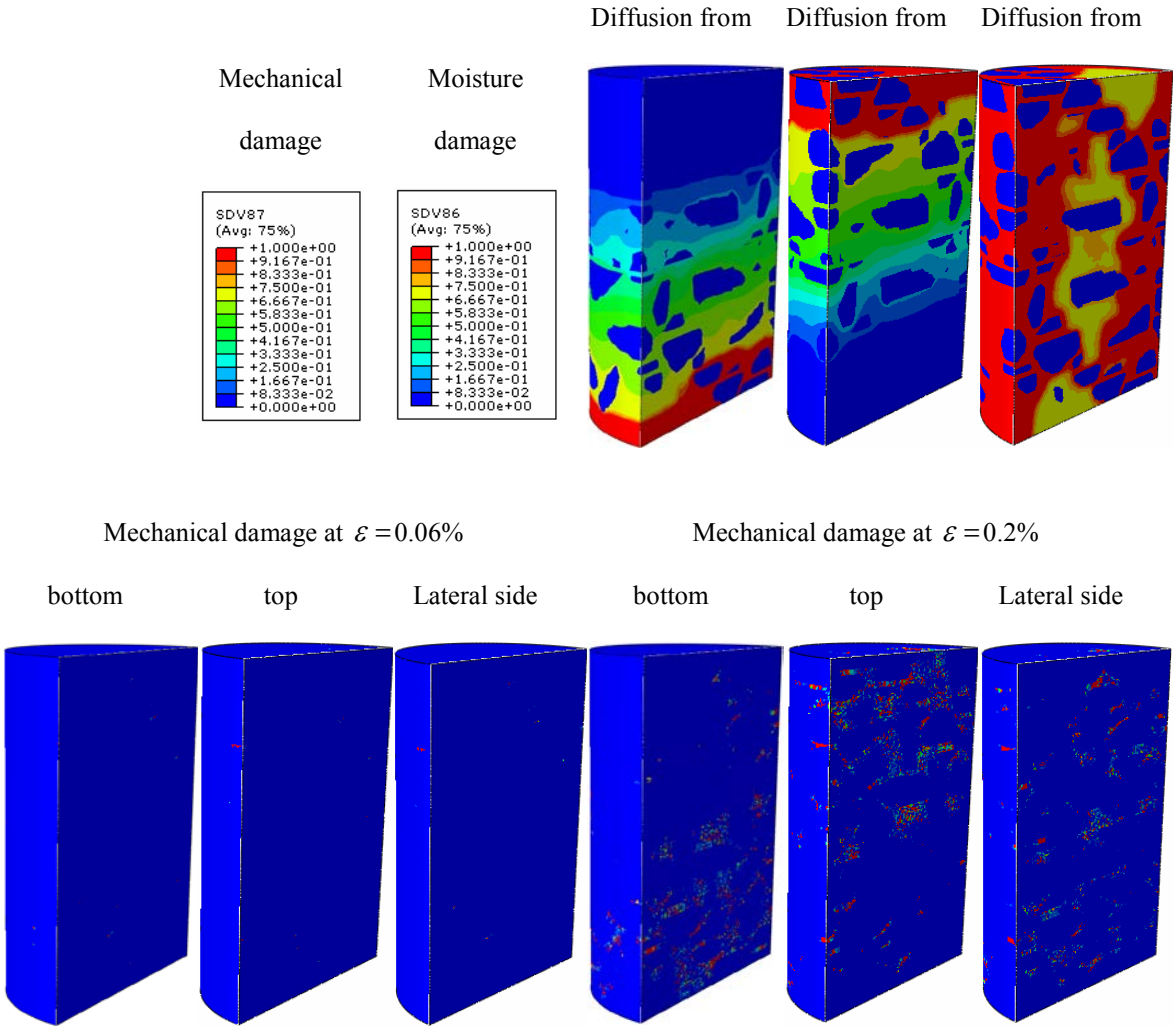

Figure 8.24. Damage distribution due to tensile loading at two different strain level and three different moisture conditioning boundary condition (strain rate= 6.66 $\times 10^{-4}$ 1/s-temperature 20°C).

The Effect of Moisture Damage Model Parameters, In this section a parametric study on the effect of model parameter associated with the material's rate of degradation (i.e. k in Eq. (4.3)) of the moisture damage model is conducted. The constant compression and tension 6.66×10^{-4} *1/s* strain rate is applied on top of the specimen after 3days moisture conditioning time at temperature 20 °C. Figure 8.25 shows the stress-

strain diagram for different model parameter associated with rate of moisture degradation at tension and compression, respectively. It affirms that the maximum strength of the specimen decreases as this model parameter increases. Figure 8.26 and Figure 8.27 show corresponding moisture and mechanical damage distribution at different strain level for compression and tension, respectively. It is clear that with decreasing the model parameter associated with the material's rate of degradation, the moisture damage decreases and the mechanical damage distribute more evenly through the specimen.

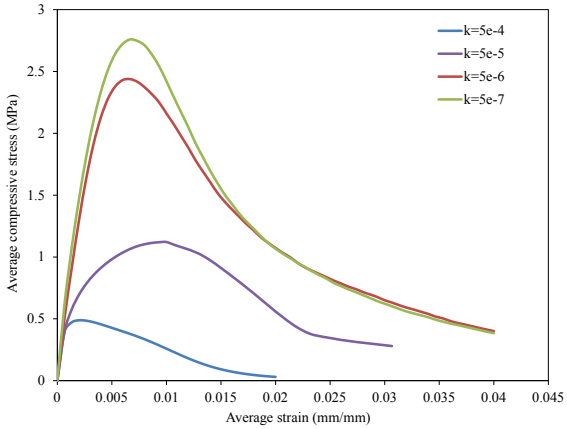

(a)

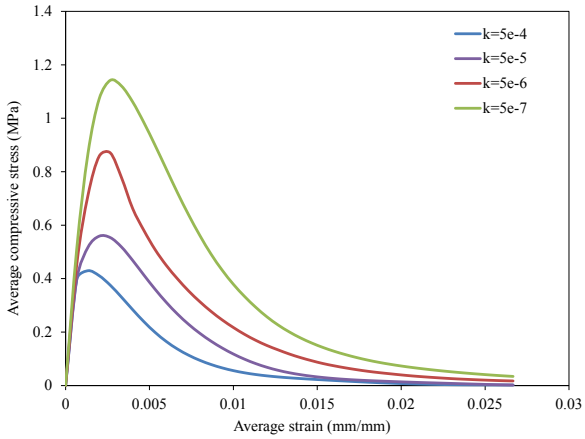

(b)

Figure 8.25. Stress-strain diagram for three different moisture damage model parameter, *k*, at 3days moisture conditioning time and under (a) compressive, (b) tensile loading (strain rate= 6.66×10^{-4} 1/s-temperature 20°C).

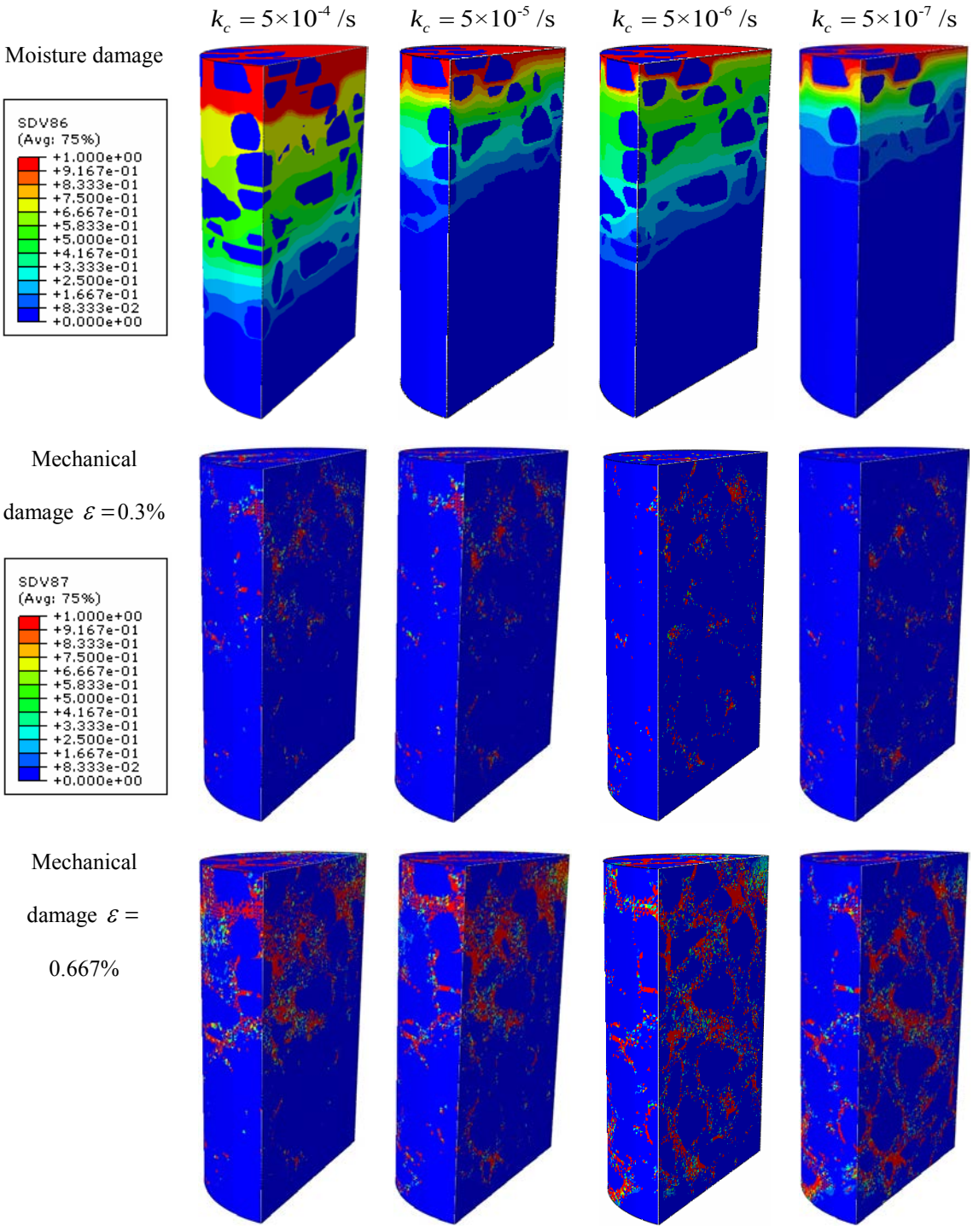

Figure 8.26. Damage distribution due to compressive loading at 3days moisture conditioning time at different strain level for different moisture damage model parameters (strain rate= 6.66 $\times10^{-4}$ 1/s-temperature 20°C).

Mechanical

damage $\varepsilon = 2.0\%$

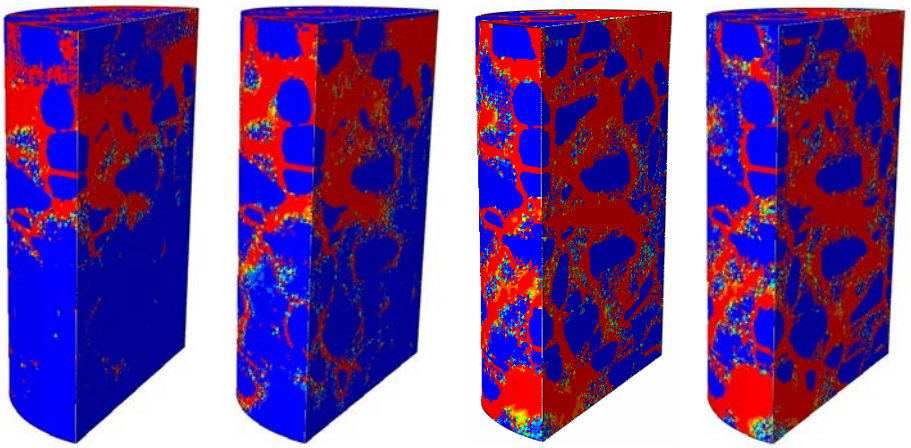

Figure 8.26. Continued.

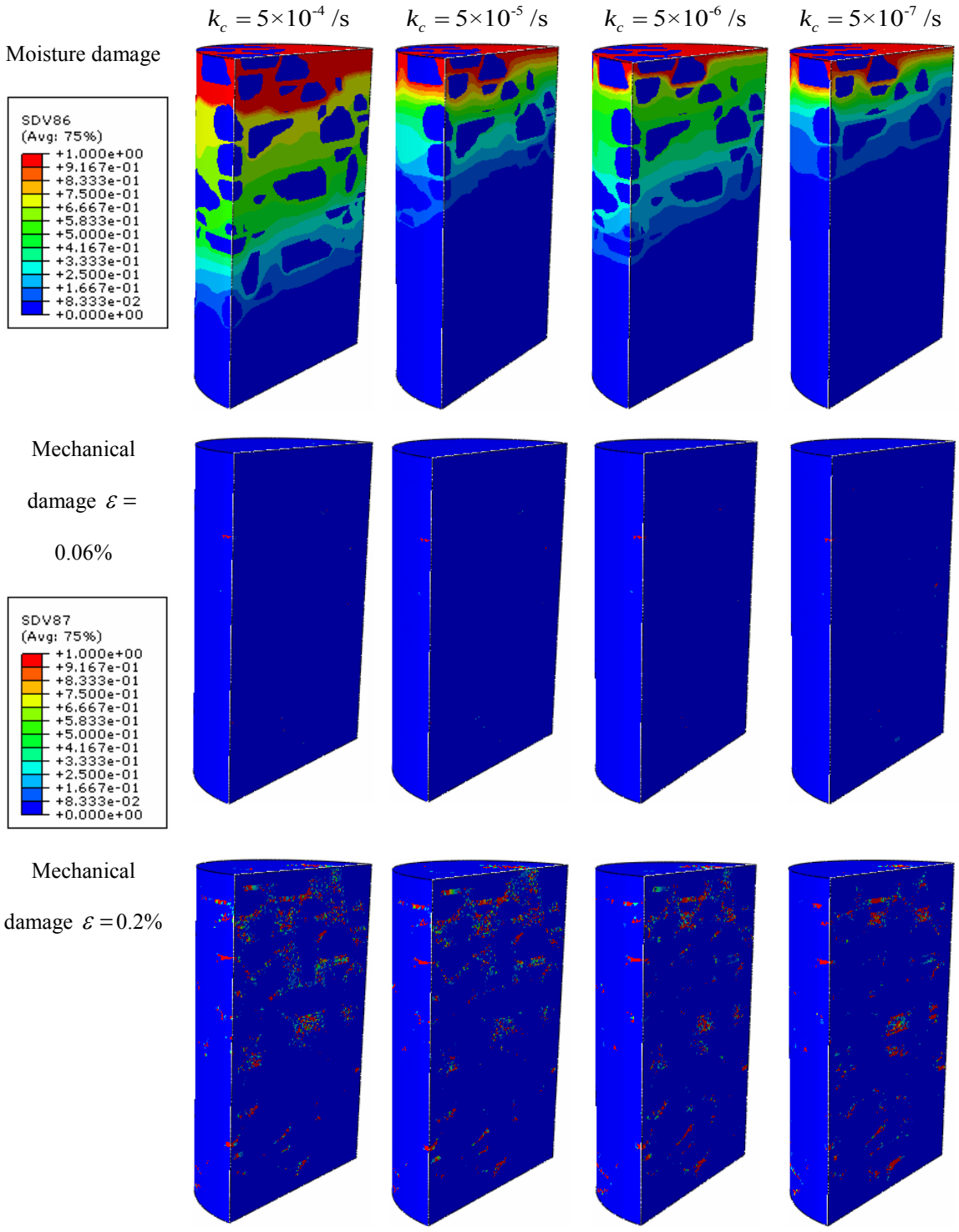

Figure 8.27. Damage distribution due to tensile loading at 3days moisture conditioning time at different strain level for different moisture damage model parameters (strain rate= 6.66 $\times10^{-4}$ 1/s-temperature 20°C).

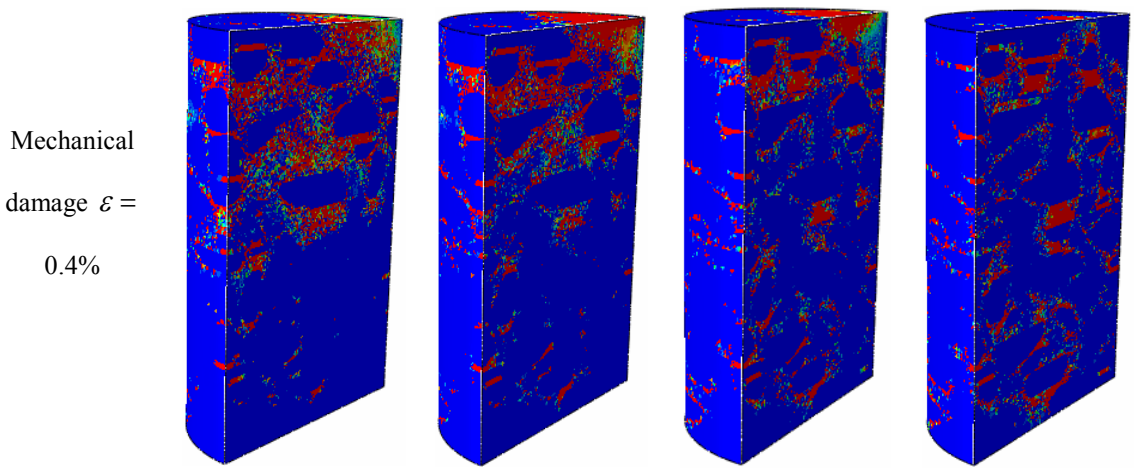

Figure 8.27. Continued.

The Effect of Strain Rate, This section investigates the effect of strain rate on the response of moisture-conditioned samples. Two different compressive and tensile strain rates, 6.66×10^{-4} 1/s and 1.33×10^{-3} *1/s*, were applied to dry and 10 days moisture conditioned 3D cylindrical asphalt concrete at temperature 20°c. Figure 8.28 (a) and (b) illustrate the resulting stress-strain diagram for compression and tension, respectively. It declares that the initial stiffness, the ultimate strength, and the strain to failure decreased with reduction of strain rate and with moisture conditioning. They clearly demonstrate that the asphalt concrete behaves more brittle by increasing the strain rate, as it is expected for the viscous materials. Apparently, the time and temperature dependent materials show less viscous behavior as the loading rate increases. The percentage of ultimate strength's reduction in the moisture-conditioned samples with decreasing the applied strain rate is more than the reduction in the dry ones. It can be interpreted that

the material becomes more brittle with moisture conditioning, so it becomes more sensitive to the strain rate and also existence of water makes the material more viscous, so it becomes more rate sensitive. The result shows that the model can capture the effect of strain rate on the overall response of such viscous material. The figure also clearly declares that the reduction of the ultimate strength is greater at compressive loading than the tension and this reduction increases with decreasing the strain rate. Figure 8.29 and Figure 8.30 illustrate moisture and mechanical damage distribution at different strain level for two cases of strain rate. The figures clearly depict that there is more mechanical damage at lower strain rate, which leads to the lower strength.

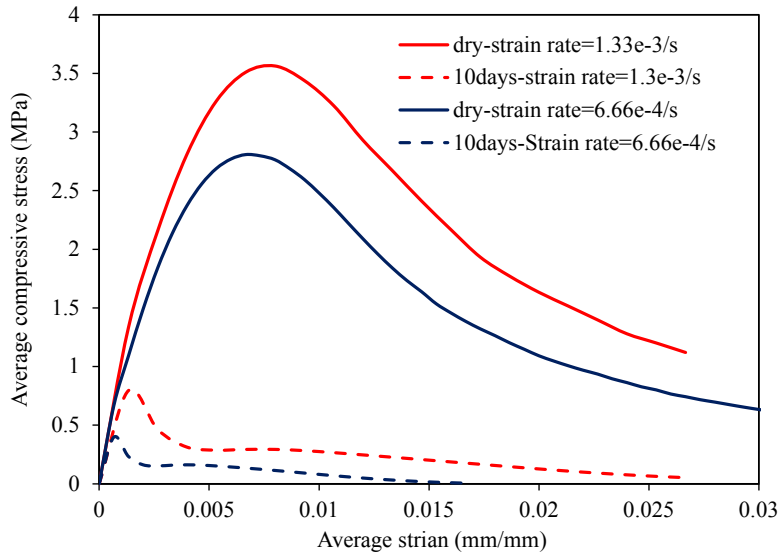

(a)

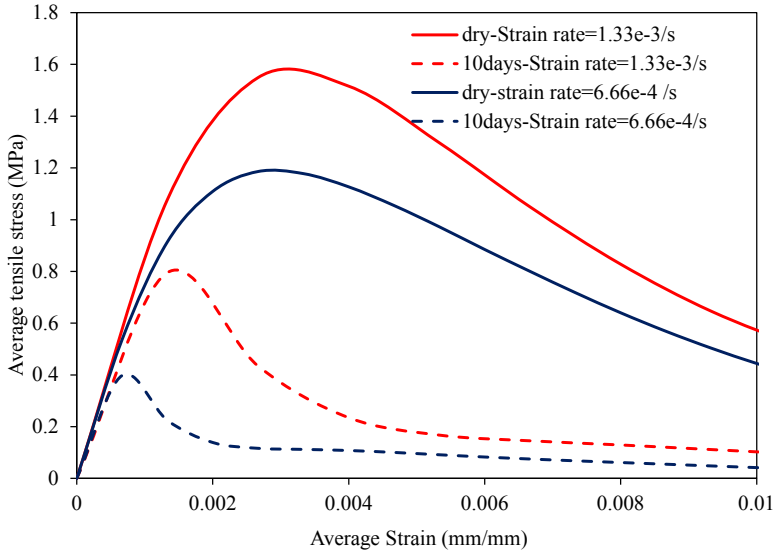

(b)

Figure 8.28. Stress-strain diagrams for two different strain rates at dry and 10days moisture conditioning time under (a) compression and (b) tension loading (temperature 20 °C).

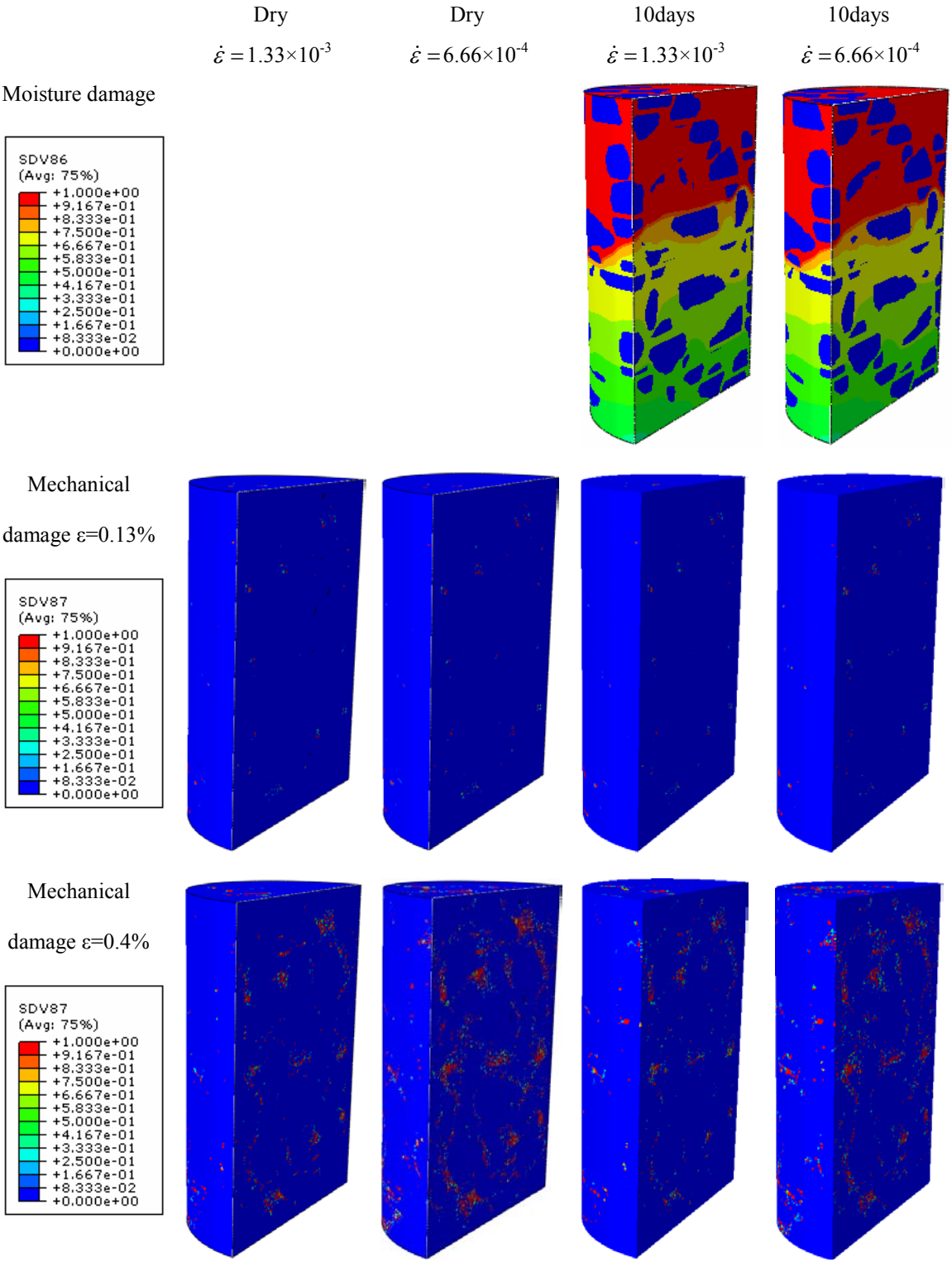

Figure 8.29. Damage distribution due to compressive loading at different strain level for two different strain rates (temperature 20°C).

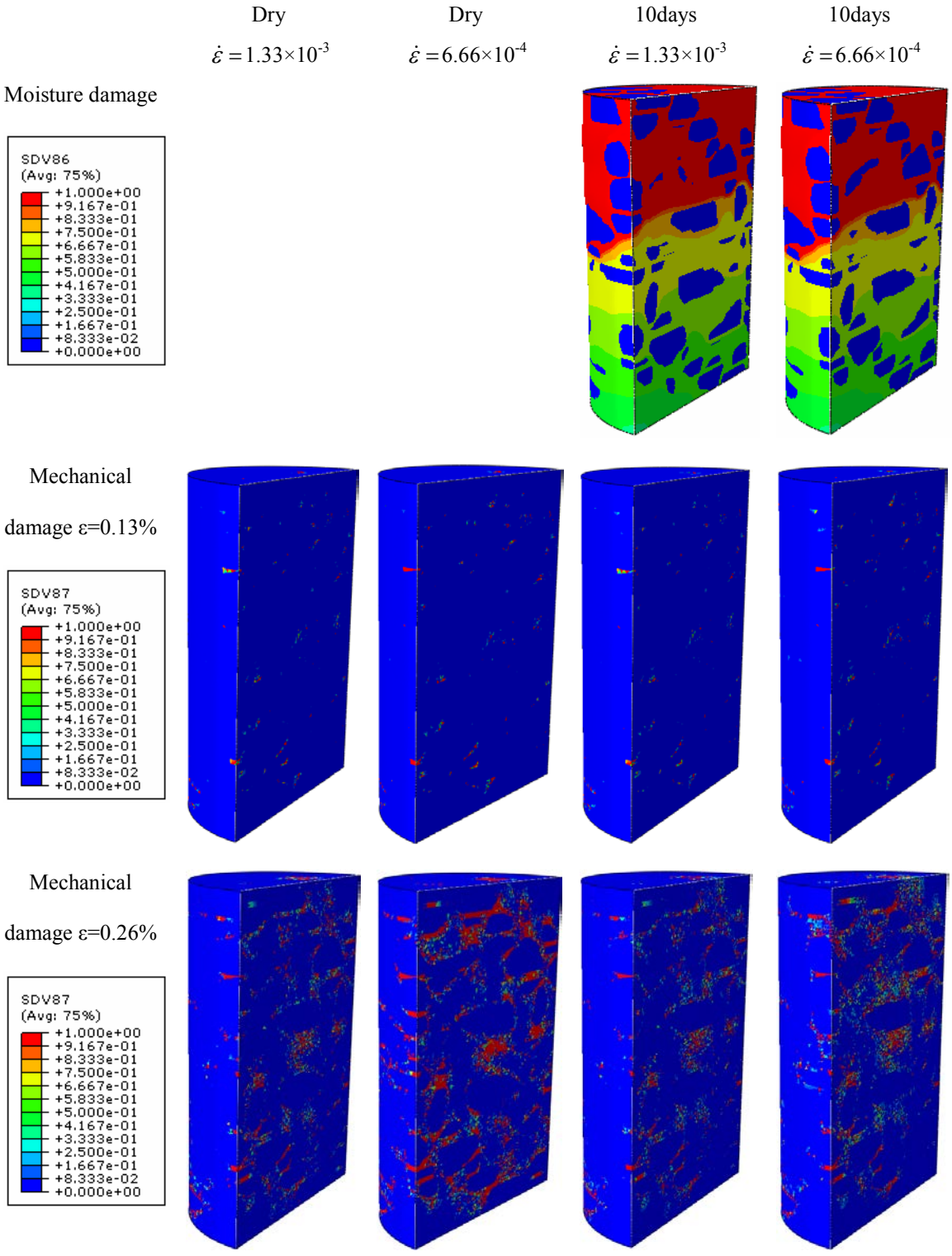

Figure 8.30. Damage distribution due to tensile loading at different strain level for two different strain rates (temperature 20°C).

The Effect of Temperature, This section tries to scrutinize the temperature effect on the behavior of moisture-conditioned asphalt concrete specimens. The 3D cylindrical specimens were subjected to uniaxial compressive and tensile loading at three different temperatures (i.e. 10, 20, and 40) at a 6.66×10-4 *1/s* strain rate for three cases of dry, 3 and 10days moisture conditioning time. Figure 8.31 depicts the average stress-strain diagram results. It declares that the overall behavior of asphalt concrete strongly depends on the temperature. The asphalt concrete's initial stiffness and the ultimate strength significantly decrease as the temperature increases. The percentage of ultimate strength's reduction with increasing moisture-conditioning time rises as the temperature goes up since the material becomes more viscous in higher temperature. Figure 8.32 illustrates mechanical damage distribution at dry condition under compressive loading at three different temperatures. Mechanical damage decreases at higher temperature as the material becomes softer. Figure 8.33 depicts moisture and mechanical damage distribution under compressive loading after 3days moisture conditioning at different temperatures. This figure shows the same approach as at dry state. The mechanical damage decreases at higher temperature because the material becomes softer. The mechanical damage also is concentrating on top of the specimen due to moisture degradation effect. Figure 8.34 and Figure 8.35 depict the damage distribution contours under tensile loading at dry and 3days conditioned cases at three different temperatures. The mechanical damage is concentrating on top of the specimen because of the moisture degradation effect and decreasing at higher temperature.

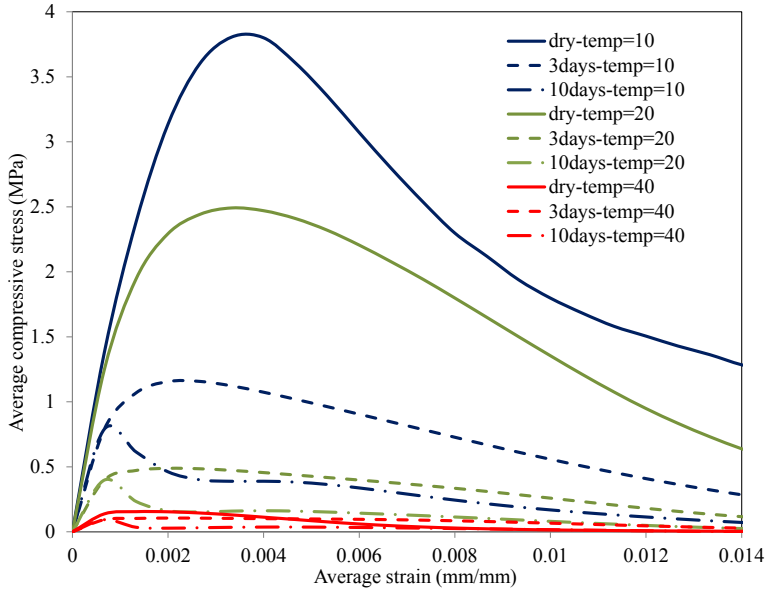

(a)

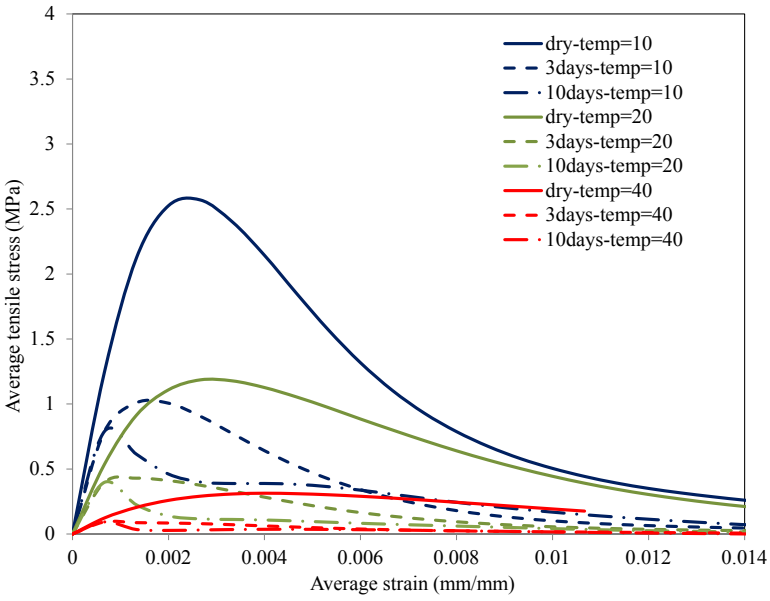

(b)

Figure 8.31. Stress-strain responses at different temperatures for dry and two moisture conditioned specimens under a (a) compressive, (b) tensile loading (strain rate= 6.66×10^{-4} 1/s).

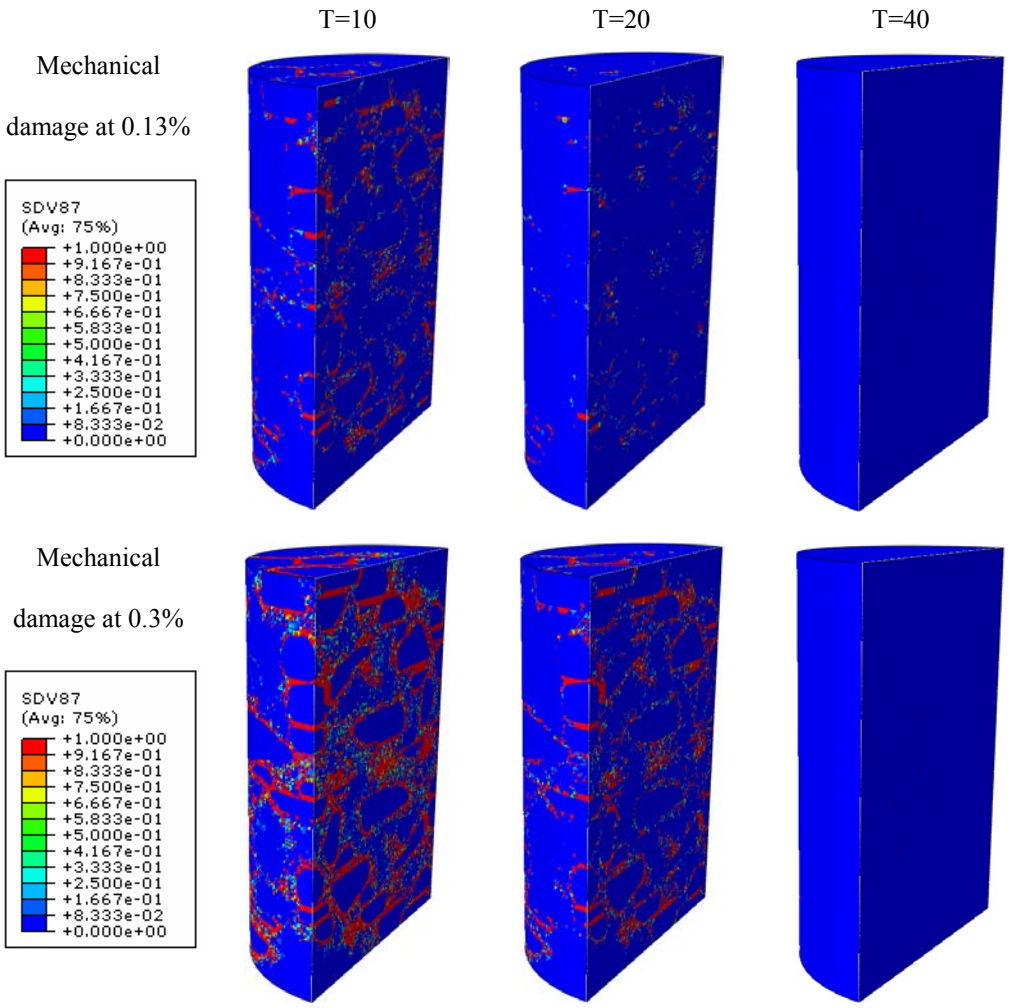

Figure 8.32. Damage distribution due to compressive loading at three different temperatures at dry condition (strain rate= 6.66×10^{-4} 1/s).

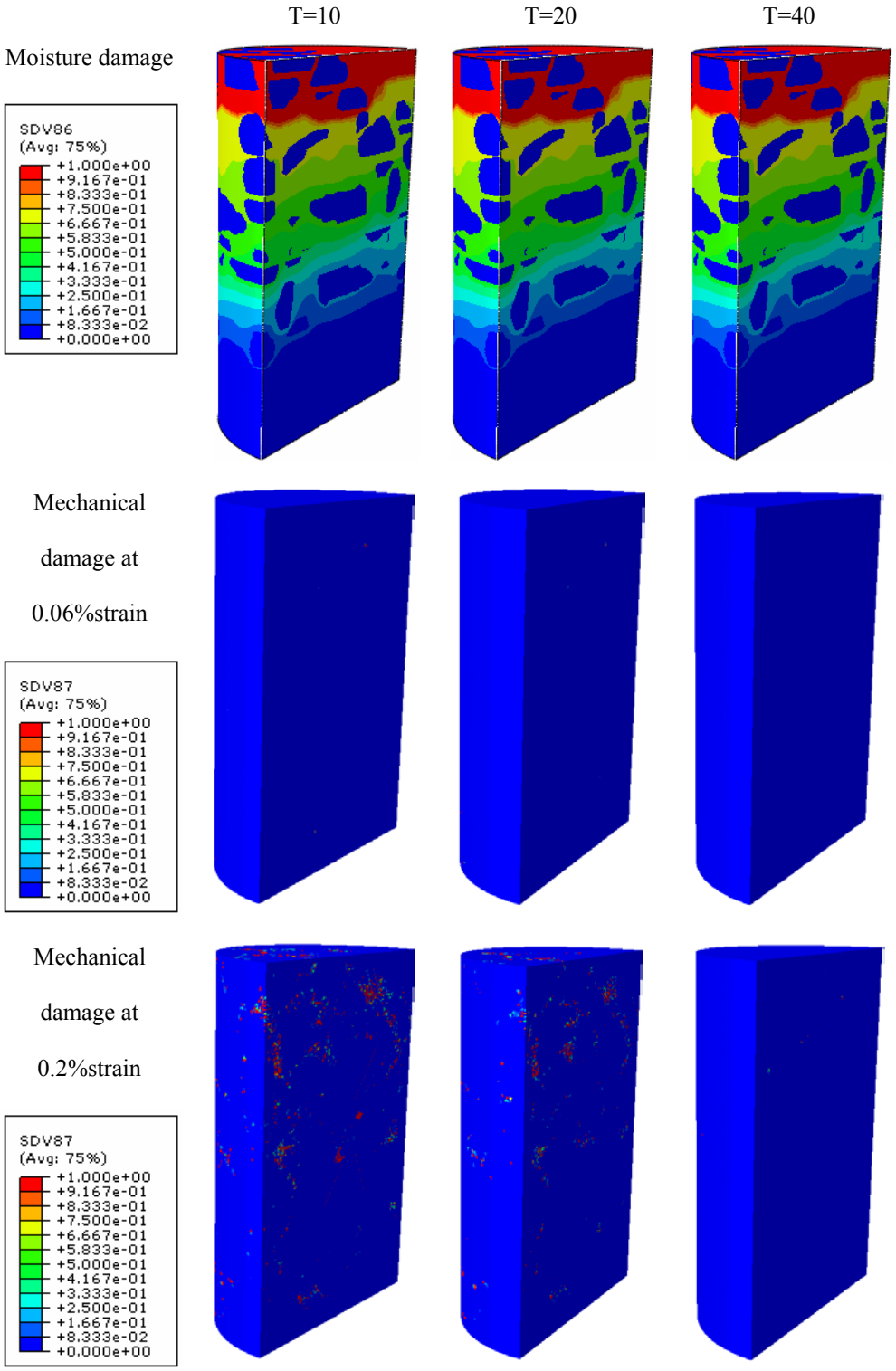

Figure 8.33. Damage distribution due to compressive loading at three different temperatures at 3days moisture conditioning time (strain rate= 6.66 $\times 10^{-4}$ 1/s).

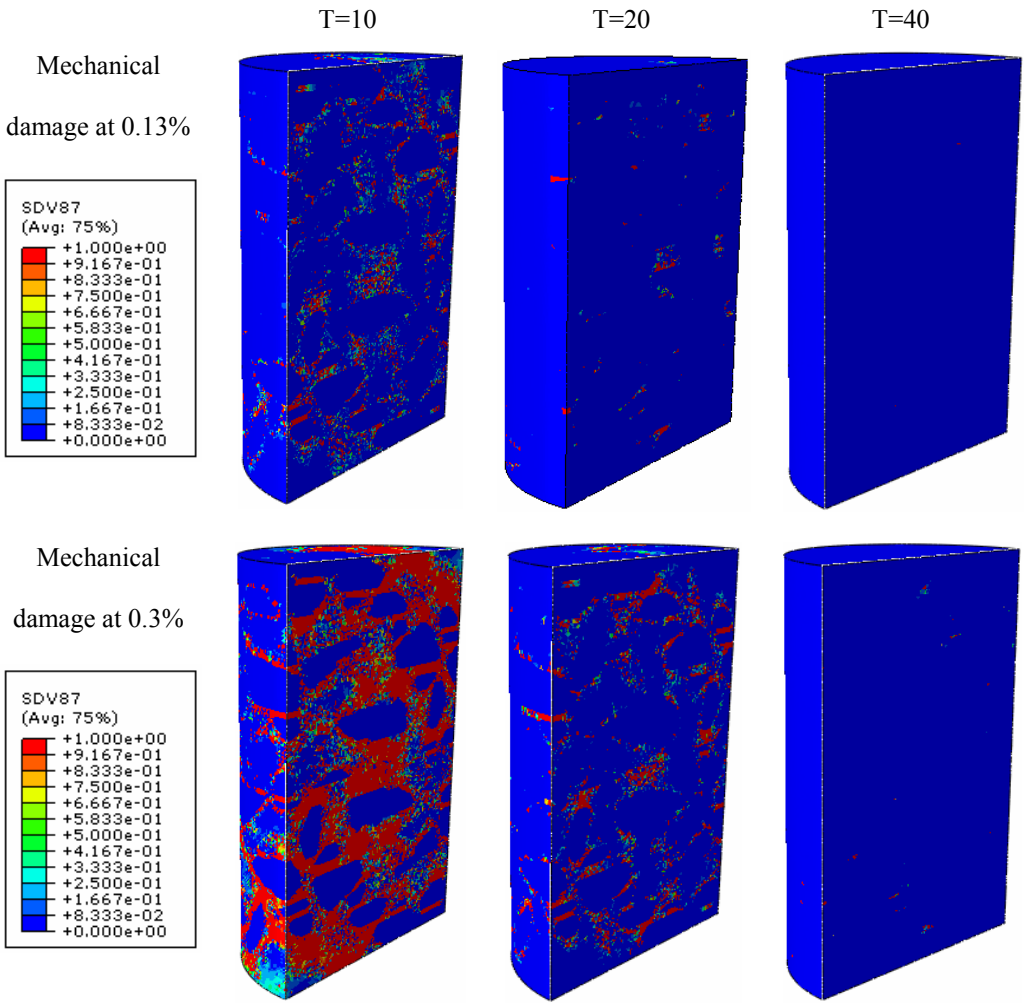

Figure 8.34. Damage distribution due to tensile loading at three different temperatures at dry condition (strain rate= 6.66×10^{-4} 1/s).

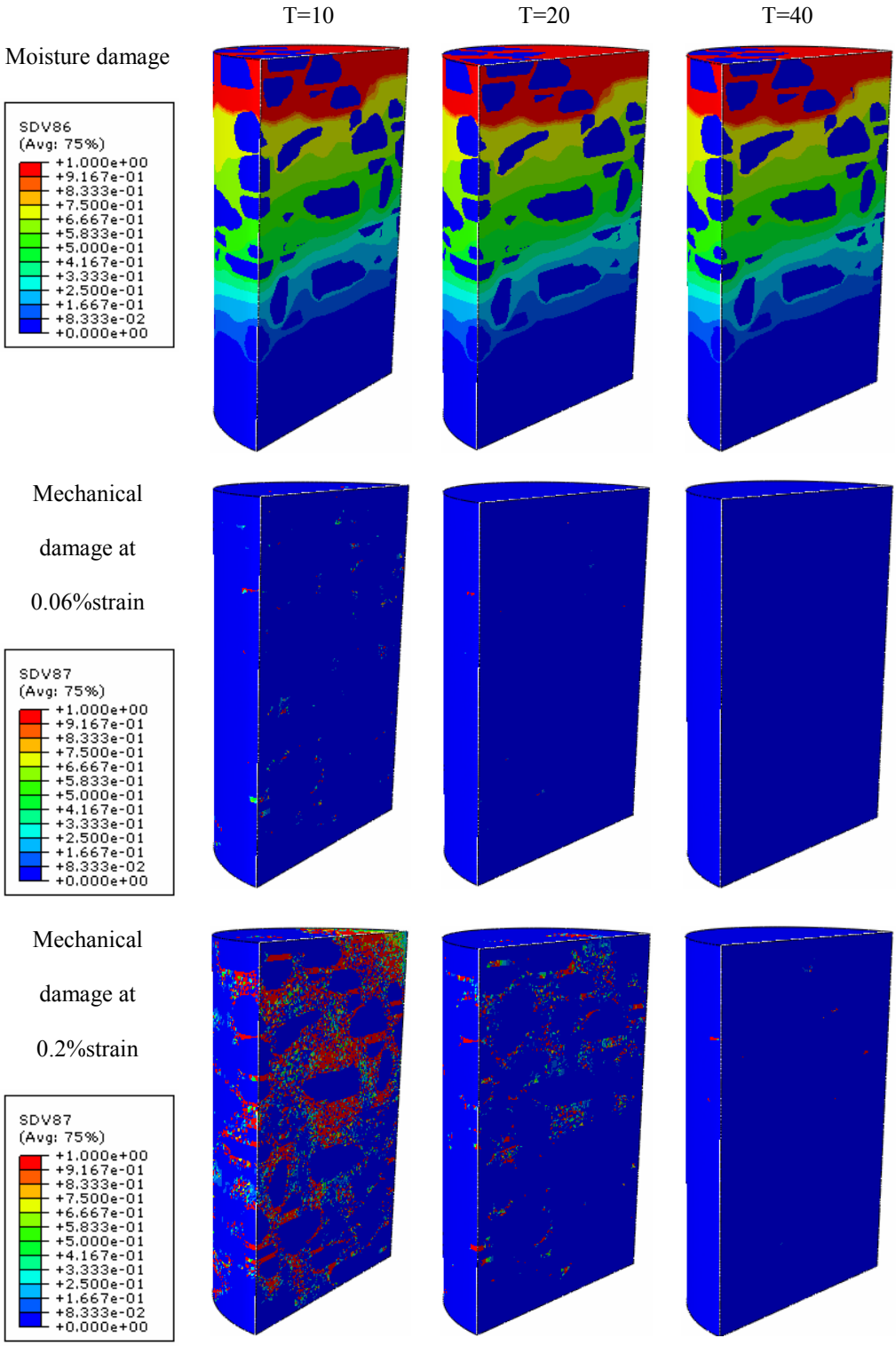

Figure 8.35. Damage distribution due to tensile loading at three different temperatures at 3days moisture conditioning time (strain rate= 6.66 $\times 10^{-4}$ 1/s).

It can be concluded via these results that the mechanical-moisture damaged viscoelastic-viscoplastic model presented here is well-suited to micro-scale simulations of asphalt concrete. It can predict damage propagation through the mixture. The presented micromechanical results have not been verified against experimental results due to lack of experimental data. However, it should be mentioned that the trend is compatible with experimental observations and can be used to obtain an insight toward microstructural behavior of such complicated material. The microstructure model used in this study did not include air voids as a separate phase. Future work will focus on including air voids and accounting for the effects of their interconnectivity on moisture diffusion. In addition, this study assumed constant diffusion coefficients that remain constant during the damage process. However, mechanical damage and moisture damage (in the form of stripping) could affect the rate of moisture diffusion. This process can be modeled in future works by making the diffusion coefficient changes as a function of moisture damage and levels of mechanical damage.

9. CONCLUSION AND RECOMMENDATIONS

The aim of this research was the development of a constitutive relationship and a computational tool for the fundamental analysis of combined mechanical and moisture-induced damage of asphalt concrete. Such a tool contributes greatly to the understanding of the dominant material parameters, which cause moisture-induced failures and helps in improving material selection procedures.

In this dissertation, a continuum coupled moisture mechanical damage mechanics (CCMMDM) framework was developed to couple the degradation effect of moisture to the thermo-mechanical response of asphalt concrete. Thermodynamic, chemical, physical, and mechanical moisture-induced damage processes were identified. A thermodynamic based formulation was developed to consider different effects of moisture in a partially saturated viscous media representing asphalt concrete. Based on the thermodynamic formulation, a moisture damage evolution function was proposed to capture the degradation effect of moisture diffusion and presence inside the asphalt pavement. The effect of pore water pressure was incorporated in the framework to account for damage caused by the increases in stresses.

The developed evolution function was calibrated using pull-off and constant strain rate tests results. The calibrated constitutive relationship was validated against several repeated creep-recovery tests under tension and compression. The calibrated and validated constitutive relationship was applied then to study the effect of moisture on

pavement response. Finally, micromechanical simulations of 2D and 3D microstructural representations of asphalt concrete were conducted. The results of this thesis have led to the following conclusions and recommendations.

9.1.Conclusions

- The moisture damage constitutive relationship along with the micro- and macro-mechanical simulations s can be used to predict damage in asphalt concrete.
- The constituted evolution function represents proper trends regarding the effect of moisture on the mechanical response and permanent deformation of asphalt concrete materials.
- An approach was developed to determine the parametrs of the moisture damage model. Consequently,the PANDA models can be used to predict the moisture susceptibility of different asphalt concrete.
- The micromechanical simulations can be used to compare the moisture susceptibility of different asphalt concrete mixtures. These simulations can help in the selection of materials and mixture design that provide good resistacne to moisture damage.
- The continuum moisture-mechanical damage mechanics (CMMDM) coupling framework provides a simple and robust approach for constitutive modeling of the coupled moisture-mechanical phenomenon.
- The developed thermodynamic framework provides a physically based framework to incorporate the effects of moisture in a partially saturated viscous media.

- The moisture damage constitutive relationship is an improvement over previous relationships for representing moisture damage by making the evolution function time-dependent, sensitive to damage history, and an irreversible mechanism.
- The proposed moisture damage evolution function has the capability of simulating the adhesive and cohesive moisture damage separately as well as simulating the combined effects of adhesive and cohesive damage and the transition between them.
- The incorporated effect of pore water pressure is capable of predicting the coupling between the detrimental effects of moisture presence, pore water pressure, and the mechanical response of asphalt concrete.
- The simulations results declare that the incorporated pore water pressure effect can predict the stress concentration and extra damage around the air voids leading to propagation of damage through the susceptible mastic-aggregate interfaces.
- The moisture damage constitutive relationship can be used effectively to predict the amount of permanent deformation of a moisture-conditioned asphalt pavement.
- The pavement performance simulations demonstrate that the moisture damage can alter the mechanical damage paradigm of asphalt pavement. Moisture damage causes a change in a place of damage concentration.

- Simulation results demonstrate that the coupled moisture-mechanical constitutive relationship presented herein can be effectively used to conduct micromechanical simulations of asphalt concrete. Furthermore, these micromechanical simulations show that moisture-conditioning period, strain rate, and temperature significantly impact the response of asphalt concrete materials.

- The coupled moisture-mechanical constitutive relationship along with the micromechanical simulations can be used effectively to simulate the evolution of damage as well as the region for damage localization within the asphalt concrete microstructure.
- The simulations results illustrate that moisture damage can alter the mechanical damage paradigm and contributes to damage localization within the moisture-degraded region, which can lead to the local and premature failure of pavement structures.
- Micromechanical simulations demonstrate that ultimate strength, stiffness moduli, and failure strain during the monotonic tests decrease as the level of moisture damage increases.
- The presented framework can be used to provide insight on the influence of the asphalt concrete microstructure on its macroscopic response. It can provide an effective tool to design the asphalt concrete.

9.2.Recommendations

- *Enhance the thermodynamic framework;* The developed thermodynamic framework includes several simplifying assumptions. Therefore, extension of the thermodynamic framework in order to consider those assumptions will be helpful in ensuring the robustness of the constitutive model.
- *Incorporate the effect of mastic's washing away*; This study did not consider the effect of mastic erosion due to fast flow of water through interconnected cracks and voids. The ultimate goal of developing constitutive models is to predict the response

of asphalt pavements subjected to realistic loading and environmental conditions. Therefore, it is important to include the effect of mastic's erosion.

- *Construct effective procedures to conduct experimental tests;* In addition to the standard moisture susceptibility experiments, which are currently performed, effective experimental procedures have to be developed for moisture conditioning the specimens and to measure the moisture susceptibility model parameters. The experiment should be designed in a way to be able to consider the effect of different moisture conditioning period and different moisture content. The paramount advantage of such an experiment would be that, instead of disapproving an asphalt mixture because of failing an empirical test, the pavement engineer starts to understand which material property should be improved.
- *Enhancing the numerical implementation;* The implementation procedure should be enhanced to consider the effect of pore water pressure in a partially saturated states. Pore water pressure can be induced in partially saturated cracks and voids as well the saturated ones.
- *Considering the effects of air voids in micromechanical simulations;* Air voids have a substantial effect on the amount of pore water pressure and also on the moisture transform through the asphalt pavement. Simulation of air voids in microstructural representation of asphalt concrete should be considered in future works.
- *Extending the constitutive relationships for the anisotropic cases:* This study presents the isotropic damage response of asphalt mixes. However, the asphalt concrete is highly heterogeneous and anisotropic. Therefore, extension of the

proposed configuration to the anisotropic cases and subsequently proposing anisotropic damage evolution functions will be helpful in ensuring the robustness of the constitutive model for different loading paths and conditions.

REFERENCES

AASHTO, 2007. Standard method of test for resistance of compacted asphalt mixtures to moisture-induced damage. American Association of State and Highway Transportation Officials

Abaqus, 2008. Version 6.8, Habbit, Karlsson and Sorensen, Inc, Providence, RI.

Abu Al-Rub, R., You, T., Masad, E., Little, D., 2011a. Mesomechanical modeling of the thermo-viscoelastic, thermo-viscoplastic, and thermo-viscodamage response of asphalt concrete. International Journal of Advances in Engineering Sciences and Applied Mathematics 3, 14-33.

Abu Al-Rub, R.K., Darabi, M.K., 2012. A thermodynamic framework for constitutive modeling of time-and rate-dependent materials. Part I: Theory. International Journal of Plasticity 34, 61-92.

Abu Al-Rub, R.K., Darabi, M.K., Little, D., Masad, E.A., 2010. A micro-damage healing model that improves prediction of fatigue life of asphalt mixes. International Journal of Engineering Science 48, 966-990.

Abu Al-Rub, R.K., Darabi, M.K., You, T., Masad, E.A., Little, D.N., 2011b. A unified continuum damage mechanics model for predicting the mechanical response of asphalt mixtures and pavements. international Journal of Roads and Airports(IJRA) 1, 68-84.

Abu Al-Rub, R.K., Voyiadjis, G.Z., 2003. On the coupling of anisotropic damage and plasticity models for ductile materials. Int J Solids Struct 40, 2611-2643.

Al-Swailmi, S., Terrel, R.L., 1992. Evaluation of water damage of aphalt concrete mixtures using the environmental conditioning system(ECS). Journal of Association of Asphalt Paving Technologists 61, 405-445.

Arambula, E., Caro, S., Masad, E., 2009. Experimental measurements and numerical simulation of water vapour diffusion through asphalt pavement materials. Journal of Materials in Civil Engineering (ASCE) submitted for evaluation.

Arson, C., Gatmiri, B., 2012. Thermo-hydro-mechanical modeling of damage in unsaturated porous media: Theoretical framework and numerical study of the edz. International Journal for Numerical and Analytical Methods in Geomechanics 36, 272-306.

Aschenbrener, T., McGennis, R.B., Terrel, R.L., 1995. Comparison of several moisture susceptibilty tests to pavements of known field performance. Journal of Association of Asphalt Paving Technologists 64, 163-208.

Avizo, 2009. Avizo user's guide. Visualization Sciences Group, Vordeaux, Frace.

Biot, M.A., 1954. Theory of stress-strain relations in anisotropic viscoelasticity and relaxation phenomena. Journal of Applied Physics 25, 1385-1391.

Birgisson, B., Roque, R., Tia, M., Masad, E., 2005. Development and evaluation of test methods to evaluate water damage and effectiveness of antistripping agents. University of Florida.

Caro, S., Masad, E., Bhasin, A., Little, D., 2008. Moisture susceptibility of asphalt mixtures, part I: Mechanisms. International Journal of Engineering Pavements 9(2), 81-98.

Caro, S., Masad, E., Bhasin, A., Little, D., 2010a. Micromechanical modeling of the influence of material properties on moisture-induced damage in asphalt mixtures. Construction and building materials 24, 1184-1192.

Caro, S., Masad, E.A., Bhasin, A., Little, D., 2010b. Coupled micromechanical model of moisture-induced damage in asphalt mixtures. J Mater Civil Eng 22, 380-388.

Chaboche, J.L., 2003. Damage mechanics. Comprehensive Structural Integrity 2, 213-284.

Cheng, D., Little, D.N., Lytton, R.L., Holste, J.C., 2002. Use of surface free energy properties of the asphalt-aggregate system to predict moisture damage potential. Journal of the Association of Asphalt Paving Technologists (AAPT) 71, 59-88.

Coussy, O., 2004. Poromechanics. Wiley. com.

Darabi, M., Al-Rub, A., RK, M., EA, L., 2012a. A thermodynamic framework for constitutive modeling of time-and rate-dependent materials, part II: Numerical aspects and application to asphalt concrete. International Journal of Plasticity. http://dx. doi. org/10.1016/j. ijplas 3.

Darabi, M.K., Abu Al-Rub, R.K., Masad, E.A., Huang, C.-W., Little, D.N., 2011a. A thermo-viscoelastic–viscoplastic–viscodamage constitutive model for asphaltic materials. Int J Solids Struct 48, 191-207.

Darabi, M.K., Abu Al-Rub, R.K., Masad, E.A., Huang, C.W., Little, D.N., 2011b. A thermo-viscoelastic-viscoplastic-viscodamage constitutive model for asphaltic materials. International Journal of Solids and Structures 48, 191-207.

Darabi, M.K., Abu Al-Rub, R.K., Masad, E.A., Little, D.N., 2011c. Thermodynamic-based model for coupling temperature-dependent viscoelastic, viscoplastic, and viscodamage constitutive behavior of asphalt mixtures. International Journal for Numerical and Analytical Methods in Geomechanics In press, DOI: 10.1002/nag.1030.

Darabi, M.K., Al-Rub, R.K.A., Masad, E.A., Huang, C.-W., Little, D.N., 2011d. A thermo-viscoelastic–viscoplastic–viscodamage constitutive model for asphaltic materials. Int J Solids Struct 48, 191-207.

Darabi, M.K., Al-Rub, R.K.A., Masad, E.A., Little, D.N., 2011e. Thermodynamic-based model for coupling temperature-dependent viscoelastic, viscoplastic, and viscodamage constitutive behavior of asphalt mixtures. International Journal for Numerical and Analytical Methods in Geomechanics, n/a-n/a.

Darabi, M.K., Al-Rub, R.K.A., Masad, E.A., Little, D.N., 2012b. Thermodynamic-based model for coupling temperature-dependent viscoelastic, viscoplastic, and viscodamage constitutive behavior of asphalt mixtures. International Journal for Numerical and Analytical Methods in Geomechanics 36, 817-854.

Dessouky, S.H., 2006. Multiscale approach for modeling hot mix asphalt. Texas A&M University, College Station.

Frémond, M., Nedjar, B., 1996. Damage, gradient of damage and principle of virtual power. Int J Solids Struct 33, 1083-1103.

Graham, M.A., 2009. Damaged viscoelastic-viscoplastic model for asphalt mixes. Texas A&M University, College Station, Texas.

Grandy, J.W.T., 2008. Entropy and the time evolution of macroscopic systems. Oxford University Press.

Gurtin, M.E., 2003. On a framework for small-deformation viscoplasticity: Free energy, microforces, strain gradients. International Journal of Plasticity 19, 47-90.

Haj-Ali, R., Muliana, A., 2004a. Numerical finite element formulation of the schapery non-linear viscoelastic material model. International Journal for Numerical Methods in Engineering 59, 25-45.

Haj-Ali, R.M., Muliana, A.H., 2004b. Numerical finite element formulation of the schapery non-linear viscoelastic material model. International Journal for Numerical Methods in Engineering 59, 25-45.

Huang, C., Masad, E., Muliana, A., Bahia, H., 2007. Nonlinearly viscoelastic analysis of asphalt mixes subjected to shear loading. Mechanics of time-dependent materials 11, 91-110.

Huang, C.W., Abu Al-Rub, R.K., Masad, E.A., Little, D., Airey, G., 2011. Numerical implementation and validation of a nonlinear-viscoelastic and viscoplastic model for asphalt concrete mixes. *International Journal of Pavement Engineering* 12, 433-447.

Kachanov, L.M., 1958. On the concept of damage in creep and in the brittle-elastic range. International Journal of Damage Mechanics 3, 329-337.

Kandhal, P.S., 1992. Moisture susceptibility of HMA mixes: Identification of problem and recommended solutions. National Asphalt Pavement Association.

Karra, S., Rajagopal, K., 2011. Modeling the non-linear viscoelastic response of high temperature polyimides. Mechanics of Materials 43, 54-61.

Kassem, E., Masad, E., Bulut, R., Lytton, R., 2006. Measurements of moisture suction and diffusion-coefficient in hot-mix asphalt and their relationships to moisture damage. Transport Res Rec, 45-54.

Kiggundu, B.M., Roberts, F.L., 1988. Stripping in HMA mixtures: State-of-the-art and critical review of test methods. National Center for Asphalt Technology.

Kim, Y.R., Little, D.N., Lytton, R.L., 2004. Effect of moisture damage on material properties and fatigue resistance of asphalt mixtures, Transportation Research Record: Journal of the Transportation Research Board. TRB, National Research Council, Washington D.C.

Kringos, N., Scarpas, A., 2008. Physical and mechanical moisture susceptibility of asphaltic mixtures. Int J Solids Struct 45, 2671-2685.

Kringos, N., Scarpas, A., Copeland, A., Youtcheff, J., 2008a. Modelling of combined physical-mechanical moisture-induced damage in asphaltic mixes, part 1: Governing processes and formulations. International Journal of Pavement Engineering 9, 115-128.

Kringos, N., Scarpas, A., Copeland, A., Youtcheff, J., 2008b. Modelling of combined physical-mechanical moisture-induced damage in asphaltic mixes, part 2: Moisture susceptible parameters International Journal of Pavement Engineering 9, 129-151.

Kringos, N., Scarpas, A., deBondt, A., 2008c. Determination of moisture susceptibility of mastic-stone bond strength and comparison to thermodynamical properties. Journal of the Association of Asphalt Paving Technologists (AAPT) 77, 475-478.

Kringos, N., Scarpas, A., Kasbergen, C., 2007. Three dimensional elasto-visco-plastic finite element model for combined physical-mechanical moisture induced damage in asphaltic mixes. Journal of the Association of Asphalt Paving Technologists (AAPT) 76, 495-524.

Kringos, N., Scarpas, A., Kasbergen, C., Selvadurai, P., 2008d. Modelling of combined physical-mechanical moisture-induced damage in asphaltic mixes, part 1: Governing processes and formulations. International Journal of Pavement Engineering 9, 115-118.

Kutay, M.E., Aydilek, A.H., Masad, E., 2007a. Computational and experimental evaluation of hydraulic conductivity anisotropy in hot-mix asphalt. International Journal of Pavement Engineering 8(1), 29-43.

Kutay, M.E., Aydilek, A.H., Masad, E., 2007b. Estimation of directional permeability of HMA based on numerical simulation of micro-scale water flow. Estimation of Directional Permeability of HMA Based on Numerical Simulation of Micro-scale Water Flow 2001, 29-36.

Lai, J., Bakker, A., 1996a. 3-D schapery representation for non-linear viscoelasticity and finite element implementation. Computational Mechanics 18, 182-191.

Lai, J.J., Bakker, A., 1996b. 3-D schapery representation for non-linear viscoelasticity and finite element implementation. Computational Mechanics 18, 182-191.

Lemaitre, J., Chaboche, J., 1990. Mechanics of solid materials. Cambridge University Press, Cambridge.

Liu, X., 2003. Numerical modeling of porous media response under static and dynamic load conditions. Delft Univeristy of Technology.

Lottman, R.P., 1982. Laboratory test method for predicting moisture-induced damage to asphalt concrete, Transportation Research Record: Journal of the Transportation Research Board. TRB, National Research Council, Washington D.C., pp. 88-95.

Majidzadeh, K., Brovold, F.N., 1966-9. Effect of water on bitumen-aggregate mixtures Florida State Road Department, Washington D.C.

Martyushev, L., Seleznev, V., 2006. Maximum entropy production principle in physics, chemistry and biology. Physics reports 426, 1-45.

Masad, E., Al-Rousan, T., Button, J., Little, D.N., Tutumluer, E., 2005a. Tests methods for characterizing aggregate shape, texture and angualrity, National Cooperative Highway Research Program, National Research Council. Publication NCHRP-4-30A, Washington, D. C.

Masad, E., Al Omari, A., Chen, H.C., 2007a. Computations of permeability tensor coefficients and anisotropy of asphalt concrete based on microstructure simulation of fluid flow. Comp Mater Sci 40, 449-459.

Masad, E., Arambula, E., Ketcham, R.A., Abbas, A.R., Martin, A.E., 2007b. Nondestructive measurements of moisture transport in asphalt mixtures. Journal of the Association of Asphalt Paving Technologists (AAPT) 76, 919-952.

Masad, E., Dessouky, S., Little, D., 2007c. Development of an elastoviscoplastic microstructural-based continuum model to predict permanent deformation in hot mix asphalt. International Journal of Geomechanics 7, 119.

Masad, E., Tashman, L., Little, D., Zbib, H., 2005b. Viscoplastic modeling of asphalt mixes with the effects of anisotropy, damage and aggregate characteristics. Mechanics of Materials 37, 1242-1256.

Murali Krishnan, J., Rajagopal, K., 2004. Thermodynamic framework for the constitutive modeling of asphalt concrete: Theory and applications. J Mater Civil Eng 16, 155-166.

Odqvist, F., J., H., 1961. Some aspects of creep rupture. Arkiv for Fysik 19, 379-382.

Perzyna, P., 1971a. Thermodynamic theory of viscoelasticity. Advances in Applied Mechanics 11, 313-354.

Perzyna, P., 1971b. Thermodynamic theory of viscoplasticity. Advances in Applied Mechanics 11, 313-354.

Pinto, I., Kim, Y., Ban, G., 2009. Moisture sensitivity of hot mix asphalt (HMA) mixtures in nebrreska-phaseii`. University of Nebraska-Lincoln (Department of Civil Engineering), Lincoln.

Plancher, H., Miyake, G., Venable, R.L., Petersen, J.C., A simple laboratory test to indicate the susceptibility of asphalt-aggregate mixtures to moisture damage during freeze-thaw cycling. Proc., Canadian Technical Asphalt Association Meeting 25, 246-264.

Pocius, 1997. Adhesion and adhesives thechnology. Hanser/Gardner Publications Inc., Columbus, OH.

Rabotnov, Y.N., 1969. Thermodynamic theory of viscoplastcity. Advances in Applied Mechanics 11, 212-354.

Rahmani, E., Darabi, M.K., Abu Al-Rub, R.K., Kassem, E., Masad, E., Little, D.N., in press. Effect of confinement pressure on the nonlinear-viscoelastic response of asphalt concrete at high temperatures. Construction and Building Materials.

Rahmani, E., Darabi, M.K., Abu Al-Rub, R.K., Kassem, E., Masad, E.A., Little, D.N., 2013. Effect of confinement pressure on the nonlinear-viscoelastic response of asphalt concrete at high temperatures. Construction and Building Materials 47, 779-788.

Schapery, R.A., 1969. The characterization of nonlinear viscoelastic materials. Polymer Engineering and Science 9, 295–310.

Shakiba, M., Abu Al-Rub, R.K., Darabi, M.K., You, T., Masad, E.A., Little, D.N., 2013. A continuum coupled moisture-mechanical damage model for asphalt concrete, Transportation Research Board 92nd Annual Meeting.

Tarrar, A.R., Wagh, V.P., 1991. The effects of the physical and chemical charactristics of the aggregate on bonding, Strategic Highway Research Program, National Research Council. Publication SHRP-A/UIR-91-507, Washington, D. C.

Tarrar, A.R., Wagh, V.P., 1992. Innovative tests to predict the strength and type of asphalt-aggregate bonds. Fuel Science and Technology International 10, 457-474.

Tashman, L., Masad, E., Little, D., Zbib, H., 2005. A micro structure-based viscoplastic model for asphalt concrete. International Journal of Plasticity 21, 1659-1685.

Taylor, M.A., Khosla, N.P., 1983. Stripping of asphalt pavements: State of the art, Journal of the Transportation Research Board, TRB. Transportation Research Board, Washington D.C., pp. 150-158.

Voyiadjis, G.Z., Deliktas, B., 2000. A coupled anisotropic damage model for the inelastic response of composite materials. Computer Methods in Applied Mechanics and Engineering 183, 159-199.

Voyiadjis, G.Z., Kattan, P.I., 1992. A plasticity-damage theory for large deformation of solids—I. Theoretical formulation. International Journal of Engineering Science 30, 1089-1108.

Voyiadjis, G.Z., Kattan, P.I., 1999. Advances in damage mechanics: Metals and metal matrix composites. Elsevier.

Yang, Q., Tham, L., Swoboda, G., 2005. Normality structures with homogeneous kinetic rate laws. Journal of applied mechanics 72, 322-329.

You, T., Abu Al-Rub, R.K., Darabi, M.K., Masad, E.A., Little, D.N., 2012. Three-dimensional microstructural modeling of asphalt concrete using a unified viscoelastic–viscoplastic–viscodamage model. Construction and Building Materials 28, 531-548.

You, T., Al-Rub, R.K.A., Darabi, M.K., Masad, E.A., Little, D.N., 2011. Three-dimensional microstructural modeling of asphalt concrete using a unified viscoelastic-viscoplastic-viscodamage model.

Youtcheff, J., Aurilio, V., 1997. Moisture sensitivity of asphalt binder: Evaluation and modeling of the pneumatic adhesion test results. 42nd Annual Conference of Canadian Technical Aphalt Association.

Ziegler, H., 1977. An introduction to thermodynamics. North-Holland.

Ziegler, H., 1981. Discussion of some objections to thermomechanical orthogonality. Ingenieur-Archiv 50, 149-164.